Vol. 8
Issue 2
July 2020
ISSN: 2321-3388

Science & Technology Journal

MIZORAM UNIVERSITY
(Accredited 'A' Grade by NAAC)
Aizawl-796004, India

Science and Technology Journal

Vol. 8, Issue 2, July 2020

ISSN: 2321–3388

DISCLAIMER

Publishing Consultancy
EXCEL INDIA PUBLISHERS
91 A, Ground Floor
Pratik Market, Munirka, New Delhi-110067
Tel: +91-11-2671 1755/ 2755/ 3755/ 5755
Fax: +91-11-2671 6755
E-mail: publishing@groupexcelindia.com
Web: www.groupexcelindia.com

Typeset by
Excel Prepress Services, New Delhi–110067
E-mail: prepress@groupexcelindia.com

Printed by
Excel Printing Universe, New Delhi–110067
E-mail: printing@groupexcelindia.com

Science and Technology Journal

Editorial Board

Patron

Advisor

Editor-in-Chief

Editorial Board

National Advisory Board

Contents

Science and Technology Journal Vol. 8 Issue 2 July 2020 ISSN: 2321-3388

Root Mass and Elemental Concentrations in an Irish Oak Woodland

Francis Q. Brearley
Department of Natural Sciences, Manchester Metropolitan University,
Chester Street, Manchester, M1 5GD, UK
(Adjunct Faculty at Department of Forestry, Mizoram University, Aizawl 796004, India)
E-mail: f.q.brearley@mmu.ac.uk

Abstract—Fine roots (< 2 mm diameter) are key for nutrient and carbon cycling in forests but less well studied for oak than other European trees. To better understand controls on root mass and nutrient concentrations in oak stands a study was conducted at Glendalough in Ireland. Roots were removed from soils and measured for biomass, length and nutrient concentrations along with soil nutrients. Fine root mass was 360 g m^{-2} and comparable to other oak stands. Whilst root N concentrations were high, P concentrations were low and N, P, K, Mg but not C or Ca were at greater cocentrations in fine roots compared to coarse (2- 5 mm) roots. The root Ca:Al ratio suggested Al toxicity although this was less marked in organic-rich soils. Neither root mass nor root nutrient concentrations showed particularly strong correlations with soil nutrients or pH. Whilst our data agree well with other similar studies, improved analysis by separating live and dead roots will further advance our understanding of controls on forest fine root dynamics.

INTRODUCTION

Roots are the key organ through which plants obtain nutrients and water from the soil. Roots are a dynamic component of ecosystems and can be responsible for more than half of forest net primary productivity playing an important role in forest biogeochemical cycling (Vogt *et al*. 1986). Additionally, they act as carbon stocks in forest ecosystems and return organic carbon and other elements to the soil upon their senescence. Whilst we know that root biomass can be influenced by forest above-ground biomass (Finér *et al*. 2011), stand age (Leuschner & Hertel 2003; Singha *et al*. 2020), climate (Leuschner & Hertel 2003), seasonality (Lalnunzira *et al*. 2019) and soil fertility (Aber *et al*. 1985; Brearley 2011) among others, clear controls over forest fine root (< 2 mm diameter) biomass are still not fully understood. This is important for a better understanding of forest carbon dynamics. In general, root biomass decreases in more fertile soils as trees do not need to invest so much in below-ground components to obtain essential resources but toxic elements such as aluminium may negatively affect roots in acidic soils. Roots contain a sizeable proportion of ecosystem nutrient stocks and the ratios between elements in plant tissues ('ecological stoichiometry') can be used to help us understand nutrient limitation in ecosystems (Yuan *et al*. 2011), stress due to soil acidity (Vanguelova *et al*. 2007) and other physiological or biogeochemical processes. Roots often proliferate into moister and more nutrient-rich patches in soil to obtain the resources within and this may then influence their nutrient budgets and it has been shown that root nutrient concentrations are broadly associated with nutrient concentrations in soil (Yuan *et al*. 2011) but also differ according to plant type and biome. Numerous studies of root biomass have been conducted in European forests (Leuschner & Hertel 2003; Wang *et al*. 2019a) but oak has been less studied than other tree taxa. The aim of this study was, therefore, to determine root biomass and nutrient concentrations and the linkages between them in an oak woodland in Ireland.

MATERIALS AND METHODS

Root mass was determined in a sessile oak (*Quercus petraea* (Matt.) Liebl., Fagaceae) stand at Glendalough (53° 0' N, 6° 19' W) in eastern Ireland in October 2006. The trees here are about 150-200 years old having been replanted after intensive coppicing. Soil cores were taken with a cylindrical 4.2 cm diameter x 10 cm depth corer and live and dead roots were removed by washing the cores over a sieve (1 mm) and picking all identifiable root material off using tweezers. Root length was estimated by the gridline intersect method of

Newman (1966). Roots were then divided into two diameter classes (< 2 mm diameter and 2-5 mm diameter), oven-dried and weighed. Soils were taken from each core hole and analysed for pH with a 1:2.5 suspension in deionised water using a Sartorius PB-11 pH meter. Loss-on-ignition was determined by ignition at 550 ° C for 5 hours and total carbon and nitrogen were assessed using a Leco TruSpec CN elemental analyser. Extractable phosphorus and cations were determined by extraction with Mehlich 1 solution (1:10 soil:solution ratio) and analysis on a Thermo iCAP 6300 Duo ICP-OES. Root elemental concentrations for both of the root diameter classes were assessed by using a Leco TruSpec CN elemental analyser or a microwave-assisted nitric acid digestion followed by dilution with deionised water and subsequent analysis on a Thermo iCAP 6300 Duo ICP-OES.

RESULTS AND DISCUSSION

Mean fine root (< 2 mm) mass was 360 ± 104 (standard deviation) g m^{-2} (Figure 1) which falls within the range of data from European *Quercus* stands presented by Leuschner & Hertel (2003) that was 163 to 415 g m^{-2}. Coarse roots (2-5 mm) contributed a similar mass of 385 ± 179 g m^{-2} (Figure 1) which contrasts with Leuschner *et al.* (2001) who found this category of roots to contribute about three-quarters of the root biomass in the upper soil horizon in a German woodland. Of course, we have to take care when making such comparisons with other studies as this study included both live and dead roots that will increase the overall mass, but it only examined the top 10 cm of soil which is shallower than many other studies thereby decreasing the comparative mass. Nevertheless, oak appears to have a lesser root biomass than other deciduous species (Leuschner & Hertel 2003; Jagodzinki *et al.* 2016). The total root length for all roots (< 5 mm) was 2020 m m^{-2}, i.e. just over 2 km, and the specific root length including both diameter classes was 634 ± 351 cm g^{-1}.

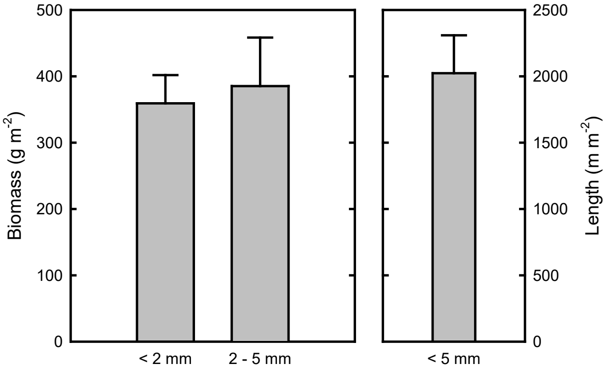

Fig. 1: Root Mass and Length in a *Quercus petraea* Woodland at Glendalough, Ireland. Bars Represent Mean ± Standard Error

The soils were acidic although the organic matter, and hence nutrient concentrations, were quite variable among samples (Table 1). Fine root (< 2 mm) mass was positively correlated with soil nutrients and negatively with pH; the only one of these that was statistically significant was the correlation between fine root mass and soil P ($p < 0.05$). Correlations between total (< 5 mm) root mass or root length were generally much weaker. This was broadly in agreement with the study of Wang *et al.* (2019a) who showed soil C concentrations were a strong predictor of fine root biomass (and necromass) across a number of studies, however, they also found pH to be positively correlated with root mass in contrast to this study. This data also indicates that root mass of oak is not insensitive to soil acidity as suggested by Leuschner & Hertel (2003) and actually increases in more acidic pH soils although this could be related to such soils having a greater amount of organic matter within them and this could be a mechanism to obtain nutrients from more recalcitrant litter. Alternatively, the data presented here could represent an increase in root necromass in more acidic soils, but this suggestion would need further work for confirmation.

Table 1: Soil Nutrient Parameters in a *Quercus petraea* Woodland at Glendalough, Ireland Values Represent Mean ± Standard Deviation

pH	3.57 ± 0.20
Loss-on-ignition (%)	24.9 ± 14.7
Total C (%)	12.6 ± 7.6
Total N (%)	0.77 ± 0.30
Extractable P (μg g^{-1})	72.2 ± 55.2
Extractable K (μg g^{-1})	186 ± 132
Extractable Ca (μg g^{-1})	237 ± 194
Extractable Mg (μg g^{-1})	203 ± 242

Fine root nutrient concentrations showed a C:N:P of 750:19:1. Compared to the global mean for root nutrient concentrations in Wang *et al.* (2019b), N concentrations were greater whereas P concentrations were less (Table 2), leading to an N:P ratio of 19:1 which is wider than the global mean of 12:1 in Wang *et al.* (2019b) and suggestive of an ecosystem leaning towards P, rather than N, limitation which is supported by the correlation between fine root mass and soil P concentrations. Also likely is that the inclusion of dead roots in our analysis led to a wider N:P ratio (Yuan *et al.* 2011). Nitrogen, K and Mg were at greater concentrations in the fine (< 2 mm) roots (P showed a similar magnitude of increase but was not significantly different) whilst no differences were seen for C and Ca between diameter classes (Table 2). This agrees with the overall analyses of Gordon & Jackson (2000) and Yuan *et al.* (2011) who showed declines in N, P and Mg with diameter but not Ca or K although there is some variation with K (Yanai *et al.* 2018). Correlations between fine root mass and soil nutrient concentrations were mostly positive although not statistically significant. The Ca:Al ratios mostly averaged around 0.40 in broad agreement with the study of ten European *Quercus* stands by Bakker (1999) but one root sample that was actually from the most acidic soil had a Ca:Al ratio of around 5, due to markedly lower Al concentrations. The soil this sample was removed from was much more organic-rich compared to the others and it has been shown that Ca:Al ratios in organic horizons are generally greater than unity (Vanguelova *et al.* 2007).

Table 2: Root Elemental Concentrations for Two Diameter Classes in a *Quercus petraea* Woodland at Glendalough, Ireland Values Represent Mean ± Standard Error and the Final Column Shows Differences between Diameter Classes using a *t*-test with * = *p* < 0.001, ** = *p* < 0.01, * = *p* < 0.05, and ns = Not Significant**

	< 2 mm	2-5 mm	
Carbon (%)	47.5 ± 0.09	46.8 ± 0.06	ns
Nitrogen (mg g^{-1})	12.1 ± 0.71	9.0 ± 0.59	**
Phosphorus (mg g^{-1})	0.63 ± 0.09	0.44 ± 0.08	ns
Potassium (mg g^{-1})	1.97 ± 0.07	1.09 ± 0.12	***
Calcium (mg g^{-1})	1.36 ± 0.15	1.32 ± 0.46	ns
Magnesium (mg g^{-1})	0.93 ± 0.05	0.60 ± 0.09	*

In conclusion, this study adds data on root mass and nutrient concentrations from this Irish *Quercus* stand and found they were comparable to other European oaks from which there is surprisingly little data compared to members of the Pinaceae. Additional sampling and comparison of deeper soil layers along with separation of live and dead roots and more detailed analysis of root morphology will further improve our knowledge on oak root ecological functioning.

REFERENCES

Aber, J. D., Melillo, J. M., Nadelhoffer, K. J., McClaughty, A. A., & Pastor, J. (1985) Fine root turnover in forest ecosystems in relation to quantity and form of nitrogen availability: a comparison of two methods. Oecologia 66, 317–321.

Bakker, M. R. (1999) Fine-root parameters as indicators of sustainability of forest ecosystems. Forest Ecology and Management 122, 7-16.

Brearley, F. Q. (2011) Below-ground secondary succession in tropical forests of Borneo. Journal of Tropical Ecology 27, 413–420.

Finér, L., Ohashi, M., Noguchi, K. & Hirano, Y. (2011) Factors causing variation in fine root biomass in forest ecosystems. Forest Ecology and Management 261, 265–277.

Gordon, W. S. & Jackson, R. B. (2000) Nutrient concentrations in fine roots. Ecology 81, 275-280.

Jagodzinski, A. M., Ziółkowski, J. & Warnkowska A. (2016) Tree age effects on fine root biomass and morphology over chronosequences of *Fagus sylvatica*, *Quercus robur* and *Alnus glutinosa*. PLoS One 11, e0148668.

Lalnunzira, C., Brearley, F. Q. & Tripathi, S. K. (2019) Root growth dynamics during recovery of tropical mountain forest in North-east India. Journal of Mountain Science 16, 2335–2347.

Leuschner, C. & Hertel, D. (2003) Fine root biomass of temperate forests in relation to soil acidity and fertility, climate, age and species. Progress in Botany 64, 405-438.

Leuschner, C., Hertel, D., Coners, H. & Büttner, V. (2001) Root competition between beech and oak: a hypothesis. Oecologia 126, 276-284.

Newman, E. I. (1966) A method of estimating the total length of root in a sample. Journal of Applied Ecology 3, 139-145.

Singha, D., Brearley, F. Q. & Tripathi, S. K. (2020) Fine root and soil nitrogen dynamics during stand development following shifting agriculture in Northeast India. Forests 11, 1236.

Vanguelova, E. I., Hirano, Y., Eldhuset, T. D., Sas-Paszt, L., Bakker, M. R., Püttsepp, Brunner, I., Lõhmus, K. & Godbold, D. (2007) Tree fine root Ca/Al molar ratio –indicator of Al and acidity stress. Plant Biosystems 141, 460-480.

Wang, C., Brunner, I., Zong, S. & Li, M.-H. (2019a) The dynamics of living and dead fine roots of forest biomes across the northern hemisphere. Forests 10, 953.

Vogt, K. A., Grier, C. C. & Vogt, D. J. (1986) Production, turnover, and nutrient dynamics of above- and belowground detritus of world forests. Advances in Ecological Research 15, 303-377.

Wang, Z., Yu, K., Lv, S., Niklas, K. J., Mipam, T. D., Crowther, T. W., Umaña, M. N., Zhao, Q., Huang, H. & Reich, P. B. (2019b) The scaling of fine root nitrogen versus phosphorus in terrestrial plants: a global synthesis. *Functional Ecology* 33, 2081- 2094.

Yanai, R. D., Walsh, G. E., Yang, Y., Blodgett, C. A., Bae, K. & Park, B. B. (2018) Nutrient concentrations of roots vary with diameter, depth, and site in New Hampshire northern hardwoods. Canadian Journal of Forest Research 48, 32-41.

Yuan, Z. Y., Chen, H. Y. H. & Reich, P. B. (2011) Global-scale latitudinal patterns of plant fine-root nitrogen and phosphorus. Nature Communications 2, 344.

Science and Technology Journal Vol. 8 Issue 2 July 2020 ISSN: 2321-3388

Effects of Disturbance on Seed Production and Seed Rain Dynamics of *Dendrocalamus longispathus* Kurz in Bamboo Natural Forests of Mizoram, North-East, India

Lalrammuana Sailo[1], F. Lalnunmawia[2]* and Kalidas Upadhyaya[3]
[1,2]Department. of Botany, Mizoram University, Aizawl, Mizoram–796004, India
[2]Department. of Forestry, Mizoram University, Aizawl, Mizoram–796009, India
Email: [1]muantea.sailo@gmail.com, *[2]fmawia@rediffmail.com

Abstract—*Dendrocalamus longispathus* Kurz clumps located in Mamit District, Mizoram, India was observed to study the quality and quantity of seed produced during the sporadic, flowering as an ecological indicator for further flowering precaution in Mizoram. Soil seed bank and seed drop quantity of seeds in a culm were estimted for further afforestation of *D. longispathus* in a barren or wasteland lands in tropical sloppy mountainous conditions. The study would be applicable in reforestation, programme by dispersing the collected seeds into a forest areas decreasing in numbers of *D. longispathus*. The study between the disturbed site and undisturbed site compared to understand the difference between the two sites in terms of their seed quantity, seed drop, seed viability and soil seed bank. The number of seed produced by a flowering *D. longispathus* culm was higher in undisturbed bamboo forest. Seed viability test using tissue paper test indicated that there was 50.5% and 55.7% viability for disturbed and undisturbed sites respectively. However, using 1% solution of 2, 3, 5-triphenyltetrazolium chloride from a disturbed and undisturbed sitess showed 52.2 % and 56 % viability respectively. Adoption of scientific management techniques advocated for both bamboo plantations and natural bamboo forests to improve the quality and growing stock volume of bamboo in Mizoram.

Keyword: *Dendrocalamus longispathus* Kurz, sporadic flowering, soil seed bank, afforestation, seed viability.

INTRODUCTION

Dendrocalamus longispathus Kurz commonly found in Mizoram, Tripura and Bihar of Northeast India. Out of the 150 bamboo species in India, more than 58 species occur in the North-East India and in Mizoram 22 species were recorded (Lalramnghinglova and Jha, 1995). *Melocanna baccifera* occupied about 95% of the total bamboo, they dominated the land of Mizoram. Other bamboo species like *Dendrocalamus hamiltonii*, *D. longispathus* and *Bambusa tulda* are also found as co-dominantor (Vanlalfakawma, 2014). Bamboos are multipurpose plants with high economic and environmental values and have the high potential to convert solar radiation into useful goods and services due to their fast growth rate compared to tree species (Embaye *et al*., 2005). *D. longispathus* Kurz culms usually reach a height of 10 to 18 meters with an internodal length of 25 to 60cm. The diameter of the species recorded around 6 to 10 cm. 1,34,880 to 1,35,220 seeds boimass weighed about one kilogram. Vegetative propagation by rhizome and two-noded-culm cuttings treated with NAA or IBA are technically promising (Somen *et al.,* 2011). *D. longispathus* usually occurs in moist hill slopes and along streams in the moist fertile loamy soil and particularly shaded fringes of the natural forest covered by this bamboo species (Yadav *et al*., 2019). Bamboo species grows for many years vegetatively by putting up of a fresh set of new shoots every year. At the end of the flowering cycle, all conspecific individuals of the bamboos species flower simultaneously. The vulnerability of some bamboo species increased due to simultaneous flowering and, subsequent death of entire culms populations in cycles of 20-120 years. Thus, from economic point of view, bamboo flowering and fruiting is a natural calamity. Bamboos typically flower only once in their life span and die afterwards (Dhar, 2003), the scientific reasons for it are still not clearly understood. Bamboo seeds play a very important role as a 100 grams of bamboo seeds contains 60.36 gram of carbohydrate and 265.6 kg calorie of energy. Because bamboo flowering is such an infrequent event for the bamboo species, henceforth its seeds were picked with extra fuel. Generally, large-sized bamboos produced a smaller seeds compared to small-sized bamboos (Anantachote, 1988). Seed production per culm varied from 3-80g in *Bambusa bambos*, and 40-90g in *D. longispathus* Kurz. One full-grown clump of *Melocanna baccifera* produced 5-7 kg seeds. In general, the number of seeds per kg varied depending on the species (Banik, 1987; Liese, 1985). The deterioration of seed quality depends on two environmental factors such as relative humidity that regulates seed moisture content and temperature on which both factors influences the metabolic rate of seeds (Bhumibhamon, 1980). Crone *et al*., (2015) also revealed that synchronous reproduction among conspecifics has several demonstrated fitness benefits, including enhanced rates of pollination, increased attraction of seed dispersers, and reduced seed predation. The lifespan of the seeds varied among species. In *Bambusa tulda* seeds are viable for 30-35 days, in *D. longispathus* the lifespan of the seeds was 55 days and in *Bambusa arundinacea* var. *spinosa* they are viable for 65 days (Sur *et al.,* 1989). Seeds of *Dendrocalamus membranaceus* Munro germinated in 5–7 days after sowing and the germination period lasted 10–15 days (Xie *et al*., 2016). Plant growth driven by the environmental conditions, and partitioning defined entirely in terms of the shoot: root ratio and carbon and nitrogen status of the plant (Johnson *et al*., 1987). Bamboo based agroforestry system can be an ecological and economically viable system to rehabilitate abandoned jhum land, provided farmers adopt the desire management practices to minimize the negative effect of root interaction and to increase the sunlight penetration in order to maintain sustainability (Lalnunmawia, 2002).

The scope of the study to concentrates on the quality and quantity of seed produced during the sporadic flowering, which could be an ecological indicator for expectation of further flowering precaution. The quality of the seeds that were to be collected for afforestation in a barren land to create a forest would be easier as the estimated soil seed bank and seed drop quantity of seeds in a culm or clump were quantified. The studies will be potentially applicable for reforestation in similar tropical forest areas, by dispersing the collected seeds into a forest sites that is decreasing in numbers of *D. longispathus*. The studies between the disturbed and undisturbed sites compared in order to understand the significant difference between the two forest sites in terms of their seed quantity, seed drop, seed viability and soil seed bank.

MATERIALS AND METHODS

Study Site: The study was conducted in Lengte village (Figure 1) of Mamit District, located 33 km North West of Aizawl, the Capital City of Mizoram, North-East India. The study site was located between 23°46’25.2”N, 092°35’48.1”E and 23°90’06.3”N, 092°65’54.8”E at an elevation of 400m - 500m above mean sea level and with moderate slope. Natural stands of *D. longispathus* Kurz selected to study the various parameters where sporadic flowering observed in the study site during 2014-2019. For the purpose of the study, the study area further divided into disturbed and undisturbed stands. The disturbed stands frequently exposed to anthropogenic disturbances wherein the nearby villagers used to harvest matured bamboo culms and bamboo shoots for their livelihood and subsistence needs.

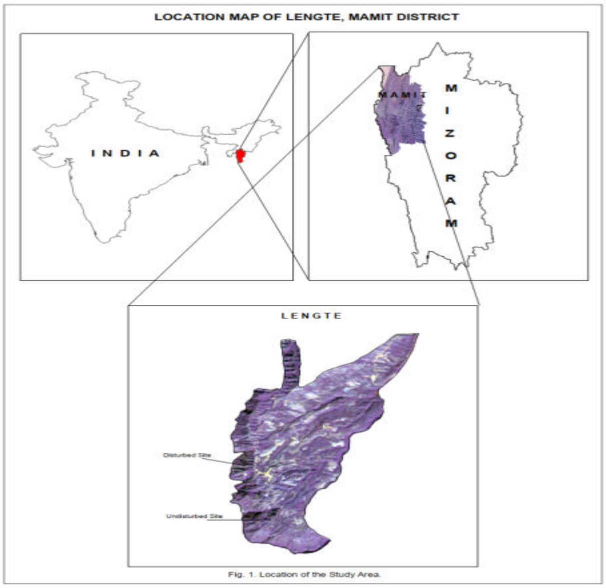

Fig. 1: Map showing Study Site

Seed Production: Seed production in *D. longispathus* was studied according to Arun *et al.,* (2012). For the purpose of the study, 3 (Three) random plots of size 10m x 10m were laid in both the disturbed and undisturbed stands. Within each selected plot number of clumps and the number of flowering culms per clump was counted. 10 (Ten) flowering bamboo culms in each plot were randomly selected and in each culm, number of nodes and flowering branches in each node were recorded. The average number of seeds per culm estimated by taking 6 flowering branches, two each from base, middle and top portion of the selected individuals of bamboo before complete seed maturity. Number of seeds per culm was calculated as follows:

No. of seeds per culm = Average no. of seeds from six selected flowering branches x No. of

flowering branches per node x No. of nodes in a culm

Seed Weight*:* Three replicated plots of 300 freshly collected seeds were taken and their fresh weight was recorded. The fresh seeds were dried at room temperature for 10 (Ten) days and weighed again. Number of seeds per Kg weight was calculated using the following formula:

No. of seeds/Kg = (No. of seeds in the seed lot) x 1000/ Weight of seeds in the seed lot (g)

Seed Rain: Seed rain was observed from its maturity until the maximum seed rain occurred. For this purpose, three replicated plots each of 1.5m x 1.5m size in both disturbed and undisturbed sites were laid in February (Peak season of seed maturity) and the floor of the demarcated plots were cleared of any vegetation and plant litter. Starting from February, 2016 till September, 2016, at the end of every month the seeds were collected from the plots and the number of seed fall occurred naturally were recorded.

Soil Seed Bank: The bulk soil sample was analyzed using two methods (Bernhardt & Hurka, 1989; Bernhardt, 1995). Three sampling plots of 1.5 m × 1.5 m on disturbed sites and undisturbed site of seed along with soil and organic fraction was taken, by separating the organic fraction by washing and floating (sieving method) and then recovered by sieving, followed by counting the seeds under a microscope. Then, collected seeds were randomly spread in the greenhouse and germinated seeds were counted and identification of the seedlings (seedling emergence method) was done for both the study sites.

Seed Viability: Seed collection surface samples was tested for viability using two techniques (Radford *et al*., 1974) which was slightly modified by experimenting each 300 seeds for one replicate on disturbed area and undisturbed area: First, seeds were placed on moist filter paper (Qualitative Filter paper circle disc, 9cm) in a petri dishes and the number of seeds that germinated within 30 days was recorded. The second method test of viability test was done by using a 1% solution of 2,3,5-triphenyltetrazolium. 1% solution of 2,3,5-triphenyltetrazolium chloride was prepared by taking 1 gram (1000mg) of 2,3,5-triphenyltetrazolium chloride and it was dissolved in 100 ml of distilled water and was kept in the dark (Waes and Deburg, 1986). Seeds that stain red after immersion in the solution for 48 hours was assumed as viable.

Statistical Analysis: The data were subjected to ANOVA analysis using PASW Statistica 18 and the difference in mean values between the disturbed and undisturbed stands were compared.

RESULTS AND DISCUSSION

Seed Production Per Culm: The numbers of seeds produced by a flowering *Dendrocalamus longispathus* culm is given in Table 1. The number of flowering branches in a node per culm were 114 and 116 for the disturbed and undisturbed sites, respectively. On each flowering branch, there were 72 seeds in disturbed site and 93 seeds in undisturbed site. The average number of seeds produced per culm was estimated to be 8203 seeds for disturbed site and 10800 seeds per culm for undisturbed site (Table 1) of the study area. ANOVA analysis revealed significant variation where p-value obtained in number of seed per flowering branch was, number of seed per node was and number of seed per culm was 0.007, 0.015 and 0.015 respectively, in seed production between disturbed and undisturbed sites where seed production was found to be significantly higher in undisturbed site (Table 2).

Table 1*:* **Number of Seed Produced per Culm of *D. longispathus***

Parameters	Disturbed Site	Undisturbed Site
No of Node/ Culm	19 ± 0.58	19 ± 0.58
No. of Branches/ Culm	114 ± 6.00	116 ± 1.53
No of Seeds/ Branch	72 ± 4.58	93 ± 6.25
No. of Seeds/ Node	432 ± 6.7	568 ± 8.33
No. of Seeds/ Culm	8,203 ± 5.29	10,800 ± 6.21

Table 2: ANOVA Table for Number of Seed Produced Per Culm

Parameters (Disturbed Area X Undisturbed Area)	F - Value	P - Value
No of Seed/ Flowering branch	147	0.007**
No. of Seed/ Node	65.97	0.015**
No. of Seed/ Culm	64.73	0.015**
**values are significant at P<0.05; P<0.01*		

Fresh Weight and Dry Weight of Seeds*:* Average fresh weight of *Dendrocalamus longispathus* seeds was 0.0088 g per seed and on the other hand, average dry weight was found to be 0.0065 g per seed. The average number of fresh seeds per kg was found to be 1,14,069 and 1,54,742 for air dried seeds (Table 3). The approximate number of seeds per kg for some bamboo species, such as *Bambusa tulda* was 20,000-25,000, *Bambusa bambos* 60,000-75,000, *Bambusa nutans* 65,000, *Bambusa polymorpha* 125,000, *Dendrocalamus brandisii* 20,000, *Dendrocalamus hamiltonii* 26,000, *Dendrocalamus giganteus* 40,000, *Dendrocalamus strictus* 35,000-50,000, *Dendrocalamus asper* 75,000-80,000, *Thyrsostachys oliveri* 15,000-18,000, *Melocanna baccifera* 10-20, *Ochlandra travancorica* 45-50 (Thapliyal *et al.*, 2015).

Table 3: Fresh Weight and Dry Weight of *D. longispathus* Seeds

Parameters	Mean
Fresh Weight (g) per Seed	0.0088 ± 0.0002
Dry Weight (g) per Seed	0.0065 ± 0.00012
No. of seeds per Kg of Fresh Weight	1,14,069 ± 2.977
No. of seeds per Kg of Dry Weight	1,54,742 ± 3.630

Seed Rain: The seed rain was observed to happen when there were folks of White-Rumped Munia or White-Rumped Mannikin (*Lonchura striata*) visitited frequently to consume the seeds of the bamboo. This indicated that the seeds were at ripening stage and thus the seed rain data were taken at the end of February, 2016 till the end of September, 2016 during the study period. The monthly seed rain of *Dendrocalamus longispathus* Kurz on the study sites within $2.25m^2$ were shown in Figure 2, wherein average seed fall for disturbed site was 6,792.7 seeds and in undisturbed site it was 8,869 seeds. Monthly peak in seed rain was recorded in the month of March, 2016 thereafter the quantity of fallen seeds declined significantly where p-value obtained in the month of July, 2016 against disturbed and undisturbed sites was 0.04983 and September, 2016 was 0.05289. The rate of seed fall (seed drop) was found to be higher in undisturbed site toinitiate seed germination. However, the monthly variation in quantity of fallen seeds was not significant except for the month of July, 2016 and September, 2016 (Table 4).

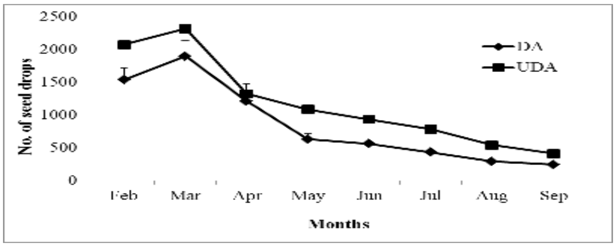

Fig. 2: Monthly Seed Drop on 2016 (Seed Rain) of *D. longispathus* Kurz Within 2.25 m^2 Plot

Table 4: ANOVA Table showing Variation in Seed Drop (Seed Rain) of *D. longispathus*

Months (2016)	Parameters	F - value	P - value
February	Disturbed Site X Undisturbed Site	11.871	0.0749
March	Disturbed Site X Undisturbed Site	2.045	0.28895
April	Disturbed Site X Undisturbed Site	0.621	0.51326
May	Disturbed Site X Undisturbed Site	11.59	0.07651
June	Disturbed Site X Undisturbed Site	9.798	0.08869
July	Disturbed Site X Undisturbed Site	18.58	0.04983*
August	Disturbed Site X Undisturbed Site	10.537	0.08323
September	Disturbed Site X Undisturbed Site	17.421	0.05289*
**values are significant at $P<0.05$*			

Soil Seed Bank: The average soil seed bank of *D. longispathus* in disturbed and undisturbed sites was 649 and 2,128 respectively (Figure 3). The germination trial revealed that, the seeds collected from soil seed bank during the month of March, 2016 showed the highest germination rate in comparisons to the rest of the months (Figure 4). Anova analysis (Table 5) indicates that there was a significant variation where p-value obtained in the month of March, May, June, July, August and September were found to be 0.00719, 0.00079, 0.00058, 0.00301, 0.03136 and 0.00269, respectively, between the disturbed site and undisturbed site from the month of March until September, 2016. Whereas, in February and April, 2016 the p-value were 0.15482 and 0.0601, respectively and no significant variation observed.

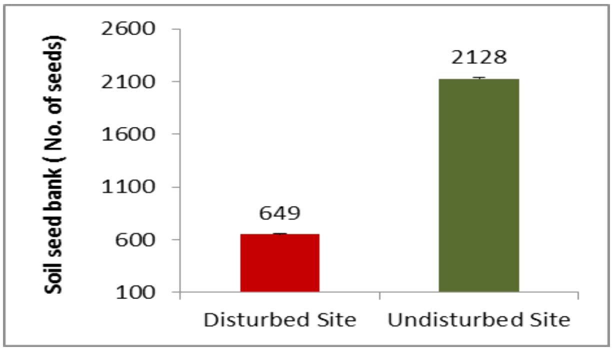

Fig. 3: Average no. of Seeds on 2016 of *D. longispathus* in Soil Seed Bank Within 2.25 m^2 Plot

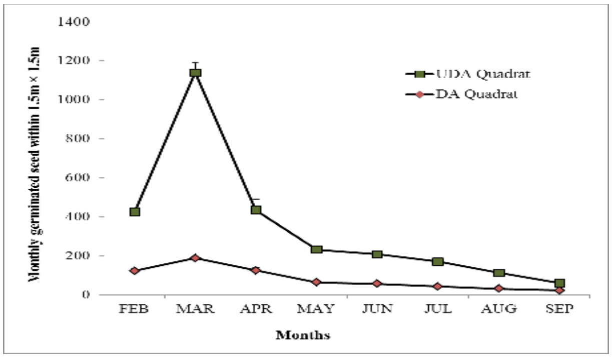

Fig. 4: Monthly Soil Seed Bank on 2016 of *D. longispathus* (No. of Germinated Seeds per Month)

Table 5: ANOVA Table Showing Differences in Soil Seed Bank of *D. longispathus* between Disturbed and Undisturbed Sites

Parameters (2016)	F - value	P - value
(Disturbed X Undisturbed area) February	5.001	0.15482
(Disturbed X Undisturbed area) March	137.535	0.00719**
(Disturbed X Undisturbed area) April	17.09	0.0601
(Disturbed X Undisturbed area) May	1,264.47	0.00079***
(Disturbed X Undisturbed area) June	1,716.33	0.00058***
(Disturbed X Undisturbed area) July	331.164	0.00301**
(Disturbed X Undisturbed area) August	10.565	0.03136*
(Disturbed X Undisturbed area) September	43.89	0.00269**
values are significant at P<0.05, ** values are significant at P<0.01,*values are significant at P<0.001*		

Seed Viability: Seed viability test using filter paper using qualitative filter paper circle disc of 9cm test indicated that there was 50.5% viability of seeds for disturbed sites and 55.7% viability for undisturbed sites. On the other hand, using the second method of dissolving the seeds to 1% solution of 2, 3, 5-triphenyltetrazolium chloride from a disturbed site showed 52.2 % viability while 56 % of the seeds collected from undisturbed site were viable (Figure 5). Anova analysis (Table 6) indicated that the two methods resulted in significant difference in seed viability where p-value on percentage of disturbed area using filter papre test against disturbed area using Tetrazolium test was 0.00127 and percentage of undisturbed area using filter papre test against undisturbed area using Tetrazolium test was 0.01287. Seeds of *D. longispathus* was found to be vary minute weighing for 0.0065 gram (on air dry basis) and accounting for 1,54,742 seeds per Kg. In figure 6, different stages and experimental pictures were display.

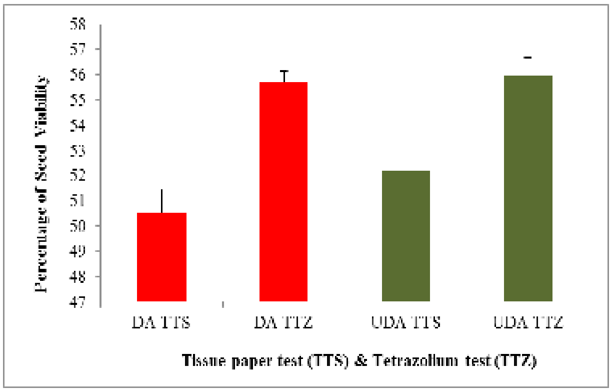

Fig. 5: Seed Viability of *D. longispathus* (Note: DA TTS = Disturbed Area Tissue Paper Test, UDA TTS = Undisturbed Area Tissue Paper Test, DA TTZ = Disturbed Area Tetrazolium Test & UDA TTZ = Undisturbed Area Tetrazolium Test)

Table 6: ANOVA Table for Seed Viability Test of *D. Longispathus*

Parameters	F - value	P - value
% DA TTS v/s % UDA TTS	4.808	0.08
% DA TTZ v/s % UDA TTZ	0.455	0.53
% DA TTS v/s % DA TTZ	42.52	0.00127**
% UDA TTS v/s UDA TTZ	14.3	0.01287**
*** values are significant at P<0.01*		

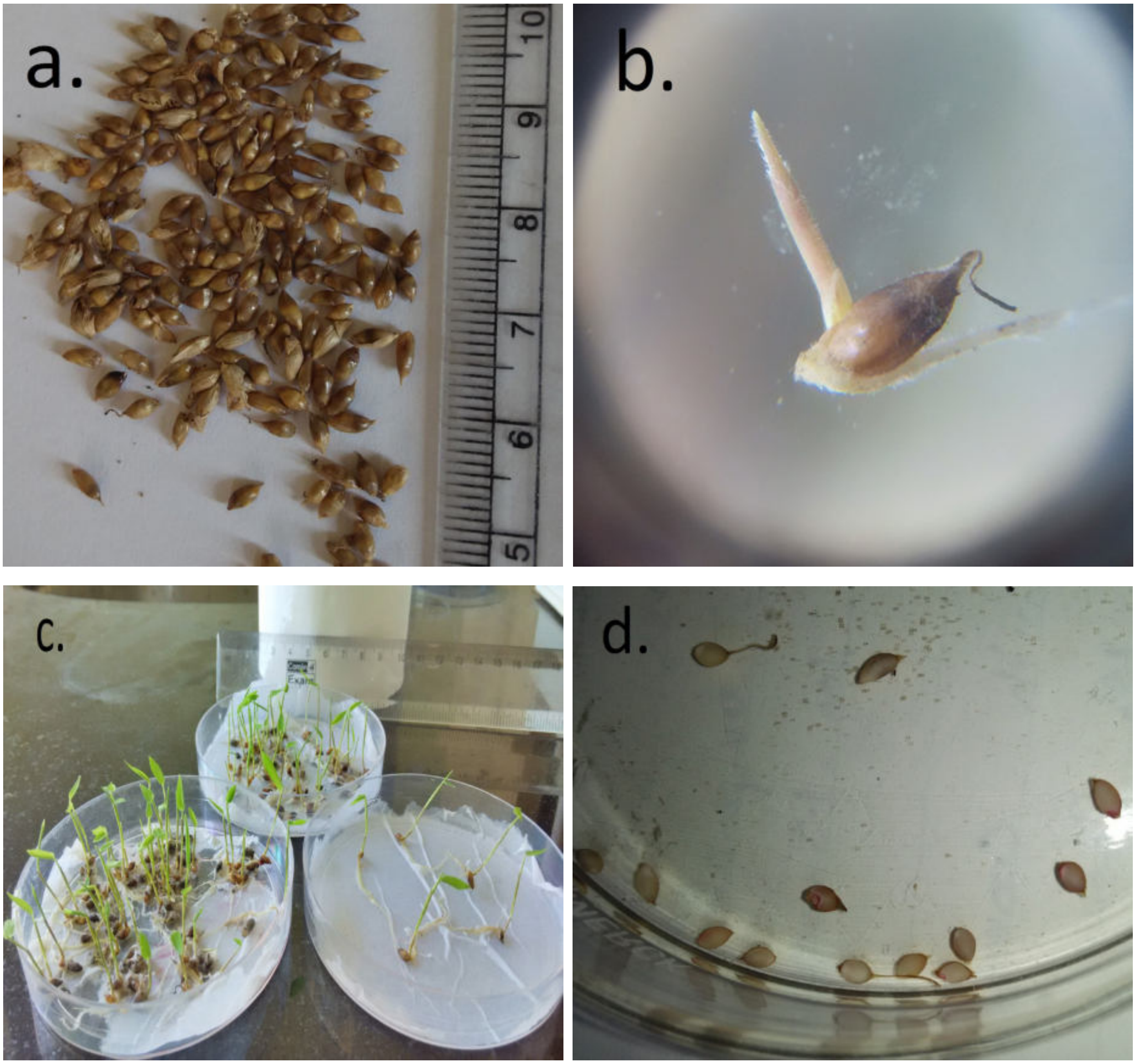

Fig. 6: Seeds of *D. longispathus*; a) Matured Seeds, b) Initiation on Seed Germination, c) Treatment with Filter Paper and d) Treatment with 1% Solution of 2, 3, 5-triphenyltetrazolium Chloride

CONCLUSION

The seed setting was observed to happen when there were flocks of White-Rumped Munia or White-Rumped Mannikin (*Lonchura striata*) visitited frequently to consume the bamboo seeds. This indicated that the bamboo seeds were at ripened stage and thus the seed setting data were taken at the end month of February, 2016 during the study period. The number of seed produced by a flowered *D. longispathus* culm was much higher in the undisturbed bamboo forest. This may be due to the availability of proper anthesis and pollination, which affect in a significant way of seed fertilization. On the other hand, seed production was lesser at disturbed habitat which might be caused by an open forest canopy that interrupted anthesis and pollination. Monthly seed setting of *D. longispathus* Kurz was comparatively higher in the undisturbed than the disturbed sites, especially during the end season of seed setting. This may be due to the higher number of flower of *D. longispathus* Kurz and seed production at the undisturbed sites. The activity of birds and other beneficiaries could be the reason of major seed falls during the month of March, 2016 as the fruit starts to ripen. The study also revealed that the bamboo species has high seed rain during pre-monsoon and monsoon periods contributing sufficient seed stock in soil pool for subsequent regeneration. Overall, disturbance seemed to have significant effect on seed production, seed rain and soil seed bank of *D. longispathus* in natural bamboo forests. Slash-and-burn agriculture, also called fire-fallow cultivation where large-scale deforestation of forests for agricultural use was practiced at the study site by the local peoples. Henceforth, significant afforestation and regeneration of bamboo natural forest suggested, through introduction of the viable seeds of *D. longispathus* Kurz to different abandoned fallow lands. Adoption of scientific management techniques advocated for both bamboo plantations and natural bamboo in order to achieve the objectives of Green Mizoram initiatives.

ACKNOWLEDGMENT

The authors acknowledge to Department of Botany, Mizoram University for providing facilities and assistance during this study.

REFERENCES

Anantachote A (1988) Flowering characteristics of some bamboos in Thailand. In: Ramanuja Rao, I.V., Gnanaharan, R., Sastry, C.B. (eds.) Bamboos: Current Research, KFRI/ IDRC: pp. 66-75.

Arun JN, Donald CF, Michael J, Lawes M, Das C, Das AK (2012) Impact of Culm Harvest on Seed Production in a Monocarpic Bamboo. Biotropica. Vol. 44, No. 5 (September, 2012). pp. 699-704.

Banik RL (1987) Seed germination of some bamboo species. Indian Forester. 113(8): 578-586.

Bernhardt KG (1995) The seed bank in soil and its use for species conservation and restoration management. Z. Kulturtechnik Landentwicklung. 36: 274-282.

Bernhardt, Hurka (1989) Dynamik des Samenspeichers in einigen mediterranen Kulturboden.Weed Research. 29: 247-254.

Bhumibhamon S (1980) Seed testing. In: Regional Training Course in Forest Tree Improvement, Thailand. BIOTROP/KU/RFD. 21 April-31 May, 1980.

Crone EE, McIntire EJB, Brodie J (2015) What defines mast seeding? Spatio-temporal patterns of cone production by whitebark pine. J. Ecol. 99: 438-444. doi: 10.1111/j.1365-2745.2010.01790.x

Dhar A (2003) When flowering spells famine. The Hindu, 26 October 2003. pp. 3.

Embaye K, Weih M, Ledin S, Christersson L (2005) Biomass and nutrient distribution in a highland bamboo forest in southwest Ethiopia: implications for management. For: Ecol. Manag. 204: 159-169.

Johnson IR, Thornley JHM (1987) A Model of Shoot: Root Partitioning with Optimal Growth. Annals of Botany.60(2): 133-142.

Lalnunmawia, F. 2002. Comparative studies on growth and productivity of three edible bamboo species grown with ginger crop. Ph.D Thesis. Department of Forestry. Mizoram University. Shodh ganga.inflibnet.ac.in. pp. 98-99.

Lalramnghinglova and Jha (1995) Management Problems of Bamboo in Mizoram. Indian Forester. 121(4): 321-324.

Liese W (1985) Bamboos-Biology, silvics, properties, utilization. GTZ, Eschborn, Germany.

Radford AE, Dickson WC, Massey JR, Bell CR (1974) Vascular plant systematic. Harper & Row, New York. (http://www.amazon.com/Vascular-Plant-Systematics-Albert-Radford/dp/0060453095).

Somen CK, Seethalakshmi KK, Unni KK, Raveendran VP (2011) Planting stock production of selected commercial species of bamboos. Thrissur, Kerala, India. An Institution of the Kerala State Council for Science, Technology and Environment. KFRI Research Report No. 391.ISSN. No.0970-8103: pp. 13.

Sur K, Lahiri AK, Basu RN (1989) Maintenance of bamboo (*Dendrocalamus*) seed viability by hydration dehydration treatment. Indian Journal of Forestry. 12(2): 142-144.

Thapliyal M, Joshi G, Behera F (2015) Bamboo: Flowering, Seed Germination and Storage. Bamboo in India. Kerala Forest Research Institute: *ISBN* 81-86247-25-4. frienvis.nic.in. 4:89-108.

Vanlalfakawma DC (2014) Carbon and Nitrogen Sequestration Potential of Bamboo Forests of Mizoram. Ph.D. Thesis. Mizoram University. Dept. of Forestry. pp. 121.

Waes J, Deburg P (1986) Adaptation off the Tetrazolium method for testing the seed viability and scaning electron microscopy study of some Western European Orchids Copenhagen. Physiol Plant. 66: 435-442.

Welbaum GE (1999) Cucurbit Seed Development and Production. Hort. Technology. 9(3): 341-348.

Yadav S, Raj H, Lalnunmawia (2019) Annual flowering of *Dendrocalamus longispathus* (Kurz) Kurz in Mizoram. Tropical Plant Research. 6(1): 46–48.

Xie N, Chen L-N, Wong K-M, Cui Y-Z, Yang H-Q (2016) Seed Set and Natural Regeneration of *Dendrocalamus membranaceus* Munro after Mass and Sporadic Flowering in Yunnan, China. PLoS ONE 11(4): e0153845. https://doi.org/10.1371/journal.pone.0153845.

Science and Technology Journal Vol. 8 Issue 2 July 2020 ISSN: 2321-3388

Lignocellulosic Content and Biofuel Potential of Post-harvest Sugarcane Leaves from Commonly Cultivated Indian Varieties

Suchithra Pallipath[1], Najya Jabeen Poolakkalody[2],
Kaviraj Ramesh[3] and Chithra Manisseri[4]*
Department of Plant Science, Central University of Kerala,
Tejaswini Hills, Periye, Kasaragod, 671 320 (India)
*E-mail: mchithra@cukerala.ac.in

Abstract—Sugarcane is one of the most important crops in India and its post-harvest leaves having low fodder value compared to many other agri residues, can be utilized for biofuel production. There is no detailed information on the lignocellulosic content of cane straw from different varieties, which could be helpful for the selection of potential biofuel feedstock and designing suitable pretreatment methods. Hence, in the present study, lignocellulosic content of post-harvest leaves from seventeen Indian cane varieties was analyzed for its better utilization in bioethanol production. Major cell wall polymers such as cellulose, hemicellulose and lignin were estimated in a range of 53.8-38.7%, 34.4-23.6% and 18.9-13.3% dry weight of biomass respectively in these varieties. Cellulose, hemicellulose and lignin contents in Nayana (CO 86032) were found to be 53.8%, 31% and 18.4% respectively. Among the tested varieties, Nayana was selected for further pretreatment studies being one of the candidates widely cultivated in India with high sucrose and cellulose content. 1-ethyl 3-methylimidazolium acetate ([Emim][Ac]) pretreatment at 150°C for 3 hr was found to be effective in biomass depolymerization. Higher degree of delignification was observed in [Emim][Ac] (62.1%) compared to hot water pretreatment (13.4%). FTIR spectra also confirmed the effective depolymerization of the biomass. The biofuel potential of [Emim][Ac] pretreated biomass was assessed in terms of saccharification efficiency and was found 3.8 fold higher compared to untreated biomass at 72 hr of enzymatic hydrolysis.

Keywords: Bioethanol; Delignification; 1-ethyl 3-methylimidazolium acetate; Enzymatic saccharification; Ionic liquid; Pretreatment; Sugarcane; Agro-residues

INTRODUCTION

Agro-residues constitute a potential sustainable energy resource for bioethanol production which can lead to the reduced consumption of fossil fuels. Sugarcane is one of the major cultivated crops in India and plays a pivotal role in the nation's economy. Even being the second largest producer of sugarcane globally, India depends mainly on molasses, which is a byproduct of sugar industry for ethanol production leaving the large amount of cane straw unexplored. If we look at global level, Brazil stands first in utilizing sugarcane for bioethanol production. But cane juice is mainly used for fuel production in Brazil. The fodder value of cane straw is also low compared to other agri residues due to its rough nature and extreme silica content (Chandel et al. 2012; Patel and Kumari 1990; Fox et al. 1969). Hence they are usually burnt in the field itself which leads to serious issues of air pollution. In the present study, the biofuel potential of leaves after crop harvest from different cane varieties is screened for their use as a promising feedstock for ethanol production.

The biofuel potential of any feedstock depends on the cell wall composition and its complexity. Pant cell wall is mainly composed of polymers such as cellulose, hemicellulose and lignin. The content of these polymers and their complex inter linkages may vary among different plant species, cells or tissues. Over the years, different cane varieties have been developed in India and some of them are suited for cultivation in tropical and others in subtropical zones. They may differ in plant height, internode length, number of internodes, stalk girth, single cane weight, cane yield and sucrose content (Tawadare et al. 2019). Varietal differences may be also evident in their cell wall composition, which is considered as an important criteria for bioethanol production. Environmental conditions of the cultivated area are also crucial and may affect wall polymer content or complexity among varieties.

The cross-links through lignin-carbohydrate complexes increases cell wall rigidity and resistance to enzymatic digestion (Brandt et al. 2013; Limayem and Ricke 2013; Knauf et al. 2004; Dadi et al. 2006). The major hemicellulose found in grasses is glucuronoarabinoxylan (Carpita 1996). Xylose residues in glucuronoarabinoxylan is substituted with α-1,2, and/or α-1,3-linked L-arabinofuranose residues. In grasses, some of the arabinose residues are esterified with ferulic acid on C5. Grass cell walls also contain p-coumaric acid esters, but they are mainly linked to lignin rather than xylan. The ferulate esters can be oxidatively cross-linked to each other forming intra/ inter-molecular diferulate bridges, and they can be cross-linked with the lignin network through ether bonds. The whole complex interlinkages result in strengthening of the plant cell wall and making grass cell walls recalcitrant to enzymatic digestion (Carpita 1996). To disintegrate these linkages and convert cellulose into porous amorphous form accessible to cellulose degrading enzymes, an efficient pretreatment is required. Woody plants are generally characterized with high lignin content compared to grasses and this demands harsh pretreatment methods. There is a wide range of physical, chemical, biological and combined pretreatment approaches that are currently being explored to reduce the biomass recalcitrance. Ionic liquid (IL) pretreatment is one of the advanced methods due to its green nature, excellent cellulose solubility, delignification and extensive biomass degradation (Brandt et al. 2013; Chen et al. 2018; Carvalho et al. 2015; Hyvarinen et al. 2014). ILs hold many advantages like thermal and chemical stability, low vapor pressure and are recyclable (Fort et al. 2007). In addition, ionic liquids have excellent dissolvability of polar and non-polar organic materials and hence are commonly used for material separations and chemical conversions (Lee and Lee 2005). Therefore, the application of ionic liquids in biomass dissolution and pretreatment has attracted considerable attention recently and different ILs are used for the purpose. In the current study, 1-ethyl,3-methylimidazolium acetate ([Emim][Ac]) is used for pretreatment of cane leaves.

MATERIALS AND METHODS

Feedstock

Post-harvest leaves of seventeen cane varieties were collected from different agricultural research stations in India. Co 86032 (Nayana), CoC 671 (Vasant-1), VCF 0517 (CoVC 14061, Bahubali) were collected from V C Farm-Mandya (Karnataka); TNAU Si7, TNAU Si8, Co 99004 (Damodar), CoG 93076, Co 85004 (Prabha), CoC (Sc) 24, Co 94012 (Phule Savithri), and Co 94008 (Shyama) were from sugarcane research station-Sirugamani (Tamil Nadu); CoS NK 03632, CoTI 88322 (Madhuri), Cul 527/85 (Madhurima), Co 88017 (Madhumathi), CoTI 1153 (Aromal) and CoTI 1358 (Abhay) were collected from agricultural research station-Thiruvalla (Kerala). Three biological replicates were taken from each variety and the samples were cut, air dried and milled separately to 20 mesh particle size using wiley mill.

Preparation of Alcohol Insoluble Residue (AIR)

Cane leaves (500 mg, 20 mesh size) were extracted with ethanol (95%, 1:4 w/v) at 100°C for 30 min. After the treatment, the sample was centrifuged (10,000×g, 10 min) and the residue was subsequently washed with 70% ethanol and dried under vacuum. The dried powder obtained after ethanol (70%) wash is designated as alcohol insoluble residue (Arora et al. 2010). Destarching of AIR was done using amylase and amyloglucosidase hydrolysis. AIR was treated with heat stable amylase from *Bacillus licheniformis* (Megazyme, Bray, Ireland) at 0.3 U per 10 mg AIR in sodium acetate buffer (200 mM, pH 5) at 85°C for 1 hr. Subsequently, the sample was incubated with amyloglucosidase from *Aspergillus niger* (Megazyme, Bray, Ireland) at 0.33 U per 10 mg AIR at 50°C for 2 hr. The reaction was arrested by adding three volumes of ethanol (95%), vortexed and centrifuged (10,000×g for 10 min). The residue obtained after centrifugation was washed with ethanol (70%) and dried under vacuum. The destarched AIR was used for all experiments in this study.

Cellulose and Hemicellulose Quantification

Cellulose and hemicellulose quantification was done by a modified protocol of Meineke et al (2014). The results are expressed in percentage dry weight of biomass. Destarched AIR (5 mg) was mixed with 50 µl of 72% (w/w) sulfuric acid and incubated at 30°C for 1 hr in a heat block. After cooling down, this mixture was diluted with water to 4% (w/w) sulfuric acid. Then it was incubated at 120°C for 1 hr followed by centrifugation at 13,000×g for 5 min. The supernatant obtained was diluted 1:200 with water. 0.5 ml of these dilutions were taken into fresh test tubes and 0.3 ml of 5% saturated phenol and 1.8 ml sulfuric acid was added to it. The solution was incubated at room temperature for 20 min. The absorbance was measured at 480 nm. Glucose was used as the standard (5-25 µg). For hemicellulose estimation, AIR (5 mg) was treated with trifluoroacetic acid (TFA, 2 M) at 120°C for 1 hr. The samples were vortexed and centrifuged (13000xg for 5 min). After centrifugation, the supernatants were diluted to 1:100. To 0.5 ml of diluted sample, 0.3 ml 5% saturated phenol and 1.8 ml of sulfuric acid were added and incubated at room temperature for 20 min. Absorbance was measured at 480 nm. For hemicellulose quantification xylose was used as the standard (5-25 µg). Amount of hemicellulose was calculated according to Meineke et al. 2014.

LIGNIN QUANTIFICATION

Lignin was quantified using acetyl bromide method as mentioned by Arora et al. (2010). AIR (5 mg) was incubated with 200 µl of freshly prepared acetyl bromide (25% v/v in acetic acid) at 50°C for 2hr on a thermomixer at 1050 rpm. After incubation, the solutions were thoroughly mixed using a vortex mixer and diluted with three volumes of glacial acetic acid and centrifuged. 100 µl of the solution was taken into fresh tubes and 500 µL of glacial acetic acid was added to it. The solutions were thoroughly mixed followed by the addition of 300 µl of 0.3 M NaOH and 100 µl of 0.5 M hydroxylamine hydrochloride. The final volume was made to 2 ml by the addition of glacial acetic acid. The solutions were thoroughly mixed and absorption was measured at 280 nm. The lignin content in the sample was determined with an extinction coefficient of 18.1951 L/g cm corresponding to average values for grass samples (Arora et al. 2010) and the results are expressed in percentage dry weight of biomass.

[EMIM][AC] PRETREATMENT OF BIOMASS

AIR was treated with [Emim][Ac] (100%, Sigma-Aldrich, St Louis, MO, USA) at a loading of 5% at 150°C for 3 hr in an oven. The reaction mixture was cooled to room temperature and deionised water was added as an antisolvent to precipitate and regenerate the dissolved cellulose followed by centrifugation at 10,000×g for 20 min. The sample was washed five times with deionized water until a clear supernatant was obtained to ensure complete removal of ionic liquid. The residue was dried under vacuum (Fig 1).

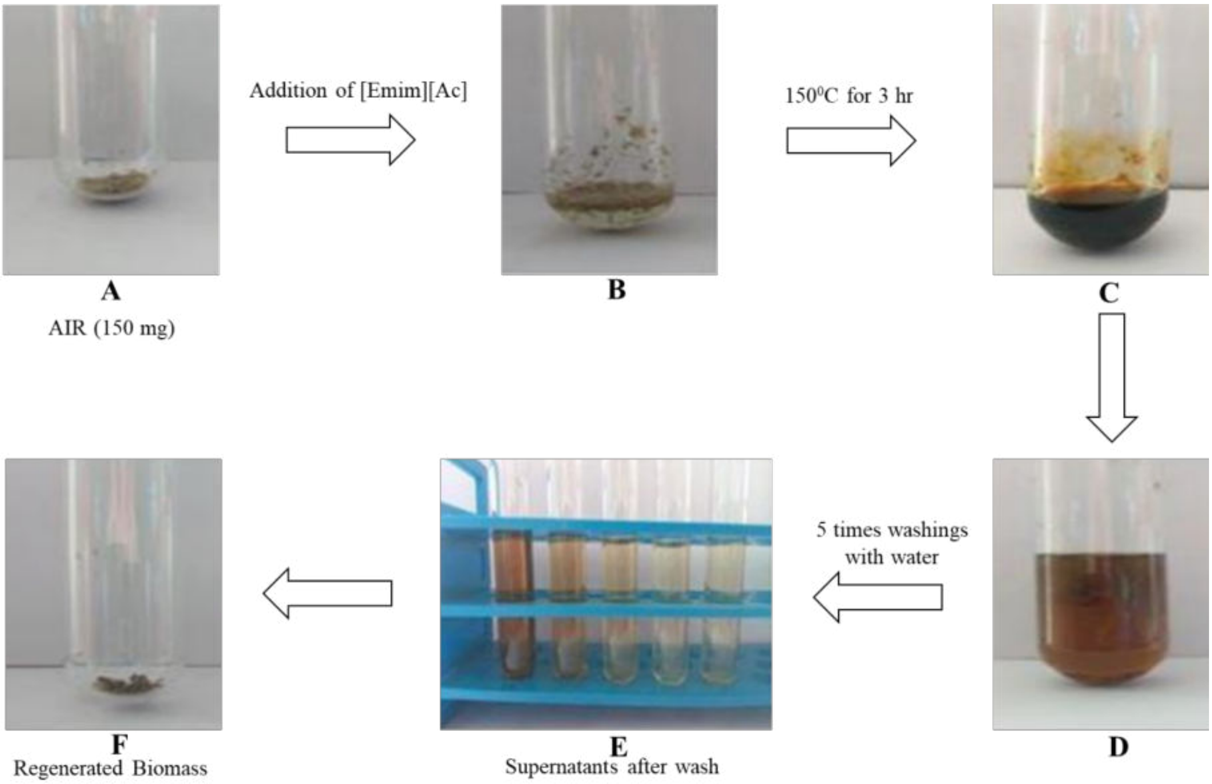

Fig. 1: Diagrammatic Representation of [Emim][Ac] Pretreatment

A. Alcohol Insoluble Residue (AIR) of Nayana leaves **B.** AIR with [Emim][Ac] **C.** AIR in [Emim][Ac] after pretreatment **D.** Cellulose precipitation after addition of water **E.** Supernatants of 5 consecutive washes until clear solution was obtained **F.** Regenerated biomass after pretreatment

HOT WATER PRETREATMENT OF BIOMASS

AIR was treated with hot water at a loading of 5% at 150°C for 3 hr in an oven and the residue was dried under vacuum.

FTIR ANALYSIS

Fourier Transform infrared spectroscopic analysis of both untreated and [Emim][Ac] pretreated residues were carried out. FTIR spectrum was obtained between the ranges of 4000 and 800 cm^{-1} using Jasco spectrometer with detector at 4 cm^{-1} resolution and 32 scan per sample. Pellets were prepared by mixing 300 mg of KBr (Spectroscopic grade) with 3 mg of dried samples in an agate mortar. The resulting mixture was successfully pressed at 0.0785 Mpa for 1 min. FTIR spectra was plotted in spectragryph v 1.2.13.

ENZYMATIC SACCHARIFICATION

The untreated and regenerated biomass after pretreatments (5 mg) were hydrolyzed with cellulase (0.64 U/mg biomass, MP Biomedicals, New Zealand) and β-glucosidase (1.44 U/mg biomass, MP Biomedicals, New Zealand). Biomass (5 mg) in 614 µl acetate buffer was incubated in a thermo mixer at 50°C, 300 rpm for different time periods (0.5 hr, 1 hr, 3 hr, 6 hr, 12 hr, 24 hr, 48 hr and 72 hr). The release of soluble reducing sugars was measured by using 3, 5 dinitrosalicylic acid (DNS) assay with glucose (50-500 µg) as standard. Absorbance was measured at 540 nm.

RESULTS AND DISCUSSION

COMPOSITIONAL ANALYSIS OF POST-HARVEST LEAVES FROM DIFFERENT CANE VARIETIES

Post-harvest leaves collected from 17 Indian cane varieties were screened for their lignocellulosic content for utilizing as an efficient biofuel feedstock. The varieties differed in their sucrose content, maturity period and tolerance against biotic and abiotic stresses. The important characteristics of the samples are listed in Table 1. Morphological and agronomical variability among cane varieties were also reported earlier by Govindaraj et al. 2016. The sucrose content of the varieties selected for the present study is shown in

Table. 2. There are limited information which compare the agro/industrial residues generated from different cane varieties. However, a detailed study on the cell wall composition of post-harvest cane leaves based on varietal differences for their potential use as an alternative energy resource is lacking.

Major cell wall polymers such as cellulose, hemicellulose and lignin were analyzed in the samples. The summary of compositional analysis is shown in Table 3. Cellulose, hemicellulose and lignin content of leaves tested in the present study varied in the range of 53.8-38.7%, 34.7-23.6% and 18.9-13.2% dry weight of biomass respectively. TNAU Si7, TNAU Si8 and CoS NK 03632 showed reduced lignin content (13.2- 14.9%) among the tested varieties. Since their cultivation is mainly restricted to Tamil Nadu, they were not selected for further pretreatment experiments in the present study, for which comparatively a wide distributed variety is suitable. Apart from cane leaves, bagasse can also be used for bioethanol production reducing the sole dependence on molasses. *Santosh et al (2017) had conducted studies on* bagasse from different cultivars for ethanol production using co-culture of *S.cerevisiae and Scheffersomyces stipites.* Also there are reports on hemicellulose distribution in different cane hybrids and their role in cell wall recalcitrance (Costa et al. 2016). Among the tested varieties, Co 86032 commonly known as Nayana showed high cellulose (53.8.3%) and hemicellulose (31%) content. Also this variety is widely cultivated in India and holds high sucrose content. It is important to use a variety which is popular in sugar industry, widely cultivated in India and also with preferred cell wall composition for fuel production. Hence, Nayana was selected for further pretreatment and saccharification experiments in the current study for sustainable ethanol production.

Environmental conditions may also have effects on the yield, sugar quality and cell wall complexity among different varieties (Schultz et al. 2017). In such cases, a unique pretreatment method may not be effective for commercial fuel production from a particular variety cultivated in different regions in the country. To assess the effects of environmental conditions on cell wall composition, wall profiling of Nayana from different locations, ie, from Mandya (Karnataka), Sirugamani (Tamil Nadu) and Thiruvalla (Kerala) was carried out. These locations differed in their soil types. The soil types were red gravelly, clay loam and red loam in Mandya, Sirugamani and Thiruvalla respectively.

But, ANOVA indicated no significant differences in cellulose, hemicellulose and lignin content in Nayana leaves collected from these three locations. (Critical difference for cellulose=10.29; hemicellulose 2.02; lignin 1.10) (Table 4). Hence, the same pretreatment method could be applicable to Nayana leaves collected from these three regions.

PRETREATMENT OF NAYANA LEAVES

Nayana leaves were subjected to hot water and [Emim][Ac] pretreatments. The untreated sample was estimated with 18.4 % lignin whereas, the residue recovered after hot water and IL pretreatment showed 15.9 and 7% lignin respectively. Delignification was very less in hot water compared to [Emim][Ac] pretreated samples. 62.1% delignification was observed in the biomass recovered after IL pretreatment, whereas hot water pretreatment resulted in only 13.4% delignification. Comparatively similar result was observed in previous study with switchgrass wherein [Emim][Ac] pretreatment at 160^{0}C for 3 hr resulted in 69% delignification (Li et al. 2010). The slightly higher delignification observed in switchgrass may be due to the elevated pretreatment temperature since it can accelerate the swelling and dissolution rates of lignocellulose in ILs (Sun et al. 2009; Wang et al. 2012; Singh et al. 2009; Sochaa et al. 2014; Asakawa et al. 2015; Wang et al. 2015). Fu and Mazza (2011) had reported 29% of delignification in wheat straw with [Emim][Ac] pretreatment at 150^{0}C for 1.5 hr and this result is in accordance with the delignification rate obtained in the present study. [Emim][Ac] was also reported as an efficient pretreatment method in pine and oak wood (Sun et al. 2009). Emim acetate can be recycled and used in many cycles of pretreatment and this can compensate with their slightly elevated price. Also it won't cause serious issues of environmental pollution as observed with acid/alkali pretreatment. Various ILs are also used for biomass dissolution and lignin extraction in previous studies (Tan et al. 2009). Cholinium based ILs were found to be effective pretreatment solvents for grass lignocelluloses as well as eucalyptus, resulting in significant improvements in glucose yields (58-75%) in subsequent enzymatic hydrolysis (An et al. 2015). ILs combined with other solvents also used for biomass conversion for subsequent fuel production (Mai et al. 2014).

ANALYSIS OF IL PRETREATED NAYANA LEAVES BY FTIR

FTIR spectroscopy was used to characterize the structural alterations in the [Emim][Ac] pretreated sample. The spectra of untreated and [Emim][Ac] pretreated samples are shown in Fig 2. The band at 2921 cm^{-1} is assigned for CH_2 and CH_3 groups in cellulose (Pereira et al. 2016). When compared to the untreated cane leaf, the peak at 2921 cm^{-1} was reduced for IL pretreated leaf sample, indicating lignin removal during pretreatment. Similar peak reduction was observed in water hyacinth treated with [Bmim][Br] (Singh et al. 2018). Absorption band at 897 cm^{-1} corresponds to the C-O-C valence of crystalline cellulose I. Cellulose I, is more resistant to enzymatic hydrolysis than cellulose II. The peak reduction at 897 cm^{-1} after pretreatment indicated conversion of cellulose I to II during pretreatment. Similar peak reduction was observed in rice straw pretreated with [Bmim][Cl] at 120^0 C for 5 hr (Poornejad et al. 2012). Water hyacinth treated with different ILs such as [Emim][Br], [Edmim][Br], [Bmim][Br], [Hmim][Br], and [Omim][Br] at 100^{0}C for 1 hr also reported the peak reduction at 897 cm^{-1} (Singh et al. 2018). The Peak at 1378 cm^{-1} corresponds to C-H deformation of crystalline cellulose (Pereira et al. 2016) and this peak was found reduced in IL pretreated sample. This indicated the reduction in cellulose crystallinity after pretreatment. Wang et al. (2017) had reported this peak reduction at 1378 cm^{-1} in poplar pretreated with [Emim][Ac].

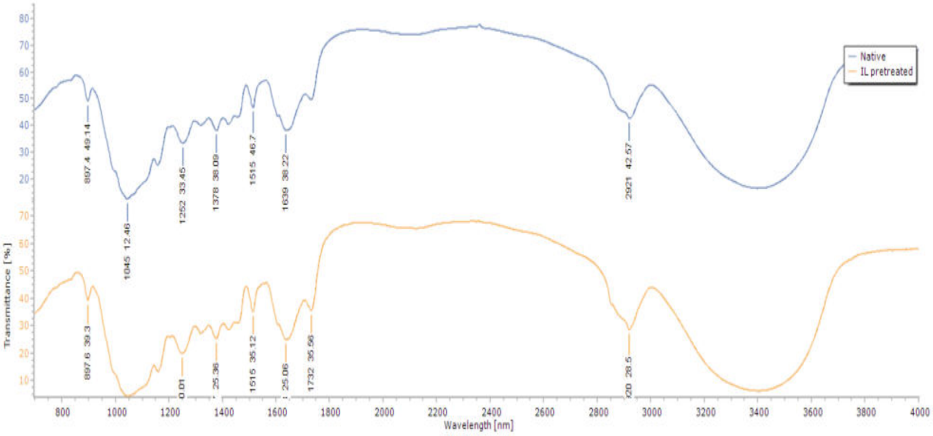

Fig. 2: FTIR Spectra of Untreated and [Emim][Ac] Pretreated Nayana Leaves

Peak at 1639 cm^{-1} referring to C=C stretching of lignin aromatic ring (Poornejad et al. 2012) was also found reduced in the pretreated sample indicating delignification. The peak at 1516 cm^{-1}, assigned for C=C aromatic skeletal vibrations of lignin was reduced in the IL pretreated leaf revealing lignin removal during pretreatment. Similarly, the peak at 1045cm^{-1} formed due to guaiacyl group aromatic C-H vibration in lignin (Rana et al. 2013) was absent in the pretreated biomass suggesting delignification.

ENZYMATIC SACCHARIFICATION OF UNTREATED AND PRETREATED NAYANA SAMPLES

Enzymatic hydrolysis efficiency in untreated Nayana leaves was compared with hot water and [Emim][Ac] pretreated samples. The data is shown in figure 3. [Emim][Ac] pretreated leaves exhibited maximum glucose yield (0.41 mg/mg sample) compared to untreated and hot water pretreated leaves at 72 hr. Glucose yield of hot water treated leaves was only 0.18 mg over the same time period. In untreated leaves, the hydrolysis rate was very low. The sugar recovery was found continuously increased up to 72 hr in [Emim][Ac] treated leaves in the present study, Enzymatic saccharification efficiency of IL pretreated biomass was 3.8 fold higher than untreated biomass and 2.3 fold greater than water pretreated biomass at 72h of enzymatic hydrolysis. High glucose yield was reported in [Emim][Ac] pretreated sugarcane bagasse and rice straw previously (da Silva et al. 2011; Bian et al.2014; Cheenkachorn et al. 2016). During IL pretreatment the intra and inter molecular hydrogen bonding may be disrupted which results in the conversion of crystalline cellulose to amorphous form thereby providing increased surface area for enzymatic hydrolysis. In switchgrass, IL pretreated samples also reported higher enzymatic saccharification rate compared to dilute acid treated samples (Li et al., 2010). Similar results were also reported in rye straw. Enzymatic hydrolysis of [Emim] [Cl] pretreated rye straw was reported to yield almost three times reducing sugars compared to the untreated sample at 72 hr (Smuga-Kogut et al. 2017). [Emim][Ac] treated softwood (*Cryptomeria japonica*) also showed increased glucose yield compared to the untreated sample (Hamidah et al. 2018). Apart from the conversion of cellulose from crystalline to amorphous form, delignification may be adding to the increased saccharification efficiency in IL pretreated samples.

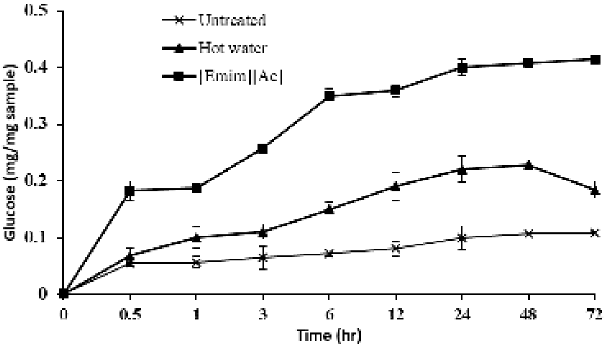

Fig. 3: Enzymatic Saccharification of Untreated and Pretreated Nayana Leaves at Different Time Periods

(Each value represents mean ±standard deviation, n=3)

Table 1: Characteristic Features of Selected Cane Varieties

Variety	Parents	Maturity Period	Leaf Size	Cultivating Zones
Co 86032 (*Nayana*)	Co 62198 X CoC 671	Mid-late	Medium	Peninsular zone Gujarat, Maharashtra, Kerala, Karnataka, Tamil Nadu, Andhra Pradesh, Orissa, Madhya Pradesh and Chhattisgarh
CoC 671 (*Vasant-1*)	Q 63 X Co 775	Early	Medium-broad	Peninsular zone Maharashtra, Kerala, Karnataka, interior of Tamil Nadu and Andhra Pradesh and Madhya Pradesh
VCF 0517 (CoVC 14061, *Bahubali*)	Co 6119 X CoC 671	Mid-late	Medium-broad	Peninsular zone Southern Karnataka
TNAU Si7	Co 99034 X CoG 93076	Mid-late	Medium	Tamil Nadu
TNAU Si8	CoC 90063 X Co 8213	Mid-late	Medium	Tamil Nadu
Co 99004 (*Damodar*)	Co 62175 X Co 86250	Mid-late	Medium	Peninsular Zone Gujarat, Maharashtra, Kerala, Karnataka, Tamil Nadu, Andhra Pradesh, Madhya Pradesh and Chhattisgarh

Table 1 Contd...

...Table 1 Contd.

Variety	Parents	Maturity Period	Leaf Size	Cultivating Zones
CoG 93076	CoC 772 X Co 419	Mid-late	Medium	Peninsular zone
Co 85004 (*Prabha*)	Co 6304 X Co 740	Early	Medium	Peninsular Zone Gujarat, Maharashtra, Kerala, Karnataka, Tamil Nadu, Andhra Pradesh, Madhya Pradesh and Chhattisgarh
CoC (Sc) 24	Co 8371 X MS 6847	Mid-late	Medium	Tamil Nadu
Co 94012 (*Phule Savithri*)	Somaclonal variant of CoC 671	Early	Medium-broad	Maharashtra
Co 94008 (*Shyama*)	Co 7201 X Co 775	Early	Medium	Peninsular Zone Gujarat, Maharashtra, Kerala, Karnataka, Tamil Nadu, Andhra Pradesh, Madhya Pradesh and Chhattisgarh
CoSNK 03632	Co 8013 Polycross	Mid-late	Medium	South Gujarat
Co TI 88322 (*Madhuri*)	Co 740 X Co775	Mid-late	Medium	Kerala
Cul 527/85 (*Madhurima*)	Co740 X Co7318	Mid-late	Medium	Kerala
Co 88017 (*Madhumathi*)	Co 63 X Co 740	Mid-late	Medium	Kerala
Co TI 1153 (*Aromal*)	Co 86062 X Co 6806	Mid-late	Medium	Kerala
Co TI 1358 (*Abhay*)	Co 8213 X GC	Mid-late	Medium	Kerala

Table 2: Sucrose Content (%) of Selected Cane Varieties

Sucrose Content (%)	Varieties
11-14	TNAU Si7, TNAU Si8,CoG 93072,CoC (Sc) 24, CoTI 88322, Cul 527/85, Co 88017
14-17	Co 94012,CoTI 1153, CoTI 1358
17-20	Co 86032, CoC 671, VCF 0517,Co 99004, Co 85004, Co 94008, CoSNK 03632

Source: The data was provided by the respective collection centers (VC Farm, Mandya; SRS Sirugamani, Tamil Nadu; ARS Thiruvalla, Kerala)

Table 3: Cellulose, Hemicellulose and Lignin Estimated in Post-harvest Leaves of Different Cane Varieties

Varieties	Cellulose (%)	Hemicellulose (%)	Lignin (%)
Co 86032 (*Nayana*)	53.8±4.8	31±0.1	18.4±0.8
CoC 671 (*Vasant*-1)	41.3±0.7	33.4±0.5	18±0.5
VCF 0517 (CoVC 14061, *Bahubali*)	53±0.8	24±1.3	17.3±0.4
TNAU Si7	44.5 ±2.8	31.2±1.2	13.2±1.2
TNAU Si8	44.1±0.9	31.9±1.1	14.8±0.4
CoG 93076	38.9±1	26.4±0.6	17.5±0.5
Co 99004 *(Damodar)*	43±1.2	24±1.5	18.9±0.15
Co 85004 (*Prabha*)	38.7 ±5.9	23.6±1.5	15.3±0.3
CoC (Sc) 24	48.5±2.3	29.2±0.9	17±0.5
Co 94012 *(Phule Savithri)*	39±3.5	28.1±1.6	17.5±0.6
Co 94008 (*Shyama*)	39.3±0.9	28.3±0.2	17.2±0.5

Table 3 Contd...

...Table 3 Contd.

Varieties	Cellulose (%)	Hemicellulose (%)	Lignin (%)
CoS NK 03632	52.3 ±1.2	29±0.6	14.9±0.5
Co TI 88322 (*Madhuri*)	49.2 ±0.9	31.9±1.4	17.1±0.3
Cul 527/85 (*Madhurima*)	53.3±0.5	27.9±0.4	16.6±0.2
Co 88017 (*Madhumathi*)	49 ±0.1	29.9±0.5	16.9±0.6
Co TI 1153 (*Aromal)*	51.2 ±2.3	32.4±1.8	16..9±0.2
Co TI 1358 (*Abhay*)	49.2 ±0.9	34.4±0.54	18±0.8

The values are mean ±standard deviation, n=3; % dry weight of biomass

Table 4: Cellulose, Hemicellulose and Lignin Estimated in Nayana Leaves Collected from Different Locations

Location	Cellulose (%)	Hemicellulose (%)	Lignin (%)
VC farm, Mandya (Karnataka)	53.8±4.97	31±0.1	18.4±0.8
ARS, Thiruvalla (Kerala)	52.4±4	32±1.5	17.7±0.7
SRS, Sirugamani (Tamil Nadu)	53.6±4.9	31.1±1.6	17.7±0.6

The values are mean ±standard deviation, n=3; % dry weight of biomass

CONCLUSION

Sustainable energy resources are highly required in the current scenario of increasing energy demands worldwide. Finding a potential feedstock is one of the crucial criteria in biofuel production. Post-harvest cane leaves have a great role in acting as a renewable energy resource. Though India is the second largest producer of sugar cane, this feedstock is not explored effectively for contributing to commercial fuel production. Understanding the lignocellulosic content of feedstocks plays an important role in bioethanol production and this can vary in different varieties of a crop. So in the current study the lignocellulosic content of seventeen majorly cultivated Indian cane varieties was tested. The present study points that post-harvest leaves of widely cultivated variety, Nayana, can serve as a potential biofuel feedstock and can contribute in decreasing India's sole dependence on molasses for commercial bioethanol production.

ACKNOWLEDGEMENTS

The authors thank UGC start-up grant and UGC research fellowships for financial support for the current work and VC Farm, Mandya (Karnataka), Agricultural research station Sirugamani (Tamil Nadu) and Thiruvalla (Kerala) for providing the cane samples.

REFERENCES

Arora R, Manisseri C, Li C, Ong MD, Scheller HV, Vogel K, Simmons BA, Singh S (2010) Monitoring and Analyzing Process Streams Towards Understanding Ionic Liquid Pretreatment of Switchgrass (*Panicum virgatum* L.). Bioenerg Res 3:134–145

An YX, Zong MH, Wu H, Li N (2015) Pretreatment of lignocellulosic biomass with renewable cholinium ionic liquids: Biomass fractionation, enzymatic digestion and ionic liquid reuse. Bioresour technol 192:165-171

Asakawa A, Kohara M, Sasaki C, Asada C, Nakamura Y (2015) Comparison of choline acetate ionic liquid pretreatment with various pretreatments for enhancing the enzymatic saccharification of sugarcane bagasse. Ind Crop Prod 71:147-152

Badger PC (2002) Ethanol from cellulose: a general review. In: Janick J and Whipkey A (ed) Trends in new crops and new uses. ASHS Press, Alexandria VA, pp. 17-21

Bian J, Peng F, Peng XP, Xiao X, Peng P, Xu F, Sun RC (2014) Effect of [Emim] Ac pretreatment on the structure and enzymatic hydrolysis of sugarcane bagasse cellulose. Carbohydr polym 100:211-217

Brandt A, Grasvik J, Hallet JP, Welton T (2013) Deconstruction of lignocellulosic biomass with ionic liquids. Green Chem 15:550-583

Carpita NC (1996) Structure and biogenesis of the cell walls of grasses. Annu Rev Plant Physiol Plant Mol Biol 47: 445–476

Carvalho AV, da Costa lupes AM, Bogel- Lukasik R (2015) Relevance of the acidic 1-butyl -3 methylimidazolium hydrogen sulphate ionic liquid in the selective catalysis of the biomass hemicellulose fraction. RSC Adv 5: 47153-47164

Chandel AK, da Silva SS, Carvalho W, Singh OV (2012) Sugarcane bagasse and leaves: foreseeable biomass of biofuel and bio-products. J Chem Technol Biotechnol 87:11-20

Cheenkachorn K, Douzou T, Roddecha S, Tantayotai P, Sriariyanun M (2016) Enzymatic saccharification of rice straw under influence of recycled ionic liquid pretreatments. Energy Procedia100:160-165

Chen S, Ling Z, Zhang X, Kim YS, Xu F (2018) Towards a multi-scale understanding of dilute hydrochloric acid and mild 1-ethyl-3-methylimidazolium acetate pretreatment for improving enzymatic hydrolysis of poplar wood. Ind Crop Prod 114:123-131

Costa T, Vega- Sanchez ME, Milagres AM, Scheller HV (2016) Tissue-specific distribution of hemicelluloses in six different sugarcane hybrids as related to cell wall recalcitrance. Biotech Biofuels 9:99-111

Dadi AP, Varanasi S, Schall CA (2006) Enhancement of cellulose saccharification kinetics using an ionic liquid pretreatment step. Biotechnol Bioeng 95: 904–910

da Silva AS, Lee SH, Endo T, Bon EP (2011) Major improvement in the rate and yield of enzymatic saccharification of sugarcane bagasse via pretreatment with the ionic liquid 1-ethyl-3-methylimidazolium acetate ([Emim][Ac]). Bioresour technol 102(22):10505-10509

Fort DA, Remsing RC, Swatloski RP, Moyna G, Rogers RD (2007) Can ionic liquids dissolve wood? Processing and analysis of lignocellulosic materials with 1-n-butyl imidazolium chloride. Green Chem 9:63-69

Fox RL, Silva JA, Plucknett DL, Teranishi DY (1969) Soluble and total silicon in sugarcane. Plant Soil 1: 81-92

Fu D, Mazza G (2011) Optimization of processing conditions for the pretreatment of wheat straw using aqueous ionic liquid. Bioresour Technol 102: 8003-8010

Geng X, Henderson WA (2012) Pretreatment of corn stover by combining ionic liquid dissolution with alkali extraction. Biotech Bioeng 109:84-91

Govindaraj P, Karthigeyan S, Pazhany AS (2016) Exploration and genetic diversity analysis of *Saccharum spontaneum* in Maharashtra state, India. J Sugarcane Res 6:72-84

Hamidah U, Arakawa T, H'ng YY, Nakagawa-izumi A, Kishino M (2018) Recycled ionic liquid 1-ethyl-3-methylimidazolium acetate pretreatment for enhancing enzymatic saccharification of softwood without cellulose regeneration. J Wood Sci 64:149-156

Hyvarinen S, Mikkola JP, Murzin DY, Vaher M, Kaljurand M, Koel M (2014) Sugars and sugar derivatives in ionic liquid media obtained from lignocellulosic biomass. Comparison of capillary electrophoresis and chromatographic analysis. Catl Today 223:18-24

Karatzos SK (2011) Ionic liquid pretreatment and fractionation of sugarcane bagasse for the production of bioethanol. Dissertation, Queensland University of Technology

Knauf M, Moniruzzaman M (2004) Lignocellulosic biomass processing. Persp Int Sugar J 106:147 -150

Lee SH, Doherty TN, Linhardt RJ (2009) Ionic liquid mediated selective extraction of lignin from wood leading to enhanced cellulose hydrolysis. Biotechnol Bioeng 102:1368-1376

Lee SH, Lee SB (2005) The Hildebrand solubility parameters, cohesive energy densities and internal energies of 1-alkyl-3-methylimidazolium-based room temperature ionic liquids. Chem Commun 27: 3469–3471

Li C, Knierism B, Manisseri C, Arora R, Auer M, Vogel KP, Scheller HV, Singh S (2010). Comparison of dilute acid and ionic liquid pretreatment of switchgrass: Biomass recalcitrance, delignification and enzymatic saccharification. Bioresour technol 101:4900-4906

Limayem A, Ricke SC (2012) Lignocellulosic biomass for bioethanol production: Current prospective, potential issues and future prospects. Prog Energy Combust Sci 38:449-467

Mai NL, Ha SH, Koo YM (2014) Efficient pretreatment of lignocellulose in ionic liquids/co-solvent for enzymatic hydrolysis enhancement into fermentable sugars. Process Biochem 49:1144-1151

Meineke T, Manisseri C, Voigt CA (2014) Phylogeny in Defining Model Plants for Lignocellulosic Ethanol Production: A Comparative Study of *Brachypodium distachyon*, Wheat, Maize, and *Miscanthus x giganteus* Leaf and Stem Biomass. Plos one 9: e103580

Patel M, Kumari P (1990) Silicon carbide from sugarcane leaf and rice straw. J Mater Sci Lett 9:375–376

Pereira SC, Maehara L, Machado CMM, Farinas CS (2016) Physical, chemical and morphological characterization of the whole sugarcane lignocellulosic biomass used for 2G ethanol production by spectroscopy and microscopy techniques. Renew Energy 87:607-617

Poornejad N, Karimi K, Behzad T (2013) Improvement of saccharification and ethanol production from rice straw by NMMO and [BMIM][OAc] pretreatments. Ind Crop Prod 41:408-413

Rana S, Adak A, Tiwari R, Sharma A, Saritha M, Singh S, Nain L (2015) Pretreatment and Designing Energy Crops: Technological Innovations and Prospects. Res J Microbiol 10: 557-570

Santosh I, Ashtavinayak P, Amol D, Sanjay P (2017) Enhanced bioethanol production from different sugarcane bagasse cultivars using co- culture of *Saccharomyces cerevisiae* and *Scheffersomyces* (Pichia) *stipites*. J Environ Chem Eng 5: 2861-286

Schultz N, Pereira W, de Albuquerque Silva P, Baldani JI, Boddey RM, Alves BJ, Urquiaga S, Reis VM (2017) Yield of sugarcane varieties and their sugar quality grown in different soil types and inoculated with a diazotrophic bacteria consortium. Plant Prod Sci 20:366-74

Singh JK, Sharma RK, Ghosh P, Kumar A, Khan ML (2018) Imidazolium based ionic liquids: a promising green solvent for water hyacinth biomass deconstruction. Front chem 6:548-575

Singh S, Simmons BA, Vogel KP (2009) Visualisation of cellulose regeneration during ionic liquid pretreatment of switch grass. Biotechnol Bioeng 104:68-75

Smuga-Kogut M, Zgorska K, Kogut T, Kukielka K, Wojdalski J, Kupczyk A, Drozde B, Widewska I (2017) The use of ionic liquid pre-treatment of rye straw for bioethanol production. Fuel 191: 266–274.

Sochaa AM, Parthasarathi R, Shi J, Pattathil S, Whyt D, Bergeron M, George A, Tran K, Stavil V, Venkatachalam S, Hahn MG, Simmons BA, Singh S (2014) Efficient biomass pretreatment using ionic liquids derived from lignin and hemicellulose. PNAS 111:E3587–E3595

Sun N, Rahman M, Quin Y, Maxim ML, Rodriguez H (2009) Complete dissolution and partial delignification of 1-ethyl 3-methyl imidazolium acetate. Green Chem 11: 646-65

Tan SSY, MacFarlane DR, Upfal J, Edye LA, Doherty WO, Patti AF, Pringle JM, Scott JL (2009) Extraction of lignin from lignocellulose at atmospheric pressure using alkylbenzenesulfonate ionic liquid. Green Chem 11:339–345

Tawadare R, Thangadurai D, Khandagave RB, Mundaragi A, Sangeetha J (2019) Phenotypic Characterization and Genetic Diversity of Sugarcane Varieties Cultivated in Northern Karnataka of India based on Principal Component and Cluster Analyses. Braz arch biol technol 62:e19180376

Wang H, Gurau G, Rogers RD (2012) Ionic liquid processing of cellulose. Chem Soc Rev 41:1519–1537

Wang FL, Li S, Sun YX, Han HY, Zhang BX, Hu BZ, Gao YF, Hu XM (2017) Ionic liquids as efficient pretreatment solvents for lignocellulosic biomass. RSC adv 7:47990- 47998

Wang G, Zhang S, Xu W, Qi W, Yan Y, Xu Q (2015) Efficient saccharification by pretreatment of bagasse pith with ionic liquid and acid solutions simultaneously. Energ Convers Manage 89:120-126

Science and Technology Journal Vol. 8 Issue 2 July 2020 ISSN: 2321-3388

Inclusion of Ingredients and Traits Enrichment of Assorted Recipes with Nutri-Rich Powder

Pushpanjali Mishra[1], Shraddha Shukla[2], Alka Gupta[1#*], Pragya Singh[1], Awadhesh Kumar[3] and Shashi Kant Shukla[4*]
[1]Department of Food, Nutrition and Dietetics,
Ethelind College of Home Science, SHUATS, Prayagraj–211007
[2]Nanotechnology Application Centre, University of Allahabad, Prayagraj–211002
[3]Department of Horticulture, Aromatic and Medicinal Plant, Mizoram University Aizawl–796004
[4]Anupam Rural Laboratory, Centre of Science and Society, University of Allahabad,
Prayagraj–211002
E-mail *shashibplau@rediffmail.com, #alkagupta@shiats.edu.in

Abstract—The present study was carried to develop the enriched food products with the incorporation of nutri-rich powder and assess the sensory qualities of prepared food products. It was concerned with development of nutri-rich powder prepared from finger millet *(Eleusine coracana),*cauliflower leaves (*BrassicaOleracea*) *and* papaya (*Carica papaya*) leaves*.* Food materials,namakpara*,* laddoo*,* samosaand batiwere made by incorporation of nutri-rich powder, indigenous foods and served as treatments T_1, T_2 and T_3 respectively, T_0 without addition of dehydrated leaves and coarse grains served as control. Sensory evaluation was carried out. Data obtained were statistically analyzed by using analysis of variance (ANOVA), critical difference (CD). Amylose and amylopectin contents of indian finger millet starches ranged from 15.8 to 16.2% and 83.8 to 84.2% respectively.Chemical analysis of nutri-rich powder for mosisture(31.9%), ash(9.79gm), protein(37.7gm), fat(6.1gm) and fiber(13.9gm)content was done by using AOAC (2005) standard procedures. And calcium (415mg), vitamin C (185.38mg), Iron(73.6mg), β-Carotene (239.01μg), DPPH- 140.92%, TPC- 243.40mg. On the basis of findings, it was observed that T_1, T_2 was found to be best with regards to flavour and taste and overall acceptability. In nutshell it can be concluded that indigenous foods can be integrated in the preparation of different food products to improve their sensory acceptability.

Keywords: Multi rich-powder, Sensory, DPPH, ANOVA, Indigenous

INTRODUCTION

Different types of indigenous foods are available in India, but are not utilized to the extent they should be in spite of their higher nutritive value. Indian subcontinent is the foremost producer of the major millet crops of pearl millet (*Pennisetumtyphoideum*) and finger millet (*Eleusinecoracana*). A number of minor millets are proso millet (*panicummiliacuem*), foxtail millet (*Setaria italic*) and kodo millet (*Paspalumscorbiculatum*) (Verma and Patel., 2013). Ragi or finger millet is a short, profusely tillering plant which attains the characteristic of finger like terminal inflorescences, bearing small reddish seedswhich is also known as finger millet. It is widely consumed practically without any refining by the poorer section of the population it varies in colour from deep brown shades ranging from red to almost black.Ragi is the principal food grain of the rural population in India, especially in the southern region. Nutritionally it is almost as good as or better than wheat or rice. The husk forms 5.6 % of the weight of the grain which is rich in calcium, phosphorous and iron. The calcium content is higher than in the common cereals and millets. Though, its phosphorous content is high, much of it (75.0%)in the form of phytin phosphorous. It contains B vitamins, but is poor in riboflavin. The major proteins of ragi are prolamins and glutelin(Shakuntala and Shadaksharaswamy., 1998). Finger millet is a popular weaning food. Finger millet flour has been traditionally used as a weaning food from 6 months of age. It is ide as baby food because of its high-level of calcium and protein.They are adequate in all the essential amino acids(Kumari et al., 2017).The nutritive value of starch is dependent on the content of ressistant starch (RS).

Low level of resistant starch at lowtemperature suggests, that at this temperature, although crystallites forming the structure of RS in the native flour is torn apart, no new compensating or additional crystallites are formed between amylose chains since the extrusion temperature is probably below the threshold for starch fragmentation.

Infinger millet carbohydrate(72.6g/100g), protein(7.7g/100g), fat(1.5g/100g), crude fibre (3.6g/100g), ash(2.7g/100g), calcium(344mg/100g), iron(6.3mg/100g), Moisture(11g/100g), calcium(357mg/100g) (Verma and Patel., 2013).

Cauliflower green leaves (‘*Brassicaoleracea L.var. botrytis*) are rich source of micro nutrients and belong to the family *Brassicaceae*. It comes from the Latin words *caulis*, meaning-stalk and floris-flower(Chauhan and Inteli., 2015). Cauliflower leaves are cheap and within reach of common man but they are available only for a short period of time. These vegetables are also rich in beneficial plant’s metabolites, which include sulfur containing glucosinolates, anthocyanin’s, flavonoids, trepans, S-methyleysteinesulfoxide, and other compound to improve the nutritional, physico-chemical and sensory quality and very beneficial to health. Phytochemicals of cauliflower leaves are stronger antioxidants and are thought to reduce the risk of chronic diseases by protecting against free radical damage(Shivani and Deepak., 2018). They are highly perishable due to their high moisture content (80g %). 100g fresh Cauliflower leaves contain 5.9g protein, 1.3g fat, 7.6g carbohydrate, 2g crude fiber and 66kcal energy (Kumari et al., 2018).Vitamin A deficiency is the common cause of blindness in children in the developing age(Nath and Dutta., 2016). Cauliflower leaves powder is rich source ofVitamin C (54.27mg/100g)(Buvaneshwari and Ramya., 2014**).** The enzymes present in fresh cauliflower leaves were deactivated which further increases the shelf life of the food and makes the food ready-to-use(Kumari et al., 2018).

Papaya belongs to the genus *Carica*.Itcontains the enzyme papain, which is present in the fruits, stem and leaves(Peter et al., 2014). Papaya leaf extracts have phenolic compounds, such as protocatechuic acid, p-coumaric acid, 5, 7-dimethoxycoumarin, caffeic acid, kaempferol, quercetin, chlorogenic acid.These leaf juices have become popular among the dengue suffering patients due to the platelet increasing activity (Hossain et al., 2016).

The energy content of papaya leaves powder (163kcal), iron(10mg), crude fiber(1.8g), calcium (344mg), protein (5.1g), fat (1.14g), ash(2.1), carbohydrate (10.8), vitamin C (235mg) (Aravind et al., 2013)**.**

The present research aimed with objective to evaluate to develop the enriched food products with the incorporation of nutri-rich powder and assess the sensory qualities of prepared food products.

MATERIALS AND METHODS

Collection of Samples

Finger millets *(Eleusinecoracana),*cauliflower leaves (*Brassica Oleracea*) *and* papaya (*Carica papaya*) leaveswere procured from Nainilocal market, Pryagraj District, Uttar Pradesh. Millet and leaves were thoroughly cleaned for removal of dirt, unwanted particles and insects.

Chemical Analysis

Moisture, ash, fat, fiber and minerals were determined according to A.O.A.C (2012)(AOAC., 2012). The carbohydrate [nitrogen free extract (NFE)] was calculated. The phytic acid was estimated by using trichloroacetic acid and precipitates as ferric salt as a standard (Sadasivam and Manickam., 2008). The oxalate is precipitated as calcium oxalate. The precipitated is filtered, washed and dissolved in a hot dilute sulphuric acid and titrated the formed oxalic acid with the standard $KMnO_4$ solution (Gupta 2007)(Gupta.,2007). Protein was estimated by lowry’s method(Lowry et al., 1951).Total phenolic content was based on folin- ciocalteau reagent followed by spectrophotometrically determination carried out 760 nm and the result was calculated asgallic acid equivalent (sigma chemicals, USA) as a standard (Singleton et al., 1999). It is mainly comprised of amylose and amylopectin fraction. Starch granules are composed of two types of alphagulucans, amylose and amylopectin, which represent approximately 98-99% of the dry weight. The amylose content of finger millet varieties was found to range from 19.43 to 30.88%. Finger millet canactasa wheat subsutute given their quite similar protein structure yet then on glutinous nature. In this respect, they have considerable potential to be developed as functional food (Taylor et al., 2006; Taylor and Emmambux, 2008; Chandrasekara and Shahidi, 2012b). DPPH radical has intense violet colour but turns colourless as unpaired electrons are sequestered by antioxidants. In this method, extracted sample, were made to react with the radical solution and rested for 30 minutes at room temperature, it was measured for absorbance at 517nm, the inhibition percentage of DPPH free radical was calculated (Brand *et al*., 1995).

Fig. 1: Finger Millet (Brown)

Formulation and Preparation of Products

These leaves were sort and clean with the help of the water to prevent from the disease and remove the dirt. These leaves were dehydrated under the hot air oven. The leaves and finger millet converted into powder. Four products were prepared with the incorporation of nutri-rich powder namely Namakpara, Laddoo, Samosaand Bati. For each product, the basic recipes (control T_0) have three variants T_1, T_2 T_3 respectively where the amounts of incorporation of different nutri-rich powder were varied. In namakpara T_1 nutri-rich powder ratio is (90:10), in T_2 (80:20), T_3 (70:30), in laddoo, T_1 nutri-rich powder ratio is (90:10), T_2 (80:20), T_3 (70:30), samosa T_1 nutri-rich powder ratio is (90:10), T_2 (80:20), T_3 (70:30), in bati T_1 nutri-rich powder ratio is (90:10), T_2 (80:20), T_3 (70:30)were selected for the study; details of treatments are given in table 1. Each treatment has its three replicates. Evaluation of sensory characteristics like colour and appearance, body and texture, flavour and taste and overall acceptability of products was performed by 9 point hedonic scale 17. The results were rated that on points as ; Like extremely: 9, Like very much :8, Like moderately:7, Like slightly :6, Neither like nor dislike:5, Dislike slightly:4, Dislike moderately :3, Dislike very much :2, Dislike extremely: 1.The results were evaluated by five trained panelist among staff.

Statistical Analysis

The data obtained from sensory evaluation were statistically analyzed by ANOVA (2 way classification) and Critical difference (CD) were used to analyze the data (Gupta and Kapoor.,2002).

RESULTS AND DISCUSSION

Nutritionally, it was found that the nutrients content in nutri-rich powder (per 100 g) obtained by chemical analysis which are as follows – moisture content was found to be 31.99%, ash content was found to be 4.79g, protein content was found to be 7.567g, fat content was found to be 1.15g, crude fibre was found to be 3.92g, carbohydrate content was found to be 56.90g, calcium was found to be 1.98g, vitamin C was found to be 9.32mg, Iron was found to be 0.074g, β-carotene was found to be 9.225 µg and energy was found to be 321.32 kcal. (Table-2)

Namakpara, Laddoo, Samosaand Batiwere prepared using different ratios of nutri rich powder. The acceptability of food products was judged by the panel of six semi-trained members.

Table 1: Proportions of Addition of Nutri-rich Powder in Food Products

Ingredients	T0 (%)	T1 (%)	T2 (%)	T3 (%)
Finger Millet	-	5g	10g	20 g
Cauliflower leaves	-	2.5g	5g	10g
Papaya leaves	-	2.5g	5g	10g
Refined Flour	100g	90g	80g	70g
Sattu	50g	40g	30g	20g
SamosaMasala	50g	40g	30g	20g
Bengal gram	100g	90g	80g	70g

Sensory evaluation using Nine Point Hedonic scale revealed that 70 per cent of panelists liked extremely the Namakpara, batiandsamosawith nutri-rich powder at the ratio of 10% and 20% in ladoo. In table-3,Namkpara, T_1 scores the best with regard to all sensory characteristics viz. colour and appearance (7.93±0.57), body and texture (7.86±0.38), taste and flavor (7.46±0.30) and overall acceptability (7.77±0.25). In table-4,Laddoo, T_2 scores the best with regard to all sensory characteristics viz. colour and appearance (8.5±0.39), body and texture (7.96±0.19), taste and flavour (8.2±0.06) and overall acceptability (8.2±0.08).

Table 2: Nutritional Composition of Nutri-rich Powder in Food Products

Nutrient	Nutri-rich Powder (100g)
Moisture (%)	31.9
Ash (g)	9.79
Protein (g)	37.7
Fat (g)	6.1
Crude fibre (g)	13.9

Carbohydrate (g)	65.9
Calcium (mg)	415
Vitamin C (mg)	185.38
Iron (mg)	73.6
β-carotene (µg)	239.01
Energy (kcal)	821.32

Table 3: Antioxidant and Radical Scavenging Activity of Dehydrated Nutri-rich Powder per 100g

Parameters	Nutri-rich Powder
Polyphenols (TPC) (mg)	243.40mg
DPPH (%)	130.92

In table-5,Samosa, T_1 scores the best with regard to all sensory characteristics viz. colour and appearance (8.53±0.39), body and texture (7.23±0.19), taste and flavour (8.9±0.06) and overall acceptability (8.53±0.08).

Table 4: Average Sensory Score of Different Parameters in Control and Treated Sample of Namakpara

Control and Treatments	Colour and Appearance	Body and Texture	Taste and Flavour	Overall Acceptability
T_0	8.2 ± 0.326	7.9 ± 0.294	8.03 ± 0.2599	7.95 ± 0.1855
T_1	7.93 ± 0.578	7.86 ± 0.381	7.46 ± 0.302	7.77 ± 0.2510
T_2	6.6 ± 0.163	6.2 ± 0.4271	5.4 ± 0	5.90 ± 0.204
T_3	5.46 ± 0.0543	4.93 ± 0.1450	3.9 ± 0.057	4.73 ± 0.056
F%	30.26 (S)	12.823 (S)	21.017 (S)	34.210 (S)
C.D	0.79	1.384	1.419	0.882

S = Significant, NS = Non- Significant, ± S.E

Table 5: Average Sensory Score of Different Parameters in Control and Treated Sample of Laddoo

Control and Treatments	Colour and Appearance	Body and Texture	Taste and Flavour	Overall Acceptability
T_0	8.53 ± 0.05	8.23 ± 0.267	8.23 ± 0.205	8.32 ± 0.111
T_1	7.83 ± 0.123	7.13 ± 0.108	6.2 ± 0.133	7.02 ± 0.080
T_2	8.56 ± 0.395	7.96 ± 0.190	8.2 ± 0.065	8.2 ± 0.086
T_3	6.26 ± 0.144	5.46 ± 0.144	4.6 ± 0.093	5.06 ± 0.212
F%	86.5 (S)	24.55 (S)	196.153 (S)	56.186 (S)
C.D	0.39	0.83	0.430	0.700

S = Significant, NS = Non- Significant, ± S.E

In table-6 Bati, T_1 scores the best with regard to all sensory characteristics viz. colour and appearance (8.1±0.39), body and texture (8.6±0.19), taste and flavour (9.2±0.06) and overall acceptability (8.61±0.08).

Table 6: Average Sensory Score of Different Parameters in Control and Treated Sample of Samosa

Control and Treatments	Colour and Appearance	Body and Texture	Taste and Flavour	Overall Acceptability
T_0	7.56 ± 0.053	7.23 ± 0.178	7.9 ± 0.1001	7.56 ± 0.0168
T_1	8.53 ± 0.040	7.23 ± 0.584	8.9 ± 0.1450	8.53 ± 0.0539
T_2	6.8 ± 0.0093	6.5 ± 0.066	5.3 ± 0.1672	6.3 ± 0.0749
T_3	6.06 ± 0.1081	5.9 ± 0.0469	4.46 ± 0.1381	5.44 ± 0.0182
F%	296.460 (S)	67.5 (S)	521.6 (S)	371.33 (S)
C.D	0.2047	0.415	0.73	0.2447

S = Significant, NS = Non- Significant, ± S.E

Based on the price of the raw ingredients at prevailing market price, the average cost of Namakparaper 100g of raw ingredients was Rs. 8.4 for control, Rs. 8.35 for T_1, Rs. 8.3 for $T_2$and Rs. 8.25 for T_3. Average cost of Laddoo per 100g of raw ingredients was Rs. 19 for control, Rs. 18.45 for T_1, Rs.18.32 for $T_2$and Rs. 17.95 for T_3. Average cost of Samosa per 100g of raw ingredients was Rs. 10.8 for control, Rs. 10.65 for T_1, Rs.10.5 for T_2 and Rs. 10.35 for T_3. Average cost of Bati per 100g of raw ingredients was Rs. 10.2 for control, Rs. 9.75 for T_1, Rs. 9.2 for $T_2$and Rs. 8.65 for T_3.

Table 7: Average Sensory Score of Different Parameters in Control and Treated Sample of Bati

Control and Treatments	Colour and Appearance	Body and Texture	Taste and Flavour	Overall Acceptability
T_0	7.3 ± 0.1156	7.5 ± 0.0942	8 ± 0.0942	7.63 ± 0.117
T_1	8.1 ± 0.0817	8.6 ± 0.3076	9.2 ± 0.0469	8.61 ± 0.0349
T_2	6.9 ± 0.0942	6.4 ± 0.2056	5.1 ± 0.066	6.45 ± 0.309
T_3	6.2 ± 0.1857	5.7 ± 0.2238	4.4 ± 0.1491	5.45 ± 0.1481
F%	22.60 (S)	46.28 (S)	521.6 (S)	41.108 (S)
C.D	0.557	0.685	0.342	0.73

S = Significant, NS = Non-Significant, ± S.E

The prepared nutri-rich powder have the property of increasing hemoglobin and platelets counts in the body therefore this nutri- rich powder can be taken or by the patients having low level of platelets counts and anemic to maintain it to a normal level(Sharma and Alka., 2015).

CONCLUSION

On the basis of findings, it can be concluded that incorporation of nutri-rich powder in the prepared products increases the nutrient density.A physical property of extruded products depends greatly on the extrusion parameters. Nutri-rich powder can be successfully incorporated in various products which are beneficial to health.Popularization and incorporation of nutri-rich powder in value added food products enhance the nutritional value of food products.

ACKNOWLEDGEMENTS

Authors are thankful to Head, Department of Food, Nutrition and Dietetics, Ethelind College of Home Science, SHUATS, Prayagraj for providing facilities; to UGC for financial support.

REFERENCES

AOAC (2012) Official methods of analysis.Association of official analytical chemist 19th edition, Washington D.C., USA.

Aravind G, Bhowmik D, Duraivel S, Harish G (2013)Traditional and medicinal uses of *Carica papaya*. Journal of Medicinal Plants Studies.1(1): 7-15.

Brand WW, Cuvelier ME, Berset C (1995) Use of a free radical method to evaluate antioxidant activity. Food Science and Technology. 28: 25-30.

Buvaneswari KM, Ramya GA (2014) Study on over all acceptability of *Brassicaoleracea* leaves (Cauliflower Leaves) incorporated food products and its impact on treating anemic college going girls.International Journal of Current Research and Development. 2 (1): 38-47.

Chauhan A, Inteli (2014)Product development and Sensory evaluation of value added food products made by incorporating dried cauliflower green leaves. International Journal of Nutrition and Agriculture Research. 1(2); 93 - 98.

Gupta SC, Kapoor UK (2002) Fundamentals of applied statistics"2nd edition, Chand& Son. 51-85, ISBN-81-7014-791-3.

Gupta AK (2007) Practical Manual of Agricultural Chemistry. Analysis of Plant, Food & Biological Samples, 3rd edition.

Hossain N, Kumar PV, Wei YS (2016) Dengue and drawbacks of marketed *Carica papaya*leaves supplements. International Journal of Green Pharmacy.10 (1): 2-4.

Kumari R, Gupta A, Prasad R, Tripathi J (2018) Prevalence of Vitamin A deficiency among school going children of Jasra block of Allahabad, India.Journal of Applied and Natural Science. 10 (1): 4-5.

Kumari R**, Gupta A,** Sheikh S (2017) Development of nutrient dense supplementary products for children by using locally available whole wheat flour, ragi flour, green gram flour, soy flour, roasted groundnut flour and jiggery. *The Allahabad Farmer, 73 (2); 30-33.*

Lowry OH, Roserbrough NJ, Farr AL,Randall RJ (1951) Protein measurement with folin phenol reagent. Journal Biological Chemistry.193: 265-275.

Nath R, and Dutta M (2016)Phytochemical and proximate analysis of papaya (*Carica papaya*) leaves.ScholarsJournal of Agriculture and Veterinary Sciences.3(2): 85-87.

Peter JK, Kumar Y, Pandey P, and Masih H (2014) Antibacterial activity of seed and leaf extract of *Carica papaya*var. Pusa dwarf Linn. IOSR Journal of Pharmacy and Biological Sciences. 9(2): 29-37

Sadasivam S,Manickam A (2008) Biochemical Method. Antinutritional factors, 3rd New Age International Pvt. Ltd.

Shakuntala MN, Shadaksharaswamy M (1998) Foods, Facts and principles. New age International Publishers, New Delhi, ISBN: 9780852267318.

Sharma M, Gupta A (2015) Value addition in beverages with Papaya leaves extract (*Carica papaya*). International Journal of Science and Research (IJSR).doi:10.21275/art20175797.

Shivani AP, Deepak TB (2018) Studies on cauliflower leaves powder and its waste utilization in traditional product. International Journal of Agricultural Engineering. 11:95-98

Singleton VL, Orthofer R, Lamuela RRM (1999) Analysis of total phenols and other oxidation substrates and antioxidants by means of folin-ciocalteaue reagents. Methods in Enzymology. https://doi.org/10.1016/S0076-6879(99)99017-1.

Verma V, Patel S (2013) Value added products from nutri-cereals: Finger millet (*Eleusinecoracana*). Nutrition and Food Science. 25 (3): 169-176.

Science and Technology Journal Vol. 8 Issue 2 July 2020 ISSN: 2321-3388

Phytochemical Screening and Allelopathic Effects of *Ageratum conyzoides* L.

J.C. Angel Lalrindiki[1]*, Alex Zohmachhuana[2] and F. Lalnunmawia[3]
[1,2,3]Laboratory of Ecology, Department of Botany,
School of Life Sciences, Mizoram University Tanhril–796004, India
*E-mail: angeljc009@gmail.com

Abstract—A weed is a plant that grows and compete with other plants for food, light, moisture and space. *Ageratum conyzoides* L. is a common weed belonging to the Asteraceae family. They are annual aromatic weed. They are invasive of pastures, vacant lots and even entire forest areas. Phytochemicals are secondary metabolites that are known to influence various activities of plants. The qualitative phytochemical analysis of the methanol leaf extract of *A. conyzoides* revealed the presence of phenols, flavonoids, alkaloids, quinones, cardiac glycosides, terpenoids and tannins except saponins and anthraquinones, whereas the quantification revealed that the methanol extract contained flavonoid content (27.8±0.685 mg/g), phenol content (8.6±0.446 mg/g) and alkaloid content (2.06±0.53 mg/g). The fresh leaf extract of *A. conyzoides* was treated to the seeds of *Zea mays* to study the allelopathic effect of the weed. The germination rate shows a gradual decline with increase in the concentration of the weed extracts.

Keywords: *A.conyzoides*, weeds, allelopathy, secondary metabolites, phytochemical screening, ANOVA.

INTRODUCTION

Ageratum conyzoides L. is an invasive weed that adversely affects the growth of crops. Among the weeds, *Ageratum* is found to be the most commonly thriving weed in agricultural fields worldwide. The species is known to possess various biological activities starting from its various phytochemical contents and offers many opportunities to investigate the various functions and prospects in pharmaceutical studies (Chauhan and Rijhwani 2015). They belong to the Asteraceae family. It is an annual herb, 30- 40 cm. high, stems erect, hairy-green or purple. Leaves are opposite, broadly ovate, creanate, coarsely hairy on both sides, 3- nerved at the base. The inflorescence is a terminal corymb of many small heads; flowers violet or white (Borkataky *et al*., 2013). Allelopathy is an interference mechanism in which live or dead plant materials release chemical substances, which inhibit or stimulate the associated plant growth (May and Ash, 1990). Both weeds and agricultural crops are plants, so they require the similar conditions for normal growth and development. They compete for an adequate supply of the same nutrients, moisture, light, heat energy (temperature), carbon dioxide and growing space. Competition and the presence of vegetative and reproductive parts of weeds at or near to harvest have the greatest adverse affect on crop quality (Anderson 1983).

Plants produce secondary metabolites like phenols, flavonoids, alkaloids, tannins, terpenoids, polyacetylenes, fatty acids and steroids, which provides the plant with an allelopathic effect on the development of neighbouring plants or the same plant. Considerable knowledge has been obtained concerning the chemicals involved in allelopathy (Rice 1984; Narwal and Tauro 1994). Rice (1984) and Putnam (1983) stated that leaves are the major sources of allelochemicals. Rice (1984) stated that allelochemicals are known to affect numerous physical and biochemical processes in plants.The phytochemicals like alkaloids, saponins, flavonoids and phenolic compounds present in plants are responsible for many biological activities (Saswade 2019). Phytochemical analysis is an essential part towards the discovery of useful and novel drugs. Screenings for biological activity using simple bioassays have now been added to give a better identification of the usefulness of weeds.The present work aimed to study the phytochemicals and the effect of weed (*A. conyzoides*) on agricultural crop (*Z. mays*).

MATERIALS AND METHOD

Preparation of Plant Extracts

The plants samples were collected locally. The leaves were properly cleaned and air dried in room temperature. The dried plant materials were crushed into fine powder. 10 grams of air dried weed plant material was also taken by using Digital Electronic Weighing Machine and added in 100 ml of distilled water. After a storage period of 24 hours at room temperature, it was then filtered through Whatman filter paper no.1 and the volume of the filtrate was made to 1000ml.

The methanol extract was prepared by adding 400ml of Methanol to 100 grams of air dried sample and incubated for 72 hours with regular stirring.The extracts were filtered and dried using rotary evaporator. The extracts obtained were collected and stored at -20°C until further used.

Qualitative Phytochemical Analysis

The preliminary phytochemical analysis of methanol extract of *A.conyzoides* was performed by standard procedures given by (Krishnaiah *et* al., 2009) to detect phenol, flavonoid, alkaloid, saponin, quinone, cardiac glycoside, terpenoid, tannin and anthraquinone in the plant sample.

Tannin Test: 1 ml of the plant extract was taken in a test tube. To this, 2 ml of 0.7 M Sodium bicarbonate ($NaHCO_3$) and a few drops of Folin's reagent were added. Formation of greenish black or dark blue indicates the presence of tannin.

Saponin Test: 2 ml of distilled H_2O was mixed with 2 ml of plant extract in a test tube and it was mixed vigorously. The formation of foam layer indicates the presence of saponin.

Flavonoid Test: 2 ml of plant extracts was mixed with 5 ml of dilute ammonia and concentrated sulphuric acid (H_2SO_4). White precipitate appearance indicates the presence of flavonoid.

Alkaloid Test: A few drops of Dragendorff's reagent was added to 1 ml of plant extract. Orange red precipitate form indicates the presence of alkaloid.

Quinone Test: 1 ml of plant extracts was mixed with 1 ml of concentrated sulphuric acid (H_2SO_4). The presence of quinone was indicated by the formation of red colour.

Cardiac Glycosides Test: 2 ml of glacial acetic acid and a few drop of 5 % ferric chloride ($FeCl_3$) solution was mixed with 1 ml of plant extract and concentrated H_2SO_4. A brown ring formed between the layers showed the presence of cardiac glycosides.

Terpenoid Test: 1 ml of plant extracts along with 2 ml of chloroform was mixed in a test tube. Then, concentrated sulphuric acid (H_2SO_4) was added carefully. A red brown colour ring formed between the layers showed the presence of terpenoids.

Phenol Test: A few drops of 15 % sodium carbonate (Na_2CO_3) and Folin's Reagent were added to 1 ml of plant extract. The formation of blue colour indicates presence of phenol.

Anthraquinone Test: Few drops of 10 % ammonia (NH_3) was added to 1 ml of plant extracts and shaken vigorously. The appearance of pink colour precipitate indicates the presence of anthraquinone.

Quantitative Phytochemical Analysis

The quantitative analysis for the methanol extract of *A. conyzoides* was carried out for phenol (Ainsworth and Gillespie 2007), flavonoid (Chang *et al*., 2002) and alkaloid content (Luyang *et al*., 2014).

Allelopathic Effects

The fresh leaf filtrate was made for different dilutions such as 2%, 4%, 6%, 8% and 10% of the extract were prepared from the stock solution. The seeds *of Z. mays* were soaked separately in a petri plates in distilled water overnight. The next day, the seeds were surface sterilized with 0.1% of mercuric chloride solution for two minutes and washed twice with distilled water and kept for germination. The petri-dishes were autoclaved before use in order to prevent any type of contamination or infection. Paper towels were used for germination tests and the towel was wrapped with the tissue paper. Each paper towel was moistened with approximately 10ml of respective extracts. The soaked seeds were then placed in the petri dishes with the respective concentration and the number of seeds placed were counted. After placing the seeds they were then covered with a layer of moistened paper towel. In each set of treatment two replicates were kept containing the same number of seeds. Observation of germination percentage and seedling length was done after an interval of one week.

Statistical Analysis

The experimental data pertaining to each parameter were analyzed statistically using SPSS16 with the help of analyses of variance technique (ANOVA). Significant level at 5% levels of significance was considered.

RESULTS AND DISCUSSION

The phytochemical analysis of methanol extract of *A. conyzoides* shows the presence of phenols, flavonoids, alkaloids, quinones, cardiac glycosides, terpenoids and tannins, however saponins and anthraquinones were absent (Table 1). The results were supported by the findings of Borkataky *et al* (2013) who reported that the phytochemical analysis of *A. conyzoides* revealed the presence of alkaloids, flavonoids, phenolics and tannins, steroids and glycosides. The above results are also in accordance with the findings of Selvakumar *et al* (2012) who stated the presence of phytochemical active compounds such as tannins and cardiac glycosides in the leaf and stem extraction of *Euphorbia hirta*.

The quantitative estimation for phenols, flavonoids and alkaloid content showed 8.6±0.446 mg/g, 27.8±0.685 mg/g, and 2.06±0.53 mg/g, respectively (Table 1). The results were akin to the to the studies of Dian *et al* (2019) who reported that *A. conyzoides* leaf extract possessed active compounds such as saponin, alkaloid, steroid, flavonoid, tannin and phenol in various concentration. *A. conyzoides* extract had the flavonoid (6.15%w/v), phenol (3.86%w/v) and alkaloid (0.14%w/v) contents.The phytochemicals revealed in *A.conyzoides*, plant extracts had been documented in previous works (Ponchang *et al*.,2017; Diepreye *et al*.,2014; Ezeokeke *et al*.,2015).

Table 1: Phytochemical Analysis of Methanol Extract of *A.conyzoides*

Qualitative Phytochemical Analysis using Standard Protocol									
Test	**Phenols**	**Flavonoids**	**Alkaloids**	**Saponins**	**Quinones**	**Cardiac Glycosides**	**Terpenoids**	**Tannins**	**Anthraquinones**
Results	+	+	+	-	+	+	+	+	-
Quantitative Phytochemical Analysis (mg/g of Dry Tissue)									
Phenol	8.6±0.446								
Flavonoid	27.8± 0.68								
Alkaloid	2.06±0.53								

Germination percentage (%) of *Z. mays* when treated with aqueous leaf extract of *A. Conyzoides*: Table 2 shows a slow but gradual decline in germination percentage when treated with *A. conyzoides*. As seen from the table, all the seeds in control germinated. This maybe due to absence of weed extracts. However, as the concentration of the weed extracts increases the rate of germination declines. This shows that the phytochemicals present in *A. conyzoides* inhibits the germination rate of *Z. mays*. The study also revealed that the effects of the selected weed on the germination percentage (%) of *Z. mays* are found to be statistically significant (p≤0.05).

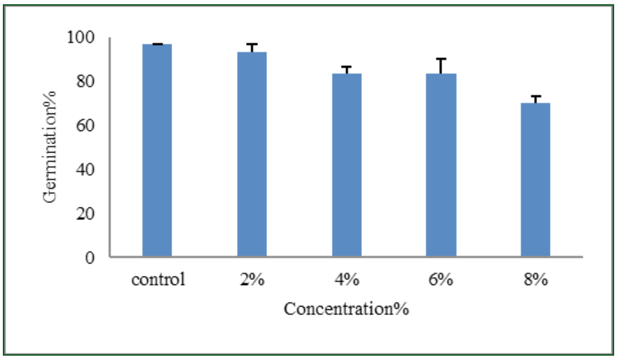

Fig. 1a: Effect of *A. conyzoides* Extracts on the Germination of *Z. mays*

Table 2: Germination percentage (%) of *Z. mays* when Treated with *A. conyzoides*

Dilutions	**No. of Seeds**	**No of Seeds Germinated**	**Germination Percentage**	**F-value**	**p-value**
Control	60	60	100%	9.486	0.001*
2%	60	58	96.6%		
4%	60	56	93.3%		
6%	60	50	83.3%		
8%	60	50	83.3%		
10%	60	42	70%		

The chemicals exudates from allelopathic plants play an important role in the allelopathic mode of action. The allelopathic effect of these chemicals causes inhibition of seed germination (Gupta and Mittal, 2012). From the above data collected, it can be concluded that all target species demonstrated a significant degree of suppression and a negative response to the increasing concentration of different weed extracts. The germination of *Z. mays* treated with aqueous extracts of *A. conyzoides* was found to be higher in control and the germination rate decreases with increase in concentration of *A. conyzoides* extracts (Figure 1a and 1b). Similar findings were also shown by the work done by Gupta and Mittal (2012) who reported the effect of allelopathic leaf extract of five selected weeds on *Triticum aestivum L.* The five selected weeds *Phalaris minor L., Chenopodium murale L., Sonchu soleraceus L., Cyanodon dactylon L. and Convolvulus arvensis L.* shows a certain degree of suppression and a negative response to the increase in concentration of their extracts when treated on *Triticum aestivum* L. Similar observation was also found by Ballester *et al* (1982).

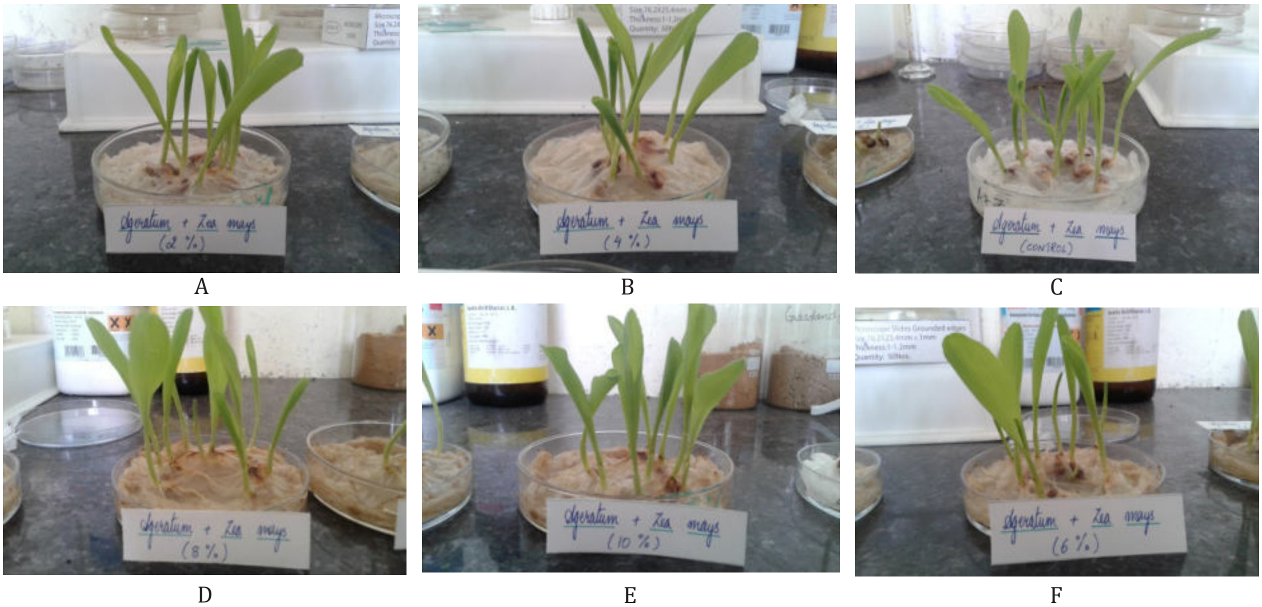

Fig. 1b: Effect of *A. conyzoides* Extracts on the Germination of *Z. mays*

A. ***Zea mays* seeds at control.**
B. ***Zea mays* seeds at 2% concentration.**
C. ***Zea mays* seeds at 4% concentration.**
D. ***Zea mays* seeds at 6% concentration.**
E. ***Zea mays* seeds at 8% concentration.**
F. ***Zea mays* seeds at 10% concentration.**

CONCLUSION

The results of present comprehensive analysis demonstrated that *A. conyzoides* possess high phenolic, flavonoid and alkaloid contents with potential antioxidant activity. The allelopathic effect of *A. conyzoides* studied on *Z. mays* shows a gradual decline in the germination rate of *Z. mays* with increase in the weed extract concentration. Further studies can be done to analyse the phytochemical properties as well as their antioxidant activity on different agricultural crops. Screenings for biological activity using simple bioassays will give us a better identification of the usefulness of different weeds.

ACKNOWLEDGEMENT

The authors expressestheir gratitude to UGC-MZU fellowship, India for providing financial assistance to J.C. Angel Lalrindiki, Dept. of Botany, to carry out her Ph.D work in Mizoram University, Aizawl.

REFERENCES

Ainsworth EA and Gillespie KM (2007) Estimation of total phenolic content and other oxidation substrates in plant tissues using Folin-Ciocalteu reagent. Nat Protoc 2(4):875-7.

Anderson WP (1983) Weed science: Principles. West Publishing Co: 33-34.

Ballester A, Vieitez AM, Vieitez E (1982) Allelopathic potential of *Erica vegans, Callunga vulgaris* and *Daboeciacantabrica*.J. Chem. Ecol 8:851-857.

Borkataky M, Kakoty BB, Saikia LR (2013) Antimicrobial Activity and Phytochemical Screening of Some Common Weeds of AsteraceaeFamily.Int.J.Pharm.Sci.Rev.Res 23:1.

Chang C, Yang M, Wen H, Chern J (2002) Estimation of Total Flavonoid Content in Propolis by Two Complementary Colorimetric Methods. J. Food. Drug. Anal10 (3): 178-182.

Chauhan A, Rijhwani S (2015) A Comprehensive Review on Phytochemistry of Ageratum conyzoideslinn. (Goat weed). Int. J. Eng. Technol. Manag. Appl. Sci : 3

Dian WH, Rizke C, Wahyono, F (2018) Phytochemical properties and antibacterial activity of *Ageratum conyzoides*, *Piper betle*, *Muntingacalabura* and *Curcuma domestica* against mastitis bacteria isolates. IOP Conf. Ser.: Earth Environ. Sci 247 012049

Diepreye E, Kemebradikumo P, Queen I, Langley O (2014) Phytochemicals and Antimicrobial activity of plant parts of *Ageratum conyzoides* extracted using different solvents. J. chem. biol. phys. sci 4(4): 3429-3434.

Ezeokeke EE, Ene AC, Igwe CU (2015) In vivo antiplasmodial effect of ethanol and aqueous extracts of *Alchorneacordifolia*. Biochem.Analyt.Biochem 4: 4.

Gupta A, Mittal C (2012) Effect of allelopathic leaf extract of some selected weed flora of Ajmer district on seed germination of *Triticumaestivum L.* Sci. Res. Reporter 2(3): 311-315.

Krishnaiah D, Devi T, Bono A, Sarbatly R (2009). Studies on phytochemical constituents of six Malaysian medicinal plants. Journal of Medicinal Plants Research 3(2): 067-072.

Luyang L, Weifang Long, Xiangluan W, Qi D, Fei Z, Dingrong W (2014) Studies on Quantitative Determination of Total Alkaloids and Berberine in Five Origins of Crude Medicine "Sankezhen. J. Chromatogr. Sci 53:307– 311 doi;10:1093.

May FE and Ash JE (1990). An assessment of the allelopatic potential of eucalyptus. Aust. J. Bot. 38:245-254.

Narwal SS, Tauro P (1994)AllelopathyinAgricultureandForestry. Allelopathy Update310.

Ponchang AW, Hannatu DM, Grace CE, Davou DN, Michael DSG (2017) Phytochemicals from *Ageratum conyzoides* L. Extracts and their Antifungal Activity against Virulent Aspergillus spp.. J. Acad. Ind. Res 6: 3.

Putnam AR, Defrank J, Barnes JP (1983) Exploitation of allelopathy for weed control in annual and perennial cropping systems.J.Chem.Ecol 9: 1001-1011.

Rice EL (1984) Allelopathy.Academic press, Orlando, Florida,USA.

Saswade RR (2019) Qualitatively preliminary phytochemical analysis of some different weed species. INT. J of research and analytical reviews: 6(2).

Selvakumar P, Kaniakumari D, Loganathan V (2012) Preliminary phytochemical investigation of extract of leaves and stem of *Euphorbia hirta*. Int. J. Curr. Sci: 48-51.

Science and Technology Journal Vol. 8 Issue 2 July 2020 ISSN: 2321-3388

Morphological Characterization of Selected Jackfruits of West Garo Hills of NE India

G. Phaomei[1] and B. Mathew[2*]
[1,2]Department of Rural Development and Agricultural Production,
North Eastern Hill University, Tura Campus, Tura–794002, Meghalaya, India
*E-mail: drbmathew@gmail.com

Abstract—A survey was conducted to study the fruit characters of jackfruits grown in West Garo Hills of Meghalaya during 2016 to 2018. More than 50 jackfruit trees bearing 15 to 40 years of age were initially evaluated, out of which 10 accessions exhibiting distinct morphological characters were selected for detailed characterization. Significant variations were observed in terms of qualitative and quantitative parameters of fruit under the study. Jackfruit accession *viz*. WGHJ-1 exhibited desirable characters such as big sized flakes, big and heavy seeds, high fruit:rind ratio, flake:fruit ratio, juicy pulp etc. hence it is considered ideal for making processed products like jam, jelly, halwa, candy, juice etc. as well as for starch extraction from seeds. Considering the small sized fruit with flat spines, thin rind, high flake: fruit ratio, highest number of thick and sweet flakes, accession WGHJ-5 is recommended for table purpose. The sweet, thick, heavy and non-juicy flake makes WGHJ-8 a probable good type for chips making and table purpose. This paper presents 41 characteristic features related to the whole fruit, flakes and seeds of 10 jackfruit accessions selected from the West Garo Hills of Meghalaya.

Keywords: *Artocarpus heterophyllus*, jackfruit characters, flake characters, seed characters

INTRODUCTION

Jackfruit (*Artocarpus heterophyllus* Lam.) popularly known as 'Poor man's fruit' is an important underutilized tropical homegarden fruit grown even in a severe stressed environment. It is believed to be originated from the Western Ghats of India. In India, it is widely distributed in Assam, Tripura, Bihar, Uttar Pradesh, Kerala, Tamil Nadu and Karnataka. Jackfruit tree is a multipurpose tree and all parts of the tree are equally important. Barks, roots leaves and latex were used for preparation of medicine for treatment of different ailments; immature fruits and seeds for culinary preparation; ripe fruits as table purpose; leaves and fruit waste as animal feed; wood for making furniture. Jackfruit is declared as the official state fruit of Kerala and Tamil Nadu. Jackfruit thrives well in West Garo Hills of Meghalaya because of prevailing sub-tropical climatic conditions. It is a popular fruit among the Garos and is commonly known as 'Tebrong'. Matured fruits are consumed as dessert, unripe fruits as vegetable and seeds are boiled or roasted. Jackfruit being cross-pollinated and mostly propagated through seeds, leads to wide variations among the progeny. These variations provide immense scope for identification, collection and conservation of elite jackfruit germplasm suitable for breeding as well as crop improvement programmes. The work on collection and conservation of jackfruit started at Indian Institute of Horticultural Research (IIHR), Bangalore (India) during 2000-01 and Indian Council of Agricultural Research (ICAR) under the All India Coordinated Research Project (AICRP) with an objectives to survey, collect and characterize jackfruit diversity available in different parts of the country (APAARI, 2012). Though characterization both morphological and molecular is of utmost importance for commercialization and breeding programme, there are very limited reports on characterization of jackfruit from this region. Morphological characterization is an efficient and cost effective way of evaluation as compared to molecular evaluation, which requires a highly equipped laboratory and manpower. Hence, before going for molecular characterization carrying out of morphological characterization may prove cost effective to screen out the elite accessions exhibiting desirable characters. Therefore, in this paper morphological characterization of ten selected jackfruit accessions of West Garo Hills were carried out and 41 characters of whole fruits, flakes and seeds were recorded and presented.

MATERIALS AND METHODS

The study was carried out in West Garo Hills district of Meghalaya, India during 2016-2018. Initially several field visits were conducted in various jackfruit growing area of West Garo Hills to identify diverse types of jackfruit. Approximately 50 jackfruits exhibiting desirable characters were first identified. Out of 50 selected jackfruit trees, 10 jackfruit trees were selected for detail characterization. The fruit characters were observed and recorded as per the descriptors prescribed by IPGRI (International Plant Genetic Resources Institute, 2000) Rome, Italy. Characters *viz.* fruit shape, fruit surface, shape of spine, spine density, rind colour, flake shape, flake texture, pulp taste, pulp consistency, pulp flavor, pulp juiciness, pulp colour, stalk length, stalk diameter, fruit length and diameter, fruit weight, fruit rind weight, rind thickness etc. were recorded and tabulated. Statistical tools such as mean, standard deviation, coefficient of variance etc. were employed. Variation among the different genotypes were determined by the percentage of coefficient of variance.

RESULTS AND DISCUSSION

Morphological characters like fruit shape, fruit surface, shape of spine, spine density and fruit rind colour of 10 jackfruit accessions were recorded and are presented in Table 1. Distinct variation among the different accessions of jackfruit trees were observed. Fruits of accession WGHJ-2, WGHJ-3, WGHJ-4 and WGHJ-9 were oblong in shape. Fruits of WGHJ-6, WGHJ-7 and WGHJ-8 were ellipsoid. WGHJ-5 and WGHJ-10 are spheroid while WGHJ-1 produced irregular shaped fruits. Fruits of type WGHJ-5 had smooth fruit surface; sparse spine density while all the other types had spiny fruit surface and dense spine density. Flat fruit surface is also a desirable character. Most of the selected accessions exhibited greenish yellow rind (40%) while other showed rind colour of reddish yellow (20%), yellow (20%) and green (20%). Dey and Baruah (2019), Nipa (2013) and Ibrahim *et al.* (2013) also reported similar variations with respect to fruit morphological character of jackfruit types in their respective studies. Flake characters also varied distinctly with respect to their shape and texture, 50% of flakes were cordate followed by rectangular (30%), spheroid (10%) and oblong (10%) in shape. Taste of pulp was sweet in all the accessions with 60% of soft pulp and 50% of strong flavoured juicy pulp. The colour of pulp varied from creamy white to deep yellow (Table 1). Strong pulp flavour was recorded in WGHJ-2, WGHJ-4, WGHJ-6, WGHJ-9 and WGHJ-10. Accessions like WGHJ-1, WGHJ-2, WGHJ-6, WGHJ-7, WGHJ-9, and WGHJ-10 were juicy which is considered a desirable character for juice processing. Goswami *et al.* (2011) and Akter and Rahman (2017) also reported wide variation in flake characters of jackfruits in their study. Dey and Baruah (2019) observed flesh colour ranging from creamy white to deep yellow which corroborates with the present findings.

Stalk length varies between 28 to 93 mm among the different jackfruit accession studied. Longest stalk (93 mm) was recorded in WGHJ-6 while shortest in WGHJ-10. Largest stalk diameter of 44 mm was recorded in WGHJ-2 followed by WGHJ-1 (34 mm) and WGHJ-9 (32 mm) while smallest stalk diameter was recorded in WGHJ-5 (17 mm). Fruit length ranged between 19.9 to 49 cm. Longest fruit length was recorded in WGHJ-2 (49 cm) followed by WGHJ-1 (45 cm) and WGHJ-4 (37.7 cm) while shortest fruit length was recorded in WGHJ-10. Largest fruit diameter of 31 cm was recorded in WGHJ-1 followed by WGHJ-7 (28.5 cm) and WGHJ-8 (23.5 cm). Chandrasekhar *et al.* (2018), also reported similar ranges of fruit length (23.5 to 56.75 cm) and fruit diameter (15.50 to 31.00 cm) in their study of jackfruit diversity. High percentage of coefficient of variation (57.94 %) in fruit weight exhibited significant variations in the selected jackfruit ranging between 1.86 to 14.38 kg. In the present study average fruit weight ranged between 1.86 to 14.38 kg. Highest fruit weight was noted in WGHJ-1 (14.38 kg) closely followed by WGHJ-2 (13.51 kg) while minimum of 1.86 kg fruit weight was recorded in WGHJ-5. Akter and Rehman (2017) and Ningot *et al.* (2018) reported similar range of fruit weight in their respective study. Lowest fruit rind weight was recorded in WGHJ-5 (0.78 kg) while highest was recorded in WGHJ-2 with 8.09 kg. The rind weight constituted about 50-60 % of the total fruit weight in most of the accession studied. Notable variation was also observed in rind thickness ranging from 4.26 to 19 mm. Lowest rind thickness was observed in WGHJ-8 (4.26 mm) and highest rind thickness was recorded in WGHJ-2 (19.0 mm). Similarly, rind thickness ranging from 7.5 to 14 mm was reported by Mannan *et al.* (2006). Rachis length ranged between 8.9 to 42 cm and rachis diameter ranged between 3.8 to 16 cm. Phaomei and P ereira (2016) also reported similar observation in their study on jackfruit types of Tikrikilla block of West Garo Hills, and they reported that rachis length and diameter ranged from 11.00 to 31.50 cm and 2.5 to 6.4 cm respectively. The variation was greatly influenced by the size and shape of the fruits. Highest number of flakes per kg fruit (37.11) was recorded in accession WGHJ-6 while highest flake weight per kg fruit (0.58 kg) was recorded in accession WGHJ-5 (Table 2). Dey and Baruah (2019) recorded a maximum of 0.54 kg flake weight per kg fruit. Highest weight of fresh flakes with seeds ranged between 1.07 to 7.14 kg and without seeds ranged between 0.76 to 4.52 kg. Highest weight of fresh flake with seed (7.14 kg) and without seed (4.52 kg) was noted in WGHJ-1. Highest flake:fruit ratio of 0.58 was noted in WGHJ-5 followed by 0.5 in WGHJ-1. Flake length and width ranged between 3.4 to 7.8 cm and 2.7 to 4.1 cm respectively. Wangchu *et al.* (2013), Dey and Baruah (2019) also reported similar findings. Flake thickness ranged between 3.1 to 8.24 mm. The highest flake thickness (8.24 mm) was observed in WGHJ-8 (Table 3). Rachis length and diameter ranged between 8.9 to 42 cm and 3.8 to 16 cm respectively. Highest rind weight was recorded in WGHJ-2 (8.09 kg) and lowest in WGHJ-5 (0.78 kg). Thickest rind (19 mm) was recorded in WGHJ-2 while thinnest (4.26 mm) was recorded in WGHJ-8 (Table 2). Seed length and width ranged between 2.5-3.3 and 1.5 to 2.1 cm respectively. Similar variation in seed length and width were reported by Akter and Rahman (2017), that ranged between 2.33 to 3.17 cm and 1.24 to 1.77 cm respectively. Number of seeds per kg fruit was recorded highest (30.78) in WGHJ-6 closely followed by WGHJ-5. Highest 100-seed weight (1160 g) was recorded in WGHJ-1 followed by WGHJ-9 (815 g) and WGHJ-10 (710 g). Number of seeds per kg fruit and weight of 100-seeds varied significantly among the different genotypes under study. Number of seeds per kg of fruit ranged between 10.53 to 30.78, while weight of 100 seeds ranged between 485 to 1160 g. The finding falls between the ranged of 263.33 to 1133.33 as reported by Wangchu *et al.* (2013). Similar findings were also reported by Aswini (2015). Highest Flake:Seed ratio (4.88) was recorded in WGHJ-8 followed by WGHJ-9 (4.68) and WGHJ-10 while lowest was recorded in WGHJ-1 (2.73). It is in corroboration with the findings of Chandrashekar *et al.* (2018) who reported a range of 1.56 to 5.70. Seed shapes were ellipsoid, reniform, oblong and irregular which was in conformity with the findings of Dey and Baruah (2019). Seed coat colour varied from brown to dull brown. Seeds surface of accession WGHJ-3, WGHJ-4, WGHJ-5, WGHJ-6 and WGHJ-9 had highly slimy surface, while in WGHJ-10 it was slightly slimy and the remaining accessions showed intermediate sliminess. Seeds of all selected jackfruit types have regular striations on the seed surface. Seed coat was easily separable from the kernel in types WGHJ-2, WGHJ-8 and WGHJ-10; intermediate in adherence in WGHJ-9; and difficult to separate in the remaining types. Vivipary was observed only in WGHJ-2, WGHJ-8 and WGHJ-10 (Table 3). Adherence of seed coat is greatly influenced by the presence of viviparous nature of jackfruit seeds. These morphological variations may be due to genetic differences among the selected jackfruit accessions.

Table 1: Qualitative Characters of Fruits and Flakes of Jackfruit in West Garo Hills, Meghalaya

Jackfruit Types	GPS Coordinates	Fruit Shape	Fruit Surface	Shape of Spine	Spine Density	Fruit Rind Colour	Flake Shape	Flake Texture	Pulp Taste	Pulp Consistency	Pulp Flavour	Pulp Juiciness	Pulp Colour
WGHJ-1	N25°34.116’ E090°14.281’	Irregular	Spiny	Intermediate	Dense	Reddish Yellow	Oblong	Soft	Sweet	Soft	Intermediate	Juicy	Deep Yellow
WGHJ-2	N25°31.986’ E090°11.450’	Oblong	Spiny	Sharp Pointed	Dense	Reddish Yellow	Rectangular	Soft	Sweet	Soft	Strong	Juicy	Yellow
WGHJ-3	N25°31.001’ E090°11.450’	Oblong	Spiny	Sharp Pointed	Dense	Greenish Yellow	Spheroid	Fibrous	Sweet	Medium	Intermediate	Not Juicy	Yellow
WGHJ-4	N25°30.822’ E090°12.567’	Oblong	Spiny	Sharp Pointed	Dense	Greenish Yellow	Rectangular	Soft	Sweet	Soft	Strong	Not Juicy	Light Yellow
WGHJ-5	N25°31.512’ E090°12.644’	Spheroid	Smooth	Flat	Sparse	Green	Cordate	Fibrous	Sweet	Medium	Intermediate	Not Juicy	Light Yellow
WGHJ-6	N25°30.491’ E090°11.368’	Ellipsoid	Spiny	Intermediate	Dense	Greenish Yellow	Cordate	Soft	Sweet	Soft	Strong	Juicy	Creamy White
WGHJ-7	N25°30.737’ E090°11.729’	Ellipsoid	Spiny	Sharp Pointed	Dense	Yellow	Cordate	Fibrous	Sweet	Medium	Intermediate	Juicy	Light Yellow
WGHJ-8	N25°56.378’ E090°11.763’	Ellipsoid	Spiny	Sharp Pointed	Dense	Green	Rectangular	Fibrous	Sweet	Medium	Intermediate	Not Juicy	Light Yellow
WGHJ-9	N25°56.778’ E090°13.124’	Oblong	Spiny	Sharp Pointed	Dense	Yellow	Cordate	Fibrous	Sweet	Soft	Strong	Juicy	Yellow
WGHJ-10	N25°30.199’ E090°10.408’	Spheroid	Spiny	Intermediate	Dense	Greenish Yellow	Cordate	Soft	Sweet	Soft	Strong	Juicy	Deep Yellow

Table 2: Quantitative Characters of Fruits and Flakes of Selected Jackfruit of West Garo Hills

Jackfruit Types	Stalk Length (mm)	Stalk Diameter (mm)	Fruit Length (cm)	Fruit Diameter (cm)	Fruit Weight (Kg)	Fruit Rind Weight (Kg)	Fruit/ rind ratio	Rind thickness (mm)	Rachis Length (cm)	Rachis Diameter (cm)	Number of Flakes Per Kg Fruit	Weight of Flakes Per Kg Fruit (g)	Weight of Fresh Flakes with Seed (g)	Weight of Fresh Flakes Without Seeds (g)	Flake/ Fruit Ratio	Flake Length (cm)	Flake Width (cm)	Flake Thickness (mm)
WGHJ-1	49	34	45	31	14.38	7.24	1.986	11	26.5	14.8	15.72	500	7140	4520	0.5	7.8	3	3.1
WGHJ-2	70	44	49	16.2	13.51	8.09	1.670	19	42	6.1	12.07	330	4470	3220	0.33	4.5	4.1	7
WGHJ-3	35	24	27.4	16.1	4.22	2.38	1.773	10.51	20.3	16	22.51	440	1840	1270	0.44	3.4	3.6	3.9
WGHJ-4	46	22	37.7	15	5.98	4.6	1.300	14	33	4.6	26.76	400	2360	1640	0.4	3.9	3.1	5
WGHJ-5	49	17	23	19.3	1.86	0.78	2.385	5	13	7	29.03	580	1070	760	0.58	3.7	3.5	8
WGHJ-6	93	23	33.3	20	6.01	3.15	1.908	15	26	7.9	37.11	460	2760	1770	0.46	4.0	3.2	5
WGHJ-7	38.17	21.86	32.8	28.5	5.15	2.67	1.929	7	19.2	6.1	23.3	490	2500	1810	0.49	4.4	3.9	3.85
WGHJ-8	41.81	21.22	30	23.5	9.81	3.92	1.568	4.26	26.2	10.5	20.18	490	4830	4000	0.49	5.4	2.7	8.24
WGHJ-9	40.2	32	35.9	19.8	8.9	4.94	2.503	16.57	29.8	5.3	15.28	480	4260	3410	0.48	5.2	3.8	4.32
WGHJ-10	28	22	19.9	16.6	3.23	2.06	1.802	4.33	8.9	3.8	10.53	360	1170	920	0.36	5.7	4.1	6.29
Mean	49.018	26.108	33.4	20.6	7.305	3.983	1.882	10.667	24.49	8.21	21.249	453	3240	2332	0.453	4.8	3.5	5.47
Range (Min-Max)	28- 93	17-44	19.9- 49	15- 31	1.86- 14.38	0.78- 8.09	1.300- 2.503	4.26- 19	8.9- 42	3.8- 16	10.53- 37.11	330- 580	1070- 7140	760- 4520	0.33- 0.58	3.4- 7.8	2.7- 4.1	3.1- 8.24
SD	19.059	8.095	9.073	5.463	4.232	2.302	0.358	5.385	9.644	4.226	8.264	73.492	1908.972	1340.818	0.073	1.299	0.485	1.812
SEm±	6.03	2.56	2.87	1.73	1.34	0.73	0.11	1.70	3.05	1.34	2.61	23.24	0.19	0.13	0.02	0.41	0.15	0.57
CV %	38.882	31.008	27.166	26.521	57.939	57.812	19.008	50.491	39.379	51.479	38.895	16.223	58.918	57.496	16.223	27.074	13.866	33.13

Table 3: Seed Characters of Jackfruit Grown in West Garo Hills, Meghalaya

Jackfruit Types	Seed Length (cm)	Seed Width (cm)	Number of Seeds per kg Fruit	100-seed Weight (g)	Flake Seed Ratio	Vivipary	Seed Shape	Seed Surface Sliminess	Seed Surface Pattern	Seed Coat Colour	Adherence of Seed Coat to Kernel
WGHJ-1	2.5	1.6	15.65	1160	2.73	Absent	Oblong	Intermediate	Regular Striations	Dull Brown	Difficult to separate
WGHJ-2	3.2	2.1	12.07	760	3.66	Present	Reniform	Intermediate	Regular Striations	Brown	Easily separable
WGHJ-3	2.63	1.59	22.51	590	3.23	Absent	Ellipsoid	Highly Slimy	Regular Striations	Dull Brown	Difficult to separate
WGHJ-4	2.6	2	25.92	485	3.37	Absent	Ellipsoid	Highly Slimy	Regular Striations	Dull Brown	Difficult to separate
WGHJ-5	2.9	2.1	29.03	592	3.34	Absent	Irregular	Highly Slimy	Regular Striations	Dull Brown	Difficult to separate
WGHJ-6	2.9	1.5	30.78	500	3	Absent	Irregular	Highly Slimy	Regular Striations	Dull Brown	Difficult to separate
WGHJ-7	2.8	1.8	23.11	505	4.03	Absent	Ellipsoid	Intermediate	Regular Striations	Brown	Difficult to separate
WGHJ-8	2.8	1.9	20.18	635	4.88	Present	Oblong	Intermediate	Regular Striations	Dull Brown	Easily separable
WGHJ-9	2.78	2	15.17	815	4.68	Absent	Ellipsoid	Highly Slimy	Regular Striations	Brown	Intermediate
WGHJ-10	3.3	1.8	10.53	770	4.5	Present	Irregular	Slightly Slimy	Regular Striations	Brown	Easily separable
Mean	2.841	1.839	20.495	681.2	3.742						
Range (Min-Max)	2.5- 3.3	1.5- 2.1	10.53- 30.78	485- 1160	2.73-4.88						
SD	0.252	0.218	7.001	206.028	209.403						
SEm±	0.08	0.07	2.21	65.15	66.22						
CV %	8.877	11.870	34.161	30.244	42.886						

CONCLUSION

Out of the ten jackfruit accessions studied, it was found that three jackfruit accessions *viz*. WGHJ-1, WGHJ-5 and WGHJ-8 exhibited desirable characters for various purposes. WGHJ-1 produced heaviest fruits with big sized flakes and heavy seeds, high fruit:rind ratio and flake:fruit ratio, juicy pulp etc. were relatively good, hence it is found ideal for processing industry for making products like jam, jelly, halwa, candy, juice, powder etc. as well as for starch extraction from seeds. WGHJ-5 was found to be a good type for local market for both culinary as well as table purpose as it produced comparatively smaller sized fruit with flat spines, thin rind, high flake: fruit ratio, highest number of thick and sweet flakes. The sweet, thick, heavy and non-juicy flake makes WGHJ-8 a probable good type for chips industry. The present study was restricted to morphological characterization; however, molecular characterization of selected accessions maybe considered for future research.

REFERENCES

Akter A and Rahman H (2017) Evaluation of jackfruit (*Artocarpus heterophyllus* Lam.) germplasm. Research & Reviews: Journal of Botany, 7(1): 38-53.

APAARI (2012) *Jackfruit Improvement in the Asia-Pacific Region* – A Status Report. Asia-Pacific Association of Agricultural Research Institutions, Bangkok, Thailand.

Aswini A (2015) *Morpho-molecular characterization of jackfruit (Artocarpus heterophyllus Lam.) accessions*. M.Sc thesis submitted to the Depatment of Pomology and Floriculture, College of Horticulture, Vellanikkara Thrissur, Kerela, India

Chandrashekar KG, Vijayakumar RM, Subramanian S, Kavino M and Joel, AJ (2018) Morphological characterization of jackfruit (*Artocarpus heterophyllus* Lam.) local genotypes under coffee ecosystem of lower Pulney Hills. Int.J.Curr.Microbiol.App.Sci., 7(3): 2210-2224.

Dey, B and Baruah, K. (2019). Morphological Characterization of Jackfruit (*Artocarpus heterophyllus* Lam.) of Assam, India. Int. J. Curr. Microbiol. App. Sci., 8(11): 1005-1016.

Goswami C, Hosain, MA, Kader, HA and Islam R (2011) Assessment of Physico-chemical Properties of Jackfruits' (*Artocarpus heterophyllus* Lamk.) Pulps*. J. Hort. Forestry and Biotech*., 15(3): 26-31.

Ibrahim M, Islam, MS, Helali, MOH, Alam, AKMS and Shafique, MZ (2013) Morphological fruit characters and nutritional food value of different jackfruit (*Artocarpus heterophyllus* Lam.) cultivars in Rajshahi region of Bangladesh. Bangladesh J. Sci. Ind. Res., 48(4), 287-292.

Mannan MA, Sultana, S and Khan, SAKU (2006) Evaluation of physical characteristics of some off-season jackfruit germplasms from south-western region of Bangladesh. Khulna University Studies, **7**(2): 71-76.

Mitra SK, Maity CS (2002) A summary of the genetic resources of jackfruit (*Artocarpus heterophyllus* Lamk.) in West Bengal, India. Acta Hort 575: 269-271.

Mitra SK, Mani D (2000) Conservation and utilisation of genetic resources in jackfruit (*Artocarpus heterophyllus* Lamk.)- a potential underutilised fruit. Acta Hort 523: 229-232.

Ningot EP, Dahale MH, Uikey AC and Naitam PC (2018) Variability Studies on Physico-Chemical Characteristics of Jackfruit Genotypes from Eastern Maharashtra, India. Int.J.Curr. Microbiol.App.Sci., 6: 2294-2298.

Nipa JN (2013) *Study on Morphological and Nutritional properties of jackfruit germplasm.* M.Sc. Thesis submitted to the Department of Horticulture, Bangladesh Agricultural University, Mymensing, Bangladesh.

Phaomei G and Pereira LS (2016) Fruit characterization of jackfruit in Tikrikilla Block of West Garo Hills, Meghalaya. J Agric Technol 3(2): 44-48.

Wangchu L, Singh D and Mitra SK (2013) Studies on the diversity and selection of superior types in jackfruit (*Artocarpus heterophyllus* Lamk.). Genet. Res. and Crop Evol., 60(5): 1749-1762.

Science and Technology Journal Vol. 8 Issue 2 July 2020 ISSN: 2321-3388

Exploring 3D Modelling of Architectural Plan using Camera Tracing

Shylesh Kumar[1] and Shiva Ji[2]*
[1,2]Indian Institute of Technology Hyderabad, India
E-mail: [1]shyleshkumar4012@gmail.com, [2]*shivaji@des.iith.ac.in

Abstract—With the advent of technology, architecture has also benefitted by applying tools and equipment instead of conventional manual works. Computational technology has come to the aid of the design process. There is a shift from hand drawing to computer-aided design. Drawing had become more of a tool to explore design ideas and express proposed solutions. The coordination between hand and mind will remain superior until those tools progress. The physical human conditional gesture continues with reliability and is still relevant in idea generation and presentations. But in recent years, technology has driven architectural computing into a new exploratory domain. This research aims on building a procedural 3D model using a pixel-based tracing of the sketch of an architectural plan. The proposed method blurs the line between hand sketching and CAD, thus providing a quicker solution in visualizing the design. The point generated by vectorizing the bitmap data is used to achieve the desired curve. It is all done in a fully parametric model where the user has control over the properties for modeling. Finally, we validate our result with a study in which we compare the conventional modeling tools and establish a system to build the 3D model from an architectural plan. This study helps in believing that CAD and hand drawing could perfectly coexist and finding the right balance in architectural design.

Keywords: OpenCV, CAD, Pixel Trace, Potrace, Curve Fitting.

INTRODUCTION

Architecture is often considered as drafting discipline. Architecture translates the design into execution on the ground. From concept to reality, it shapes and forms a combination of spaces, surfaces, and materials into a meaningful existence. Architectural working starts with sketches, drawings, specifications, models, etc. [Sweeting, B. (2011)]. The construction process translates all this set of ideas into a reality. Freehand sketching is an integral part of the architectural thinking process [Alfonso Martín-Erro, M. D. (2016)]. It is considered as the most effective tool for creative expression and visual thinking for design. A sketch which a drawing made informally, approximate details, and dimension; on the other hand, drafting is a detailed description of the system of design with exact size [Alfonso Martín-Erro, M. D. (2016)].

In the framework of the design process, freehand sketching allows its designer to register and manipulate imprecise and uncertain information. Sketching has remained a fundamental and primary course in classroom teaching and is considered to be one of the important ones. The architectural expressions are supposed to be conveyed through sketches and support of drawings [Hua, M. (2019)]. The sketching plays a vital role in conceptual and exploration stages; it helps in bringing in a concrete form to the whole process from where it takes the form of formal drawings, etc. During the initial design process stage, the initial drawings are typically unstructured and informal, but as the process continues and the form evolves, the drawing becomes scaled and structured. This stage is later detailed into the technical drawing, which can be further used for the construction of the building. In recent times, technological growth has boosted architecture in the extensive use of computers for middle to last design process. But despite the improvement of technology in the process of design, it appears that architects and architecture school value and uses freehand sketching in early conceptual stages of the design process.

OBJECTIVE

This study focuses on developing a user-friendly workflow for creating an architectural floorplan sketch into a parameterizable 3d model; the research helps us in the time and expertise required for creating the 3d model. By connecting freehand sketching with 3d conversion workflow, the fuzzy sketching helps in the development of conceptual 3d models characterized by flexible parameters and interactions. This research intends to use Webcam to pull in live stream in Grasshopper3d, where the sketching is rasterized to curve, which can be further parametrized into 3d model.

DRAWINGS IN ARCHITECTURE

FREEHAND SKETCHING

Sketching is a form of informal drawing; probably all humans engage in [Bar-Eli, S. (2013)]. In the case of designers, it's a way of visualizing an idea, with the help of sketching the abstract world is linked with the material world. Hence the roles of sketching in design have been emphasized frequently as tools for thinking [Sema Soygenis, M. S. (2010)]. Architects use sketching to conceptualize the early stage of design problems; these sketches are usually fast, informal, and spontaneous, with which different ideas are brainstormed and recorded randomly [Alberti, L. B. (1988)].

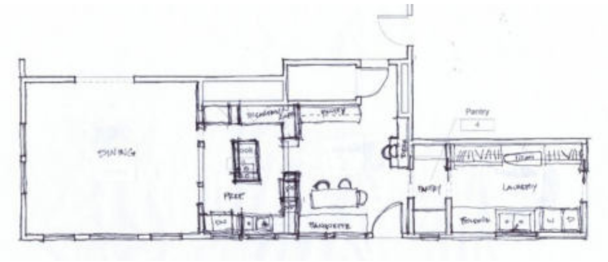

Fig. 1: Freehand Architectural Sketching

ARCHITECTURAL DRAFTING

It all started with the renaissance period; this period defined a paradigm of what architectural drawing is today. As the availability of paper increases, it became possible for the architects to use drawing as a means of ideation and communication [8]. Orthogonal drawings became a status quo in the field of architecture, where the primary purpose of architectural drawings was used to translate the designer's abstraction to others. More than being just means of transferring information for the construction process, architectural drawings and model allows the designer to develop and understand the character of a building, which can be used to revise the scheme [Sweeting, B. (2011)]. This type of scaled technical drawings helps us in making decisions on a small scale rather than live site.

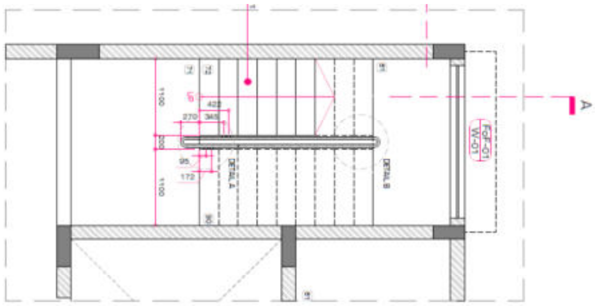

Fig. 2: Architectural Drafting

METHODOLOGY

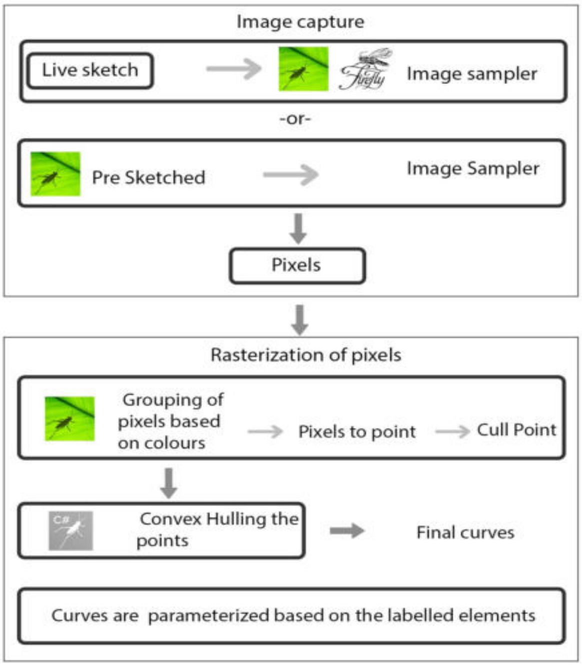

Fig. 3: Workflow

TOOLS USED IN THE EXPERIMENT

The following equipment and tools were used for the experiment. 1. Logitech camera, 2. Rhino3D Software, 3. Grasshopper3D Software, and 4. Firefly and C# (Plugins for Grasshopper).

SETUP FOR SKETCHING

Fig. 5: Camera Setup

The web camera used is placed perpendicular to the sketching; it covers all the sketch area or the sheet used for drawing orthogonally. Different color markers should be used to represent a different element, namely walls, doors, and windows. The color with distinct contrast helps in simplifying the rasterizing process. The live sketching is streamed in grasshopper3D, where it is processed further. On for simple computing, instead of live sketching, the sketched file is upload into grasshopper using firefly plugin.

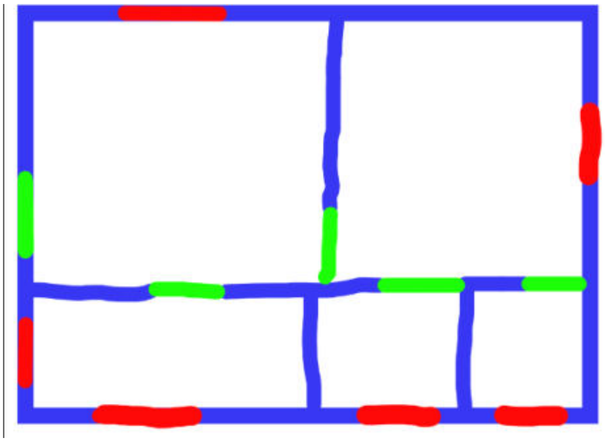

Fig. 6: Sketch of Floor Plan

RESULT AND DISCUSSION

VECTORIZING THE CURVE

The data is read as an image and which was processed using the image sampler component to read it as pixels. By converting the pixels in points, the points are then culled using the RGB value of the pixel; And by picking the marker color used on the image, the pixels are rasterized into the curve. The point is grouped using the convex hull algorithm, Where the curve encloses the point entirely with the smallest polygonal length possible. The curve generated from the previous step is grouped based on the color of the marker used, which is labeled as a wall, door, windows, etc.

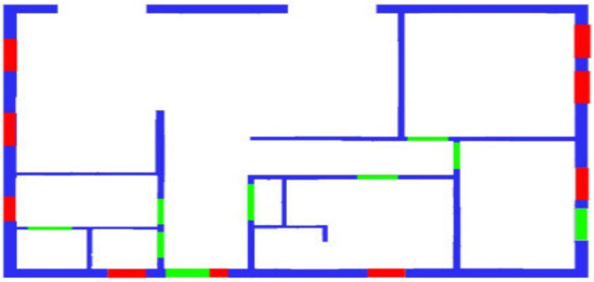

Fig. 7: Vectorizing the Floor Plan

These curves, due to vectorizing, contain numerous control points, which is simplified by rebuilding the curve and reducing the control point. The curve processed from smaller elements such as door and windows are bounding using a bounding box component to further optimizing the curve. These curves generated are also evaluated depending on the labels.

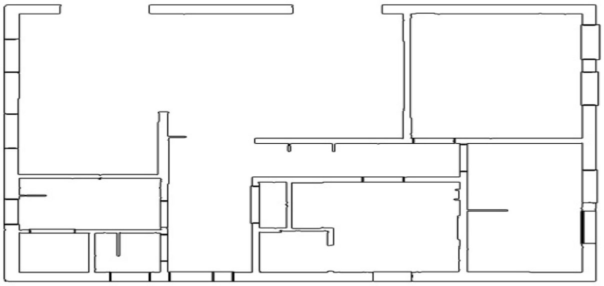

Fig. 8: Final Generated Curve

PARAMETERIZE THE CURVE

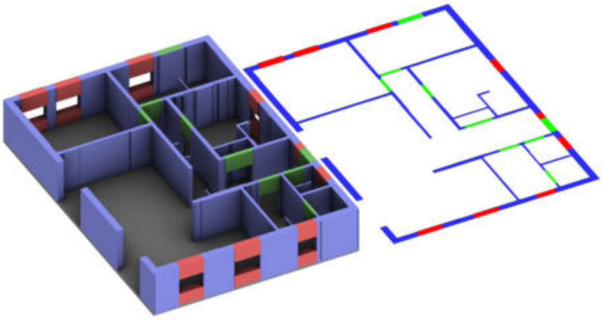

Fig. 9: Parameterizing the Curve

The curve is parameterized depending upon the label of the curve, i.e., curve vectorized from the wall representation can be extruded for the required height. To simplify the process, the height of the wall is proportionally calculated from the sketch using the building footprints dimension. The above study was done with a conceptual sketch of a 1500sqft apartment. In the case of windows and doors, the generated curve can be used as a reference box of importing 3D representations.

The 3D building model generated contains an uneven smooth surface while extruding the rasterized curve. Moreover, many elements can be added using a bounding box as a reference and importing it into the model. And for further improvement, some manual intervention and editing for further use of the model. The major limitation with 3D generation are the heights; the model is not to scale; the value of height is generated by rationing with the proportional extends of the drawing. And computing is a significant issue as the complexity of the architectural drawing increases in the case of curve walls.

CONCLUSION

This study describes a workflow to generate the 3D parameterizable model from a user-friendly architectural sketch; the methodology helps in creating a 3D model directly from the 2D floor plan. The process includes parameterizing the curve to provide a coherent 3D model of the desirable elements. These models are majorly intended from easy visualization for the conceptual ideation stage of the design process, but it can be used in further study.

ACKNOWLEDGEMENT

This work is carried out under the research project titled “Creating Digital Heritage of Representative Architectural Marvels from Each State of North East India”, PI: Dr. Shiva Ji, IIT Hyderabad, India.; funded by Department of Science and Technology, Ministry of Science and Technology, Govt. of India, under ICPS/IHDSR scheme.

REFERENCES

Sweeting, B (2011) Conversing with drawings and buildings: From abstract to actual in architecture. Kybernetes, 1159-1165.

Alfonso Martín-Erro, M D (2016) The role of sketching in engineering design and its presence on engg edu. 10th Int Tech, Edu, and Devp Conf. Valencia.

Hua, M (2019) The Roles of Sketching in Supporting Creative Design. An Int Jr for All Aspects of Design, 895-904.

Bar-Eli, S (2013) Sketching profiles: Awareness to individual differences in sketching as a means of enhancing design solution devp. Design Studies, 472–493.

Sema Soygenis, M S (2010) Writing as a Tool in Teaching Sketching: Implications for Architectural Design Education. Int Jr of Art & Design Edu, 283 - 293.

Alberti, L B (1988) On the Art of Building in Ten Books. Massachusetts: MIT Press.

Science and Technology Journal Vol. 8 Issue 2 July 2020 ISSN: 2321-3388

Computational Designing of Low Energy Band Gap of New Donor-Acceptor (D-A) Copolymer Monomers for Organic Solar Cells: DFT and TD-DFT Study

Sri Charitha Annam[1], K.V. Padmavathi[2], N. Murali Krishna[3] and Mannam Subbarao*[1]
[1]Department of Chemistry, Acharya Nagarjuna University,
Nagarjuna Nagar, Andhra Pradesh–522510, India
[2]Department of Chemistry, D.S. Government Degree College for Women,
Ongole, Andhra Pradesh–523001, India
[3]Department of Chemistry, V.R. Siddhartha Engineering College, Kanuru,
Vijayawada, Andhra Pradesh, 520007, India
**E-mail: mannamsrao@gmail.com*

Abstract—Via this look at efforts have been made to increase a chain of latest donor-acceptor (D-A) systems through the usage of 4-methoxy-2,7,nine-trimethyl-9H-carbazole (2,7-MMCB) as a electron donor and benzo[c][1,2,5] oxadiazole (BCO); benzo[c] [1,2,5] thiadiazole (BCT); benzo[c][1,2,5]selenadiazole (BCS); [1,2,5]oxadiazolo[3,4-c]pyridine (OCP); [1,2,5] thiadiazolo [3,4-c]pyridine (TCP); [1,2,5] selenadiazolo [3,4-c]pyridine (SCP); [1,2,5] oxadiazolo[3,4-d]pyridazine (ODP); [1,2,5] thiadiazolo[3,4-d]pyridazine (TDP) as electron acceptors. In this work, we executed calculations of DFT and TD-DFT/B3LYPmethod with /6-31G basis. Calculated and explored theoretical expertise of the HOMO, LUMO oenergies, the band gap (Eg), and the open-circuit voltage (Voc) of the studied compounds. To take a look at the relationship between molecularstructure and optoelectronic properties, the consequences of the extraordinary acceptor effect on the geometries and optoelectronic residences of those substances were discussed. The outcomes acquired show how the digital residences can be modified with many lessons of acceptors through the substituent and suggest that 2,7MMCB-ODP, 2,7MM CB-TDP, and 2,7MM CB-SDP are these compounds as suitable candidates for optoelectronic packages in solar cells inclusive of BHJ.

Keywords: Carbazole, DFT and TD-DFT methods, donor acceptor (D-A) and optoelectronic properties

INTRODUCTION

The discovery of efficient and new forms of energy is one of the most exciting and challenging fields of research (Fadeyi 2013). Historically, the world has depended on energy sources from fossil fuels such as coal, natural gas and oil (Hasib 2011). These energy sources were created by the gradual decay of prehistoric plants and animals that died and were buried under layers of rock that are millions of years old. These energy sources are non-renewable and are known as major sources of emissions. Some of the drawbacks associated with over-dependence on fossil fuels are the production of acidic gases such as sulfur dioxide and carbon dioxide, which can result in acid rain, a greenhouse effect that is the gradual warming of the Earth and the destruction of landscapes during mining for fossils fuel (Motisemi 2012; Kiran 2014). The increase in world energy consumption that increases environmental pollution has accelerated research into alternative energy forms of energy. One of the ways to meet the emerging need for sustainable energy sources is through the production of large-scale, inexpensive and easily process solar cells. This has led to the development of organic photovoltaic devices (OPVs) based on carbon-based semiconductors (conjugated polymers and small molecules) as an exciting and rapidly growing field of research and technology.

Conjugated polymers now offer new research fields, both in experimental and theoretical chemistry and in physics due to fascinating optoelectronic properties. However, conventional, organic materials usually have optical energy gaps greater than 2 eV and only cover the Solar Spectrum visible range (300-650 nm). The absorption of smaller energy gaps in the long wavelength region to gain from the higher flux, red light or even near infrared region of the solar spectrum are needed. It was therefore a significant endeavor in recent years to develop and synthesize new conjugated polymers with narrow energy gaps.Recent advances in organic polymer solar cell devices have led to a power conversion efficiency (PCE) efficiency of almost 17.5% (Yongsheng Chen 2018).

For several years, carbazole (Figure 1) and its derivatives attracted a lot of attention because of the photochemical properties they possess, as well as their high chemistry and environmental stability.Another fascinating advantage is its versatile reactive sites that can be substituted with a wide variety of functional groups to tune the optical and electrical properties.When carbazoles are linked together to form oligomers or even polymers, it has at least two ways of elongation. One is through the 2,7-linkage, with the formation of a nonplanar structure characterized with successive nitrogen connected benzidines, (Figure.1). It was well acknowledged that π-conjugation is terminated at each nitrogen atom, so that the π-conjugation is always confined within two repeating units,and accordingly, the absorption wavelength is insensitive to the degree of polymerization(Sonntag 2004; Morin 2005) Before 2000, almost all studies on polycarbazole were focused on 2,7-polycarbazole since it is more feasible to be synthesized than any other isomers due to the highly activated 3,6-positions(Lmimouni 1998).

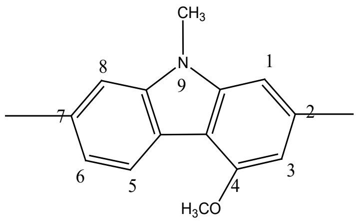

Fig. 1: 4-methoxy-2,7,9-trimethyl-9H-carbazole(2,7-MMCB)

Quantum-chemical techniques provide a powerfully-driven toolbox both for the layout and overall performance comprehension of bulk-heterojunction (BHJ) devices and for the definition of interplay among neighboring molecules inside the bulk and at the interface. the usage of the donor-aceptor (D-A) copolymer is useful. Model oligomer structures research on the theory of wave functions (i.e., Hartree – Fock [HF] strategies, publish-HF techniques that cover electron correlation and semiempirical HF methods) and purposeful density functional theory (DFT) had been used in the layout and comprehension of a small optical band gap D-A copolymer for natural digital applications and mainly for OPVs (Risko 2011). Previously, numerous procedures had been utilized in evaluating the the electronic and optical properties of conjugated polymers, such as the oligomer technique(Sahu 2013; Zhang 2013; Zade 2011) and periodic boundary condition (PBC) (Pappenfus 2011; Kaloni 2015; Rittmeyer 2015). Density functional theory (DFT) in addition to time-dependent density functional theory (TD-DFT) have supplied cheaper theoretical answers for calculations during the last to a few years (Wong 2010; Richard 2011).

In this research paper we have produced a variety of compounds with the polymer monomer system Donor-Acceptor (D-A). In this study 2,7-linked donor carbazols (2,7-MMCB) were used as carbazoles ware and small molecular accepters, for example benzo[c][1,2,5] oxadiazole(BCO); benzo[c][1,2,5]thiadiazole (BCT); benzo[c][1,2,5]selenadiazole(BCS); [1,2,5]oxadiazolo[3,4-c] pyridine(OCP); [1,2,5]thiadiazolo[3,3-c]pyridine(TCP); [1,2,5]selenadiazolo[3,4-c]pyridine (SPL); In order to predict electronic and optical properties of engineered substances, quantum chemical methods were used. The molecular structures of the donor and the accepter are shown in Fig. 2. The sequence of nine acceptors gives a description of the effects of the heteroatome and fused rings on the geometric and electronic properties of the test copolymers. The Density Functional Theory (DFT) at B3LYP level and the 6-31 G bases were examined for geometrical structures and electronic properties. Also studied were the effects of acceptor power on electronic properties like the HOMO level, LUMO level, band gap and the maximum wavelength absorption (λ_{abs}).

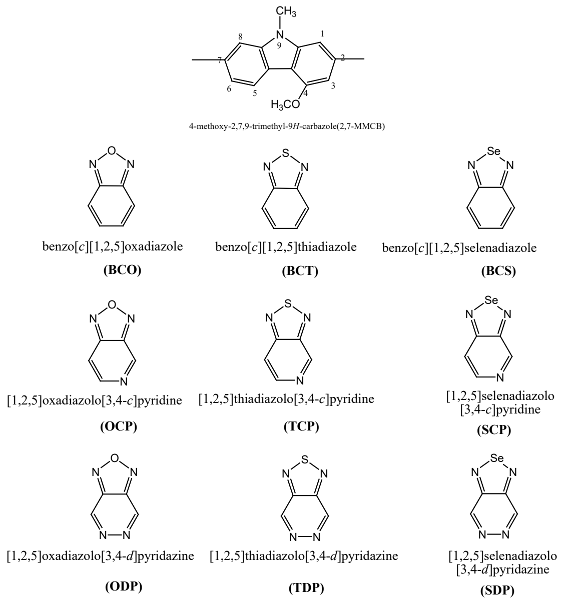

Fig. 2: Building Units as Donor/ Acceptor Moieties

COMPUTATIONAL METHODOLOGY

The geometries and the optoelectronic properties of all molecules were calculated by Gaussian 09 program supported by Gauss View 5.0(Frisch 2009) using a hybrid density functional(Becke 1993) and Becke's three parameter exchange functional combined with the B3LYP correlation functional (B3LYP) and with the 6-31G(d) basis set by using DFT method in the gas and solvent cholobenzene. The geometry structures of neutral and doped molecules were optimized under no constraint. The highest occupied molecule *orbital* (*HOMO)* and the lowest un-occupied molecular *orbital* (LUMO) energiesand gap energy (which evaluated as the difference between the HOMO and LUMO energies) energies were also deduced from the optimized structures. The vertical electronic excitation spectra, including wavelengths, oscillators strengths, and main configuration assignment, were systematically investigated using TD-DFT calculations with the 6-31G (d) basis set in the fully DFT-optimized structure of the ground state. (Zerner 1991)In fact, these calculation methods have been successfully applied to other conjugated organic molecules and polymers (Tomasi 2005).

Furthermore, the impacts of solvents on the underlying properties were concentrated by methods for the self-consistent reaction-field (SCRF) technique dependent on Polarizable Continuum Model (PCM)created by Tomasi et al. furthermore, Pascual-Ahuir et al.(Miertu 1981). These useful and basis set mixes were picked because of previous work on the D-A framework, demonstrating that they performed enough to portray the ideal properties, for example, the general security over a scope of dissolvable polarities and optical properties including the absorption spectra.

RESULTS AND DISCUSSION

Structure and Geometric Properties

The structures of the optimized geometries are shown in Figure. 3. The selected dihedral angle (θi) and bond distance (d_{BL}) parameters exists between the donor and acceptor moieties are presented in Table 1. After full optimization in the ground state, the results indicate that all the studied monomers maintained non planar expect 2,7-MMCB-ODP, 2,7-MMCB-TDP, and 2,7-MMCB-SDP in both gas and solvent (≈180°). It was somewhat surprising that our geometry optimization led to a nonplanar structure for the 2,7-linkage polycarbazole in opposition to an earlier obervation. The torsion angle between the connected carbazole units is found to be insensitive to the way of linkage and to the degree of polymerization and ranges from 145° to ≈180° in gas and in solvent. The monomers 2,7-MM CB-ODP, 2,7-MM CB-TDP, and 2,7-MM CB-SDP torsion angles have ≈180° shows, an out-of-plane orientation relative to the plane of conjugation and the electron-donating effect of the oxygen (O), sulfur (S) and selenium (Se).

The selected bond lengths of these copolymers are also given in table1; herein, the central bond lengths that connects the donor and acceptor. All the studied copolymers have different central bonds (Fig.4) which suggest that all the polymers are rigid backbones. The nitrogen- (N-) hydrogen (H) or sulfur (S)/oxygen- (O-) nitrogen (Se) interactions forming stable six or five-member rings reduce the dihedral angles and keep the molecular coplanarity, thus benefitting to the rigidity of the copolymers.

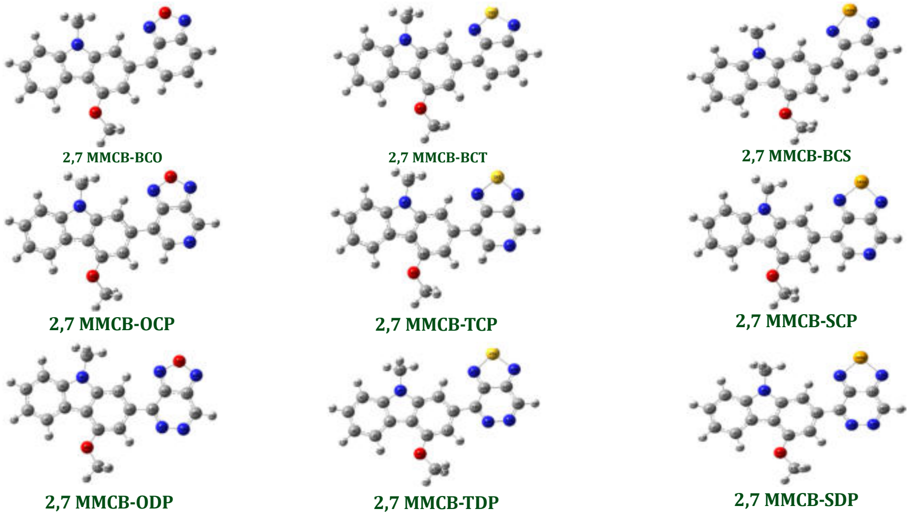

2,7 MMCB-BCO 2,7 MMCB-BCT 2,7 MMCB-BCS

2,7 MMCB-OCP 2,7 MMCB-TCP 2,7 MMCB-SCP

2,7 MMCB-ODP 2,7 MMCB-TDP 2,7 MMCB-SDP

Fig. 3: Optimized Molecular structures obtained by DFT/B3LYP/6-31G of the 2,7 linkage carbazole copolymer monomers (D-A) in gas phase

Table 1: Dihedral Angle (θ), Bridge Length (d_B) and Dipole Moments (μ) for D-A Polymer Monomers Calculated by DFT/B3LYP/6-31G Levelin Gas and Solvent Chlorobenzene

S.NO	POLYMER	θ (°)		dB		μ debye	
		Gas	Sol	Gas	Sol	Gas	Sol
10	2,7-MMCB-BCO	154.67	151.22	1.47955	1.48049	4.0698	5.1472
11	2,7-MMCB-BCT	149.14	145.98	1.48293	1.48384	1.9831	2.6094
12	2,7-MMCB-BCS	150.04	147.13	1.48354	1.48447	1.0864	1.5384
13	2,7-MMCB-OCP	157.08	153.08	1.47511	1.48982	2.6389	2.8782
14	2,7-MMCB-TCP	151.33	149.44	1.47884	1.48900	1.1247	1.1981
15	2,7-MMCB-SCP	153.84	150.25	1.47984	1.48051	1.9561	2.6318
16	2,7-MMCB-ODP	179.70	179.60	1.46523	1.46572	2.3964	2.6712
17	2,7-MMCB-TDP	179.90	179.85	1.47151	1.47309	3.1702	4.3954
18	2,7-MMCB-SDP	179.87	179.62	1.47233	1.47443	4.0806	5.8401

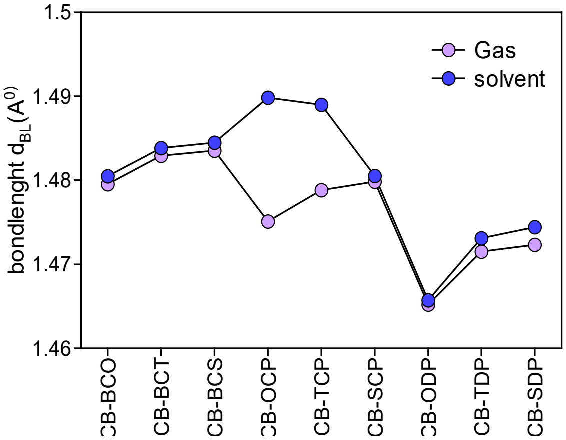

Fig. 4: the Bond Length between the Donor and Acceptor in Gas and Solvent Chlorobenzene for D-A Copolymer Monomers Calculated by DFT/B3LYP/6-31G Level

DIPOLE MOMENTS

Dipole moments of all molecules also are evaluated as proven in Table 2. Dipole moments have an exceptional have an impact on the manufacture of percent. the manufacturing process relates to solubilities in natural solvents that beautify self-meeting conduct. (Qin 2018) The dipole second and solubility are associated with each other. The better value of the dipole second approach higher solubility in an natural solvent and extended switch price.(Jo 2015; Estrada 2012) it's been proposed that the dipole moment of the donor molecules strongly affects the molecular self-meeting in film and the resulting morphology, as the adjacent molecule dipoles can align antiparallel with each other, set off self-assembly, and enhance order and crystallinity. The calculated dipole moments of the model copolymer monomers inside the floor nation are excessive values for oxygen substitutes in fuel and solvent.

The quadrupole moment values for the model compounds are given in Tabe 2, where the mean diagonal quadrupole moment tensor elements Qii and the unique quadrupole moment Q are defined as follows:

$$Q_{ii} = \frac{(Q_{xx} + Q_{yy} + Q_{zz})}{3} \qquad (1)$$

$$Q = Q_{xx} - Q_{yy} \qquad (2)$$

As proven in Table 2, all of the diagonal elements of the quadrupole moment tensor for the version compounds are terrible, indicating that the bad rate distribution is further removed from the molecular center of the nuclear masses. The values of the non-diagonal factors Q_{xz} and Q_{yz} of the molecules are surprisingly lower, which can be attributed to its symmetrical aircraft nearly perpendicular to the z-axis. It must be cited that the dipole and quadrupole moment values of 2,7 MMCB-TDP and copolymer monomers are large than those of CB copolymer monomers which suggests that the sulfur (S) atom and selenium (Se) are simply more potent electron acceptors.

Table 2: Quadrupole Moments (in Debye. Å) of 2,7-Carbazole Based Polymer Monomers, Calculated by B3LYP/6-31G Method

Gas								
Polymer Monomer	**XX**	**YY**	**ZZ**	**XY**	**YZ**	**XZ**	**Q_{ii}**	**Q**
Gas								
2,7-MMCB-BCO	-128.23	-139.93	-149.90	21.81	-1.32	4.26	-139.353	11.7
2,7-MMCB-BCT	-146.89	-132.51	-156.91	11.26	-1.63	6.28	-145.437	-14.38
2,7-MMCB-BCS	-153.72	-132.63	-162.94	4.92	-4.24	6.77	-149.763	-21.09
2,7-MMCB-OCP	-134.14	-146.76	-148.31	7.21	0.15	5.37	-143.07	12.62
2,7-MMCB-TCP	-149.71	-140.98	-155.39	-2.97	0.25	7.91	-148.693	-8.73
2,7-MMCB-SCP	-143.13	-153.13	-161.97	-5.18	-0.12	5.17	-152.743	10
2,7-MMCB-ODP	-132.41	-144.95	-146.43	2.39	-1.05	10.19	-141.263	12.54
2,7-MMCB-TDP	-139.19	-147.35	-153.87	-7.15	0.63	8.89	-146.803	8.16
2,7-MMCB-SDP	-141.88	-152.69	-159.90	-8.91	-2.40	9.87	-151.49	10.81
Chlorobenzene								
2,7-MMCB-BCO	-128.23	-139.93	-149.90	21.81	-1.32	4.26	-139.353	11.7
2,7-MMCB-BCT	-146.89	-132.51	-156.91	11.26	-1.63	6.28	-145.437	-14.38
2,7-MMCB-BCS	-153.72	-132.63	-162.94	4.92	-4.24	6.77	-149.763	-21.09
2,7-MMCB-OCP	-134.14	-146.76	-148.31	7.21	0.15	5.37	-143.07	12.62
2,7-MMCB-TCP	-149.71	-140.98	-155.39	-2.97	0.25	7.91	-148.693	-8.73
2,7-MMCB-SCP	-143.13	-153.13	-161.97	-5.18	-0.12	5.17	-152.743	10
2,7-MMCB-ODP	-132.41	-144.95	-146.43	2.39	-1.05	10.19	-141.263	12.54
2,7-MMCB-TDP	-139.19	-147.35	-153.87	-7.15	0.63	8.89	-146.803	8.16
2,7-MMCB-SDP	-141.88	-152.69	-159.90	-8.91	-2.40	9.87	-151.49	10.81

ELECTRONIC PROPERTIES

The various electronic applications of those materials are their use as organic solar cells, it is referred to that theoretical knowledge of the HOMO and LUMO strength levels of the additives is vital in the study of organic solar cells. The HOMO and LUMO energy tiers of the donor and the acceptor additives for photovoltaic devices are very vital factors in figuring out whether or not there can be an effective switch of price between the donor and the acceptor. Frontier strength ranges of conjugated polymers are vital to their performance in natural digital gadgets together with natural sun cells and electrochemical supercapacitors(Kim 2012). In natural solar cells, the value of the HOMO–LUMO electricity hole directly impacts the fast-circuit modern, at the same time as the HOMO strength of the electron donor is proportional to the LUMO energy of the electron receptor.

The values of HOMO/LUMO energies of donor and acceptor units are 5.4818/-0.6272 eV for CB,-7.0487/-2.8594 eV for BCO,-6.7259/-2.8017 eV for BCT,-6.5537/-2.6763 eV for BCS,-7.6920/-3.4485 eV for OCP,-7.3260/-3.3405 eV for TCP,-7.1355/-3.2017 eV for SCP,-7.6403/-4.0091 eV for ODP,-7.2762/-3.8592 eV for TDP, -7.0996/-3.7090 eV for SDP, and corresponding values of energy gaps are -4.8546 eV for CB, -4.1892 eV for BCO,-3.9242 eV for BCT,-3.8774 eV for BCS,-4.2434 eV for OCP,-3.9854 eV for TCP,-3.9337 eV for SCP,-3.6311 eV for ODP,-3.4170 eV for TDP,-3.3906 eV for SDP in gas phase and similar trend in solavent phase. Those values all are greater than 3eV, so the donor and acceptor separate units are not suitable for organic solar cells applications.

The calculated frontier orbitals HOMO, LUMO and band gaps values for deign D-A monomers are listed in Table 3., and Figure 5 summarises the E_{HOMO}, E_{LUMO}, and E_{Gap} values. The band gaps values are below 3 eV and the calculated band gap E_g of the studied model compounds increases in the following order in gas: 2,7-CB-TDP > 2,7-CB-SDP > 2,7-CB-ODP > 2,7-CB-TCP >2,7-CB-SCP > 2,7-CB-OCP > 2,7-CB-BCT > 2,7-CB-BCS > 2,7-CB-BCO.The much lower E_g of 3,6-CB-TDP and 3,6-CB-SDP compared to other monomers indicates a significant effect of intramolecular charge transfer, which would make the absorption spectra red shifted. However, the Eg values studied model compounds increases in the following order in solvent: 2,7-CB-OCP > 2,7-CB-TCP > 2,7-CB-TDP > 2,7-CB-ODP >2,7-CB-SDP > 2,7-CB-SCP > 2,7-CB-BCT > 2,7-CB-BCO > 2,7-CB-BCC. This is clearly due to the effect of the electron-donor unit which is strong for 2,7-MMCB-OCP and 2,7-MMCB-TCP than that of other monomers.

Table 3: Energy Levels of HOMO (eV), LUMO (eV) and energy gap (E_g) for Donor and Acceptors Calculated by B3LYP/6-31G Method

D-A Polymer Monomers	Gas			Solvent		
	HOMO eV	LUMO eV	Eg	HOMO eV	LUMO eV	Eg
	Gas			Chlorobenzene		
2,7-MMCB-BCO	-5.3940	-2.7666	2.6273	-5.4680	-2.8804	2.5876
2,7-MMCB-BCT	-5.2682	-2.7520	2.5163	-5.3918	-2.8382	2.5536
2,7-MMCB-BCS	-5.2070	-2.6592	2.5479	-5.3531	-2.7296	2.6235
2,7-MMCB-OCP	-5.5355	-3.2497	2.2858	-5.4098	-3.6459	1.7639
2,7-MMCB-TCP	-5.3975	-3.2127	2.1848	-5.3126	-3.5367	1.7759
2,7-MMCB-SCP	-5.3338	-3.1139	2.2200	-5.4302	-3.1427	2.2874
2,7-MMCB-ODP	-5.6111	-3.6197	1.9914	-5.6326	-3.6815	1.9511
2,7-MMCB-TDP	-5.4598	-3.6197	1.8401	-5.5401	-3.5923	1.9478
2,7-MMCB-SDP	-5.3899	-3.4761	1.9138	-5.4957	-3.4698	2.0259

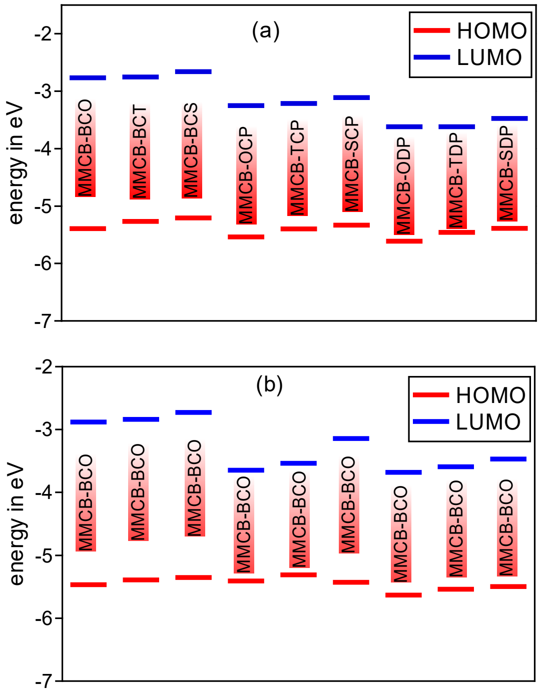

Fig. 5: Calculated HOMO and LUMO Energy Values (eV) at the DFT/B3lYP/6-31G Level for 2,7 Linkage Carbazole Copolymer Monomers (D-A) in gas (a) and in Solvent Chlorobenzene (b)

Figure 6 shows the boundary of all studied D-A monomers in molecular orbits. The analog manipulate traits of the FMOs are all 9 sorts. each HOMOs show off the same old fragrant traits, the electron delocation of the entire conjugate molecule, and is normally localized to the donor sections and to the conjugate spacer. On another hand, the HOMO has an anti-binding man or woman among successive subunits, even as the LUMO of the two adjacent fragments has a bonding man or woman, so the bottom-mendacity singlet conditions are regular with the digital transition of the μ-т * form. consequently, in the course of the stimulation manner, the photoexcited electron might be transmitted from the donor motion (electron donor) to the acceptor organization. then again, we notice that the acceptor organization of all compounds contributes substantially to the Lumos, which can increase the performance of injection of electrons and thereby increase J_{sc} present-day brief-circuit density.

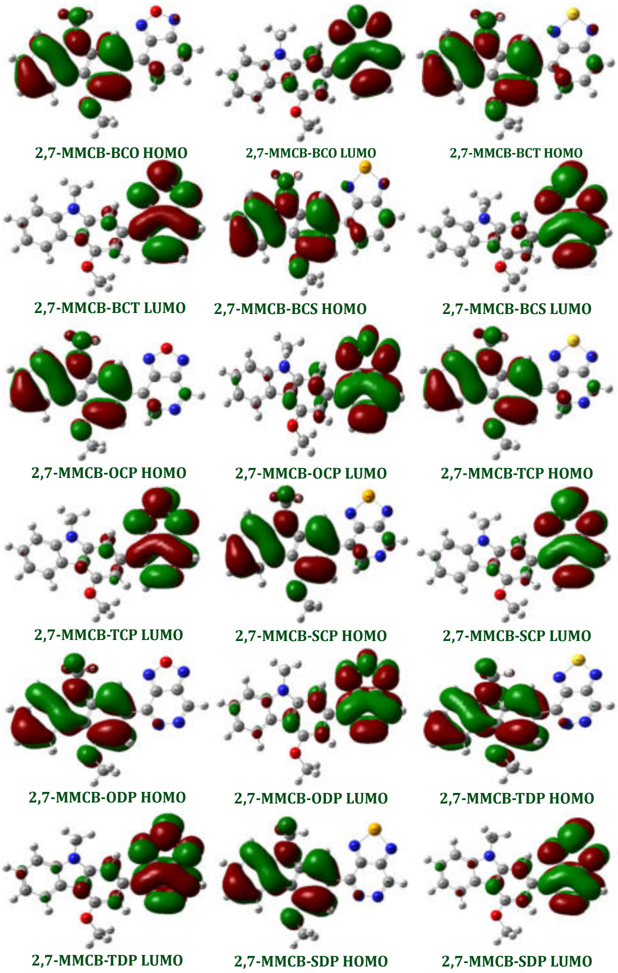

Fig. 6: The Contour Plots of HOMO and LUMO Orbitals Calculated by DFT/B3LYP/6-31G of the 2,7 Linkage Carbazole Copolymer Monomers (D-A) in Gas Phase

Exciton Binding Energies (EB) and Triplet Excitation Energy (E_T)

Exciton binding energies (EB) can be estimated as described in equation (Deibel 2010; Banerji 2012)

$$E_B = E_{Gap} - E_{Opt} \quad (3)$$

The energy gap (E_{gap}) is the required energy to separate electrons and holes for transport.(Burrows 2002)

However, the first singlet excitation electricity (E_{opt}) is the minimal electricity required for an electronic transition to arise, producing certain electron-hole pairs (excitons) due to Coulombic appeal. consequently, the essential strength gap is generally large than the optical gap.

The excitone energy binding (E_B) values are presented in table 4 in the gas and solvent phase respectively. The measured E_B values had been among 0.34 and 0.15 eV and -0.21 and 0.28 eV. however, the low-binding energy monomer 2,7-MMCB-ODP within the gas and 2,7-MMCB-BCT within the solvent levels reveals that the monomer has excessive levels of the restriction.

In addition, the majority attempts have been complete to research the absorption resultant from a single excitation, which leaves a one-triplete excitation fewer studied, in the simulation of electronic excitement of small molecules and molecular materials. A vital motive for this omission became that three-kingdom energy isn't always smooth to a degree through an immediate optical absorption. Triplet testing in conjugated polymers is especially via recharge or transfer of electricity to single triplet crossing (T_1-S_0 or S_1-T_1). The residences of the triplet have been discovered to have a direct impact on system performance. therefore it is important to study triple physical activities simply so the electroluminescence of the conjugated natural polymers is higher understood and new technologies are evolved.

The excited energies of the lowest singlet and excited triplets calculated from thumb law (Shaheen 2001).

$$E_T \approx 2E_S/3 \quad (4)$$

where E_T is the triplet excitation energy and E_S is the singlet-singlet excitation energy. In estimation of triple excitation energies for D-A monomers, present Table 4 in the gas and solvent phase. It can be shown that the smallest triple excitement energy in solution is red compared to water. This solvent stabilization is due to a strong transition time S_0-T_1 and is consistent with what we find for monomers.

Table 4: First Singlet Excitation Energy (E_{Opt}), Exciton Binding Energy (E_B) and Triplet Excitation Energy (E^T) in eV.

Polymer Monomers	Gas				
	E^{opt}	E_B	E^T	E_{D-R}	V_{oc}
Gas					
2,7-MMCB-BCO	2.1629	0.2019	1.4419	1.9106	1.394
2,7-MMCB-BCT	2.0448	0.2299	1.3632	1.8249	1.2682
2,7-MMCB-BCS	2.0748	0.3356	1.3832	1.5937	1.207
2,7-MMCB-OCP	1.8315	0.1569	1.2210	2.5447	1.5355
2,7-MMCB-TCP	1.7260	0.2715	1.1507	2.3221	1.3975
2,7-MMCB-SCP	1.7598	0.3225	1.1732	2.1323	1.3338
2,7-MMCB-ODP	1.5216	0.1782	1.0144	3.0840	1.6111
2,7-MMCB-TDP	1.4106	0.2988	0.9404	2.8134	1.4598
2,7-MMCB-SDP	1.4425	0.3491	0.9617	2.6129	1.3899
Chlorobenzene					
2,7-MMCB-BCO	2.0984	0.2664	1.3989	2.0080	1.468
2,7-MMCB-BCT	2.0597	0.2150	1.3731	2.0240	1.3918
2,7-MMCB-BCS	2.1275	0.2829	1.4183	1.8380	1.3531
2,7-MMCB-OCP	1.7346	0.2538	1.1564	2.5330	1.4098
2,7-MMCB-TCP	1.7274	0.2701	1.1516	2.4247	1.3126
2,7-MMCB-SCP	1.8098	0.2725	1.2065	2.2898	1.4302
2,7-MMCB-ODP	1.4694	0.2304	0.9796	3.0157	1.6326
2,7-MMCB-TDP	1.4675	0.2419	0.9783	2.8646	1.5401
2,7-MMCB-SDP	1.5445	0.2471	1.0297	2.7160	1.4957

ABSORPTION SPECTRA

To recognize the electronic transitions from the studied compounds, the quantum calculation on electronic absorption spectra in the gs and solventphase become achieved the use of TD-DFT/B3LYP/6–31G level. The calculated absorption wavelengths (λ_{max}), oscillator strengths (ƒ) and molecular orbital contribution percentage for gas and solvent were carried out and listed in Table 5.

All electronic transitions by π – π* orbital involed and consist of all molecule subunits. Electronic transition S0 to S1 is the reason for the biggest oscillator energy (f). The pleasure of the S1 country is the transfer of an electron from the HOMO to the LUMO solely. As with the strengths of the oscillator, the wavelengths attributable to the digital transition to S_0 to S_1 are slowly extended because the conjugation lengths grow. it's far rational because in S_0 to S_1 the transition from HOMO to LUMO is principal and, as can be shown, the HOMO to LUMO decreases inside the study above.

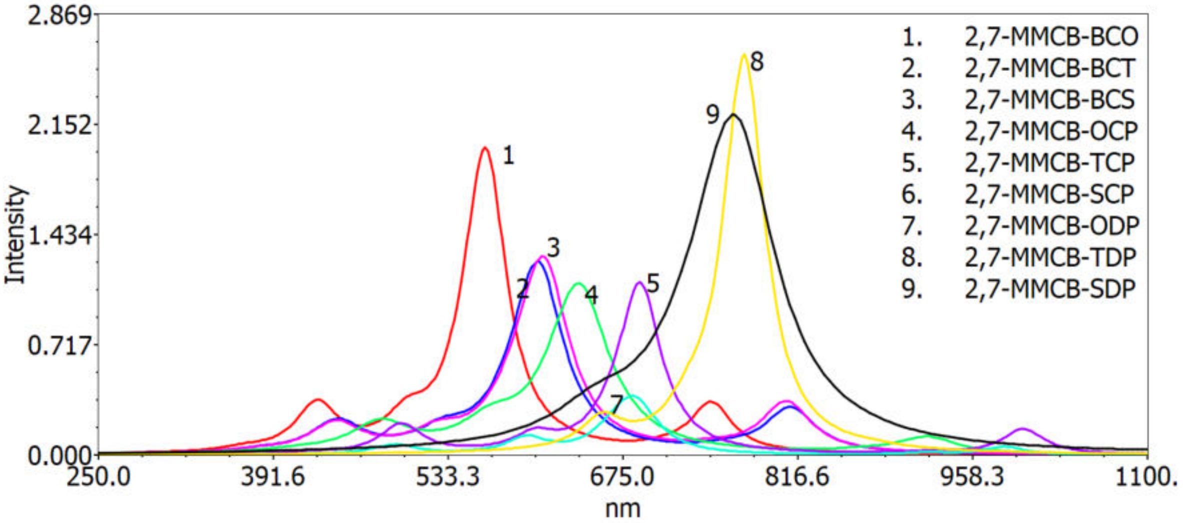

Fig. 7: Simulated UV-Visible Optical Absorption Spectra of the Studied Carbazole Copolymer Monomers (D-A) Calculated by TD/DFT/B3LYP/6-31G Level in Gas Phase

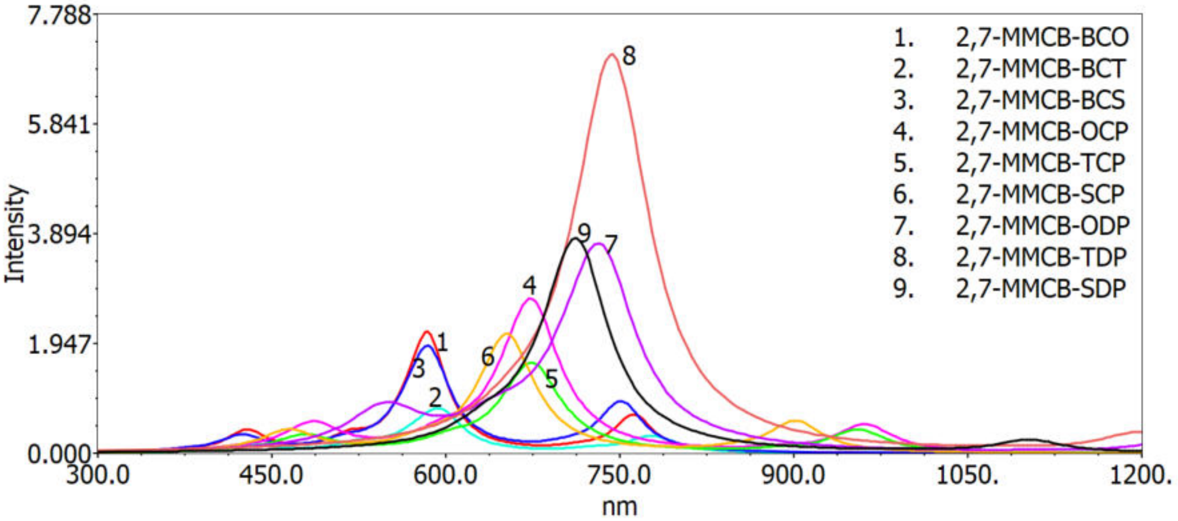

Fig. 8: Simulated UV-Visible Optical Absorption Spectra of the Studied Carbazole Copolymer Monomers (D-A) Calculated by TD/DFT/B3LYP/6-31G Level in Solvent Phase

Table 5: Electronic Transition Data Obtained by the TD/DFT-B3LYP/6-31G Calculation for all D-A Monomers in Gas and Solvent Chlorobenzene

Polymer	State	λ_{max}	f	MOcontribution	Values
1	S1	590.85	0.0627	HOMO → LUMO	99.32
	S2	517.08	0.2055	HOMO-1 → LUMO	99.44
	S3	374.63	0.0331	HOMO-2 → LUMO	98.71
2	S1	601.95	0.0583	HOMO → LUMO	99.32
	S2	526.29	0.1403	HOMO-1→ LUMO	99.28
	S3	379.29	0.0287	HOMO-2 → LUMO	98.44
3	S1	582.77	0.0654	HOMO → LUMO	99.30
	S2	513.43	0.1392	HOMO-1→ LUMO	99.23
	S3	374.08	0.0283	HOMO-2→ LUMO	97.94
4	S1	714.77	0.0417	HOMO → LUMO	99.33
	S2	599.08	0.2248	HOMO-1 → LUMO	99.54
	S3	420.32	0.0272	HOMO-2 → LUMO	99.17
5	S1	717.76	0.0402	HOMO → LUMO	99.41
	S2	604.45	0.1589	HOMO-1 → LUMO	99.48
	S3	419.14	0.0206	HOMO-2 → LUMO	98.97
6	S1	685.05	0.0450	HOMO → LUMO	99.39
	S2	582.36	0.1521	HOMO-1→ LUMO	99.44
	S3	407.85	0.0212	HOMO-2→ LUMO	96.99
7	S1	843.75	0.0263	HOMO → LUMO	99.12
	S2	644.21	0.3521	HOMO-1 → LUMO	99.57
	S3	506.13	0.0000	HOMO-2 → LUMO	99.41
8	S1	844.87	0.0252	HOMO → LUMO	99.34
	S2	656.44	0.3005	HOMO-1 → LUMO	99.63
	S3	526.85	0.0000	HOMO-3 → LUMO	99.41
9	S1	802.73	0.0265	HOMO → LUMO	99.40
	S2	635.35	0.2936	HOMO-1 → LUMO	99.63
	S3	522.09	0.0000	HOMO-3 → LUMO	99.38

PHOTOVOLTAIC PROPERTIES

Typically, the power conversion efficiency (PCE) is the most normally used parameter to compare the overall performance of various solar cells and to explain it for any compounds, a few important parameters have been evaluated consisting of the short-circuit current density (J_{SC}), the open-circuit voltage (VOC), the fill factor (FF), and the incident photon to contemporary efficiency (Pinc). The power conversion efficiency (PCE) was calculated according to the following Eq. (5):

$$PCE = \frac{J_{SC} V_{OC} FF}{P_{inc}} \qquad (5)$$

where the JSC is estimated by the maximum current which flows in the device under illumination when no voltage is applied, which depends on the morphology of the device and on the lifetime and the mobility of the charge carriers (Wu 2010).The maximum open-circuit voltage (Voc) of the BHJ is determined by the difference between the HOMO of the donor (π-conjugated molecule) and the LUMO of the acceptor, taking into account the energy lost during the photo-charge generation. It has been found that the V_{OC} is not very dependent on the work functions of the electrodes.

The theoretical values of open-circuit voltage Voc of the BHJ solar cell have been calculated from the following expression (Scharber 2006 ; Brabec 2001):

$$V_{OC} = \left|E^{Donor}_{HOMO}\right| - \left|E^{Acceptor}_{LUMO}\right| - 0.3 \qquad (6)$$

where the represents the elementary charge, and the value of 0.3 V is an empirical factor. Scharber et al. [36] proposed the Eq (6) using −3.7 eV as LUMO energy for the PCBM and -2.9 eV for C60-OMe. In addition, low LUMO of the π-conjugated compounds and a high LUMO of the acceptor of the electron (PCBM) increase the value of V_{OC}, which contributes a high efficiency of the solar cells (Brabec 2002). The theoretical values of the open circuit voltage Voc of the studied molecules range from 1.51 to 1.91 eV, in gas phase and 1.61 to 1.93 in the solvent phase, these values are sufficient for a possible efficient electron injection into LUMO of the acceptor.

Table 6: The Open Circuit Voltage Voc (eV) and $HOMO_{donor}$–$LUMO_{acceptor}$ of the Studied Molecules Obtained by B3LYP/6-31G(d,p) Level

D-A Polymer Monomers	Gas				Chlorobenzene			
	HOMO eV	LUMO eV	V_{oc}		HOMO eV	LUMO eV	V_{oc}	
			PBCM	C60-OMe			PBCM	C60-OMe
2,7-CB-BCO	-5.3940	-2.7666	1.69	2.49	-5.4680	-2.8804	1.77	2.57
2,7-CB-BCT	-5.2682	-2.7520	1.57	2.37	-5.3918	-2.8382	1.69	2.49
2,7-CB-BCS	-5.2070	-2.6592	1.51	2.31	-5.3531	-2.7296	1.65	2.45
2,7-CB-OCP	-5.5355	-3.2497	1.84	2.64	-5.4098	-3.6459	1.71	2.51
2,7-CB-TCP	-5.3975	-3.2127	1.70	2.50	-5.3126	-3.5367	1.61	2.41
2,7-CB-SCP	-5.3338	-3.1139	1.63	2.43	-5.4302	-3.1427	1.73	2.53
2,7-CB-ODP	-5.6111	-3.6197	1.91	2.71	-5.6326	-3.6815	1.93	2.73
2,7-CB-TDP	-5.4598	-3.6197	1.76	2.56	-5.5401	-3.5923	1.84	2.64
2,7-CB-SDP	-5.3899	-3.4761	1.69	2.49	-5.4957	-3.4698	1.80	2.60
PCBM	-6.1	-3.7	---	---	---	---	---	---
C60-OMe	---	-2.90	---	---	---	---	---	---

CONCLUSIONS

In order to demonstrate the structural and opto-electronic characteristics of these compounds, a quantum chemical analysis was carried out on the geomectrical and optoelectronic characteristics obtained by DFT / B3LYP/6-31 G and TDDFT / B3LYP/5-31 G, by several acceptor groups, in calculations based on 2,7-carbazole. The angle of torsion between the connected carbazole units was found to be insensitive to the way of bonding and to the degree of polymerization, ranging from 145 ° to 179 ° in gas and solvent. The torsional angles of the monomers 2,7-MMCB-ODP, 2,7-MMCB-TDP, and 2,7-MMCB-SDP show an out-of-plane orientation relative to the conjugation plane and the electron-donating effects of oxygen (O), sulfur (S) and selenium (Se) significantly changed.

The Eg values studied model compounds increases in the following order in solvent: 2,7-CB-OCP > 2,7-CB-TCP > 2,7-CB-TDP > 2,7-CB-ODP >2,7-CB-SDP > 2,7-CB-SCP > 2,7-CB-BCT > 2,7-CB-BCO > 2,7-CB-BCC. This is clearly due to the effect of the electron-donor unit which is strong for 3,6-CB-OCP and 3,6-CB-TCP than that of other monomers. As a result, significant changes were observed for the optoelectronic properties calculated: E_{HOMO}, E_{LUMO}, E_{gap}, EOpt, and E_B energies.

The absorption properties of UV – Vis were obtained using the TDDFT / B3LYP/6-31G(d) method. The maximum absorption obtained is between 590.85 and 844.87nm in the solvent. The theoretical photovoltaic values of Voc of the molecules studied range from 1.51 to 1.91 eV in the gas and 1.61 to 1.93eV in the solvent phase. Finally, the results obtained show how the electronic properties can be tuned by a substitute with several groups of acceptors and suggest that 2,7-MMCB-ODP, 2,7-MMCBCB-TDP and 2,7MMCB-SDP compounds are good candidates for optoelectronic applications such as BHJ in solar cells.

REFERENCES

Fadeyi S, Ustadi I, fath H, et al. Evaluation of CO2 post combustion capture integration with combined cycle power and desalination co-generation plant, energy procedia.,2013;37:2595-2601.

Haseeb ASMA, Fazal MA, Jahirul MI, et al. compatibility of automotive materials in biodiesel: A review, Fuel.,2011: 90: 922–931.

Motasemi F, Ani FN, A review on microwave-assisted production of biodiesel, Renewable and Sustainable Energy Reviews., Renew. Sustain. Energ. Rev.2012; 16 (7): 4719–4733.

Kiran B, Kumar R, Deshmukh D, Perspectives of microalgal biofuels as a renewable source of energy.,Energy Convers. Manag.2014; 88. 1228–1244.

Yongsheng Chen, Lingxian Meng, Yamin Zhang, Organic and solution-processed tandem solar cells with 17.3% efficiency., Science.2018; 361: 1094–1098.

Sonntag M, Strohriegl P. Novel 2,7-Linked Carbazole Trimers as Model Compounds for Conjugated Carbazole Polymers,Chem. Mater. 2004; 16: 4736–4742.

Morin, JF, Leclerc M, Adès D, et al. Polycarbazoles: 25 Years of Progress. Macromol. Rapid Commun. 2005; 26: 761–778.

Lmimouni K, Legrand C, Chapoton A. Optical and electrical characterizations of poly(*N*-alkylcarbazole) light-emitting diodes. Interpretation of electrical behaviour, Synth. Met. 1998; 97: 151–155.

Risko C, Michael D. McGeheeb et al. A quantum-chemical perspective into low optical-gap polymers for highly-efficient organic solar cells. Chem. Sci., 2011; 2: 1200-1218,

Sahu H, Panda AN. Computational study on the effect of substituents on the structural and electronic properties of thiophene–pyrrolebased π-conjugated oligomers. Macromolecules. 2013; 46: 844–855.

Zhang L, Yu M, Zhao H, et al. Theoretical investigations on the electronic and optical characteristics of fused-ring homopolymers: comparison of oligomer method and PBC–DFT method. Chem Phys Lett. 2013;570:153–158.

Zade SS, Zamoshchik N, Bendikov M. From short conjugated oligomers to conjugated polymers. Lessons from studies on long conjugated oligomers. Acc Chem Res. 2011;44:14–24.

Pappenfus TM, Schmidt JA, Koehn RE, et al. PBC-DFT applied to donor–acceptor copolymers in organic solar cells: comparisons between theoretical methods and experimental data. Macromolecules. 2011;44:2354–2357.

Kaloni TP, Schreckenbach G, Freund MS. Structural and electronic properties of pristine and doped polythiophene: periodic versus molecular calculations. J Phys Chem C. 2015;119: 3979–3989.

Rittmeyer SP, Groß A. Structural and electronic properties of oligo- and polythiophenes modified by substituents. Beilstein J Nanotechnol. 2012;3: 909–919.

Wong BM, Hsieh TH.Optoelectronic and Excitonic Properties of Oligoacenes: Substantial Improvements from Range-Separated Time-Dependent Density Functional Theory,J. Chem. Theory Comput. 2010; 6: 3704–3712.

Richard RM, Herbert JM. Time-Dependent Density-Functional Description of the ^1L_a State in Polycyclic Aromatic Hydrocarbons: Charge-Transfer Character in Disguise?. J. Chem.Theory Comput. 2011; 7: 1296–1306.

Frisch MJ, Trucks GW, Schlegel HB, Scuseria GE, Robb MA, Cheeseman JR, Montgomery JA Jr, Vreven T, Kudin KN, Burant JC, Millam JM, Iyengar SS, Tomasi J, Barone V, Mennucci B, Cossi M, Scalmani G, Rega N, Petersson GA, Nakatsuji H, Hada M, Ehara M, Toyota K, Ukuda R, Hasegawa J, Ishida M, Nakajima T, Honda Y, Kitao O, Nakai H, Klene M, Li X, Knox JE, Hratchian HP, Cross JB, Adamo C, Jaramillo J, Gomperts R, Stratmann RE, Yazyev O, Austin AJ, Cammi R, Pomelli C, Ochterski JW, Ayala PY, Morokuma K, Voth GA, Salvador P, Dannenberg JJ, Zakrzewski VG, Dapprich S, Daniels AD, Strain MC, Farkas O, Malick DK, Rabuck AD, Raghavachari K, Foresman JB, Ortiz JV, Cui Q, Baboul AG, Clifford S, Cioslowski J, Stefanov BB, Liu G, Liashenko A, Piskorz P, Komaromi I, Martin RL, Fox DJ, Keith T, Al-Laham MA, Peng CY, Anayakkara A, Challacombe M, Gill PMW, Johnson B, Chen W, Wong MW, Gonzalez C, Pople JA (2009) Gaussian 09, Revision A02. Gaussian Inc, Wallingford CT

Becke AD. Perspective on Density functional thermochemistry. 111. The role of exact exchange J. Chem. Phys. 1993; 98; 5648-5652. Zerner M, Lipkowitz KB, Boyd D. B. Reviews in Computational Chemistry, Volume 2, Eds.VCH, New York, 313, 1991.

Tomasi J, Mennucci B, Cammi R. Quantum mechanical continuum solvation models. Chem Rev. 2005; 105(8): 2999–3094.

Miertuˇs, S.; Scrocco, E.; Tomasi, J. Electrostatic interaction of a solute with a continuum. A direct utilizaion of ab initio molecular potentials for the prevision of solvent effects. Chem. Phys. 1981, 55, 117–129.

Qin Y, Gu H, Liu S, et al. Efficient hetero junction solar cells based on the synergy between planarity and dipole moment in fluorinated-thienothiophenes-based donor-acceptor polymers, Synthetic Metals, 2018;245:42-50.

Jo JW, Bae S, Liu F, et al. Comparison of two D– A type polymers with each being fluorinated on D and A unit for high performance solar cells, Advanced Functional Materials, 2015;25;120-125.

Estrada LA, Liu DY, Salazar DH, et al. Poly[Bis-EDOT-Isoindigo]: An Electroactive Polymer Applied to Electrochemical Supercapacitors,Macromolecules 2012;45: 8211–8220.

Kim BG, Zhen CG, Jeong EJ, et al. Organic dye design tools for efficient photocurrent generation in dye-sensitized solar cells: exciton binding energy and electron acceptors. Adv Funct Mater [Internet]. 2012; 22: 1606–1612.

Deibel C, Mack D, Gorenflot J, et al. Energetics of excited states in the conjugated polymer poly(3-hexylthiophene). Phys Rev B.2010;81(8):8-15.

Banerji N, Gagnon E, Morgantini PY, et al. Breaking down the problem: optical transitions, electronic structure, and photoconductivity in conjugated polymer PCDTBT and in its separate building blocks. J Phys Chem C. 2012; 116:11456–11469.

Burrows HD, Seixas de Melo J, Serpa C, et al. Triplet state dynamics on isolated conjugated polymer chins. Chem.Phys.2002; 3: 285-290.

Shaheen SE, Brabec CJ, Sariciftci NS, et al. 2.5% efficient organic plastic solar cells. Appl Phys Lett 2001; 78(6):841–843.

Wu Z, Fan B, Xue F, et al. J.Organic molecules based on dithienyl-2,1,3-benzothiadiazole as new donor materials for solution-processed organic photovoltaic cells. Sol Energy Mater Sol Cells 2010; 94(12):2230–2237.

Scharber MC, Mühlbacher D, Koppe M, et al. Design rules for donors in bulk-heterojunction solar cells—towards 10% energy-conversion efficiency. Adv Mater.2006;18(6):789–794.

Brabec CJ, Cravino A, Meissner D, et al. Origin of the open circuit voltage of plastic solar cells. Adv Funct Mater.2001; 11(5):374–380.

C H, Shaheen SE, Brabec CJ, et al. Influence of the anodic work function on the performance of organic solar cells. Chem Phys Chem.2002; 3(9):795–799.

Science and Technology Journal Vol. 8 Issue 2 July 2020 ISSN: 2321-3388

X-aggregates and their Influence on Solid-State Emission of Organic Luminophores

Lalhmunsiama[1] and Aniket Chowdhury[2]*
[1,2]Department of Industrial Chemistry,
School of Physical Sciences, Mizoram University, Tanhril, Aizawl–796004, Mizoram, India
E-mail: *mzut239@mzu.edu.in

Abstract—The organic luminophores consist of a diverse array of compounds exhibiting well understood conventional emission behaviour. Though their solution-state luminescence is well established, few luminophores are capable of exhibiting bright solid-state emission. Therefore, various theories to afford high solid-state emission from organic compounds, are currently under development. The formation of cross aggregate or X-aggregate is a novel way, where the energy-consuming p-p stacking of planar luminophores are disrupted using steric requirements. In this review, the recent reports on the X-aggregates along with their luminescence mechanism and effect of packing on emission behaviour are discussed.

Keywords: Luminescence, X-aggregates, Crystal Packing, Organic Luminophore

INTRODUCTION

The organic luminophores are a class of purely organic molecules that exhibit bright fluorescence in their solution as well as in solid-state under the influence of ultraviolet irradiation. The solution-state luminescence of the organic luminophores is well established by theories that mainly utilize Jablonski Diagram and Kasha's Rule (A. Jabłoński, 1993). When the luminophores are solidified, numerous different mechanisms get involved which are yet to be completely understood. It is well known that, in solution, the molecules behave as a singular entity and their photophysical characteristics are easy to interpret. But when solidified, they tend to form various types of regular and irregular aggregates which require detailed experimental analysis (K. Zhang *et al.*, 2019). The irregular packing of the molecules mostly leads to non-emissive amorphous aggregates, but it is the crystalline aggregates that are of utmost importance. The precision and functional capability of organic electronics including Organic Thin Film Transistors, Light Emitting Diodes etc. strongly correlate to the crystallinity of the substance(L. J. Guo *et al.*, 2008). The migration of charge, electron as well as energy is superior for a regular crystalline material.

In this regard, the crystalline regular type aggregates of organic luminophores have been investigated by several research groups in detail (B. Liu *et al.*, 2019). The organic molecules in their crystalline aggregated form mostly organize into two major types of aggregates, the parallel type aggregate or H-aggregate and the head to tail type aggregate or J-aggregate (F. C. Spano et al., 2017). One of the major drawbacks of such aggregates is that the molecules lose their luminescence property when they are in their H-aggregate form and it is almost impossible to predict which organic molecule will provide which type of aggregate. Based on the experimental evidence the crystalline packing of the organic molecules generally follows three types of patterns shown below. They are a) Ladder type, b) Staircase type, and c) Brick work type as shown in Figure 1 (A. Vannikov *et al.* 2012).

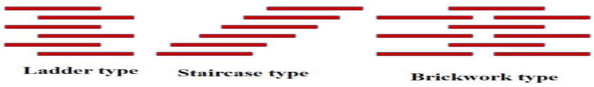

Fig. 1: Various Parallel Packing Pattern of the Organic Molecules in Crystals (A. Vannikov *et al.* 2012)

The key factor, that determines whether an aggregate will exhibit H-type or J-type behaviour is the slip angle between two consecutive molecules. Hiroshi Yao in his seminal paper described the method to determine the aggregate type from the calculation of the slip angle (H. Yao *et al.* 2005). The slip angle or the angle of slippage is the angle between the long axis and one of the organic molecules present in the crystalline packing structure. It was estimated that when the slip angle is less than 32°, then the system tends to show pattern and photophysical behaviour of J-aggregates and when it is higher then the crystalline pacing transforms into H-aggregate. Though this experimental evaluation is accurate in determining the formation of the type of aggregate, it is the theoretical aspect that provides a clear opportunity to understand the mechanism through which the radiative emission or fluorescence of the molecules decay.

EXCITONIC THEORY

The crystal packing pattern of solid samples can estimate the tendency to form the J and H-aggregates but it is the excitonic theory that helps in explaining the photophysical behavior of these aggregates. As per the theory, all organic molecules are considered to be point dipoles. In their singular form, the ground and excited states are not coupled and the molecule can easily get excited, and de-excited and exhibit strong luminescence. But in their J and H-aggregate, the molecules are parallel and form two different excited states depending on the orientation of the molecules as shown in Figure 2 (F.C. Spano *et al*. 2017).

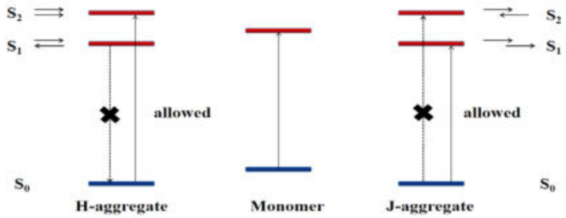

Fig. 2: The Exciton Energy Diagram of the H-aggregate, Monomer, and J-aggregate (F. C. Spano *et al*. 2017)

Among the two excited states of the aggregates, in one of the states, due to the opposite orientation of the transition dipole moments, the net transition dipole is zero, and excitation to these states or de-excitation from these states are optically forbidden. For H-aggregate it is the ground excited state S_1 and for J-aggregate it is the higher excited state S_2 which is optically forbidden. Therefore, for H-aggregates, upon photo-irradiation the system arrives from S_0 to S_2 state and relaxes to the S_1 state. But as the S_1 to S_0 transition is optically forbidden, it cannot release energy in non-radiative pathway, and fluorescence is quenched by different mechanisms including molecular motion, collision, thermal radiation etc. Finally, it can be concluded that for organic luminophores it is not only difficult to predict the type of aggregates that it will form but also, the luminescence property it is going to exhibit. These issues have plagued the scientific community dealing with organic electronics and optoelectronics for decades. As a way out of this dilemma, Jean-Lucas Bredas and coworkers proposed a slightly altered geometric control over the organic molecules that will make it difficult to pack them in parallel fashion during crystallization (J-L. Bredas *et al*. 2001). It was suggested that if sufficient branches are added to the core of the organic luminophores, then the steric interaction will make it difficult to organize the molecules for p-p stacking and they will orient in a criss-cross manner or in the staggered orientation which he named as the X-aggregates. This unique orientation will make it difficult to couple the transition dipole moment of any two neighbouring molecules and they will behave as independent entities. The concept was not only proposed but the theoretical aspect was further elaborated using the excitonic model and quantum chemical calculation. As per the proposition, in both the excited states of a potential X-aggregate dimer the transition dipole moments of the molecules will be oriented in a perpendicular fashion and thus they will not be optically coupled. Therefore, excitation, as well as de-excittion to between the ground and excited sates will be allowed making them highly luminescent. The excitonic diagram is shown in Figure 3.

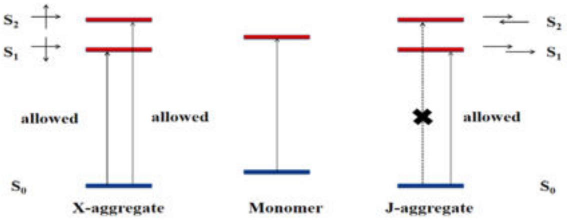

Fig. 3: The Excitonic Energy Diagram of X-aggregate, Monomer, and J-aggregate (J-L. Bredas *et al*. 2001)

The proof of concept was further elaborated using various molecular backbone including polyphenylenevinylene, pyrene, triphenylamine, tetraphenylpyrene, tetraphenylethylene etc. Various types of molecular systems where the X-aggregates were deliberately introduced are discussed herein.

TETRAPHENYLPYRENE DERIVATIVE AS X-AGGREGATE

Although Bredas and coworkers first proposed the theory of X-aggregates in 2001, the first such molecule was reported in 2004 (J-L. Bredas *et al*. 2004). The research group reported the synthesis, crystal structure, and elusive photophysical behaviour of tetrapehnylpyrene derivatives. An array of 1,3,6,8-substituted tetraphenylpyrene compounds were designed in such a way that the physical properties of the molecule such as polarity, solubility etc. Can easily be modulated. Among several compounds, the compound **4** was the smallest and was experimented in detail. The structures of the molecules are elaborated in Figure 4.

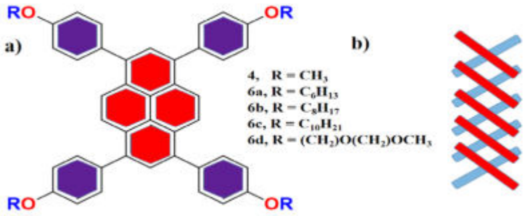

Fig. 4: a) The Structure of the Tetraphenylpyrene Derivatives, b) The Cross-Type Packing of Neighbouring Layers (J-L. Bredas *et al.* 2004)

When the photophysical experiments on compound 4 were carried out, it showed absorption peaks at 393 and 397 for the solution, and thin film respectively and emission peaks at 432 and 477 in solution and in the thin film. The slight red shift was attributed to the weak p-p interaction among the neighbouring units.

The crystal structure analysis revealed that compound 4 forms parallel 1-D stacking of molecules and two such neighbouring layers are oriented in X-shape fashion. Therefore, the formation of X-aggregate which was long predicted was finally established. The other compounds also showed similar type of strong absorption and emission behaviour in solution and thin films.

OLIGOMERIC PHYNELNEVINYLENE AND ITS DERIVATIVES:

The first example of the X-aggregate based on oligophenylenevinylene system was reported by Yuguang Ma in 2005 (Y. Ma *et al.* 2005). A polyphenylenevinylene oligomer 1 was developed and its photophysical properties was evaluated. The structure of oligomer 1 is shown in Figure 5.

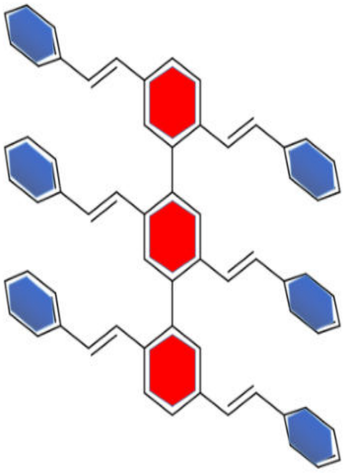

Fig. 5: The Structure of Oligomer 1 (Y. Ma *et al.* 2005)

The molecule was carefully designed in such as way that it contained substitution both along X and Y axes of the central benzene ring. The photophysical behaviour of this luminophore was evaluated and it was found that the system exhibits bright blue fluorescence in toluene with absorption and emission maxima centred around 417 and 437 nm. As predicted, the solid sample also demonstrated strong bluish green fluorescence with a slightly red shift at 450 nm. The solid-state fluorescence efficiency was found to be 32% which is comparatively higher than conventional polyaromatic compounds. But the efforts to get a good quality crystal for packing pattern examination was futile and the solid sample turned out to be amorphous. It was proposed that the very bulky substitutes and high molecular weight compromised the crystallization process. However, this initial breakthrough provided an opportunity to develope more X-aggregates.

Following the footsteps, Yuguang Ma and coworkers developed a more simple substituted Styrylbenzene derivative 2 called trans-DPDSB (Y. Ma *et al.* 2005). The structure of the molecule is elucidated below in Figure 6.

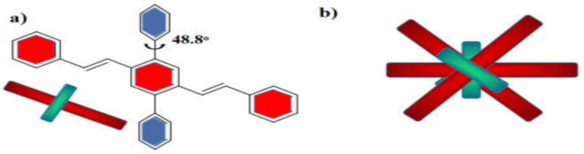

Fig. 6: a) The Twisted Structure of Trans-DPDSB, and b) The Staggered Type Solid-State Packing Pattern (Y. Ma *et al.* 2005)

As shown in the Figure 6, the central styryl ring contains two additional benzene rings on the main core and the structure is highly non-planar. The three phenyl rings along the minor axis are at a torsion angle of 48.8^o. The crystal structure exhibit a highly staggered packing pattern and the neighbouring molecules are held together by weak p-p and C-H-p interactions. After careful inspection of the packing, the needle-like crystal was exposed to the UV irradiation of 365 nm and bright blue fluorescence with maxima around 420 nm was observed. The stability of the sample was verified using DSC and it was found to be in the range of 252-254^{o}C. The study indicated that the crystallinity, staggered packing, thermal stability, and bright blue luminescence made the system an excellent candidate for blue LED.

In 2008 reported another X-aggregate luminophore where the previously reported system was slightly modified with methyl groups on the periphery to enhance the steric interaction among the neighbouring molecules was reported (Y. Ma *et al.* 2008). A comparative analysis of the newly developed systems with the unsubstituted isomer was carried out and stark improvement in fluorescence efficiency was observed. The molecular structure and packing pattern of the molecule is shown in Figure 7.

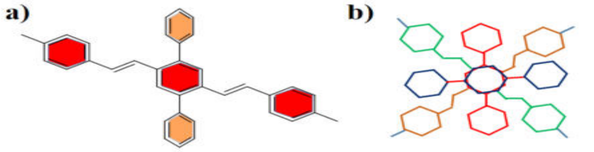

Fig. 7: a) The Structure of the Molecule *trans*-DPDSB, and b) The Packing Pattern of *trans*-DPDSB showing X-Aggregate (Y. Ma *et al.* 2008)

Several attempts were made to crystallize the molecule *trans*-DPDSB and finally, plate-shaped crystals were obtained from a solvent mixture of ethanol and hexane. The structure resembled the previously reported trans DPDSB with a smaller intermolecular cross angle of 25 ° only. The emission maxima of the methylated DPDSB showed a stark red shift from solution (420 nm) to solid (450 nm). The methylated DPDSB was found to be a good material for the construction of electroluminescent thin film and it showed deep blue emission. The maximum efficiency was compared with conventional luminophores and under the non-doped conditions the luminous efficiency, external quantum efficiency was found to be 4.2 cd/A and 3.9%.

Apart from pure polyphenylenevinylene several other groups of compounds was also investigated to design X-aggregates. Some of them are illustrated below.

PHEYLBENZOXAZOLE BASED COMPOUNDS

In 2012, Wei Huang and coworkers have reported a unique Phenylbenzoxazole based molecule named N-(4-benzo[*d*] oxazol-2-yl) phenyl)-4-*tert*-butylbenzamide or OTB which was not only found to be forming X-aggregates in crystalline form but also was showing aggregation-induced emission or AIE property (W. Huang *et al.* 2012).

The inspiration of this work stemmed out of the fact that all the prior literature had achieved 1-dimensional or two dimensional X-aggregates but a three dimensional aggregate was elusive. To achieve the goal, the two different molecules were combined by a spacer phenyl ring in such a way, that the conjugation was extended throughout the system, but it had a non-planar structure. To elaborate on the importance of using two different functional groups, the the photophysical properties of the molecule in solution was first evaluated. The emission spectra of OTB in THF demonstrated two different peaks with different intensity. It was proposed that the smaller emission peak at 365 nm was originated from the radiative energy release of the Locally excited state centred on benzoxazole moiety and the more intense peak at 500 nm was due to twisted intramolecular charge transfer from the benzamide moiety. Using computational analysis and geometrical optimization they also proposed a twisted structure for the high-intensity emission as shown in figure 8.

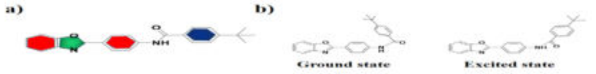

Fig. 8: a) Molecular Structure of OTB, b) Simulated Geometry of the Ground State and Twisted Excited State in Solution (W. Huang *et al.* 2012)

A completely different fluorescence behaviour was observed when the solid sample was analyzed. The solid sample showed a dominant emission at 410 nm which was attributed to the emission from the LE state. It was argued that in solid sample the rotational motion of the molecules was impossible and TICT emission was not observed. To establish the proof of concept, the single crystals of the sample were grown by slow evapouration of ethyl acetate solution. The crystal structure revealed unexpected alteration in packing pattern. The solution-state structure optimization established a dihedral angle of 60° between the benzoxazole and benzamide moiety but in crystalline state the two units were found to be almost coplanar with a dihedral angle of 173°. In each unit cell, four molecules of OTB were closely packed and various types of weak interactions such as C-H-p, H-bonding were found to be responsible for holding the moieties together. Two molecules were found to be oriented in X shape and weak H-bonding was observed between the carbonyl oxygen atom and the tert-butyl hydrogen. Two such X-units were then held together by C-H-p interactions. This unique packing was found to be propagated in all three dimensions making the system the first 3D cross aggregate in literature. The packing pattern is shown in Figure 9.

Fig. 9. a) Cross Aggregate of OTB, b) Four Molecules in A Single Unit Cell, c) 3-D Propagation of the Packing in Single Crystal (W. Huang *et al.* 2012)

This unique packing pattern contributed to the large improvement in solid-state fluorescence property. The authors were unable to examine the fluorescence of the pure crystals but the powdered sample showed a 229 fold enhancement in fluorescence quantum yield and the total quantum yield increased from 0.22% in solution to 50.3% in solid form.

The author proposed that when an X aggregate forms, the energy difference between the two excited states decrease with an increase in the angle between the long axes of the molecules in the X-aggregate. As the angle in the crystal structure was found to be 80°, the molecules were almost perpendicular and radiative emission from the S_1 to the S_0 state was allowed which led to such a strong enhancement in fluorescence.

ANTHRACENE DERIVATIVES AS X-AGGREGATE

Anthracene is a well-known fluorophore but due to planar structure, the derivative of anthracene is rarely studied. Wenping Hu and coworkers have first reported substituted anthracene derivative where cross-dipole stacking was observed (W. Hu *et al.* 2015). Instead of simply substituting the 9,10-positions, they also modified the 2,6 positions. The substitutions were carefully made to make the system look like a cross type structure with bulky groups on the periphery which can restrict the planar packing or p-p interactions. Phenyl groups were incorporated in the 2,6-positions to enhance the conjugation and trimethylsilyl groups were introduced in the 9,10 positions to improve steric crowding. The structure of the molecule is shown in Figure 10.

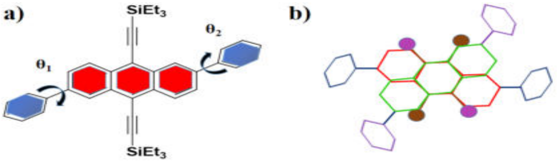

Fig. 10: a) Molecular Structure of Anthracene Derivative TES-DPA, and b) its Crystalline Packing Pattern (W. Hu *et al.* 2015)

The newly synthesized compound was named as (2,6-diphenylanthracene-9,10-diyl)bis(ethyne-2,1-diyl) bis(triethylsilane) or TES-DPA. To understand the packing tendency of the molecules, crystals were grown by slow evapouration of chlorobenzene solution. During the single crystals analysis, three different types of conformations with various torsional angles between the two phenyl rings attached to the anthracene was observed. The torsional angles of the twisted monomers are tabulated below.

Table 1: The Crystal Parameters of the Various Conformations (W. Hu *et al.* 2015)

Conformation	Torsion angle θ_1	Torsion angle θ_2
M1	28.46°	43.07°
M2	23.81°	23.81°
M3	29.59°	29.59°

But in all the conformations the neighbouring molecules were found to orient themselves into a staggered pattern to reduce the steric repulsion among the trimethylsilane group.

The effect of X-type aggregation on the solid-state fluorescence was analyzed by comparing both the solution and solid-state photophysical properties of the TES-DPA. The fluorescence quantum yields were found to be 100% and 77.3% in solution and solid-state respectively. Although the quantum yield reduced slightly during solidification the fluorescence lifetime increased almost seven-fold from 10.5 ns in solution to 69.2 ns in solid. The very high lifetime of the excited state in the solid was attributed to the formation of X-aggregate that forbids energy release in any non radiative pathway. Finally, the stability of the crystals was measured using TGA-DSC analysis and the decomposition temperature was found to be 316°C, which is considerably high. This very high quantum yield and excited-state lifetime made this molecule a good candidate to be used for OLED and OTFT.

TETRAPHENYLETHYLENE BASED COMPOUNDS

The tetrapehnylethylene compounds (TPE) were first brought into prominence for their aggregation-induced emission behaviour by Ben Zhong Tang in the early 2000 (B. Tang *et al.* 2015). Several groups have reported the unique high solid-state luminescence of the tetraphenylethylene and its derivatives for various applications. Keeping this in view, Tang and coworkers combined the tetrarpehylethylene with Perylenebisimide dye (PBI) to construct a new donor acceptor type twisted fluorophore and evaluated its solid-state emission behaviour (B. Tang *et al.* 2015). The PIB and its derivatives are well known in the literature to form J type aggregate due to geometrical requirements. Therefore, it was hypothesized that if TPE units are added to the PBI core then the steric requirement will force the conjugated dye molecules to form non-coplanar X-type aggregates which will manifest into very high solid-state fluorescence behaviour. Two systems were developed simultaneity. When a single TPE unit was attached to PBI then it was called as TPE-N-PBI and when two TPE units were kept in conjugation with PBI then it was named as DTPE-N-PBI. The structure of both the molecules are depicted in Figure 11.

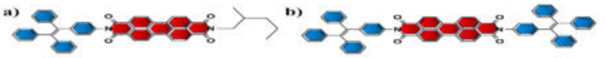

Fig. 11: The Structure of a) TPE-N-PBI, and b) DTPE-N-PBI (B. Tang *et al.* 2015)

The samples were subjected to detail photophysical experiments. In solution the TPE-N-PBI, as well as, the dimer showed very weak fluorescenc with the quantum yield of TPE-N-PBI was found to be 0.32%. The weak solution-state luminescence was attributed to the excited state phenomenon known as twisted intramolecular charge transfer. The TPE is a well-known donor whereas the PBI is an acceptor. In the excited state the energy is transferred from one unit of the molecule to the other and is lost due to nonradiative pathways such as collision, rotation, vibration etc. To understand the solid-state luminescence several attempts were made to grow suitable single crystals but no crystals with good diffraction capability were found. Therefore, nano-aggregates was generated to mimic the crystalline packing pattern by slowly adding poor solvents in the sample solution. The samples formed a clear solution in DCM and THF but showed poor solubility in Hexane and Water. Therefore when hexane was added to a DCM solution, the molecules slowly started to form nanoaggregates that was found to form stable dispersion in the medium. Similar phenomenon was observed for a Water-THF mixture. In the absorption spectra of the samples, no peaks were observed for p-p interactions and hence the formation of any parallel J or H-aggregates were excluded. The change in fluorescence intensity before and after aggregate formation are given in Table 2.

Table 2: Photophysical Characterization of TPE-N-PBI and DTPE-N-PBI (B. Tang *et al.* 2015)

Sample	Solvent composition	Abosorption maxima (nm)	Emission Maxima (nm)	Quantum Yeld (%)
TPE-N-PBI	DCM	527	539, 575	0.32
	DCM-Hexane (60%)	527	529	0.55
	THF-Water	523	535	2.65
	DCM	527	539	0.39
	DCM-Hexane (90%)	527	530	1.48

From the experimental analysis it was proposed that the molecules were definitely forming X-type aggregates in condensed state which lead to the enhancement of their fluorescence efficiency as well as lifetime. The detail theoretical calculations that was carried out in the work is beyond the scope of this review.

CONCLUSION

In conclusion, it can be summarized that the crystal packing pattern of organic luminophores holds utmost importance and control over their photophysical properties. The crystal structures can easily be modulated by judiciously controlling the substitution over the main fluorophore. Conventional planar luminescent organic molecules can also be subjected to a similar treatment to afford bright solid state emission. The organic molecules with their well characterized crystalline form and controllable luminescence is expected to find suitable applications in various sub categories of organic electronics such as printable circuits, Organic Thin film transistors, Organic Light Emitting Diodes etc.

REFERENCES

Jabłoński, A. 1993. Efficiency of Anti-Stokes Fluorescence in Dyes. Nature, 131: 839-840.

Zhang, K., Liu, J., Zhang, Y., Fan, J., Wang, C-K., and Lin, L. 2019. Theoretical Study of the Mechanism of Aggregation-Caused Quenching in Near-Infrared Thermally Activated Delayed Fluorescence Molecules: Hydrogen-Bond Effect. J. Phys. Chem. C. 123: 24705–24713.

Li, D., and Guo, L.J. 2008. Organic thin film transistors and polymer light-emitting diodes patterned by polymer inking and stamping. J. Phys. D: Appl. Phys. 41: 105115-105122.

Kenry, Chen, C., and Liu, B. 2019. Enhancing the performance of pure organic room temperature phosphorescent luminophores. doi.org/10.1038/s41467-019-10033-2.

Hestand, N. J., and Spano, F. C. 2017. Expanded Theory of H- and J-Molecular Aggregates: The Effects of Vibronic Coupling and Intermolecular Charge Transfer. Chem. Rev. 118: 7069–7163.

Prokhorov VV, Pozin SI, Lypenko D, Perelygina O, Maltsev E, Vanniov A, 2012. Molecular Arrangements in Two-Dimensional J-Aggregate Monolayer of Cyanine Dyes. Macroheterocycles, 5, 371-376.

Yao, H., Kaori, D., Isohasi, T., and Kimura, K. 2005. In Situ Detection of Birefringent Mesoscopic H and J Aggregates of Thiacarbocyanine Dye in Solution. Langmuir. 21: 1067-1073.

Cornil, J., Beljonne, D., Calbert, J-P., and Bredas, J-L. 2001. Interchain Interactions in Organic p-Conjugated Materials: Impact on Electronic Structure, Optical Response, and Charge Transport. Adv. Mater. 13: 1053-1067.

Halleux, V., Calbert, J-P., Brocorens, P., Cornil, J., Declarq, J-P., Bredas, J-L., and Geets, Y. 2004. 1,3,6,8- Tetraphenylpyrene Derivatives: Towards Fluorescent Liquid-Crystalline Columns? Adv. Func. Mater. 14: 649-660.

He, F., Xu, H., Yang, B., Duan, Y., Tiang, L., Huang, K., Ma. Y., Liu, S., Feng, S., and Seng, J. 2005. Oligomeric Phenylenevinylene with Cross Dipole Arrangement and Amorphous Morphology: Enhanced Solid-State Luminescence Efficiency and Electroluminescence Performance. Adv. Mater. 17: 2710-2714.

Xie, Z., Yang, B., Li F., Cheng, G., Liu, L., Yang, G., Xu, H., Ye, L., Hanif, M., Liu, S., Ma, D., and Ma Y. 2005. Cross Dipole Stacking in the Crystal of Distyrylbenzene Derivative: The Approach toward High Solid-State Luminescence Efficiency. J. Am. Chem. Soc. 127: 14152-14153.

Xie, Z., Xie, W., Li, F., Liu, L., Wang, H., and Ma, Y. 2008. Controlling Supramolecular Microstructure to Realize Highly Efficient Nondoped Deep Blue Organic Light-Emitting Devices: The Role of Diphenyl Substituents in Distyrylbenzene Derivatives. J. Phys. Chem. C. 112: 9066–9071.

Qian, Y., Cai, M., Zhou, X., Gao, Z., Wang, X., Zaho, Y., Yang, X., Wei, W., Xie, L., and Huang, W. 2012. More than Restriction of Twisted Intramolecular Charge Transfer: Three-Dimensional Expanded #-Shaped Cross-Molecular Packing for Emission Enhancement in Aggregates. J. Phys. Chem. C. 116: 12187−12195.

Liu, J., Meng, L., Zhu, W., Zhang, C., Zhang, H., Yao, Y., Wang, Z., He, P., Zhang, X., Wang, Y., Zhen, Y., Dong, H., Yi, Y., and Hu, W. 2015. A cross-dipole stacking molecule of an anthracene derivative: integrating optical and electrical properties. J. Mater. Chem. C. 3: 3068--3071.

Mei, J., Leung, L., Kwok, R., Lam, J., and Tang, B-Z. 2015. Aggregation-Induced Emission: Together We Shine, United We Soar. Chem. Rev. 115: 11718-11940.

Wang, Y-J., Li, Z., Tong, J., Shen, X-Y., Qin, A., Sun, J-Z., and Tang, B-Z. 2015. The fluorescence properties and aggregation behavior of tetraphenylethene–perylenebisimide dyads. J. Mater. Chem. C. 3: 3559–3568.

Science and Technology Journal Vol. 8 Issue 2 July 2020 ISSN: 2321-3388

Evaluation of Sand Quality and its Effect on Mortar and Cement Concrete

H. Laldintluanga[1*], Rebecca Ramhmachhuani[2] and Ramthlengliani[3]
[1,2,3]Civil Engineering Department, Mizoram University, Tanhril, Aizawl–796004 (India)
E-mail: *laldin99@gmail.com

Abstract—The most used raw material in concrete are cement, sand and coarse aggregate. The study involved performing a series of tests on river sand and crushed sand that was collected from different sources to find the feasibility of commonly used sand in Mizoram. The properties of sand have been checked in terms of particle size distribution, fineness modulus, specific gravity. The effect of different sources of sand which are having different properties in mortar and concrete has been investigated. The sand was collected from different source having different particle size distribution as well as different silt and clay content. The quantity of water calculated based on normal consistency value cannot be applied to mortar which has sand having cohesion. Optimum moisture content calculated using the Standard Proctor test for cohesive sand is used to find out the additional water required on the mortar mix. The mortar with an exact amount of water has higher strength and density. The bonding is weakened in strength by non- binding material like silt and clay. Test results show that a decrease in compressive strength when the ratio of silt content to fine aggregate increase. It is found out that there is a large variation in the strength of mortar and concrete due to variation in the quality of sand use.

Keywords: River sand; Crushed sand; Mortar; Compressive Strength

INTRODUCTION

There is a scarcity of natural sand due to heavy demand in construction activities which forces to find a suitable cheapest and easy way of getting substitutes for natural sand. Sand which is produced from quarry stone by crusher prepared specially to get cubical, smooth textured, well graded particles of fine aggregate are called crushed/ manufactured sand. The mostly used fine aggregate is the sand extracted from river banks. The compressive strength result of concrete has been compared and found that crushed sand result is 8% less than the river sand concrete (Ganesh V et al. 2017). Past researches identify the major causes of buildings failure as dependent on the quality of building materials used (sand, coarse aggregates, steel reinforcement, water), workmanship employed in the concrete mix proportioning and construction methodology, defective designs, and non-compliance with specifications or standards (Machuki, O.V. 2012; Ayodeji, O. 2011; Ayuba, P et al. 2011; Dimuna, K.O. 2010; Dahiru, D., et al. 2014; Oloyede, S., et al. 2010). To prevent building failure, careful selection of construction materials including building sands is paramount to ensure they meet the set construction standards. The collapses of buildings resulting in injuries, loss of lives, and investments have been largely attributed to the use of poor quality concrete ingredients (Ngugi, H.N., *et al*. 2014).

American Society for Testing and Materials (ASTM) C 117 (ASTM C117 1995) and Hong Kong [Construction Standard CS3 (2013)] construction standards give an allowable limit of 10% for silt and clay content in sand. On the other hand, BS 882 states that the percentage of clay and fine silts must not exceed 4% by weight for sand for use in concrete production (Harrison, D.J. *et al*. 1994). Fine aggregates containing more than the allowable percentages of silt are required to be washed to bring the silt content within allowable limits. As a thumb rule, the total amount of deleterious materials in a given aggregate should not exceed 5% (Anosike, N.M. 2011). The methods of determining the content of these deleterious materials are prescribed by IS 383 (IS 383. 1970), ASTM C 117 (ASTM C117. 1995) and (ASTM C40 2004). These include determination of contents organic impurities, clay, or any deleterious material or excessive fillers of sizes smaller than No. 100 sieve.

Compressive strength is decreased while using crushed sand as partial replacement of fine aggregate up to 40%. This may be because replaced fine particles may not be sufficient to fill the voids resulting in comparatively less dense concrete as compared to the referral concrete (Syed Yaqub et al. 2015). The presence of sand fines in concrete is likely to affect the workability, strength, and long-term performance of concrete. To this effect, the percentage limit of sand fines (clay/silt) is recommended by various building standards recommends 4% and 10% of fines in building sand respectively (Hyginus E. Opara, et al. 2018). Unwashed gravel exhibits the lowest compressive strength probably due to impurities embedded therein that may lower the strength of the concrete (Manjunath S, et al. 2018). Increase in sand fines (silt/clay) content beyond 4% cause a reduction in compressive strength of concrete (Yalley P P, et.al. 2018).

MATERIALS AND METHODS

Crushed sand was collected from Sakawrtuichhun, Hlimen, and Maubuang as well as river sand from Langkaih, Darlungkai, Bagha, Sairang, Chhimtuipui. The coarse aggregate has been collected from the quarries of Silchar and Sakawrtuichhun. This study is to assess the feasibility of the commonly used sand for construction works in the state of Mizoram.

The study is carried out in two stages as below:

- Mortar and Concrete M-20 (1:1.5:3, wc=0.5) were prepared with sand collected from a different source to check the effect of particle size and silt & clay on mortar and concrete.
- Concrete M-40 (1:1.3:2.2,wc=0.4) was prepared to find the effect of dust present in the compressive strength of concrete

Sieve analysis was carried out on the sand samples to determine their degrees of fineness, sand zone and grain size distribution. Wash sand samples were prepared by thoroughly washing river sand, and crushed sand with clean water to remove silt and clay and organic impurities present. Physical examination of sand particle shapes and sizes was done as well as a determination of specific gravity of sand using pycnometer glass.

Specific gravity, normal consistency, fineness value, soundness, and setting time of cement were conducted to check the quality of cement. Coarse aggregate was also tested to know their impact value, abrasion value, crushing value, specific gravity, and water absorption value. Physical properties of cement, sand, and coarse aggregate results are shown below:

Table 1: Physical Properties of Cement

Item	Specific Gravity	Normal Consistency (%)	Fineness Test (%)	Setting Time in Minutes		Soundness in mm
				Initial	Final	
Cement	4.4	35	6.49	147	470	2

Table 2: Physical Properties of Coarse Aggregate Used in M-20 & 40 Concrete

Sample	AIV %	LAAV %	WA %	Specific Gravity	ACV %
Silchar	17.8	49.8	1.5	2.54	20.25

Table 3: Physical Properties of Sand

Sl No	Source of the Sample	Specific Gravity	Fineness Modulus	Sand Zone	Silt & Clay (%)
I	River Sand				
1	Bagha	2.5	2.03	IV	3.55
2	Zatinga	2.7	2.64	IV	3.13
3	Langkaih	2.6	2.55	IV	4.14
4	Darlungkai	2.56	4.7	I	3.8
5	Sairang	2.56	4.14	I	3.83
6	Chhimtuipui	2.6	3.77	II	2.02
II	Crushed Sand				
1	Maubuang	2.57	3.19	I	28.72
2	Sakawrtuichhun	2.67	3.69	I	29.13

RESULTS AND DISCUSSIONS

COMPARISON BETWEEN CRUSHED SAND AND RIVER SAND IN MORTAR AND CONCRETE

The river sand has more compressive strength than crushed sand as shown in table 1.4. Compressive strength increases with an increase in the density of mortar and concrete. From the experimental results, it can be stated that crushed sand can be used as an alternative material for natural sand, (i.e. river sand).

Table 4: Compressive Strength of Mortar & Concrete

Sl No	Source of the samples	Silt & Clay %	Sand Zone	Compressive Strength of Mortar N/mm^2	Compressive Strength of Concrete N/mm^2
I	River Sand				
1	Bagha	3.55	Zone IV	15.6	24.3
2	Zatinga	3.13	Zone IV	28.1	27.85
3	Langkaih	4.14	Zone IV	20.3	19.12
4	Darlungkai	3.8	Zone I	27.6	21.19
5	Sairang	3.83	Zone I	18.6	21.63
II	**Crushed Sand**				
1	Maubuang	28.72	Zone I	18	20.07
2	Sakawrtuichhun	29.13	Zone I	11.22	23.85

Additional Requirement of Water on Mortar Depend on the Type of Sand

It has been observed that the quantity of water to be used on the mortar mix calculated based on Normal consistency value is fully fit for cohesion-less sand. But, it does not fit in on sand which has cohesiveness. The sand collected from different sources is having organic impurities as well as different silt and clay content. Due to this, some sand is cohesive and having binding properties. The quantity of water is calculated using the formula

$$\text{Water content required (ml)} = \left[\frac{P}{4} x \text{ Weight of Mix}\right]\% \qquad (1)$$

Where

P = Normal consistency

Water content based on P-value which is used to determine the water content for mortar cannot be applied to all types of sand. To resolve this problem, the optimum moisture content is calculated using the Proctor Compaction test to know the additional water required on particular cohesive sand as shown in table 1.5.

It is observed that the density and compressive strength of mortar is less if additional water is not added. Water content calculated using Normal consistency cannot be adopted for sand cohesiveness. Table 1.6 shows the density and compressive strength with and without additional water. The mortar with the correct amount of water has higher strength and density.

Table 5: Additional Requirement of Water on the Different Type of Sand

Sl No	Name of the Items	Normal Consistency (%)	Water Content Required (ml) = (P/4 +3)% x Weight of Mix	Sand Zone	OMC on Sand in %	New Water Content in ml
I	River Sand	Star Cement				
1	Bagha	34	92	IV	17.8	142
2	Zatinga		92	IV	14.6	117
3	Langkaih		92	IV	17.1	137
4	Darlungkai		92	I	14	112
5	Sairang		92	I	15.3	122
6	Chhimtuipui		92	II	16	128
II	Crushed Sand					
1	Maubuang		92	I	17.8	142
2	Sakawrtuichhun		92	I	17.8	142
3	Standard Sand		92	II	11.5	92

Table 1.6 Compressive strength and density of Mortar with and without additional water

Sl No	Name of the items	Silt & Clay %	With Additional Water		Without Additional Water	
			Compressive Strength of Mortar N/mm^2	Density (kg/m^3)	Compressive Strength of Mortar N/mm^2	Density (kg/m^3)
I	River Sand					
1	Bagha	3.55	**15.6**	2215.74	**11.61**	1895
2	Zatinga	3.13	**28.1**	2227.41	**9.45**	1903.8
3	Langkaih	4.14	**20.3**	2157.43	**16.37**	2027.7
4	Darlungkai	3.8	**27.6**	2332.36	**11.98**	1997.1
5	Chhimtuipui	2.02	**12.1**	2139.94	**8.1**	1924.2
6	Sairang	3.83	**18.6**	2169.1	**6.47**	1959.2
II	Crushed Sand					
1	Maubuang	28.72	**18**	2233.24	**11.13**	2020.4
2	Sakawrtuichhun	29.13	**11.22**	2157.43	**6.13**	1772.6

EFFECT OF SILT AND CLAY PRESENT ON THE COMPRESSIVE STRENGTH OF MORTAR AND CONCRETE

Silt and clay are fine aggregate particles smaller than the 75microns (No. 200) sieve. Usually, they are either silts or clayey silts and are difficult to remove from sand unless sieve or wash.

M-20 Cement Concrete (1:1.5:3, 0.5 w/c) and Mortar (1:3) were prepared with sand which was collected from different sources within Mizoram and Coarse aggregate (Sakawrtuichhun) to find out the effect of silt and clay on strength of concrete. It is found that the type of sand zone has less impact on compressive strength rather than the impact caused by the presence of silt and clay. As it is seen from Table 1.7, the presence of lesser silt and clay contributes to higher mortar and concrete strength.

Table 7: Percentage of Silt and Clay Present in a Different Source of Sand for Concrete M20

Sl No	Source of the sample	Specific Gravity	Fineness Modulus	Silt & Clay (%)	Sand Zone	Compressive Strength of Mortar (N/mm^2)	Compressive Strength of Concrete (N/mm2)
	River Sand						
1	Bagha	2.5	2.03	3.55	IV	15.6	24.3
2	Zatinga	2.7	2.64	3.13	IV	28.1	27.85
3	Langkaih	2.55	2.55	4.14	IV	20.3	19.12
4	Darlungkai	2.56	4.7	3.8	II	27.6	21.19
5	Sairang	2.56	4.14	3.83	I	18.6	21.63
	Crushed Sand						
1	Maubuang	2.57	3.19	28.72	I	12.1	20.07
2	Sakawrtuichhun	2.67	3.69	29.13	I	11.22	23.85

EFFECT OF REDUCTION OF SILT AND CLAY IN CONCRETE

It is observed that the reduction of silt and clay has a significant increase in the compressive strength of concrete. River sand of Langkaih and Sairang had been washed/cleaned with water which led to the reduction of the percentage of silt and clay to 85.5% (from 4.137% to 0.6%) and 59.79% (from 3.83% to 1.54%) respectively. The reduction of silt and clay has led to an increase in compressive strength of concrete by 45.3% and 27 % in Langkaih and Sairang respectively. At every one percent reduction in silt and clay, there are an increase of 2.45 N/mm^2 and 2.55 N/mm^2 for Langkaih and Sairang respectively

Table 8: Effect of Concrete Strength on the Reduction of Silt and Clay

SL. No	Source of the Sample	Compressive Strength (N/mm^2)	Silt & Clay %	Density (kg/m^3)
1	Langkaih	19.12	4.137	2325
	Langkaih (Wash)	27.78	0.6	2352
2	Sairang	21.63	3.83	2373
	Sairang (Wash)	27.48	1.54	2420

EFFECT OF SAND PARTICLE SIZE DISTRIBUTION ON STRENGTH OF MORTAR & CONCRETE

As it is seen from table 1.9, approximately 15-25% of Coarse Sand, 30-40% of Medium sand, 20-30 % of Fine Sand has contributed higher result on compressive strength. Fine Aggregate (sand) has been further classified into three categories as per IS 1498 (i) Course Sand 4.57-2.36 mm, (ii) Medium 2.36-0.15 mm, and (iii) Fine Sand 0.15-0.075 mm. Particle size distribution plays an important role in the compressive strength of mortar as well as concrete. Fine aggregate which is well distributed into three classifications of sand has given good results. We can say that less content of silt and clay and well distribution (good gradation) has resulted in good strength.

The particle distributes on approximately 33% on the three classifications of sand i.e Coarse, Medium, and Fine Sand respectively has given a better result.

Table 1.9 Particle Size Distribution of different sand

Sl. No	Name of the sample	Coarse Aggregate %	Fine Aggregate %			Silt & Clay %	Avg. Comp. strength of Mortar(N/mm^2)	Avg. Comp. strength of Concrete(N/mm^2)
			Coarse	Medium	Fine			
I	**River Sand**							
1	Bagha	0.46	0.26	12.80	83.93	3.55	15.6	24.30
2	Zatinga Balu	0.90	0.57	62.29	33.86	3.13	28.10	27.85
3	Langkaih	2.80	1.80	53.20	38.06	4.14	20.30	19.12
4	Darlungkai	22.00	16.60	50.80	7.60	3.80	27.60	21.19
5	Sairang No 1	12.39	7.85	48.62	28.03	3.10	18.60	21.63
II	**Crushed Sand**							
1	Maubuang	2.57	24.59	30.31	13.81	28.72	12.10	20.07
2	Sakawrtuichhun	0.44	15.14	56.07	17.93	29.13	11.22	23.85

EFFECT OF THE PRESENCE OF AGGREGATE DUST IN CONCRETE STRENGTH

It has been decided to check the effect of aggregate cover with dust in the compressive strength of concrete. The sand used in this M40 mix is in Zone II (IS 383), clean and cohesion-less. Table 1.11 has shown that dust-coated aggregate concrete has given less compressive strength and density.

When the dust coating aggregate present in the concrete, dust prevents aggregate to mix with cement as it coats aggregate. The bonding is weakened by non-binding material like silt and clay which reduce the concrete compressive strength. Test results show a decrease in compressive strength when the ratio of silt content to fine aggregate increases.

Table 1.10 Physical Properties of Fine Aggregate (Sand) Used in M-40 Concrete

Source of the sample	Specific Gravity	Fineness Modulus	Sand Zone	Silt & Clay Content (%)
Meghalaya	2.62	3.22	II	0.2

Table 11: Compressive Strength Test of M-40

Sl. No	Name of the Sample	Name of Sample	Compressive Strength (N/mm^2)	Average Strength (N/mm^2)	Density (kg/m^3)
1	Concrete Cube with dust-coated Aggregate	S1	35	33.7	2343.7
		S2	31		2347.26
		S3	38		2330.07
		S4	32.5		2311.11
		S5	32		2340.74
2	Concrete Cube without dust-coated Aggregate	S1	44.4	45.66	2417.78
		S2	44.4		2400
		S3	46.5		2370.37
		S4	46		2429.63
		S5	47		2340.74

STATISTICAL EQUATION USING REGRESSION ANALYSIS

The regression equation was generated to predict the compressive strength of mortar and concrete with varying levels of silt and clay contents, fineness modulus, and specific gravity in mortar and concrete respectively.

Compressive Strength of Concrete:

$$= 50.5 + (1.6*SG) - (0.28*FM) - (8.38*SC)\ (R^2 = 0.99) \qquad (2)$$

Compressive Strength of Mortar:

$$= -135 + (58.03*SG) + (1.96*FM) + (0.48*SC)\ (R^2 = 0.76) \qquad (3)$$

Where,

SG = Specific Gravity

SC = Silt and Clay

FM = Fineness Modulus

It cannot be ignored since the presence of silt and clay significantly affect the compressive strength of mortar and concrete, hence the need to ensure sand free from silt and clay is vital.

CONCLUSIONS

It is observed that the compressive strength is less when the silt content is high. The presence of silt and clay in the sand is not the only factor that affects the mortar/concrete strength. Other factors may be workability, particle shapes, organic impurities, and texture. It has been found that the crushed sand required more water than the river sand as the surface area of crushed sand is more. Additional water is required for mortar in which sand possesses cohesiveness and binding properties. Concrete cube without dust-coated has higher density and compressive strength as dust provides weak bonding. At every one (1%) percent reduction in silt and clay, there are an increase of 2.45 N/mm^2 and 2.55 N/mm^2 for Langkaih and Sairang respectively.

REFERENCES

Anosike, N.M. (2011). Parameters for Good Site Concrete Production Management Practice in Nigeria. Ph.D. Thesis, Department of Building Technology, College of Science & Technology, Covenant University, Ota.

Ayodeji, O. (2011). An Examination of the Causes and Effects of Building Collapse in Nigeria. Journal of Design and Built Environment. 9: 37-47.

Ayuba, P., Olagunju, R. and Akande, O. (2011) Failure and Collapse of Buildings in Nigeria: Roles of Professionals and Other Participants in the Building Industry. Interdisciplinary Journal of Contemporary Research in Business. 4: pp.1267-1272.

ASTM C40 (2004). Standard Test Method for Organic Impurities in Fine Aggregates for Concrete. ASTM International, West Conshohocken.

ASTM C117 (1995). Standard Test Method for Materials Finer than 75-um (No.200) Sieve in Mineral Aggregates by Washing. American Society for Testing Materials, West Conshohocken.

Construction Standard CS3 (2013). Aggregates for Concrete, Technology, Ed., the Government of the Hong Kong Special Administrative Region, Hong Kong.

Dahiru, D., Salau, S. and Usman, J. (2014) A Study of Underpinning Methods Used in the Construction Industry. International Journal of Engineering and Science (IJES). 3: pp.05-13.

Dimuna, K.O. (2010). Incessant Incidents of Building Collapse in Nigeria: A Challenge to Stakeholders. Global Journal of Researches in Engineering. 10(4): pp.75-84.

Ganesh V. Tapkire, Vikram J. Patel, Hemraj R. Kumavat, and Rajendra D. Patil (2017). Comparative Analysis of River & Crushed Sand in Concrete. International Journal of Innovative Research in Science, Engineering and Technology, 6(3): pp. 3525-3529.

Harrison, D.J., and Bloodworth, A.J. (1994). Construction Materials, Industrial Minerals Laboratory Manual. Technical Report WG/94/12, Nottingham.

Hyginus E. Opara, Uchechi G. Eziefula, and Bennett I. Eziefula (2018). Comparison of physical and mechanical properties of river sand concrete with quarry dust concrete. SSP - Journal of Civil Engineering Special Issue. pp.124-134

IS 383 (1970). Specification of Coarse and Fine Aggregates from Natural Sources for Concrete. Bureau of Indian Standards, India.

Machuki, O.V. (2012) Causes of Collapse of Buildings in Mombasa County. A Case of Mombasa City—Kenya.

Manjunath S, Mahadeva M, and Sunandha M R (2018). Comparative Study of Compressive Strength of Mortar Cubes Using River Sand and M Sand. International Journal of Engineering Science & Research. 7: pp.1050-1059

Ngugi, H.N., Mutuku, R.N., and Gariy, Z.A. (2014). Effects of Sand Quality on Compressive Strength of Concrete: A Case of Nairobi County and Its Environs, Kenya. Open Journal of Civil Engineering. 4:pp. 255-273.

Oloyede, S., Omoogun, C., and Akinjare, O. (2010). Tackling Causes of Frequent Building Collapse in Nigeria. Journal of Sustainable Development. 3(3): pp. 127-132.

Syed Yaqub, Abbas Vikas Srivastava, and V.C.Agarwal (2015). Effect of Crushed sand On Compressive Strength of Concrete an Experimental Investigation. International Journal of Engineering Science & Research, Abbas. 4(2): pp.538-543

Yalley P P, Sam A. Effect of Sand Fines and Water/Cement Ratio on Concrete Properties. Civil Eng Res J. 2018; 4(3): 555636.

Science and Technology Journal Vol. 8 Issue 2 July 2020 ISSN: 2321-3388

Experimental Study of Bond Strength between Existing Roof Slab and Concrete Support of Flat Roof Mounted Solar Arrays

Ashish Agarwal[1] and Hassan Irtaza[2]
[1] Research Scholar, Department of Civil Engineering, Z.H.C.E.T., A.M.U., Aligarh–202002, India
[2]Professor, Department of Civil Engineering, Z.H.C.E.T., A.M.U., Aligarh–202002, India

Abstract—Rooftop mounted solar array systems are connected to the existing concrete roof using casting concrete blocks over the existing concrete roof surface or by using precast concrete blocks. Since fixing the mounting system directly on the roof surface using a bolted connection is not advisable since it can affect roof strength, concrete blocks, either precast or cast in situ, are desirable to support the mounting system. To better understand the bonding mechanism at the interface between old and new concrete surfaces, overlaid specimens were fabricated to measure the various bond strengths. Three different bonding methods, which include cement slurry, casting over existing concrete, and epoxy, were used. The tests performed found that epoxy bonding provides better bond strength for new and existing concrete. To withstand wind loads, the foundation of the solar system should resist horizontal drag and vertical lift forces safely. Self-weight of supporting concrete blocks significantly reduces drag and lift forces coming over the solar system due to wind loads. The bonding strength between the existing concrete roof surface and array supporting concrete blocks also plays a vital role in resisting drag and lift forces. Since the weight of concrete blocks cannot exceed the design load for the roof, drag and lift forces can be resisted by increasing bond strength either by increasing the surface area of blocks (which would increase weight thus may defy purpose) or by using a superior bonding agent.

Keywords: Flat roof, Rooftop Solar, Bond Strength, Split Tensile Test, Slant Shear Test.

INTRODUCTION

With the technological advancement in the last two decades of the 21st century, the cost per watt installation of solar panels has reduced drastically. Both developed and developing countries are shifting towards solar energy at a rapid pace. Solar energy installation has overtaken other new installations of renewable and non-renewable energy generation units in China and India.

India has aimed to reach 100 GW solar installed capacity by 2022 and further raised the target to achieve 450 GW of total renewable installed capacity by 2030. Under National Solar Mission, India has aimed to reach 40 GW installed rooftop solar by 2022. The ambitious aim to achieve 40 GW rooftop solar can be done by installing solar arrays over unused rooftops of commercial, residential, and government buildings.As of 31 October 2020, the total installed capacity of solar energy in India reached 36.3 GW, out of which 6 GW is of rooftop solar.

This target would incur high capital resources, and any flaw in the solar system at a large scale would lead to a considerable investment at stake. Solar arrays are vulnerable to wind-induced loads, and many past incidents showed damages to rooftop solar arrays ona large scale. Drag and uplift forces induced due to high winds over rooftop solar arrays can damage the array system and foundation over the roof surface.

Rooftop mounted solar array systems are connected to the existing concrete roof using casting concrete blocks over the existing concrete roof surface or using precast concrete blocks. Fixing the array mounting system directly on the roof surface using the bolted connection is not advisable as it can affect roof strength; concrete blocks, either precast or cast in situ, are desirable to support the mounting system.

(a)

(b)

Fig. 1: Cast in-situ Concrete Block Foundation for Rooftop Solar Array Installed in Department of Civil Engineering

To withstand wind loads, the foundation of the solar system should resist horizontal drag and vertical lift forces safely. Self-weight of supporting concrete blocks significantly reduces drag and lift forces coming over the solar system due to wind loads. The bonding strength between the existing concrete roof surface and array supporting concrete blocks also plays an important role in resisting drag and lift forces. Since the weight of concrete blocks cannot exceed the roof's design load, drag and lift forces can be resisted by increasing bond strength either by increasing the surface area of blocks (which would increase weight thus may defy purpose) or using a superior bonding agent.

To determine the bond strength of new concrete over the existing concrete, guidelines for casting specimen are provided by ASTM C496-96 and ASTMC882-99for split tensile test and slant shear test, respectively. Very few past researches are available to determine the bond strength of concrete over existing concrete. Julio et al. (Julio et al. 2003) and Casal (Casal 1960) reported that different factors affect the bond strength and integrity, such as bonding agents, surface roughness, pre-wetting conditions, and micro-cracks on the substrate surface, etc. Branco et al. (Branco et al. 2005)showed that the mechanism of shear stresses transfer between two concrete layers is complex and influenced by the pre-wetting, surface roughness, reinforcement crossing the interface, the compressive strength of the weaker concrete, the presence of cracking or the stress caused by normal forces across the interface and differential shrinkage of the layers. Consequently, Cleland and Long (Cleland and Long 1997) concluded that the principal function of a bonding agent is to develop a bonding bridge between the repairing material and the concrete substrate. Talbot et al. (Talbot et al. 1994)have stated that usinga bonding agent reduces the variability of bond strength results.

(a)

(b)

Fig. 2: Damage of Rooftop Solar Array by High Wind

Tayeh *et al.* (Tayeh *et al.* 2013) experimentally evaluated the bond strength in spilt tensile and slant shear tests for the bond between normal concrete and high-performance fibre concrete using cast in situ bonding. Variation of bond strength was observed based on finishing of bonded surface and varied by the sandblasting, wire brush, groves, and drill holes. Bond strength in split tensile was found within the range of 1.6 MPa to 3.0 MPa, whereas bond strength in slant shear varied within the range of 7.5 MPa to 20 MPa. Bond strength in the split tensile test was compared with Sprinkel et al. (Springk el et al. 2000) based on bond quality parameters.

In our study, we have considered three different bonding methods between concrete surfaces. The method includes casting concrete over existing concrete, cement slurry as a bonding agent, and using epoxy as a bonding agent between concrete surfaces. M20 grade concrete was used for experiments, and the design mix was obtained by determining the properties of cement, sand, and aggregates used. Cement and sand were used in a proportion of 1:3 for preparing cement slurry. Whereas Epoxy Bonding Agent 211 was used, having a 1-part base and 1-part hardener. To ensure the strength of bonding against drag and lift wind forces, three different tests were performed using 6 specimens for each bonding method. Test performed were namely Slant Shear Test, Split Tensile Test, and Horizontal Shear Test.

For the split tensile test, specimens were cast in the form of semi-cylinders of diameter 75mm and 150mm height as per ASTM guidelines. Similarly, inclined cylinders at a slope of 30°, 10 mm below the base, were cast. These cylinders were bonded using three aforesaid methods and subjected to the slant shear test.

For the horizontal shear test, each 6 cubes of dimension 150mmx 150mm x 150mm were bonded over the existing concrete surface by directly casting the cube over the existing concrete rough surface, by using cement slurry, and by using epoxy as a bonding agent. A hydraulic jack with a dial gauge to determine the force was used to apply horizontal load over concrete cubes. Horizontal load uniformly provided over cubes using a steel plate to evenly spread load applied by a hydraulic jack.

MATERIALS USED AND EXPERIMENTAL SETUP

GENERAL

The experimental study consisted of the following:

a. Development specimens for split cylinder test, slant shear test, and horizontal shear test

b. Evaluate the bond strength performance of three bonding mechanisms for concrete specimens by split cylinder test, slant shear test, and horizontal shear test.

c. Studying the correlation between the bond strength values obtained from the split cylinder test, slant shear test, and horizontal shear test.

MATERIALS USED

The cement used was Ordinary Portland cement conforming to IS 1489, and the fine aggregate of zone II grading as per IS 383. Coarse aggregate used was graded crushed granite aggregate of maximum 12.50 mm size (IS 383-1970). The bonding methods used for the study were as follows:

a. Cement Slurry of flowable consistency

b. Cast over existing concrete

c. Epoxy bonding mix (base : hardener parts by weight 100 :100)

OPC43 grade Cement and standard sand were used in a proportion of 1:3 for preparing cement slurry. The water-cement ratio considered was 0.45 in the cement slurry. 40% normal consistency and 45 minutes initial setting time were observed by tests performed for OPC cement used.

The viscous epoxy mix density is 1120 kg/m^3, with a grey color, and the application life at room temperature is 30 to 40 minutes. Specimen were bonded using epoxy within the application life of epoxy mix and cured for 7 days before testing.

Design mix of M20 grade concrete with 0.46 water-cement ratio was determined based on engineering properties of materials used. The design mix ratio of M20 grade concrete calculated was 1-part OPC 43 grade cement, 2.05-part fine aggregate (Standard coarse sand), and 3.3-part coarse aggregate (40% 10mm and 60% 20mm).

Table 1: Test Performed to Determine the Bond Strength

S. No.	Test	Bonding Type	No. of Specimens
1	Split Tensile Test	No Bonding Agent	6
		Cement Slurry	6
		Epoxy	6
2	Slant shear Test	No Bonding Agent	6
		Cement Slurry	6
		Epoxy	6
3	Horizontal Shear Test	No Bonding Agent	6
		Cement Slurry	6
		Epoxy	6

**No Bonding Agent, i.e., Concrete cast over existing concrete.

Fig. 3: Epoxy Base and Hardener Used (in Containers) and 1:1 Epoxy Paste (in Pan)

RESULTS & DISCUSSIONS

Split Tensile Test

Specimens were cast, and the slant shear test was performed as per guidelines specified by ASTM C496 (1996). The dimensions of the specimen required for the split tensile test are shown in Figure 4.The surface is of the bonding plane to determine the split tensile stress at failure was 112.5cm^2.

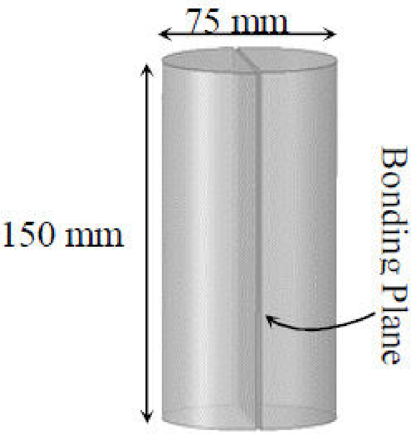

Fig. 4: Test Specimen Dimensions for Split Tensile Test

For each bond method, i.e., by directly casting a cube over the existing concrete rough surface, using cement slurry, and using epoxy as the bonding agent, 6 Specimens were cast and bonded. Each specimen was subjected to normal load using a hydraulic load machine shown in Figure 5. The load provided continuously and without shock, at a constant rate within the range of 50 to 100 kN per minute, splitting tensile stress until failure of the specimen as per ASTMC496 (1996) section 7.5. The ultimate load at failure of the bonding plane was observed during the test, and the bond strength for split tensile is calculated by following relation provided by ASTM C496 (1996).

$$T = 2P / \pi ld$$

Where,

T = Split tensile strength (MPa)

P = Maximum applied load indicated by the testing machine (N)

l = length of specimen (mm)

d = diameter of specimen (mm)

The split tensile strength of each specimen for different bonding methodsis given in Table 3. Figure 6 shows the specimen placed in the apparatus and subject to initial load before splitting. Figure 7 represents the splitting of the specimen after application load up to bond failure. Specimens after splitting are shown in Figure 8. Bond strength in split tension are compared with bond quality parameters provided by Springkel et al. (Springkel et al. 2000) as shown in table below.

Table 2: Bond Quality Parameter by Springkel *et al*

Bond Quality	Bond Strength (MPa)
Excellent	>2.1
Very Good	1.7 - 2.1
Good	1.4 - 1.7
Fair	0.7 - 1.4
Poor	0 - 0.7

Table. 3: Bond Strength from Split Tensile Test

S. No.	Bonding Method					
	Cement Slurry		Cast *in-situ*		Epoxy Layer	
	Load (kN)	Stress (MPa)	Load (kN)	Stress (MPa)	Load (kN)	Stress (MPa)
1	9	0.51 (Poor)	25	1.41 (Good)	38	2.15 (Excellent)
2	9	0.51 (Poor)	25	1.41 (Good)	40	2.26 (Excellent)
3	10	0.57 (Poor)	25	1.41 (Good)	40	2.26 (Excellent)
4	12	0.68 (Poor)	26	1.47 (Good)	44	2.49 (Excellent)
5	12	0.68 (Poor)	28	1.58 (Good)	45	2.55 (Excellent)
6	12	0.68 (Poor)	28	1.58 (Good)	46	2.60 (Excellent)

Fig. 5: Specimen for Split Tensile Test Placed in Apparatus

Fig. 6: Specimen for Split Tensile Test Placed

Fig. 7: Split Specimen Along a Bonded Plane at Ultimate Load in the Split Tensile Test

Fig. 8: Split Specimens Along Bonding Plane, Cement Slurry as the Bonding Agent

SLANT SHEAR TEST

Slant shear test was performed,and specimens were cast as specified by ASTM C882(1999) guideline, as shown in Figure 9.

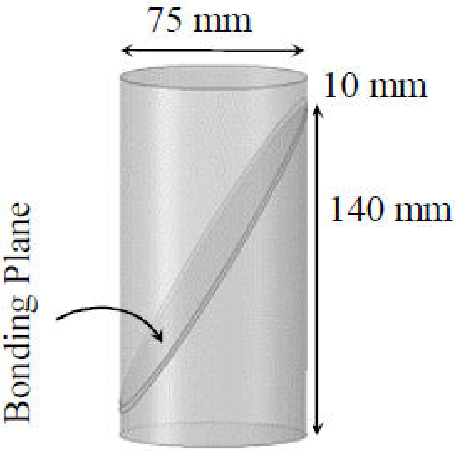

Fig. 9: Test Specimen Dimensions for Slant Shear Test

The surface area of the elliptical bonding plane to determine the shear stress at failure was 88cm^2. For each bond method, i.e.,by directly casting a cube over an existing concrete rough surface, by using cement slurry, and by using epoxy as the bonding agent, 6 Specimens were cast and bonded. Each specimen was subjected to normal load using a hydraulic load machine shown in Figure 10. The loading provided at a constant rate within the range of 50 to 100 kN per minute until failure of the specimen.The ultimate load at failure of bonding plane observed during test and bond strength (stress at failure) in slant shear strength has been calculated using the following relation.

S = P/As

Where, S = Slant shear strength (MPa), P = Load at failure (N), As = Bonded surface area (mm^2). Slant shear strength calculated of each specimen for different bonding methods are given in Table 4.Figure 11 shows the specimen placed in the apparatus and subject to initial load before splitting. Figure 12 represents the splitting of the specimen after application load up to bond failure.

Table 4: Bond Strength from Slant Shear Test

S. No.	Bonding Method					
	Cement Slurry		Cast *in-situ*		Epoxy Layer	
	Load (kN)	Stress (MPa)	Load (kN)	Stress (MPa)	Load (kN)	Stress (MPa)
1	15	1.7	40	4.55	65	7.39
2	20	2.27	40	4.55	70	7.95
3	20	2.27	45	5.11	70	7.95
4	25	2.84	45	5.11	75	8.52
5	30	3.41	50	5.68	80	9.09
6	35	3.98	50	5.68	85	9.66

Fig 10: Specimen for Slant Shear Test Placed in Apparatus

Fig. 11: Specimen for Slant Shear Test Placed

Fig. 12: Split Specimen along a Bonded Plane at Ultimate Load in Slant Shear Test

HORIZONTAL SHEAR TEST

6 cubes of dimension 150 mm x 150 mm x 150 mm were bonded on the existing concrete surface using three different bonding methods.Hydraulic jack with dial gauge was used to determine the applied force at the failure of the bonded plane by applying horizontal force over concrete cubes, as shown in Figure 13. Horizontal load uniformly provided over cubes using a steel plate to evenly spread load applied by a hydraulic jack.

Cubes bonded on the existing concrete surface, bonded with different bonding methods, and are shown in Figures 14 to 17.Detached cube after application load up to bond failureis shown in Figure 18.

Fig. 13: Specimen for Horizontal Shear Test Bonded on the Existing Concrete Floor, with Hydraulic Jack for Load Application

Table 5: Bond Strength from Horizontal Shear Test

S. No.	Bonding Method					
	Cement Slurry		Cast *in-situ*		Epoxy Layer	
	Load (kN)	Stress (MPa)	Load (kN)	Stress (MPa)	Load (kN)	Stress (MPa)
1	5	0.22	4.5	0.2	9.5	0.42
2	5	0.22	5	0.22	10	0.44
3	5	0.22	5	0.22	10	0.44
4	5	0.22	5	0.22	10.5	0.47
5	5.5	0.24	5.5	0.24	11.5	0.51
6	6	0.27	5.5	0.24	12	0.53

Fig. 14: Six Specimens for Horizontal Shear Test Bonded over an Existing Rough Concrete Floor, Bonded using Cement Slurry with Hydraulic Jack Assembly also Seen, Used for the application of Horizontal Load

Fig. 15: Six Specimens for Horizontal Shear Test Bonded over an Existing Rough Concrete Floor, Bonded using Epoxy

Variation of stress at failure under split tensile test, slant shear test, and horizontal shear tests are shown in Figures 19 to 21. Each graph represents the stress at failure for all three types of bonding methods used.

Fig. 16: Six Concrete Cubes case *in-situ* over Concrete Floor to Perform Horizontal Shear Test

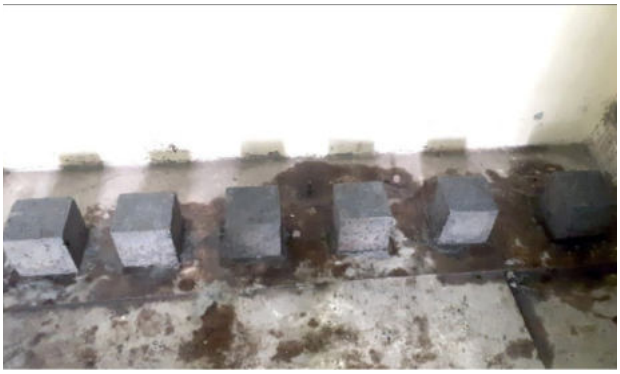

Fig. 17: Six Specimens for Horizontal Shear Test Bonded over an Existing Rough Concrete Floor, Cast-*in-situ* after 28 Days Curing

Fig. 18: Failure of the Bonded Plane in Horizontal Shear Test at Ultimate Load, for the case of Epoxy-Bonded Plane

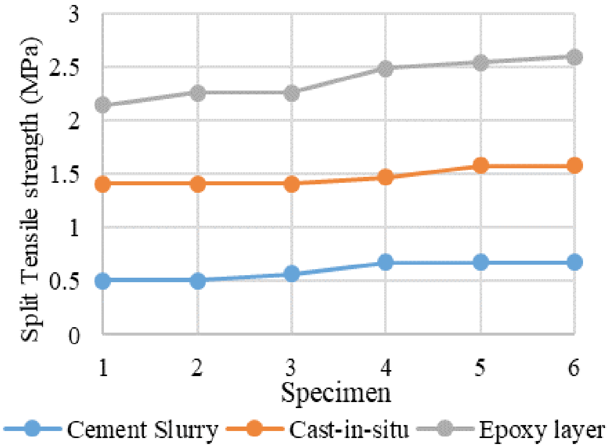

Fig. 19: Variation of Bond Stress in Split Tensile Test for Different Bonding Methods

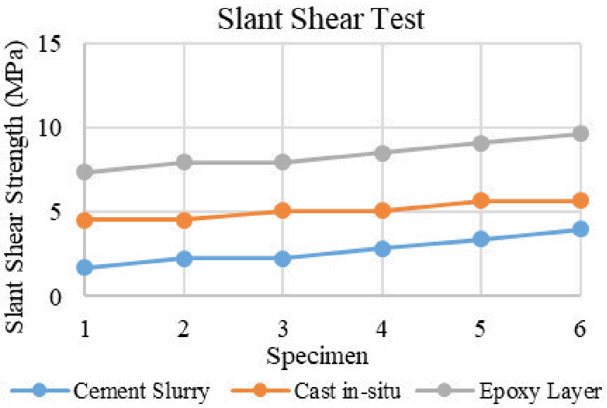

Fig. 20: Variation of Bond Stress in Split Shear Test for Different Bonding Methods

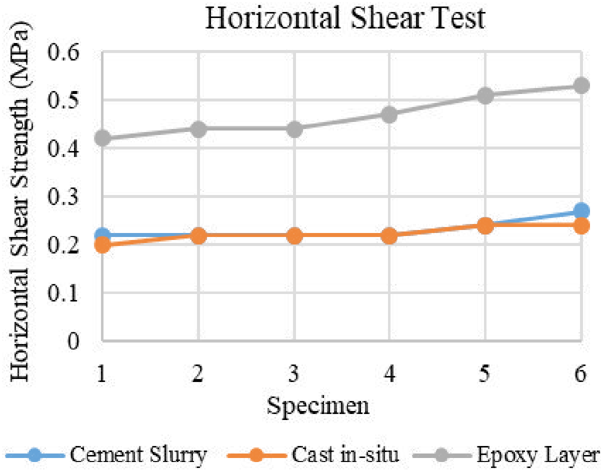

Fig. 21: Variation of Bond Stress in Horizontal Shear Test for Different Bonding Methods

CONCLUSION

- It is clearly seen that the Epoxy bond provides maximum resistance in all Split Tensile, Split Shear, and Horizontal Shear, whereas Cement slurry and cast in situ concrete shows similar resistance for each case.
- Since the weight of concrete blocks should not exceed, the design load for roof, drag, and lift forces can be resisted by increasing bond strength either by increasing the surface area of blocks or using a superior bonding agent.
- From our experimental study, epoxy bonding provides better strength to resist lift and drag forces.
- It is also advisable to place the concrete blocks supporting solar mounting systems over the existing walls or beams provided below the roof since the additional self-weight of concrete blocks and comparatively higher wind-induced loads transferred from solar arrays to the roof surface may damage and could lead to failure of the roof slab.

ACKNOWLEDGMENT

The authors wish to express their gratitude for the financial support received from the Ministry of New & Renewable Energy, Govt. of India sponsored project, and Senior Research Fellowship (09/112(0628)2K19 EMR-I) awarded to the corresponding author by the Council of Scientific and Industrial Research (CSIR) under Ministry of Human Resources Development, Govt. of India.

REFERENCES

ASTM-C496 (1996) Splitting Tensile Strength of Cylindrical Concrete Specimens.

ASTM-C822 (1999) Standard Test Method for Bond Strength of Epoxy-Resin System Used With Concrete by Slant Shear.

Branco FAB, Silva VD, and JúlioES (2005) Concrete-to-concrete bond strength: influence of an epoxy-based bonding agent on a roughened substrate surface. Magazine of Concrete Research, 57(8): 463-468.

Casal BB(1960) Connections Between Concrete Layers with Different Ages. Universidade Tecnica de Lisboa, Portugal, 1-10.

Cleland DJ and LongAE (1997) The pull-off test for concrete patch repairs. Proceedings of the Institution of Civil Engineers - Structures and Buildings. 122: 451-460.

JúlioES, Branco F, and Silva VD(2003) Structural rehabilitation of columns with reinforced concrete jacketing. Progress in Structural Engineering and Materials, 5(1):29-37.

Monthly Report on Installed Capacity, October 2020. Central Electricity Authority, India. (Accessed on: 20.11.2020)

Springkel MM, and Ozyildirim C (2000) Evaluation of high performance concrete overlays placed onRoute 60 over Lynnhaven Inlet in Virginia.

Talbot C, Pigeon M, Beaupre D and Morgan DR(1994) Influence of surface preparation on long-term bonding of shotcrete. ACI Materials Journal, 91(6): 560-566.

Tayeh BA, AbuBakar BH, Johari MAMAnd Voo YL (2013)Evaluation of Bond Strength between Normal Concrete Substrate and UltraHigh Performance Fiber Concrete as a Repair Material. Procedia Engineering 54:554-563.

The roadmap to 40 GW rooftop solar. PV Magazine India, 27 September 2019.

Science and Technology Journal Vol. 8 Issue 2 July 2020 ISSN: 2321-3388

Improved Cuckoo Search Algorithm for Future Selection

T. Mathi Murugan*[1] and E. Baburaj[2]
[1]Research Scholar, Faculty of Computer science and Engineering,
Sathyabama Institute of Science and Technology, Chennai, India
[2]Professor, Department of Computer Science Engineering,
Marian Engineering College, Trivandrum, Kerala, India
E-mail: *[1]mnamashivayam11@gmail.com, [2]alanchybabu@gmail.com

Abstract—The classification of high-dimensional dataset is challenging as it contains large amount irrelevant and noisy features. Thus, feature selection is performed in the dataset to eliminate these redundant features. It reduces the dimensionality of the dataset and increases the classification accuracy. Hence, for selecting the relevant features in high dimensional data, an improved cuckoo search algorithm (ICSA) was proposed in this paper. After feature selection, the dataset undergo classification using KNN classifier and SVM classifier. The experimental process illustrates that the improved cuckoo search algorithm effectively increases the classification accuracy by reducing the number of features in the dataset. For analysing the proposed algorithm, seven UCI repository dataset have been utilised. Also, the ICS algorithm is compared with other existing algorithms for the given dataset. From the investigation process, it was concluded that the proposed algorithm selects lesser number of features and also enhances the classification accuracy than the other existing algorithms.

Keywords: Feature selection, Improved Cuckoo Search Algorithm, KNN classifier, SVM classifier

INTRODUCTION

The advancements in the remote sensing technology have led to the growth of huge volume of data with respect to dimensionality and sample size. To automatically collect information and recognise patterns from these data machine learning algorithms are widely utilised [31]. It extracts the knowledge from the data for characterising new samples and classifies them into classes which are already specified by the domain of the problem. However, improving the learning capacity of machine learning algorithm was more complex for data containing large number of features. This is due to the existence of redundant and irrelevant features in dataset, which complicates the learning algorithm and reduce the efficiency of the algorithm [1]. Thus, it is necessary to eliminate the irrelevant features from the dataset for effective learning process. Hence, feature selection techniques are extensively utilised in the field of remote sensing for minimising the irrelevant features existent in the data [25].

Feature selection is the fundamental process in data mining and pattern recognition applications, specifically for high dimensional datasets. It minimises the dimensionality of the data and makes the learning process more efficient by consuming lesser time for learning the data. It is a commonly employed phase in machine learning for handling high dimensional data which increases the speed of the learning process by reducing the amount of features in dataset [10, 5]. It also eliminates the redundant or irrelevant features existent in the data and minimises the dimensionality of data for an effective classification process [7, 11]. Hence, it is more appropriate for datasets having features which vary in their relevance. Generally, feature selection algorithms focuses on selecting the best subset of features to reduce computational time and improve accuracy [8]. Thus, it helps in detecting the necessary features from the dataset and also improves the predictor performance. It also finds the most reliable subset of features which leads to the appropriate recognition rates for the classifiers.

Several approaches are employed for feature selection which is categorized into filter method and wrapper method. Here, the filter method is utilised for filtering the insignificant features which contains lesser options during data analysis. It does not employ any learning algorithms for evaluating the features. The filter methods select the subset with larger number of features or even select all the features in the dataset thus a suitable threshold is necessary for choosing the subset. The selected features from the filter method are analysed based on data characteristics like information measures, correlation, consistency and distance in the feature space. The wrapper method utilises predictive accuracy of a pre-determined learning algorithms for determining the quality of selected features. Generally, optimization algorithms are employed as learning algorithms in wrapper methods. Wrapper methods are widely utilised for feature selection process because filter methods have low classification accuracy than wrapper methods [3].

The meta-heuristic optimization algorithms are extensively employed for feature selection as these algorithms achieve better solutions by applying the information obtained from previous iterations [32].The development of nature inspired algorithm lies in the point that it takes its sole inspiration from nature. These inspirations experienced from nature possess the capability to define and resolve complex tasks with intrinsically effective initial aspects and procedures with small or no awareness about the search space. Numerous optimization algorithms are developed from the behaviour of some animals or insects in nature namely ant colonies, bees swarm, and so on. This was because the biological activities of birds and animals were responsible for specific roles both individually and as a group, to achieve a specific task in their daily routine or lifetime. As a result, they have attracted the attention of data analysts to resolve numerous difficulties in science and engineering sector.

Meta-heuristics were the emerging approach discovered through the inspiration of biological behaviour of birds or insects or animals and usually referred as bio-inspired algorithms. For example, Ant Colony Optimization (ACO) mimics the food searching behaviour of ant colonies [4], Artificial Bee Colony algorithm was instigated from the cooperative behaviour of bee colonies [6], Grey Wolf Optimizer (GWO) was emulated from the hunting skill and social leadership of grey wolves [26, 22, 23], the Krill Herd technique simulates the mating behaviour of firefly insects [16, 12], Particle Swarm Optimization (PSO) mimics the biological activities like bird flocking and fish schooling[2], Whale Optimization Algorithm (WOA) imitates the actions of humpback whales [27], Social Spider Optimization Algorithm inspired from the nature of spiders [24], Lion Optimization Algorithm simulates the co-operation characteristics and activities of lions [28] and so on. In mathematical designing, meta-heuristics are defined as a system that obtains solution to any kind of optimization challenges. Furthermore, these algorithms are applied in different fields like data mining, machine learning and engineering design problems.

For resolving optimization problems, ameta-heuristic algorithm was developed by Yang and Deb [13] which was known as cuckoo search algorithm. It was the newly developed and most assuring evolutionary algorithm [21, 18] stimulated from the reproduction and breeding tactic of cuckoo birds. The CS algorithm mimics the parasitic characteristics of cuckoos which lay their eggs in the nest of another bird. It utilises the Lévy flights random walk technique for exploring search area. The standard features of Lévy flights were similar to the flight behaviour of many animals [9]. The CS algorithm is most efficient for solving global optimization problems due to its capability of maintaining balance among global and local random walk by interchanging parameters. Many studies were conducted for analysing the algorithmic concept of cuckoo search contrary to other meta-heuristic algorithms like Genetic Algorithm, Particle Swarm Optimisation and Artificial Bee Colony algorithm. It is proven that the CSA has obtained better results than the other well-known meta-heuristic algorithms like genetic algorithms, particle swarm optimization and artificial bee colony algorithm. Hence, CSA have been utilised in many engineering applications such as optimising the semantic wed service composition processes [17], for training spiking neural models [14] and for training neural networks [15].

Generally, feature selection process finds the most reliable subset of features which leads to the appropriate recognition rates for the classifiers. The nature inspired algorithms utilises the information obtained while navigating the search process and thus it was taken as problem independent. For feature selection, some nature inspired algorithms like PSO and ACO were paired with rough sets and their functioning was analysed [29]. Still, these algorithms have some limitations such as premature convergence, high space complexity, slow convergence rate and consumes more time. For overcoming these limitations and for increasing the efficiency, improved cuckoo search algorithm is proposed for feature selection process. In CSA, the parameters are generally kept as constant which leads to the decrease in efficiency of the algorithm. In the proposed method, the cuckoo search parameters are properly tuned. Thus, it enhances the accuracy and convergence rate during classification. Therefore, proposed algorithm can be effectively utilised in many optimization problems.

CUCKOO SEARCH ALGORITHM

All kind of bird species follow same tactic to become maternal, that is every bird lay eggs and no one gives birth. Birds rapidly reproduce and lay an egg protected in an outer shell which is later hatched with external body. As the egg is protein-rich and high nutritional, birds must invent a secret location to hide it from its predators. However, finding the best place for security is challenging until the birds hatch and the young born become independent. For this reason, birds are naturally artistic that uses intricate designs as well as complex engineering for building the nests. That is, there is nothing in the animal kingdom that matches the diversity of nest architecture. Some birds build quarantined, unobtrusive nests, hidden inside trees to avoid the sight of predators. On the other hand, there are certain types of birds that are not concerned about the nest spinning and parenting, and be cunning to raise their young ones. These are "brood parasite" birds which may not spin their own nests and as an alternative, they lay the eggs in other bird's nest of same or different species and let them take care of its little ones.

The cuckoo is one of the brood parasite birds, which is proficient in cruel deception. Generally, the cuckoos have a unique reproductive process which was more aggressive than the other species of birds. Some cuckoo birds lay the eggs in another bird's nest and they sometimes removes the eggs of host birds from the nest for increasing the probability of hatching of its own eggs [20]. These parasitic cuckoos were good at finding the nests where the eggs are just laid and also they have good timing of laying eggs. Therefore, this entire tactic is performed just within ten seconds. Cuckoo parasitizes the shelter of huge variety of bird species and intelligently imitates the pattern as well as colour of their eggs to exactly match with host eggs. All the female cuckoos are specialized in one particular host species for brood parasites. Nevertheless, the ability of cuckoos to produce eggs similar to the eggs of host birds is one of nature's mysteries. Sometimes the host birds identify the foreign cuckoos which are lying in their nests. If that happens, they get rid of the cuckoo eggs or build their nest in some other place and moves there. Usually, the eggs laid by the cuckoos hatch earlier than the eggs of the host birds. After hatching, this newly born cuckoo pushes away the eggs of the host birds which were not hatched. This will reduce the probability of original eggs from hatching. Also, these cuckoos mimic the call of host off-springs for getting more food from the host birds. Moreover, the cuckoos continue to upgrade its mimicking skills though the hosts try to identify the parasite eggs. This fight between the cuckoo and the host is like an arm race, each demanding to out survive the other.

INITIALIZATION

The variables of the optimization task to be solved are considered in the form an array, usually called as habitat in COA. For D dimension optimization problem, a habitat is defined as a $1 \times D$ dimensional array as given in Equation (1), demonstrating the existing living point of the cuckoo.

$$X = [x_1, x_2, \dots \dots, x_D] \tag{1}$$

Each of the variable $(x_1, x_2, \dots \dots, x_D)$ exhibits a floating point number. The calculation of profit rate p gives the profit of a habitat at $(x_1, x_2, \dots \dots, x_D)$. It is described in Equation (2).

$$X_p = P(X) = P(x_1, x_2, \dots \dots, x_D) \tag{2}$$

It is known that, the main aim of COA is to maximize the profit rate. However, it can also be used in cost reduction problems C by following the Equation (3).

$$X_p = -C(X) = -C(x_1, x_2, \dots \dots, x_D) \tag{3}$$

The optimization problem for analysis is initialized with a habitat matrix. Some arbitrarily generated eggs are assigned for each of the starting habitats of cuckoos. Naturally, a cuckoo can lay about 5 to 20 eggs. In consequence, this value is taken as higher and lower value of egg perseverance to every cuckoo at each iteration. An important point to be noted about the actual cuckoos is they put down eggs within a maximal distance from their living place. In the real-world optimization problem, this distance is termed as Egg Laying Distance (ELD), and it is proportional to aspects such as total eggs, number of current cuckoos eggs and higher as well as lower variable limits (i.e., v_{high} and v_{low}). It is defined in Equation (4).

$$ELD = \alpha \times \frac{number\ of\ existing\ cuckoos\ eggs}{total\ amount\ of\ eggs} \times (v_{high} - v_{low}) \tag{4}$$

where α is an integer, utilised to control the maximal range of ELD.

EGG LAYING

The entire cuckoo starts laying eggs in specific random nests of hosts located within her ELD. When these eggs were laid in nests of other birds, some eggs that are not similar like eggs of hosts are identified and immediately thrown away from the nest by the host birds. But only $n\%$ of all eggs (generally 10%) with low profit rates will be slayed after egg laying course. Therefore, these eggs have no way for further generation. Nonetheless, the remaining eggs, not identified by the hosts can grow, incubated and are raised by the host birds. On the other hand, only one egg in the host nest will have possibility for growing since it again identifies the cuckoos while the chicks come out after hatching. At the same time, if host birds egg hatches first and then cuckoos egg hatches second, cuckoos chicks eat more food bring by the host birds to its nest. This is because, the body of cuckoo's hatchlings are three times larger than host birds and so it pushes host chicks and eats more food. In some cases, the host chicks die after a couple of days due to starvation and only the cuckoo's chick survive.

IMMIGRATION OF CUCKOOS

As the cuckoo chicks nurture and become matured, they come out and survive in their community for sometimes. Moreover, during egg laying process, they move to a fresh and healthier habitat with maximal resemblance of its eggs to hosts and additionally with more nourishment for new chicks. Once the cuckoo species are diversified, the community with more profit rate is fixed as the target land for other cuckoos to move on. Though matured cuckoos live almost in any environment, it's hard to distinguish particular group of the cuckoos where it belongs to. Then the cuckoo species were comprised and the mean profit rate is evaluated. The maximal cost of mean profit rates establishes the target groups and so that group's best habitat was taken as new endpoint habitat for immigrating cuckoos. While progressing on to target land, the cuckoos will not fly towards whole endpoint completely instead they will fly half portion of the way and take some deviance in its path. In this way, all cuckoo flies $\eta\%$ of the entire span towards target land and takes a deviance of γ radians. These two factors like η and γassist cuckoos to search some more places in its surroundings. For all cuckoos, these factors are defined as shown in Equation (5).

$$\eta \sim \cup\,(0,1)\;\gamma \sim \cup\,(-\theta,\theta) \qquad (5)$$

Where η depicts uniformly dispersed random value ranges between 0 and 1. θ is a limit that resembles the deviance from the path of target habitat.

REMOVING WORST HABITAT CUCKOOS

With the assumption that there is always balance in the inhabitants of birds, a number of N_{max} controls will bound the quantity of live cuckoos in the surroundings. This balancing is due to limited availability of food, being slayed by hunters and also incapability to discover appropriate nest for eggs. Therefore, only those N_{max} amount of cuckoos endure since it has good profit rates and the rest will demise.

THE BEHAVIOUR OF CUCKOO BREADING AND LÉVY FLIGHTS

The CS algorithm was utilised for many optimization problems and instead of random walk Lévy Flights were utilised for improving the functioning of cuckoo search algorithm. Generally, the food searching process of animals occurs in random or quasi random approach. The pathway of animals while searching for food will be actually a random walk since each will be governed by the present position and transition probability of next position. The track for foraging was completely based on probability which was modelled mathematically. The distinctive features of Lévy flights were demonstrated by the flight behaviour of insects and birds [20]. A Lévy flight was a random walk wherein step length was distributed depending on heavy tailed probability distribution. The beginning of random walk inclines on stable distribution subsequently for considerable steps.

In CS algorithm, there were two possibilities. Either the host birds identify the cuckoo's egg and choose to abandon the egg or whole nest, or the host birds cannot differentiate cuckoo's egg from their own eggs and thus the next generation of cuckoos were formed. These situations were taken in account while exploring the CS methods which includes generating new solutions for next generation by employing Lévy flights which substitutes the portion of eggs. In the nest, each egg was denoted as the solution and the cuckoo's egg represents the new solution. The objective of CSA was to produce the new and better solution (cuckoo) for substituting the worst solution in the nests. For uncomplicated cases, each nest will have one egg and for complicated cases each nest will have many eggs which signify a set of solutions. The CS algorithm was centred on the three ideal rules such as:

- The cuckoo birds will lay one egg each time and then leave the egg in host bird's neat which they choose randomly.
- The well-deserved eggs (solutions) in elite nest will be inherited to next generation.
- The available quantity of host nests was set as constant. At the probability of $p_a \in (0,1)$ the host

birds can identify the cuckoo's egg. If that happens, the bird vacates the nest and builds a new nest in the new place or throws away the egg.

The last assumption was assessed by fraction p_a of n nests which were replaced by new nests and has new random solutions. The fitness of equation was given as proportional to objective function for maximization process. The other fitness methods were described in the same way like the fitness function in genetic algorithm. Depending on the rules stated above, the fundamental phases of CS algorithm were defined as follows. While forming new solutions $x_j(s+1)$ the given Lévy flight is done for the i^{th} cuckoo.

$$x_j(s+1) = x_j(s) + \alpha \oplus L'evy\ (\lambda) \tag{6}$$

Where product $\oplus$ is denoted as entry-wise multiplication, $\alpha > 0$ was the step size and that was associated with the problem of interest scale. Here, Lévy flight was measured as the step-lengths allocated based on given probability distribution.

$$L'evy\ u = \ t^{-\lambda}, 1 < \lambda < 3 \tag{7}$$

It consists of infinite variance. Also, if the egg of cuckoo and the eggs of host birds were alike, it was hard to identify the cuckoo's egg, so the fitness is interrelated to the change in solutions. Thus, it was best for doing random walk in biased manner with certain random step-lengths.

IMPROVED CUCKOO SEARCH ALGORITHM

For finding locally and globally improved solutions, the parameters such as p_a, λ and α have been represented in the CS algorithm. In solution vectors, during fine tuning, the parameters like p_a and α are significant and these parameters can be also utilised in regulating the convergence speed of algorithm. The conventional cuckoo search algorithm utilises the fixed value for p_a and α. The parameter values were set during the initialization step and the values remain constant during new generations. While finding the optimal solution, there was a disadvantage in the number of iterations. If the value of p_a was less and α value was more, the functioning of algorithm becomes deficient which considerably increases the number of iterations. In ICSA, the parameters such as p_a and α were adjusted in such a way that it improves the functioning of cuckoo search algorithm and the limitations in fixed values of p_a and α were also eliminated. For increasing the solution vector diversity, the values of p_a and α needed to be large for enforcing the algorithm in the early generations. But, in final generations, these values were reduced for enhanced fine tuning of solution vectors. Thus, p_a and α values were changed dynamically based on sum of generations and it is given in equation 8-10. Here, gn is denoted as the current iteration and NI is denoted as the number of iterations.

$$P_a(gn) = P_{a_{max}} - \frac{gn}{NI}(P_{a_{max}} - P_{a_{min}}) \tag{8}$$

$$\alpha(gn) = \alpha_{max} \exp(c.gn) \tag{9}$$

$$c = \frac{1}{NI} L_n\left(\frac{\alpha_{min}}{\alpha_{max}}\right) \tag{10}$$

Figure 1 gives the flow chart for the proposed algorithm. The pseudo code for improved cuckoo search algorithm was given below.

Algorithm 1: Pseudo code for Improved Cuckoo Search Algorithm

```
Begin
        Create initial population: $n$ host nest $x_i (i = 1,2, \dots, n)$
        Use parameter variables $p_a$ and $\alpha$.
        Objective function: $f(x), x = (x_1, \dots\dots, x_d)$T.
        While (t<MaxGeneration) do
        Find Cuckoo and Create new solution$x_k$ via Lévy flight.
        Calculate the corresponding fitness value$F_k$.
        Choose a nest randomly, $x_j$ and the corresponding fitness value$F_j$.
                If ($F_k$>$F_j$) then
        Substitute current solution by new solution.
        $x_j$ by $x_k$
        End if.
        Adjust the $p_a$ and $\alpha$ values must decrease from final generation to result.
        Worst nest has neglected with probability $p_a$ and new nest was formed.
        Retain the best solutions.
        Rank the solutions and find current best solution.
        End while
End
```

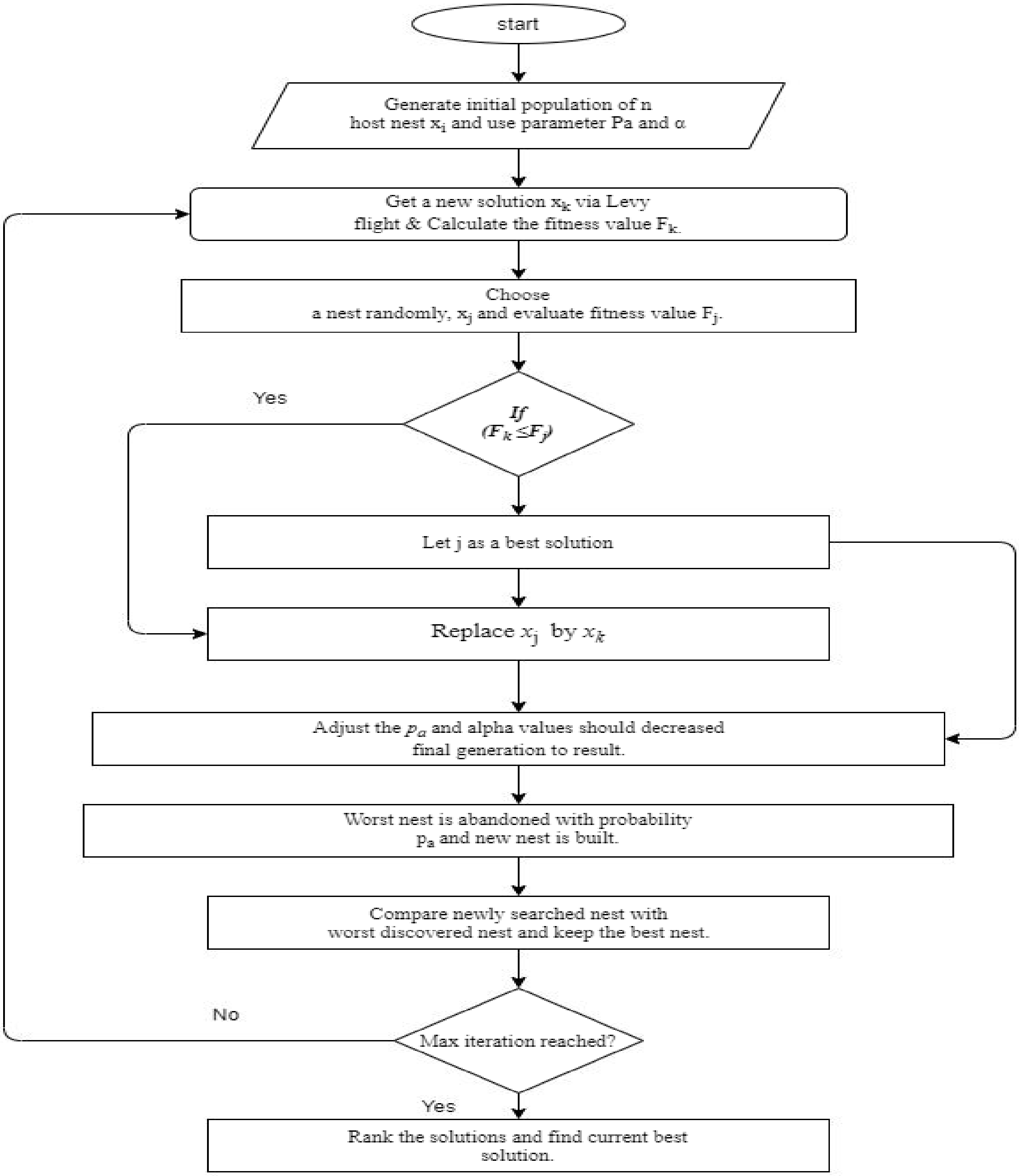

Fig. 1: Flowchart for the Improved Cuckoo Search Algorithm

EXPERIMENTAL SETUP

For investigating the functioning of proposed algorithm for feature selection, it is compared with other five optimization algorithms such as MCS, FA, GA, PSO and RS. The dataset used for the proposed algorithm have been taken from UCI machine repository [19]. Different kinds of datasets have been utilised for the future selection process. The techniques were implemented in MATLAB2018a software running on a Windows 8.1 operating system. It was indispensable to distinguish the performance of proposed algorithm to find its merits as well as demerits. Thus, the functioning of the algorithm was evaluated and compared with other similar bio-inspired algorithms on seven different dataset. Table 1 illustrates the characteristics of these dataset.

Table 1: Dataset Description

Dataset	Samples	Genes	Classes
Lung Cancer	56	32	3
Lenses	4	24	3
Pima Indians	8	768	2
Iris	4	150	3
Dermatology	34	366	6
Hepatitis	19	155	2
Breast Cancer	10	699	2

EFFECTS OF CHANGING THE OPTIMIZATION PARAMETERS ON THE PERFORMANCE OF THE ICS

The performance of improved cuckoo search algorithm after changing the parameters p_a and α was analysed in this experiment. For the dimensions N=10, N=20 and N=30, the number of generations were fixed as 500, 1000 and 2000. The parameter settings for ICS algorithm were given in table 2. For instance, thirty independent runs were carried out and the SD and mean values were calculated. In most of the cases, better results can be obtained if the minimum value of p_a was decreased without any change in the value of α. If the maximum value of p_a was increased, better results were obtained for test functions with high decision variables. The performance of the algorithm never undergo any significant effect due to the decrease in the minimum value of α with no change in the value of p_a. But an increase in the maximum value of α can have negative impact on the functioning of ICS algorithm. Various tests show that the suitable algorithm parameters leading to good results can approximately be $P_{a_{min}}$ = 0.05, $P_{a_{max}}$ = 0.5, α_{min} = 0.01, and α_{max} = 0.5.

Table 2: Algorithm Parameter Setting

Algorithm	Number of Dimensions	Number of Generation	Pa	λ	α
Improved Cuckoo Search Algorithm	N=10 N=20 N=30	500 1000 2000	Pa (min) = 0.05 Pa (max) = 0.5	1.5	α (min) = 0.01 α (max) = 0.5

EXPERIMENTAL RESULTS

In this paper, ICS algorithm is compared with other recently proposed meta-heuristic feature selection algorithms such as Improved Salp Swarm Algorithm (ISSA) [33], Quantum Whale Optimization Algorithm (QWOA) [34] and Binary Grey Wolf Optimization (BGWO) [30] for analysing the efficiency of the proposed algorithm. Figure 2 gives the number of features selected by proposed and existing meta-heuristic algorithms. It illustrates that ICS algorithm has selected lesser number of features for three datasets such as breast cancer, dermatology and lung cancer dataset.

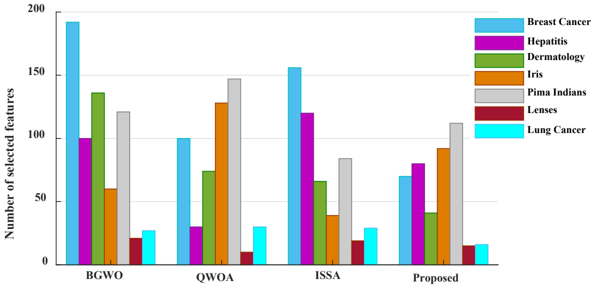

Fig. 2: Number of Selected Features

After selecting the features using ICS algorithm, the dataset undergo classification using KNN and SVM classifier. The result from the experiment gives the mean accuracy of the datasets. For evaluating the proposed algorithm, five meta-heuristic algorithms such as MCS, FA, PSO, GA and RS are utilised for the comparison process. Using KNN and SVM classifiers the accuracy of each algorithm was calculated and it is then compared with ICS algorithm. The accuracy measurements of existing algorithms and the proposed algorithm were given in Table 3. The results from the experiment illustrates that ICS algorithm obtained good results and better performance than the other existing algorithms.

The accuracy of algorithms on seven datasets using KNN and SVM were shown in figures 3 and 4. For maximum datasets the RS algorithm has less accuracy than the other algorithms. In all the tested datasets, ICS algorithm provided enhanced accuracy than other comparative algorithms. The performance of ICS algorithm with other comparative algorithms on both KNN and SVM classifiers for the seven datasets were given in Table 3. The experimental process was carried out in seven different datasets which was averaged over ten runs. From the results it was illustrated that ICS algorithm outperformed all the existing algorithms such as MCS, FA, PSO, GA and RS. Apart from the proposed algorithm the FA has attained the best accuracies in breast cancer, hepatitis and Pima Indians dataset for KNN classifier. Also, the maximum accuracy was obtained for the hepatitis dataset. For SVM classifier, the MCS algorithm has obtained best results for breast cancer, hepatitis and lung cancer datasets other than the proposed algorithm. Figures 5 and 6 represent the box plots which signify the percentage accuracy of different algorithms for the given datasets using SVM and KNN over ten runs. It illustrates that ICS algorithm has obtained better accuracy than other existing algorithms.

Table 3: Accuracy Measurements

		ICS	MCS	**FA**	**PSO**	**GA**	**RS**
Breast Cancer	**KNN**	98.12	94.96	94.83	87.40	87.08	80.41
	SVM	97.36	94.83	93.65	90.80	87.09	85.29
Hepatitis	**KNN**	98.28	92.91	96.30	91.05	87.70	79.80
	SVM	97.35	96.25	96.08	89.86	87.83	80.34
Derma-tology	**KNN**	90.95	81.43	85.72	86.27	78.50	77.26
	SVM	91.21	90.79	89.78	93.74	85.20	83.18
Iris	**KNN**	89.90	88.39	89.14	89.15	84.50	77.51
	SVM	88.23	89.17	90.00	79.80	82.24	81.17
Pima Indians	**KNN**	91.36	90.01	82.24	80.16	90.71	87.27
	SVM	89.52	87.21	87.55	83.10	88.85	86.14
Lenses	**KNN**	95.55	93.49	95.26	92.10	80.69	82.76
	SVM	92.62	91.85	92.60	91.97	81.36	84.35
Lung Cancer	**KNN**	93.97	92.12	89.17	87.42	85.69	80.16
	SVM	95.06	93.94	89.14	88.20	83.33	82.62

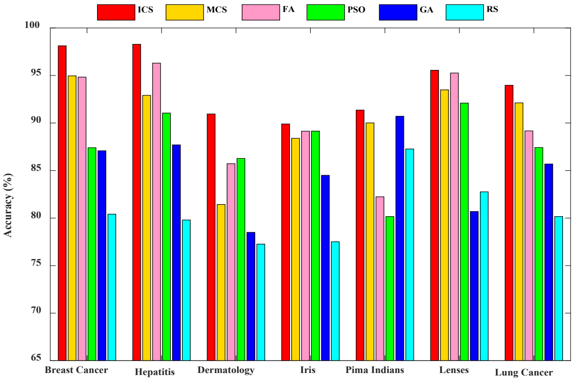

Fig. 3: Averages of Accuracy on Dataset using KNN

Figures 3 present the accuracy of all algorithms as a bar graph for the seven datasets for KNN classifier. From the bar graph of accuracy rates it was observed that the accuracy of FA was better for the hepatitis and lenses dataset other than the proposed algorithm. The proposed algorithm gives higher accuracy for Breast cancer and Hepatitis dataset. The Iris dataset gives lesser accuracy than the other datasets for the proposed algorithm. For Iris dataset the algorithms FA and PSO has same accuracy levels. Out of seven datasets the RS algorithm has occurred minimum accuracy for five dataset (breast cancer, hepatitis, dermatology, iris and lung cancer) which was the least among all the comparative algorithms used. Apart from the proposed algorithm, FA has shown better accuracy on most datasets (hepatitis, iris, lenses and lung cancer). For the Iris dataset, PSO and FA performed equally and better than other comparative algorithms other than the proposed algorithm.

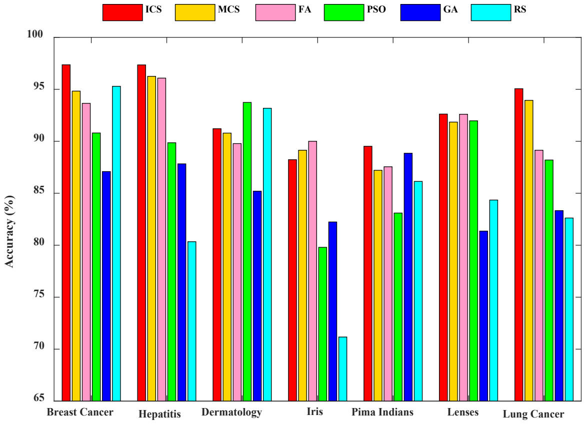

Fig. 4: Averages of Accuracy on Dataset using SVM

Figure 4 presents the classifications accuracy rate provided by the proposed algorithm and other methods for SVM classifier. The bar graph represents the different methods used in the comparison protocol and the first column has the accuracy of the proposed approach. It is seen that the optimization methods presented has reasonably similar performance for all datasets. Here, the proposed algorithm obtained best accuracy than the comparative algorithms used for all the datasets expect the Dermatology and Iris dataset. The FA and MCS algorithm outperformed the proposed algorithm for the Iris dataset. For Dermatology dataset, the PSO and RS algorithm outperformed the proposed algorithm. Also, the best accuracy for SVM classifier was obtained for the Breast cancer and Hepatitis dataset. The minimum accuracy for the proposed algorithm was obtained for the Iris dataset. The MCS and PSO algorithm has nearly similar accuracy for the Lenses dataset.

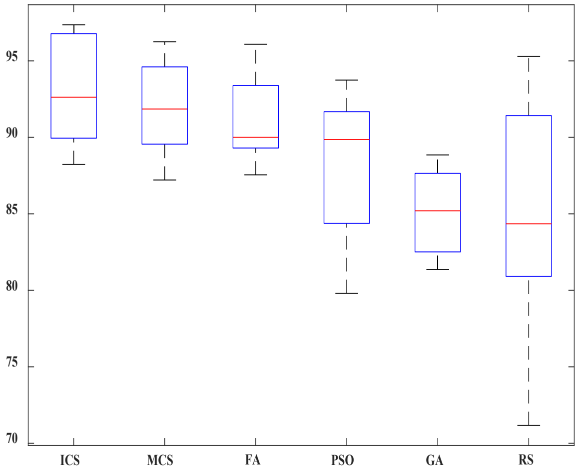

Fig. 5: Box Plots of Accuracy of the Algorithms using KNN

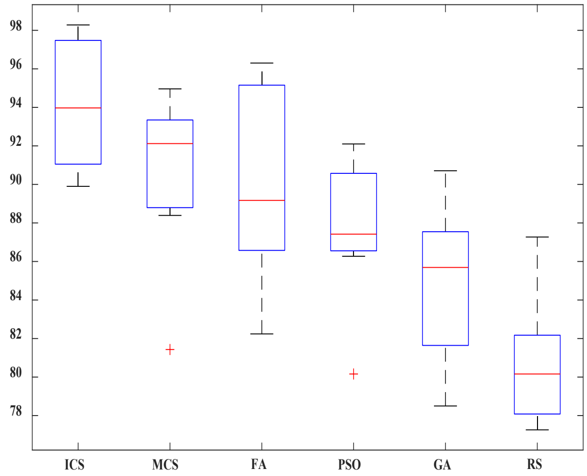

Fig. 6: Box Plots of Accuracy of the Algorithms using SVM

ANOVA Test

ANOVA test stands for analysis of variance test and it was done for strengthening the conclusions taken from the previous results. The accuracy was taken as the mean of ten runs since there may be slight variations in the accuracy during each run. For comparing the classifiers over their mean accuracies, the ANOVA test was combined with the post hoc LSD test and the analysis was done on seven datasets. Here, all the classifiers were equivalent in terms of error rate and thus it was taken as the null hypothesis for the ANOVA test. For rejecting null hypothesis, statistical analysis was conducted and after rejecting null hypothesis, the LSD test was conducted for finding the difference between the classifiers. During ANOVA test, if the significance level was greater than the p value then they were said to be considerably different. The ANOVA parameters set for the mean accuracy measure were shown in Table 4. For mean accuracy measure, the p values were significantly low and thus the null hypothesis was rejected. Thus, for obtaining the algorithm with greater effect, post hoc test was utilised.

Table 4: ANOVA Test

Source	SS	df	MS	F	Prob>F
Columns	1171.08	5	234.217	12.23	**9.20747e-09**
Error	1493.74	78	19.151		
Total	2664.83	83			

Figure 6 gives the box plots for the performance of the ANOVA test. From the ANOVA test outcomes it was verified that ICS algorithm gives the much better measure of the classification data.

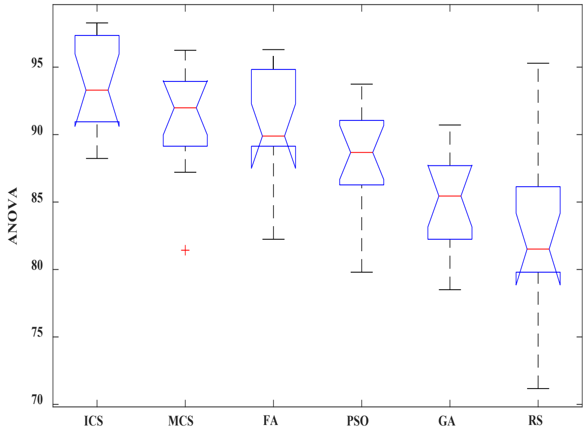

Fig. 7: Performance of ANOVA

CONCLUSION

The paper proposes an improved cuckoo search algorithm for feature selection in high-dimensional dataset. For analysing the functioning of ICS algorithm, two classifiers such as KNN and SVM have been utilised. The experimental process is carried out on seven benchmark datasets and the results are compared with other existing optimization algorithms. From experimental analysis, it have been illustrated that ICS algorithm have shown improved classification accuracy than the other existing algorithms by choosing lesser number of features and eliminating noisy, irrelevant and redundant features from the data. It demonstrates that the proposed algorithm outperformed all existing algorithms. Thus, the proposed algorithm can be effectively utilised for feature selection. In future, ICS algorithm can be effectively utilised to solve further real world problems including molecular potential energy function, scheduling problems and engineering optimization problems.

REFERENCES

Gorden F. Hughes (1968), "On the Mean Accuracy of Statistical Pattern Recognizers", IEEE Transactions on Information Theory, Volume 14, Issue 1, Pages 55-63.

James Kennedy and Russell Eberhart (1995), "Particle Swarm Optimization", International Conference on Neural Networks, Volume 4, Pages 1942–1948.

Raymer M.L., Punch W.F., Goodman E.D., Kuhn L.A. and Jain A.K. (2000), "Dimensionality Reduction using Genetic Algorithms", IEEE Transactions on Evolutionary Computation, Volume 4, Issue 2, Pages 164–171.

Rafae S. Parpinelli, Heitor S. Lopes and Alex A. Freitas (2002), "Data Mining with an Ant Colony Optimization Algorithm", IEEE Transactions on Evolutionary Computation, Volume 6, Issue 4, Pages 321-332.

Peng H, Ding C and Long F (2005), "Minimum Redundancy Maximum Relevance Feature Selection", IEEE Intelligent Systems, Volume 20, Issue 6, Pages 70–71.

Karaboga D (2005), "An Idea Based on Honey Bee Swarm for Numerical Optimization", Technical Report-TR06, Erciyes University, Engineering Faculty, Computer Engineering Department, Volume 200, Pages 1-10.

Changki Lee and Gary Geunbae Lee (2006), "Information Gain and Divergence-Based Feature Selection for Machine Learning-Based Text Categorization", Information Processing and Management, Volume 42, Issue 1, Pages 155–165.

Cheng-Lung Huang and Chieh-Jen Wang (2006), "A GA-Based Feature Selection and Parameters Optimization for Support Vector Machines", Expert Systems with Applications, Volume 31, Issue 2, Pages 231–240.

A.M. Reynolds and M. A. Frye (2007), "Free-Flight Odor Tracking in Drosophila is Consistent with an Optimal Intermittent Scale-Free Search," PLOS ONE, volume 2, Issue 4, Pages 1–9.

Mehdi Hosseinzadeh Aghdam, Nasser Ghasem-Aghaee and Mohammad Ehsan Basiri (2009), "Text Feature Selection using Ant Colony Optimization", Expert Systems with Application, Volume 36, Issue 3, Pages 6843-6853.

Kourosh Neshatian and Mengjie Zhang (2009), "Genetic Programming for Feature Subset Ranking in Binary Classification Problems", European Conference on Genetic Programming, Pages 121–132.

Xin-She Yang (2010), "Engineering Optimization: An Introduction with Metaheuristic Applications", John Wiley & Sons.

Xin-She Yang and Suash Deb (2010), "Engineering Optimization by Cuckoo Search," International Journal of Mathematical Modelling and Neumeric Optimization, Volume 1, Issue 4, Pages 330-343.

Roberto A. Vazquez (2011), "Training Spiking Neural Models using Cuckoo Search Algorithm," IEEE Congress on EvolutionaryComputation, CEC 2011, New Orleans, LA, USA, Pages 679–686.

E. Valian, S. Mohanna, and T. Saeed (2011), "Improved Cuckoo Search Algorithm For Feed Forward Neural Network Training", International Journal of Artificial Intelligence and Applications, Volume 2, Issue 3.

Amir Hossein Gandomi and Amir Hossein Alavi (2012), "Krill Herd: A New Bio-Inspired Optimization Algorithm", Communications in Nonlinear Science and Numerical Simulation, Volume 17, Issue 12, 4831-4845.

V.R. Chifu, C. B. Pop, I. Salomie, D. S. Suia, and A. N. Niculici (2012), "Optimizing the Semantic Web Service Composition Process Using Cuckoo Search" Berlin, Heidelberg: Springer Berlin Heidelberg, Pages 93–102.

P. Civicioglu and E. Besdok (2013), "A conceptual comparison of the Cuckoo Search, Particle Swarm Optimization, Differential Evolution and Artificial Bee Colony Algorithms," Artificial Intelligence Review, Volume 39, Issue 4, Pages 315–346.

K. Bache and M. Lichman (2013), "UCI Machine Learning Repository", University of California, School of Information and Computer Science, Irvine, CA.

Xin-She Yang and Suash Deb (2014), "Cuckoo Search: Recent Advances and Applications," Neural Computing and Applications, Volume 24, Issue 1, Pages 169–174.

E. Cuevas and A. Reyna-Orta (2014), "A Cuckoo Search Algorithm for Multimodal Optimization", The Scientific World Journal, Volume 2014.

Xianhai Song, Li Tang, Sutao Zhao, Xueqiang Zhang, Lei Li, Jianquan Huang and Wei Cai (2015), "Grey Wolf Optimizer for parameter estimation in surface waves", Soil Dynamics and Earthquake Engineering, Volume 75, Pages 147-157.

Mirjalili, S. (2015), "How effective is the Grey Wolf optimizer in training multi-layer perceptrons", Applied Intelligence, Volume 43, Issue 1, Pages 150-161.

Erik Cuevas, Miguel Cienfuegos, Raul Rojas and Alfredo Padilla (2015), "A Computational Intelligence Optimization Algorithm Based on the Behavior of the Social-Spider", Computational Intelligence Applications in Modeling and Control, Volume 575, Pages 123-146.

Steve De Backer, Pieter Kempeneers, Walter Debruyn and Paul Scheunders (2015), "A Band Selection Technique for Spectral Classification", IEEE Geoscience and Remote Sensing Letters, Volume 2, Issue 3, Pages 319-323.

Emary E, Hossam M. Zawbaa and Aboul Ella Hassanien (2016), "Binary Grey Wolf Optimization Approaches for Feature Selection", Neurocomputing, Volume 172, Pages 371-381.

Seyedali Mirjalili, and Andrew Lewis A (2016), "The Whale Optimization Algorithm", Advances in Engineering Software, Volume 95, Pages 51-67, May 2016.

Maziar Yazdani and Fariborz Jolai (2016), "Lion Optimization Algorithm (LOA): A Nature-Inspired Metaheuristic Algorithm", Journal of Computational Design and Engineering, Volume 3, Issue 1, Pages 24-36, January 2016.

Mohamed Abd El Aziz and Aboul Ella Hassanien (2018), "Modified Cuckoo Search Algorithm with Rough Sets for Feature Selection", Neural Computing and Applications, Volume 29, Pages 925–934.

Qasem Al-Tashi, Said Jadid Abdulkadir, Helmi Md Rais, Seyedali Mirjalili and Hitham Alhussian (2019), Binary Optimization using Hybrid Grey Wolf Optimization for Feature Selection, IEEE Access, Pages 39496-39508.

Dalwinder Singh and Birmohan Singh (2019), "Hybridization of Feature Selection and Feature Weighting for High Dimensional Data", Applied Intelligence, Volume 49, Pages 1580-1596.

Manik Sharma and Prableen Kaur (2020), "A Comprehensive Analysis of Nature-Inspired Meta-Heuristic Techniques for Feature Selection Problem", Archives of Computational Methods in Engineering.

Ah. E. Hegazy, M. A. Makhlouf and Gh. S. El-Tawel (2020), "Improved Salp Swarm Algorithm for Feature Selection", Computer and Information Sciences, Volume 32, Issue 3, Pages 335-344.

R.K. Agrawal, Baljeet Kaur and Surbhi Sharma (2020), "Quantum based Whale Optimization Algorithm for wrapper feature selection", Applied Soft Computing, Volume 89, 106092.

Science and Technology Journal Vol. 8 Issue 2 July 2020 ISSN: 2321-3388

Study on Coupling of Step and Graded Index Single Mode Optical Fiber Considering the Transverse Misalignment

Prosenjit Roy Chowdhury
Department of Electronic Science,
Acharya Prafulla Chandra College, New Barrackpore, Kolkata–700131, India
E-mail: proychow@yahoo.com

Abstract—Advance design and day to day up-gradation of communication system is the requirement of international telecommunication. The optical communication systems involve the effective fiber coupling or splicing to meet the need of long communication channel. When the studies on both the intensive and extensive properties of optical fiber are exploring new research horizons, the effectiveness of such systems can be calibrated with transmission parameters like transmitted fractional power, which is a function of 'spot size' as well. Our study of fiber junctions based on fundamental parameters like wavelength, fiber profile index etc. has touched some unrevealed areas and explored some interesting results. The profile index of optical fiber has received less attention compared to other structural parameters of optical fiber but our study at important wavelengths for different profiles has shown that the less-used fiber profiles has some interesting premier outcomes, which can introduce some significant impact on optical fiber based system design and engineering.

We have observed almost frequency or wavelength independent transmitted fractional power around the most used 1.55 micrometer wavelengths at some rarely used fiber profile index. Our study predicts the best and worst fiber profiles for transmitted fractional power (T), at the same time, we have observed the fiber profile index independent region for a band of 'T' values. The reporting and its approach are found to be premier in this field. So, our work is reporting a comparison of effective fiber-to-fiber coupling, based on fiber profile index of different fibers. It is also giving a clear view of the wavelength dependency of effective fiber coupling for different fibers having wide range of graded fiber profiles.

Keywords: Fiber couplings, Fiber misalignment, transmitted fractional power, Marcuse Spot size, Fiber Profile Index. Signal Wavelength.

INTRODUCTION

In this paper, we have discussed the transmitted fractional power (Ghatak and Thyagarajan 1998) in case of transverse misalignment (Ghatak and Thyagarajan 1998 ; Snyder and Love 1983) of optical fiber joints between graded index fiber (Cao and Chi 2001; Thyagarajan and Tewari 1985) and step index fiber (Abdulalim et al. 2003). Our approach to study the variation of transmitted fractional power with the basic parameter (Snyder and Love 1983) 'wavelength' of signal, for different graded index fiber profiles, considering the importance of the 1.55 micrometer wavelength, for optical communication systems (Zhou et al. 2020; Xiao et al. 2019). We have considered one fiber as step index and the variation of profile was considered for the other fiber.

The transmitted fractional power is a function of spot sizes (Roy Chowdhury et al. 2014; 2016) of two fibers, used for fiber joint (Yablon 2005). To determine the spot size, the well established formulation of Marcuse, known as the 'Marcuse spot size formulation' (Marcuse 1978; 1977; 1976) is used. On the other hand, the wavelength is a parameter to determine normalized frequency (Ghatak and Thyagarajan 1998) of the fiber, which determine the fiber spot size using Marcuse method (Marcuse 1978; 1977 ; 1976).

Our study on the wavelength dependency of transmitted fractional power has included common graded index (Ghatak and Thyagarajan 1998; Snyder and Love 1983) fiber profiles like Triangular profile (q=1), Parabolic profile (q=2) etc., along with our interests on higher 'q' value profiles.

Some recent reporting on mechanism to control the loss and dispersion by optimum graded refractive index fiber profiles (Rashed et al. 2019) has claimed their efficiency. At the same time, work on some complex or mixed refractive index profiles are also getting attention for its loss and dispersion compensating properties, Trapizoidal index (Roy Chowdhury et al. 2017; Dutta et al. 2018) fiber, W type fiber (Rostami and Makouei 2010; Ettabib et al., 2012, Panda type (Yang et al. 2019) etc are already in application.

Study on higher q values is not that common in major scientific literatures. So, our extended study produced some interesting observations, which is adding some value to scientific and industrial research in this field. The findings are providing some option to choose proper values of parameters to design fibers for smother and efficient data transmission.

The graded index fiber profiles has its own importance in wavelength division multiplexing (Arora and Subramaniam 2002; Al-Majali and Matarneh 2019) but to have more fiber bandwidth, introduction of multi-core fibers is in process, where the inter-core crosstalk effect are proposed to be controlled by advanced designed graded-index profile (Xie et al. 2020). It is also reported that, fiber refractive index profile reconstruction is getting attention (Azkune et al 2020), Low Noise Graded Index Plastic Fibers (Inoue and Koike 2018) are also getting importance for its robust and stable data transmission mechanism. Our proposed wavelength insensitive profile index for long haul communication system design can be the future interest in the field. So, the study on optical fiber refractive index profile gradation is getting more attention by the researchers in the field of optical communication engineering as well as material scientists. The practical implementation of our predicted fiber profile indices to have flatness of transmitted fractional power over the range of most used signal wavelength, which is basically the 'frequency independent transmitted fractional power' is expected to be materialized. The graphical presentation of variation in transmitted fractional power with fiber profile index for specific wavelength generates some guidance to the system designers also. In continuation the implementation of 'fiber profile independent' band may get applications with a compromise to small fraction of Transmitted fractional power.

ANALYSIS

In this study, we have initiated with basic parameters of fiber optics like normalized frequency 'V' values, wavelength 'λ' and different step or graded index fiber profiles. The said basic parameters are the functions of the advanced parameter like 'optical fiber spot size', transmitted fractional power 'T' etc.

Considering the Gaussian fundamental modes of two fibers having spot size w_1 and w_2 respectively, the fundamental mode expression should be

$$\psi_a(x,y) = \sqrt{2/\pi}\,\frac{e^{-\frac{x^2+y^2}{w_1^2}}}{w_1} \tag{1}$$

and

$$\psi_b(x,y) = \sqrt{2/\pi}\,\frac{e^{-\frac{(x-u)^2+y^2}{w_2^2}}}{w_2} \tag{2}$$

for the first and second fiber where 'u' is the transverse misalignment along the x axis.

The normalization factor considered as

$$\int_{-\infty}^{+\infty}\int_{-\infty}^{+\infty}\psi_{a,b}^2\,dxdy = 1 \tag{3}$$

The expression of fractional power of fundamental mode coupled to the second fiber is

$$T = \left|\int_{-\infty}^{+\infty}\int_{-\infty}^{+\infty}\psi_a\psi_b^*\,dxdy\right|^2 \tag{4}$$

And the simplified expression of T is

$$T = \left(\frac{2w_1w_2}{w_1^2+w_2^2}\right)\exp\left[-\frac{2u^2}{w_1^2+w_2^2}\right] \tag{5}$$

For maximum power coupling, 'u' should be null so the expression of 'T' should be (Ghatak and Thyagarajan 1998; Snyder and Love 1983)

$$T = \left(\frac{2w_1w_2}{w_1^2+w_2^2}\right) \tag{6}$$

The expression may be considered as the T_{Max} for the above explanation. Where w_1 is the spot size of the initial fiber, i.e. the step index fiber and w_2 is that of the second stage fiber, i.e. of graded index fiber (Snyder and Love 1983; Chao et al. 1994; Cao and Chi 2001). The profile function f(R) is defined (Ghatak and Thyagarajan 1998; Cao and Chi 2001; Thyagarajan and Tewari 1985) as

$$f(R) = \begin{cases} R^q; R \le 1 \\ 1; R > 1 \end{cases} \tag{7}$$

where R=r/a; is the normalized distance when 'r' is the effective radial distance and 'a' is the core radius value.

To determine the spot size w_1 and w_2, the following expressions of Marcuse relations (Marcuse 1978; 1977; 1976) are used

The relation for Step index Fiber is

$$\frac{w_s}{a_s} = 0.65 + \frac{1.619}{V^{\frac{2}{3}}} + \frac{2.879}{V^6} \tag{8}$$

And the relation for graded index fiber is

$$\frac{w_g}{a_g} = \frac{A}{V^{\frac{2}{q+2}}} + \frac{B}{V^{\frac{3}{2}}} + \frac{C}{V^6} \tag{9}$$

where

$A = [\frac{2}{5}\{1+4(\frac{2}{q})^{\frac{5}{6}}\}]^{\frac{1}{2}}$

$B = [e^{\frac{0.298}{q}} - 1 + 1.478(1 - e^{-.077q})]$ (10)

$C = [3.76 + e^{\frac{4.19}{q^{0.418}}}]$

are to represent w_s and w_g which are the exact spot size and a_s and a_g are the core radios of step index fiber and graded index fiber (Cao and Chi 2001; Tyagarajan and Tewari 1985) respectively. 'V' is the normalized frequency and 'q' is the fiber profile exponent (Ghatak and Thyagarajan 1998; Snyder and Love 1983).

At the same time V is defined as (Ghatak and Thyagarajan 1998)

$$V = \frac{2\pi}{\lambda} a \bullet N.A \tag{11}$$

Where 'a' is the core radius and 'N.A' stands for Numerical Aperture of the corresponding optical fiber depending on its profile.

The expression of *'V'* in Eqn. (11), relates the wavelength 'λ' to the spot size in Eqn. (8) and (9). The spot size derives the transmitted fractional power 'T' through Eqn. (5) and (6).

For our case, the expression of 'T' or precisely 'T_{Max}', should become (Ghatak and Thyagarajan 1998)

$$T = \left(\frac{2 w_s w_g}{w_s^2 + w_g^2}\right) \tag{12}$$

Where 'w_s' and 'w_g' are the spot size of the step and graded index fiber respectively.

In our study, we considered the step index fiber with the typical core radius of 3 micrometer to optimize the value of core radius with other parameters of 'V' value with single mode requirements. The core and cladding refractive index of the step index fiber considered as 1.48 and 1.47 respectively to comply the 'weakly guiding approximation' and to reduce the Numerical Aperture of the used optical fiber. On the other hand the graded profiles considered central refractive index of core as 1.5 with typical radius of 3 micrometer to match the spot size of both the fibers and other splicing requirements.

RESULTS AND INFERENCE

Our theoretical findings are represented in the following plots. We have recorded the variations of the transmitted fractional power 'T' with the variation of wavelength.'λ' for different fibers of wide varying 'q' values.

The following plots are representing our work in a consisted form, where each curve is representing a different fiber of different 'q' values.

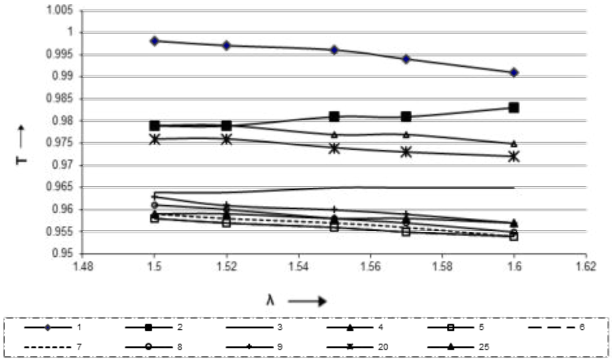

Fig. 1: Plot of Variation of T with λ for Different 'q' Values

We can observe that all the traces are more or less parallel to x axis and hence parallel to each others also. The value of 'T' is reducing with the higher 'q' values till 'q' raised upto 5 or 6 and with further higher 'q' values, the value of transmitted fractional power getting better, till we continud upto 'q'=25.

To clarify, we have plotted the same data in 3 Dimensional plot of fig.2, where the variation of transmitted fractional power 'T' has presented with variation of wavelength λ and fiber profile index 'q' in different axis. The variation of 'T' for different fibers of different fiber profiles are clearly presented in fig 3 for the lowest loss wavelength of 1.55 µm.

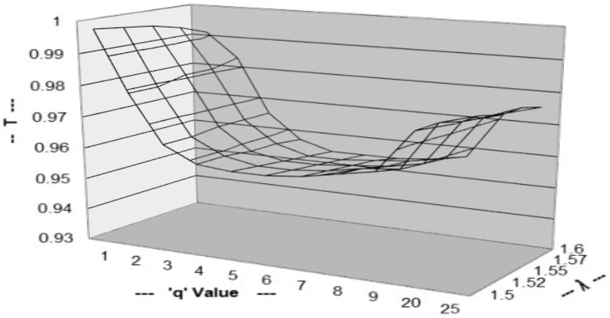

Fig. 2: 3D Representation of Variation of 'T' with Wavelength 'λ' for Different 'q' Values

In the above curves it is observed that the value of T has an interesting dependency on 'q'. We have tabled the values of Transmitted fractional Power 'T' for different profile index 'q' for 1.55 μm wavelength only. The data are plotted also in Figure 3 to visualize the effect of variation of 'q' values on Transmitted fractional Power 'T'.

Table 1: Values of Transmitted fractional power for different 'q' values at 1.55 μm wavelength.

q	T
1	0.996
2	0.981
3	0.965
4	0.958
5	0.956
6	0.956
7	0.957
8	0.958
9	0.96
20	0.974
25	0.977

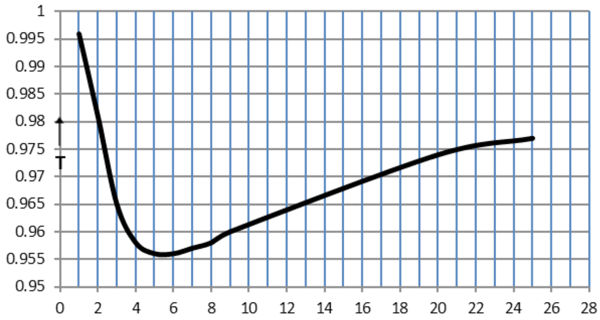

Fig. 3: Variation of T at different fiber profile index 'q' for λ =1.55 μm.

From the above plots we can report some very basic and premier observations on transmitted fractional power for different fiber profile exponent. Our most preferred wavelength 1.55 μm may vary around the target wavelength. So we have studied the variation of the transmitted fractional power around the 1.55 μm wavelength. We can plot the curves like figure 3 for any wavelength between 1.5 μm to 1.6μm wavelength extracting from the Figure 1 and 2. but all the curves should have similarity in nature except small variations.

We have interestingly observed in figure 1, that the slopes of the plots of λ vs T are not consistent. Slope of the curve for 'q'=2 is opposite to others and the slope of plot for q=3 is almost flat over the full wavelength range. From this observation we can expect a fractional 'q' value, between 3 and 4, which will provide, exact frequency independent transmitted fractional power 'T'.

The figure 2 is representing the complete information of our study. The 3 dimensional plots are showing the variation of fractional power with in the most preferred transmission wavelength band and its variation for different 'q' values.

Figure 3 is an extract from previous plots and represented the table 1. The study at most preferred wavelength 1.55 μm is showing the variation of fractional power for different 'q' values, where he can clearly identify the effect of different graded fiber profiles on Transmitted fractional power. We have observed that, for triangular ('q'=1) profile the transmitted fractional power 'T' is best and it is reducing with higher 'q' profiles till 'q'=5 and 'q' =6 but it is again improving with higher 'q' values. So, for 'q'=5 and 'q'=6 transmitted fractional power 'T' is minimum and constant. So considering the profile index exponent 5 to 6 as a separate zone, it can be considered as – fiber profile independent zone.

So, our study predicted the 'frequency independent profile index', 'fiber profile independent zone' and graphically represented the power transmission efficiency from fiber to fiber over a wide range of fiber profiles.

CONCLUSION AND FURTHER OPTIONS

We can conclude that the profile index exponent q=3 is very important finding for us, as, at around this profile index all the wavelength between 1.5μm to 1.6 μm exhibit almost constant effect of the transmitted fractional power. So, the concept of 'frequency independent transmitted fractional power' is there. We can further study to find some fractional profile index just above q=3 where the curve of transmitted fractional power should be perfectly parallel with wavelength axis but the concept of fractional profile index not established popularly.

The variation of 'T' with 'q' at 1.55 micrometer wavelength records, for 'q'=1 the transmission of power is best and it goes down till 'q'= 5 and 6. But it improves with higher 'q' values.

Like the frequency or wavelength independent profile index around 'q'=3, we can have 'profile index independent band' for Transmitted fractional power within 'q'= 5 and 6 also.

The further importance of our finding is that, the inter-core crosstalk of multi-core fibers are proposed to be controlled by air-trench assisted graded-index profile (Xie et al. 2020) where our findings may have a guiding direction to choose profile exponent of graded index fiber. On the other hand the study on profile reconstruction in Graded index polymer optical fiber (Azkune et al. 2020) may be relate as the further step in continuation of our work. So, the paper has introduced some fresh areas of study which are expected to be in application in no time to facilitate the optical fiber system design.

REFERENCES

Abdulalim MA, Hussein KF and Elhefnawi FM. Power coupling between step-index optical fiber sections with different refractive indices, Proceedings of the Twentieth National Radio Science Conference -NRSC'2003. IEEE Cat. No.03EX665, Cairo, Egypt, pp. B10-1, doi: 10.1109/NRSC.2003.157317.

Al-Majali MN and Matarneh AM (2019) Interactions between Crosstalk in Wavelength Division Multiplexing and Graded index Optical Fiber Parameters. Journal of Telecommunication, Electronic and Computer Engineering 11 (1) 7-13.

Arora A and Subramaniam S (2002) Wavelength Conversion Placement in WDM Mesh Optical Networks, Photonic Network Communications. 4 (2) 167-177.

Azkune M., Ortega-Gomez A., Ayesta I. and Zubia J. (2020) Refractive-Index Profile Reconstruction in Graded-Index Polymer Optical Fibers Using Raman Spectroscopy. Materials, 13, 2251 [DOI:10.3390/ma13102251].

Cao Q and Chi S (2001) Approximate Analytical Description for Fundamental-Mode Fields of Graded-Index Fibers: Beyond the Gaussian Approximation. Journal of Lightwave Technology 18 (1) 96-105.

Chao SC, Tsai WH and Wu MS (1994) Extended Gaussian Approximation for Single-Mode Graded-Index Fibers. Journal of Lightwave Technology 12. (3) 392-395.

Dutta I, Kumbhakar D, Sarkar SN (2018), Prediction of unknown aspect ratio of a single mode trapezoidal index fiber using splice loss technique considering angular misalignment. Optik 170, 132–139.

Ettabib MA, Parmigian F, Feng X, Jones L, Kakande J, Slavik R, Poletti F, Ponzo G.M, Shi J, pertovich MN and Loh WH. (2012) Phase regeneration of DPSK signals in a highly nonlinear lead-silicate W-type fiber. Optics Express 20, 27419- 27424.

Ghatak A and Thyagarajan K (1998) Introduction to Fiber Optics, Cambridge University Press, Cambridge, UK.

Inoue A. and Koike Y. (2018) Low-Noise Graded-Index Plastic Optical Fiber for Significantly Stable and Robust Data Transmission. Journal of Lightwave Technology 36, 5887–5892.

Marcuse D (1976) Microbending Losses of Single-Mode Step-Index and Multimode, Parabolic-Index Fibers, The Bell System Technical Journal 55. 937-955.

Marcuse D (1977) Loss analysis of single-Mode Fiber Splices. The Bell System Technical Journal 56 (6) 703-718.

Marcuse D (1978) Gaussian approximation of the fundamental modes of graded-index fibers. Journal of Optical Society of America 68(1) 103-109.

Rashed ANZ, Kumar SS, Tabbour MSF, Sundararajan TVP and Maheswar R (2019) Different Graded Refractive Index Fiber Profiles Design for the Control of Losses and Dispersion Effects. Journal of Optical Communication. [DOI: https://doi.org/10.1515/joc-2019-0036]

Rostami A. and Makouei S. (2010) Modified W-type single- mode optical fiber design with ultra low, flattened chromatic dispersion and ultra- high effective area for high bit rate long haul communications. Progress in Electromagnetics Research C, 12, 79-92.

Roy Chowdhury A, Dutta I, Mallick A. K., Sarkar S. (2017) Prediction of power transmission coefficient and the aspect ratio of a single mode trapezoidal index fiber by using splice loss technique. Optik 149, 1–8.

Roy Chowdhury P, Karak A and Pramanik S (2014) Simple approach to find out fiber parameters and characteristics using Marcuse spot sizes applied to Variational Formalism, Journal of Physical Science 18, 30-33.

Roy Chowdhury P, Pramanik S. and Sarkar SN (2016) A Simple and Elegant Technique Connecting Marcuse Spot Size Relations to Variational formulations in Single Mode Graded Index Fiber Characterization. Journal of Modern Optics 63 (6) 580-585.

Snyder AW and Love JD (1983) Optical Waveguide Theory, Chapman and Hall Ltd., New York, USA.

Thyagarajan K and Tewari R (1985) Accurate analysis of single-mode graded index fiber directional couplers. Journal of Lightwave Technology LT-3, 59-62.

Xiao Q, Tian J, Yan P, Li D and Gong M. (2019) Exploring the initiation of fiber fuse. Scientific reports natureresearch, 9,11655.

Xie Y., Pei L., Zheng J., Zhao Q., Ning T., Li J. (2020) Low-DMD and low-crosstalk few-mode multi-core fiber with air-trench/holes assisted graded-index profile, Optics Communications 474, 126155 [https://doi.org/10.1016/j.optcom.2020.126155]

Yablon AD (2005), Optical fiber fusion splicing, Springer series, 1st Edn. Springer-Verlag Berlin Heidelberg.

Yang Y, Mo Q, Fu S,, Liu B, Tang M, and Liu D (2019) Panda type elliptical core few-mode fiber. APL Photonics 4, 022901 [https://doi.org/10.1063/1.5038119].

Zhou H, Xu H and Duan J (2020) Review of the technology of a single mode fiber coupling to a laser diode, Optical Fiber Technology, 55, 102097.

Science and Technology Journal Vol. 8 Issue 2 July 2020 ISSN: 2321-3388

Certain Properties of τ -Curvature Tensor in Generalized Sasakian Space Form

C. Lalmalsawma[1]* and J.P. Singh[2]
[1,2]Department of Mathematics & Computer Science,
Mizoram University, Aizawl–796004, Mizoram, India
E-mail: *[1]sweezychawngthu@gmail.com

Abstract—In this paper we study τ-curvature tensor in generalized Sasakian-space-form. We study $\varphi-\tau$ semisymmetric generalized Sasakian-space-form and obtain results for particular cases. We also study generalized Sasakian-space-form satisfying $\tau.Z=0$. We also obtain some results for all particular cases of τ -Curvature tensor.

2010 Mathematics Subject Classification: 53C15; 53C25.

INTRODUCTION

In a Riemannian manifold, a curvature tensor given by $K(X,Y)=R(X,Y,Y,X)$ for an orthonormal pair of vectors (X,Y), is known as the sectional curvature. A Riemannian manifold with constant sectional curvature c is called a real-space-form, and its curvature tensor R satisfies

$$R(X,Y)Z=c\,\{g(Y,Z)X-g(X,Z)Y\}. \tag{1.1}$$

A Sasakian manifold with constant φ-sectional curvature c is called a Sasakian-space-form and its curvature tensor R is given by

$$R(X,Y)Z=\frac{c+3}{4}[g(Y,Z)X-g(X,Z)Y]+\frac{c-1}{4}[g(X,\varphi Z)\varphi Y-g(Y,\varphi Z)\varphi X+2g(X,\varphi Y)\varphi Z]+\frac{c-1}{4}[\eta(X)\eta(Z)Y-\eta(Y)\eta(Z)X+g(X,Z)\eta(Y)\xi-g(Y,Z)\eta(X)\xi].$$

Alegre et al. (2004) generalized the Sasakian-space-form by replacing the constant quantities $\frac{c+3}{4}$ and $\frac{c-1}{4}$ with differentiable functions. Such space is called generalized Sasakian-space-form. The generalized Sasakian-space-form has been studied by many authors such as Sarkar and De (2012), De and Sarkar (2010, 2012), Singh (2016a, 2016b), De and Majhi (2013, 2015, 2019), Kishore et al. (2017), Alegre and Carriazo (2018) and many others.

In an n-dimensional semi-Riemannian manifold, a τ-curvature tensor is a tensor of type $(1,3)$, which is defined by Tripathi (2011)

$$\tau(X,Y)Z=a_0\,R(X,Y)Z+a_1\,S(Y,Z)X+a_2\,S(X,Z)Y+a_3\,S(X,Y)Z$$
$$+a_4\,g(Y,Z)QX+a_5\,g(X,Z)Q\,Y+a_6\,g(X,Y)QZ$$
$$+a_7r[g(Y,Z)X-g(X,Z)Y]. \tag{1.2}$$

Particularly the τ-curvature tensor reduces to

1. Riemannian curvature tensor R if

$$a_0=1,\ a_1=a_2=a_3=a_4=a_5=a_6=a_7=0, \tag{1.3}$$

2. quasi-conformal curvature tensor C if

$$a_1 = -a_2 = a_4 = -a_5,\ a_3 = a_6 = 0, a_7 = -\frac{1}{n}(\frac{a_0}{n-1} + 2a_1), \tag{1.4}$$

3. conformal curvature tensor $\tilde{C}$ if

$$a_0 = 1, a_1 = -a_2 = a_4 = -a_5 = -\frac{1}{n-2}, a_3 = a_6 = 0,\ a_7 = \frac{1}{(n-1)(n-2)}, \tag{1.5}$$

4. Conharmonic curvature tensor $\hat{C}$ if

$$a_0 = 1,\ a_1 = -a_2 = a_4 = -a_5 = -\frac{1}{n-2}, a_3 = a_6 = a_7 = 0, \tag{1.6}$$

5. Concircular curvature tensor $\dot{C}$ if

$$a_0 = 1, a_1 = a_2 = a_3 = a_4 = a_5 = a_6 = 0,\ a_7 = -\frac{1}{n(n-1)}, \tag{1.7}$$

6. Pseudo-projective curvature tensor P if

$$a_1 = -a_2,\ a_3 = a_4 = a_5 = a_6 = 0,\ a_7 = \frac{1}{n-1}(\frac{a_0}{n-1} + a_1), \tag{1.8}$$

7. Projective curvature tensor $\tilde{P}$ if

$$a_0 = 1, a_1 = -a_2 = -\frac{1}{n-1},\ a_3 = a_4 = a_5 = a_6 = a_7 = 0, \tag{1.9}$$

8. m-projective curvature tensor M if

$$a_0 = 1, a_1 = -a_2 = a_4 = -a_5 = -\frac{1}{2(n-1)},\ a_3 = a_6 = a_7 = 0, \tag{1.10}$$

9. W_0 curvature tensor if

$$a_0 = 1, a_1 = -a_5 = -\frac{1}{n-1},\ a_2 = a_3 = a_4 = a_6 = a_7 = 0, \tag{1.11}$$

10. W_0^* curvature tensor if

$$a_0 = 1,\ a_1 = -a_5 = \frac{1}{n-1}, a_2 = a_3 = a_4 = a_6 = a_7 = 0, \tag{1.12}$$

11. W_1 curvature tensor if

$$a_0 = 1,\ a_1 = -a_2 = \frac{1}{n-1},\ a_3 = a_4 = a_5 = a_6 = a_7 = 0, \tag{1.13}$$

12. W_1^*curvature tensor if

$$a_0 = 1,\ a_1 = -a_2 = -\frac{1}{n-1},\ a_3 = a_4 = a_5 = a_6 = a_7 = 0, \tag{1.14}$$

13. W_2 curvature tensor if

$$a_0 = 1,\ a_4 = -a_5 = -\frac{1}{n-1}, a_1 = a_2 = a_3 = a_6 = a_7 = 0, \tag{1.15}$$

14. W_3 curvature tensor if

$$a_0 = 1,\ a_2 = -a_4 - \frac{1}{n-1}, a_1 = a_3 = a_5 = a_6 = a_7 = 0, \tag{1.16}$$

15. W_4 curvature tensor if

$$a_0 = 1,\ a_5 = -a_6 = \frac{1}{n-1}, a_1 = a_2 = a_3 = a_4 = a_7 = 0, \tag{1.17}$$

16. W_5 curvature tensor if

$$a_0 = 1,\ a_2 = -a_5 = \frac{1}{n-1}, a_1 = a_3 = a_4 = a_6 = a_7 = 0, \tag{1.18}$$

17. W_6 curvature tensor if

$$a_0 = 1, a_1 = -a_6 = -\frac{1}{n-1}, a_2 = a_3 = a_4 = a_5 = a_7 = 0, \tag{1.19}$$

18. W_7 curvature tensor if

$$a_0 = 1, a_1 = -a_4 = -\frac{1}{n-1}, a_2 = a_3 = a_5 = a_6 = a_7 = 0, \tag{1.20}$$

19. W_8 curvature tensor if

$$a_0 = 1, a_1 = -a_3 = -\frac{1}{n-1}, a_2 = a_4 = a_5 = a_6 = a_7 = 0, \tag{1.21}$$

20. W_9 curvature tensor if

$$a_0 = 1,\ a_3 = -a_4 = -\frac{1}{n-1}, a_1 = a_2 = a_5 = a_6 = a_7 = 0. \tag{1.22}$$

The τ-curvature tensor in generalized Sasakian-space-form has been studied by Bagewadi and Ingalahalli (2014) and Kumari and Chanyal (2015).

Mantica and Suh (2012a) defined the Z-tensor which is given by

$$Z(X,Y) = S(X,Y) + \varphi_1\ g(X,Y)Z(X,Y) = S(X,Y) + \varphi_1\ g(X,Y), \tag{1.23}$$

where φ_1 is an arbitrary scalar function and S and g denotes the Ricci tensor and metric tensor respectively. Particularly when $\varphi_1 = 0$, the Z-tensor reduces to the Ricci tensor. Later Z-tensor has been studied by Mallick and De (2016), De and Pal (2016), Mantica et al. (2012a, 2012b), Chaubey (2018) and many others.

De and Majhi (2015) studied generalized Sasakian space-forms and proved that an n-dimensional generalized Sasakian space-form is φ-Weyl semisymmetric and φ-projectively semi-symmetric if and only if $f_2 = 0$ and $f_3 = \frac{3f_2}{2-n}$ respectively. Motivated by this study we generalized the φ-semisymmetric by $\varphi - \tau$-semisymmetric and obtained results for particular cases. We also studied the Z-tensor in generalized Sasakian-space-form.

PRELIMINARIES

Let S and r denote the Ricci tensor of type $(0,2)$ and the scalar curvature respectively. Q denotes the symmetric tensor of type $(1,1)$ corresponding to the Ricci tensor S , that is,

$$g(QX,Y) = S(X,Y).$$

In a generalized Sasakian-space-form the following properties holds

$$R\{(X,Y)Z\} = f_1\ [g(Y,Z)X - g(X,Z)Y] + f_2\ [g(X,\varphi Z)\varphi Y$$
$$- g(Y,\varphi Z)\varphi X + 2g(X,\varphi Y)\varphi Z] + f\_3\ [\eta(X)\eta(Z)Y$$
$$-\eta(Y)\eta(Z)X + g(X,Z)\eta(Y)\xi - g(Y,Z)\eta(X)\xi], \tag{2.1}$$

$$S(X,Y) = [(n-1)f_1 + 3f_2 - f_3]g(X,Y) - [3f_2 + (n-2)f_3]\eta(X)\eta(Y), \tag{2.2}$$

$$QX = [(n-1)f_1 + 3f_2 - f_3]X - [3f_2 + (n-2)f_3]\eta(X)\xi, \tag{2.3}$$

$$S(X,\xi) = (n-1)(f_1 - f_3)\eta(X), \tag{2.4}$$

$$Q\xi = (n-1)(f_1 - f_3)\xi, \tag{2.5}$$

$$R\{(X,Y)\xi\} = (f_1 - f_3)[\eta(Y)X - \eta(X)Y], \tag{2.6}$$

$$R\{(\xi,Y)Z\} = (f_1 - f_3)[g(Y,Z)\xi - \eta(Z)Y], \tag{2.7}$$

$$R\{(\xi,Y)\xi\} = (f_1 - f_3)[\eta(Y)\xi - Y], \tag{2.8}$$

$$r = n(n-1)f_1 + 3(n-1)f_2 - 2(n-1)f_3, \tag{2.9}$$

where r is the scalar curvature.

φ–τ SEMISYMMETRIC GENERALIZED SASAKIAN-SPACE-FORM

Definition 4.1. A generalized Sasakian-space-form is $\varphi - \tau$-semisymmetric if the τ-curvature tensor satisfies

$$\tau(X,Y).\varphi\, Z \;=\; 0.$$

Theorem 4.1. In a $\varphi - \tau$-semisymmetric generalized Sasakian-space-form, we have

$$-a_0\,(f_1 - f_3) + a_1(n-1)(f_1 - f_3)$$
$$+ a_4\,\{(n-1)f_1 + 3f_2 - f_3\} + a_7 r \;=\; 0.$$

Proof: It is well known that

$$\tau(X,Y).\varphi Z \;=\; \tau(X,Y)\varphi\, Z \;-\; \varphi(\tau(X,Y)Z). \qquad (3.1)$$

Now

$$\tau(X,Y)\;\varphi Z \;=\; a_0\, R(X,Y)\;\varphi Z \;+\; a_1\, S(Y,\varphi Z)X + a_2\, S(X,\varphi Z)Y$$
$$+ a_3\, S(X,Y)\;\varphi Z \;+\; a_4\, g(Y,\varphi Z)QX \;+\; a_5\, g(X,\varphi Z)\;QY$$
$$+ a_6\, g(X,Y)Q\;\varphi Z \;+\; a_7 r[g(Y,\varphi Z)X \;+\; g(X,\varphi Z)Y]. \qquad (3.2)$$

Using (2.1), (2.2) and (2.3) in the above equation we get

$$\tau\;(X,Y)\;\varphi Z \;=\; a_0\;[f_1 g(Y,\varphi)X - g(X,\varphi Z)Y + f_2\; g(X,\varphi^2 Z)\varphi Y - g(Y,\varphi^2 Z)\varphi X$$
$$+ 2g(X,\varphi Y)\varphi^2 Z\} + f_3\{g(X,\varphi Z)\eta(Y)\xi - g(Y,\varphi Z)\eta(X)\xi\}]$$
$$+a_1\;[(n-1)f_1 + 3f_2 - f_3]g(Y,\varphi Z)X$$
$$+a_2\;[(n-1)f_1 + 3f_2 - f_3]g(X,\varphi\; Z)Y$$
$$+ a_3\;[\{(n-1)f_1 + 3f_2 - f_3\}g(X,Y)$$
$$-\{3f_2 + (n-2)f_3]\eta(X)\eta(Y)\}]\varphi Z$$
$$+ a_4\; g(Y,\varphi Z)[\{(n-1)f_1 + 3f_2 - f_3\}X - \{3f_2 + (n-2)f_3\}\eta(X)\xi]$$
$$+a_5\; g(X,\varphi)[\{(n-1)f_1 + 3f_2 - f_3\} - \{3f_2 + (n-2)f_3\}\eta(Y)\xi\;]$$
$$+ a_6\; g(X,Y)[\{(n-1)f_1 + 3f_2 - f_3\}\varphi Z\;]$$
$$+ a_7 r[g(Y,\varphi Z)X \;-\; g(X,\varphi Z)Y]. \qquad (3.3)$$

Also

$$\varphi\;(\tau(X,Y)\;Z) \;=\; \varphi(a_0 R(X,Y)Z \;+\; a_1\; S(Y,Z)X + \; a_2\; S(X,Z)Y$$
$$+ a_3\; S(X,Y)Z \;+\; a_4\; g(Y,Z)QX \;+\; a_5\; g(X,Z)Q\; Y$$
$$+ \; a_6\;\; g(X,Y)\; QZ \;+ a_7\; r[g(Y,Z)X \;+\; g(X,Z)Y]). \qquad (3.4)$$

Using (2.1), (2.2) and (2.3) in (3.4) we get

$$\varphi(\tau(X,Y)\;Z) = \; a_0\;\;[f_1\; g(Y,Z)\;\varphi X - g(X,Z)\;\varphi Y\} + \; f_2 g(X,\varphi Z)\varphi^2 Y - g(Y,\varphi Z)\varphi^2 X$$
$$+ 2g(X,\varphi Y)\varphi^2 Z\} + f_3\;\eta(X)\eta(Z)\varphi Y - \eta(Y)\eta(Z)\;\varphi X\;\}]$$
$$+ a_1\;[\{(n-1)f_1 + 3f_2 - f_3\}g(Y,Z) - \{3f_2 + (n-2)f_3]\eta(Y)\eta(Z)\}]\;\varphi X$$
$$+ a_2\;[\{(n-1)f_1 + 3f_2 - f_3\}g(X,Z) - \{3f_2 + (n-2)f_3]\eta(X)\eta(Z)\}]\;\varphi Y$$

$$+a_3\ [\{(n-1)f_1+3f_2-f_3\}g(X,Y)-\{3f_2+(n-2)f_3]\eta(X)\eta(Y)\backslash\}\ \varphi Z$$

$$+\ a_4\ g(Y,Z)\{(n-1)f_1+3f_2-f_3\}\ \varphi X$$

$$+\ a_5\ g(X,Z)\{(n-1)f_1+3f_2-f_3\}\ \varphi Y$$

$$+\ a_6\ g(X,Y)[\{(n-1)f_1+3f_2-f_3\}\ \varphi Z\ ]$$

$$+\ a_7 r[g(Y,Z)\ \varphi\ X\ -\ g(X,Z)\ \varphi Y]. \qquad (3.5)$$

Using (3.3) and (3.5) in (3.1) we get

$$\begin{aligned}\tau(X,Y).\varphi Z\ =\ a_0\ [&f_1\ \{g(Y,\varphi\ Z)X-g(X,\varphi Z)Y-g(Y,Z)\varphi X+g(X,Z)\varphi Y\}\\ &+\ f_2\{g(X,\varphi^2 Z)\varphi Y-g(Y,\varphi^2 Z)\varphi X\ +g(X,\varphi Z)\varphi^2 Y+g(Y,\varphi Z)\varphi^2 X\ \}\\ &+\ f_3\{g(X,\varphi Z)\eta(Y)\xi-g(Y,\varphi Z)\eta(X)\xi-\eta(X)\eta(Z)\varphi Y+\eta(Y)\eta(Z)\varphi X\ \}]\end{aligned}$$

$$+\ a_1[\{(n-1)f_1+3f_2-f_3\}\{g(Y,\varphi Z)X-\ g(Y,Z)\varphi X\}+\ \{3f_2+(n-2)f_3\}\eta(Y)\eta(Z)\varphi]$$

$$+\ a_2[\{(n-1)f_1+3f_2-f_3\}\{g(X,\varphi Z)Y-\ g(X,Z)\varphi Y\}+\ \{3f_2+(n-2)f_3\}\eta(X)\eta(Z)\varphi Y]$$

$$\begin{aligned}+\ a_4[&\{(n-1)f_1+3f_2-f_3\}\{g(Y,\varphi Z)X-\ g(Y,Z)\varphi X\}\\ &-\ \{3f_2+(n-2)f_3\}g(Y,\varphi Z)\eta(X)\xi]\end{aligned}$$

$$\begin{aligned}+\ a_5[&\{(n-1)f_1+3f_2-f_3\}\{g(X,\varphi Z)Y-\ g(X,Z)\varphi Y\ \}\\ &-\{3f_2+(n-2)f_3\}g(X,\varphi Z)\eta(Y)\xi]\end{aligned}$$

$$+\ a_7 r[g(Y,\varphi Z)X\ -\ g(X,\varphi Z)Y\ -\ g(Y,Z)\varphi\ +\ g(X,Z)\varphi Y]. \qquad (3.6)$$

Putting $Y=\xi$ in (3.6) we get

$$\tau\ (X,\xi).\varphi\ Z=\ -a_0\ (f_1-\ f_3)[g(X,\varphi Z)\xi\ +\ \eta\ (Z)\varphi X]$$

$$-\ a_1(n-1)(f_1-\ f_3)\eta(Z)\varphi X$$

$$+\ a_2\ [(n-1)f\_1\ +3f_2\ -\ f\_3)]g(X,\varphi Z)\ \xi$$

$$-\ a_4\ \{(n-1)f_1+3f_2-f_3\}\eta\ (Z)\varphi X$$

$$+\ a_5(n-1)(f_1-\ f_3)\ g(X,\varphi Z)\ \xi$$

$$-\ a_7\ \ r[g(X,\varphi Z)\ \xi\ +\ \eta(Z)\ \varphi X]. \qquad (3.7)$$

Again putting $Z=\xi$ in (3.7) we get

$$\tau\ (X,\xi).\varphi\ \xi\ =\ [\ -a_0\ (f_1-\ f_3)-\ a_1(n-1)(f_1-\ f_3)$$

$$-a_4\ \{(n-1)f_1+3f_2-f_3\}-\ a_7\ \ r\ ]\ \varphi X. \qquad (3.8)$$

For $\varphi-\tau$-semisymmetric we have

$$-a_0\ (f_1-\ f_3)\ +\ a_1(n-1)(f_1-\ f_3)$$

$$+\ a_4\ \{(n-1)f_1+3f_2-f_3\}\ +\ a_7 r\ \ =\ 0. \qquad (3.9)$$

This proves the theorem.

Particularly from (3.8) we have the following results

$$R(X,\xi).\varphi\,\xi = -(f_1 - f_3)\,\varphi X, \tag{3.10}$$

$$C(X,\xi).\varphi\,\xi = \frac{3f_2+(n-2)f_3}{n}\,[\,a_0 + (n-2)a_1\,]\,\varphi X, \tag{3.11}$$

$$\tilde{C}(X,\xi).\varphi\,\xi = 0, \tilde{C}(X,\xi).\varphi\,\xi = 0, \tag{3.12}$$

$$\hat{C}(X,\xi).\varphi\,\xi = \frac{nf_1+3f_2-2f_3}{n-2}\,\varphi X, \tag{3.13}$$

$$\dot{C}(X,\xi).\varphi\,\xi = \frac{3f_2+(n-2)f_3}{n}\,\varphi X, \tag{3.14}$$

$$P(X,\xi).\varphi\,\xi = \frac{3f_2+(n-2)f_3}{n}\,[\,a_0 + (n-1)a_1\,]\,\varphi X, \tag{3.15}$$

$$\tilde{P}(X,\xi).\varphi\,\xi = 0, \tag{3.16}$$

$$M(X,\xi).\varphi\,\xi = \frac{nf_1+3f_2-2f_3}{2(n-1)}\,\varphi X, \tag{3.17}$$

$$W_0(X,\xi).\varphi\,\xi = 0, \tag{3.18}$$

$$W_0^*(X,\xi).\varphi\,\xi = -2(f_1 - f_3)\varphi X, \tag{3.19}$$

$$W_1(X,\xi).\varphi\,\xi = -2(f_1 - f_3)\varphi X, \tag{3.20}$$

$$W_1^*(X,\xi).\varphi\,\xi = 0, \tag{3.21}$$

$$W_2\,(X,\xi).\varphi\,\xi = \frac{3f_2+(n-2)f_3}{n-1}\,\varphi X, \tag{3.22}$$

$$W_3\,(X,\xi).\varphi\,\xi = -\frac{2(n-1)f_1-3f_2+nf_3}{n-1}\,\varphi X, \tag{3.23}$$

$$W_4\,(X,\xi).\varphi\,\xi = -(f_1 - f_3)\varphi X, \tag{3.24}$$

$$W_5(X,\xi).\varphi\,\xi = -(f_1 - f_3)\varphi X, \tag{3.25}$$

$$W_6(X,\xi).\varphi\,\xi = 0, \tag{3.26}$$

$$W_7(X,\xi).\varphi\,\xi) = -\frac{(n-1)f_1+3f_2-f_3}{n-1}\,\varphi X, \tag{3.27}$$

$$W_8(X,\xi).\varphi\,\xi = 0, \tag{3.28}$$

$$W_9(X,\xi).\varphi\,\xi = \frac{3f_2+(n-2)f_3}{n-1}\,\varphi X. \tag{3.29}$$

From the equations (3.10)- (3.29) we have

Corollary 3.1. In a generalized Sasakian-space-form, we have the following conditions and results

Conditions	**Results**
φ-semisymmetric	$f_1 = f_3$
$\varphi - W_0^*$ semisymmetric	$f_1 = f_3$
$\varphi - W_1$ semisymmetric	$f_1 = f_3$
$\varphi - W_4$ semisymmetric	$f_1 = f_3$
$\varphi - W_5$ semisymmetric	$f_1 = f_3$
$\varphi - \dot{C}$ semisymmetric	$f_3 = \frac{3f_2}{2-n}$

$\varphi - W_2$ semisymmetric	$f_3 = \frac{3f_2}{2-n}$
$\varphi - W_9$ semisymmetric	$f_3 = \frac{3f_2}{2-n}$
$\varphi - M$ semisymmetric	$nf_1 + 3f_2 - 2f_3 = 0$
$\varphi - \hat{C}$ semisymmetric	$nf_1 + 3f_2 - 2f_3 = 0$
$\varphi - P$ semisymmetric	$f_3 = \frac{3f_2}{2-n}$ $or\ a_0 = (2-n)a_2$
$\varphi - C$ semisymmetric	$f_3 = \frac{3f_2}{2-n}$ $or\ a_0 = (1-n)a_2$
$\varphi - W_3$ semisymmetric	$2(n-1)f_1 + 3f_2 - nf_3$
$\varphi - W_7$ semisymmetric	$(n-1)f_1 + 3f_2 - f_3$

Corollary 3.2. In a generalized Sasakian-space-form, we have $\hat{C}(X,\xi).\varphi\,\xi = 0$, $\tilde{P}(X,\xi).\varphi\,\xi = 0$, $W_0(X,\xi).\varphi\,\xi = 0$, $W_1^*(X,\xi).\varphi\,\xi = 0$, $W_6(X,\xi).\varphi\,\xi = 0$ and $W_8(X,\xi).\varphi\,\xi = 0$.

De and Sarkar (2010) studied the projective curvature tensor in generalized Sasakian-space-form and proved the following theorems

Theorem 4.2. An n-dimensional generalized Sasakian-space-form is projectively semisymmetric if and only if $f_1 = f_3$.

Corollary 3.3. An n-dimensional φ-semisymmetric, $\varphi - W_0^*$ semisymmetric, $\varphi - W_1$ semisymmetric, $\varphi - W_4$ semisymmetric and $\varphi - W_5$ semisymmetric generalized Sasakian-space-form are projectively semisymmetric.

GENERALIZED SASAKIAN-SPACE-FORM SATISFYING $\tau\,.Z = 0$

Theorem 4.1. In a generalized Sasakian-space-form satisfying $\tau\,.Z = 0$, one of the following is true,

1. $a_1 + a_2 + a_3 + a_4 + a_5 + a_6 = 0$
2. $f_1 = f_3$
3. $(n-1)(f_1 - f_3) + \varphi_1 = 0.$

Proof. In this section we consider generalized Sasakian-space-form satisfying

$$\tau\,(X,Y).Z)(U,V) = 0. \tag{4.1}$$

Equation (4.1) implies

$$\tau\,(\xi,Y).Z)(U,\xi) = 0.$$

It is known that

$$\tau\,(\xi,Y).Z)(U,\xi) = Z(\tau(\xi,X)Y,\xi) + Z(Y,\tau(\xi,X)\xi). \tag{4.2}$$

Then using (1.23) in (4.2) we obtain

$$\tau\,(\xi,Y).Z)(U,\xi) = = S\,(\tau\,(\xi,X)Y,\xi) + \varphi_1\,\eta\,(\tau\,(\xi,X)Y)$$

$$+ S\,(Y,\tau\,(\xi,X)\,\xi) + \varphi_1 g(Y,\tau\,(\xi,X)\,\xi). \tag{4.3}$$

From (1.2) we have

$$\tau\,(\xi,X)\,Y = a_0\,R(\xi,X)\,Y + a_1\,S(X,Y)\,\xi + a_2\,S(\xi,Y)X$$

$$+ a_3\, S(\xi,X)Y + a_4\, g(X,Y)\, Q\, \xi + a_5\, g(\xi,Y)QX$$

$$+ a_6\, g(\xi,X)\, QY + a_7 r[g(X,Y)\, \xi - g(\xi,Y)X]. \tag{4.4}$$

Using (2.2), 2.3), (2.4), (2.5) and (2.7) in the above equation we get

$$\tau\,(\xi,X)Y = a_0\, (f_1 - f_3)[g(X,Y)\xi - \eta(Y)X]$$

$$+ a_1\, [\{(n-1)f_1 + 3f_2 - f_3\}g(X,Y) - \{3f_2 + (n-2)f_3]\eta(X)\eta(Y)\}]\xi$$

$$+ a_2\, (n-1)(f_1 - f_3)\eta(Y)X$$

$$+ a_3\, (n-1)(f_1 - f_3)\eta(X)Y$$

$$+ a_4\, (n-1)(f_1 - f_3)g(X,Y)\xi$$

$$+ a_5\, [\{(n-1)f_1 + 3f_2 - f_3\}X - [3f_2 + (n-2)f_3\}\eta(X)\xi\,]\eta(Y)$$

$$+ a_6[\{(n-1)f_1 + 3f_2 - f_3\}Y - \{3f_2 + (n-2)f_3\}\eta(Y)\xi\,]\eta(X)$$

$$+a_7 r[g(X,Y)\xi - \eta(Y)X]. \tag{4.5}$$

Using the above equation we obtain

$$S\{\,\tau\,(\xi,X)\,Y,\xi\} = a_0\, (f_1 - f_3)\, [g(X,Y)S\,\xi,\xi) - \eta\,(Y)S(X\,\xi)]$$

$$+ a_1\, [\{(n-1)f_1 + 3f_2 - f_3\,\}g(X,Y) - \{3f_2 + (n-2)f_3]\,\eta(X)\,\eta(Y)\}]S(\xi,\xi)$$

$$+ a_2\, (n-1)(f_1 - f_3)\, \eta(Y)S(X,\xi)$$

$$+ a_3(n-1)(f_1 - f_3)\, \eta(X)S(Y,\xi)$$

$$+ a_4\, (n-1)(f_1 - f_3)g(X,Y)S(\xi,\xi)$$

$$+ a_5[\{(n-1)f_1 + 3f_2 - f_3\}(X,\xi) - [3f_2 + (n-2)f_3\,\}\, \eta(X)S(\xi,\xi)]\, \eta(Y)$$

$$+ a_6\, [\{(n-1)f_1 + 3f_2 - f_3\}S(Y,\xi) - \{3f_2 + (n-2)f_3\}\, \eta(Y)S(\xi,\xi)]\, \eta(X)$$

$$+ a_7 r[g(X,Y)S(\xi,\xi) - \eta(Y)S(X,\xi)]. \tag{4.6}$$

Using (2.4) in (4.6) we obtain

$$S\{\,\tau\,(\xi,X)\,Y,\xi\} = a_0\, (n-1)(f_1 - f_3)^2\, [g(X,Y) - \eta(X)\eta(Y)]$$

$$+ a_1\, (n-1)(f_1 - f_3)\, [(n-1)f_1 + 3f_2 - f_3\}g(X,Y)$$

$$-\{3f\_2 + (n-2)f\_3]\eta(X)\eta(Y)\}]$$

$$+ (\, a_2 + a_3 + a_5 + a_6\,)\, (n-1)^2(f_1 - f_3)^2\, \eta(X)\eta(Y)$$

$$+ a_4\, (n-1)^2(f_1 - f_3)^2 g(X,Y)$$

$$+ a_7(n-1)(f_1 - f_3)r[g(X,Y) - \eta(X)\eta(Y)]. \tag{4.7}$$

From (4.5) we have

$$\eta(\,\tau\,(\xi,X)\,Y) = a_0\, (f_1 - f_3)[g(X,Y) - \eta(X)\eta(Y)$$

$$+ a_1 [\{(n-1)f_1 + 3f_2 - f_3 \}g(X,Y)$$

$$-\{3f_2 + (n-2)f_3]\eta(X)\eta(Y)\}$$

$$+ (a_2 + a_3 + a_5 + a_6)\ (n-1)(f_1 - f_3)\ \eta(X)\eta(Y)$$

$$+ a\_4\ (n-1)(f_1 - f_3)g(X,Y)$$

$$+ a_7 r[g(X,Y) - \eta(X)\eta(Y)]. \tag{4.8}$$

Again from (4.5) we have

$$\tau\ (\xi,X)\ \ \xi = a_0\ (f_1 - f_3)[\eta(X)\xi - X] + a_2\ (n-1)(f_1 - f_3)X$$

$$+ (a_1 + a_3 + a_4 + a_6)\ (n-1)(f_1 - f_3)\eta(X)\xi$$

$$+a_5\ [\{(n-1)f_1 + 3f_2 - f_3\}X$$

$$-[3f_2 + (n-2)f_3\}\eta(X)\xi\ ]$$

$$+a_7 r[\eta(X)\xi - X]. \tag{4.9}$$

From the above equation we obtain

$$S(Y,\tau\ (\xi,X)\ \ \xi) = a_0\ (f_1 - f_3)\ [\eta(X)S(Y,\xi) - S(Y,X)]$$

$$+ a_2\ (n-1)(f_1 - f_3)S(Y,X)$$

$$+ (a_1 + a_3 + a_4 + a_6)\ (n-1)(f_1 - f_3)\eta(X)S(Y,\xi)$$

$$+ a_5\ \ [\{(n-1)f_1 + 3f_2 - f_3\}S(Y,X)$$

$$- [3f_2 + (n-2)f_3\ \}\eta(X)S(Y,\xi)]$$

$$+ a_7[\eta(X)S(Y,\xi) - S(Y,X)]. \tag{4.10}$$

Using (2.2) and (2.4) in the above equation we get

$$S(Y,\tau\ (\xi,X)\ \ \xi) = a_0\ \ (f_1 - f_3)\ \{(n-1)f_1 + 3f_2 - f_3\} \times \{\eta(X)\eta(Y) - g(X,Y)\ \}$$

$$+ a_2\ (n-1)(f_1 - f_3)\ [\{(n-1)f_1 + 3f_2 - f_3\}g(X,Y)$$

$$- \{3f_2 + (n-2)f_3\ \}\eta(X)\eta(Y)]$$

$$+ (a_1 + a_3 + a_4 + a_6)\ (n-1)^2(f_1 - f_3)^2\eta(X)\eta(Y)$$

$$+ a_5\ [\{(n-1)f_1 + 3f_2 - f_3\ \}[\{(n-1)f_1 + 3f_2 - f_3\ \}g(X,Y)$$

$$-\{\ 3f_2 + (n-2)f_3\ \}\eta(X)\eta(Y)]$$

$$-(n-1)(f_1 - f_3)\ \{3f_2 + (n-2)f_3\}\eta(X)\eta(Y)]$$

$$+ a_7 r\ [\{(n-1)f_1 + 3f_2 - f_3\ \}\ \{\eta(X)\eta(Y) - g(X,Y)\}]. \tag{4.11}$$

Also from (4.9) we get

$$g\ (Y,\tau\ (\xi,X)\ \ \xi) = a_0\ (f_1 - f_3)\ [\eta(X)\eta(Y) - g(Y,X)]$$

$$+ a_2\,(n-1)(f_1-f_3)g(Y,X)$$

$$+ (a_1+a_3+a_4\,+\,a_6)\,(n-1)(f_1-f_3)\eta(X)\eta(Y)$$

$$+ a_5\,[\{(n-1)f_1+3f_2-f_3\,\}g(Y,X)$$

$$-\{3f_2+(n-2)f_3\}\eta(X)\eta(Y)\,]$$

$$+ a_7 r[\eta(X)\eta(Y)\;-\;g(Y,X)]. \tag{4.12}$$

Using (4.7), (4.8), (4.11) and (4.12) in (4.3) we get

$$(\tau\,(\xi,X)\;.Z)(Y,\xi)\;=a_0\,(f_1-f_3)\{3f_2+(n-2)f_3\}\times\{\,\eta(X)\,\eta(Y)-g(X,Y)\}$$

$$+ (a_1+\;a_2)\,(n-1)(f\_1-f\_3)[\{(n-1)f_1+3f_2-f_3\}g(X,Y)$$

$$-\{3f_2+(n-2)f_3\}\,\eta(X)\,\eta(Y)\}]$$

$$+ (a_1+\;a_2+\;2a_3+a_4+a\_5+\;2a_6)\,(n-1)^2(f_1-f_3)^2\,\eta\,(X)\,\eta(Y)$$

$$+ a_4\,(n-1)^2(f_1-f_3)^2g(X,Y)$$

$$+a_5[\{(n-1)f_1+3f_2-f_3\}[\{(n-1)f_1+3f_2-f_3\}g(X,Y)$$

$$-\{3f_2+(n-2)f_3\}\,\eta(X)\,\eta(Y)]$$

$$-(n-1)(f_1-f_3)\{3f_2+(n-2)f_3\}\,\eta(X)\,\eta(Y)\,]$$

$$+ a_7 r\{3f_2+(n-2)f_3\}\{\,\eta(X)\,\eta(Y)\;-\;g(X,Y)\}$$

$$+ \varphi_1[\,a\_1\;\;[\{(n-1)f_1+3f_2-f_3\}g(X,Y)$$

$$-\{3f_2+(n-2)f_3]\,\eta(X)\,\eta(Y)\,\}]$$

$$+ (a_1+\;a_2+\;2a_3+a_4+a\_5+\;2a_6)\,(n-1)(f_1-f_3)\,\eta(X)\,\eta(Y)$$

$$+ (a_2+a_4)\,(n-1)(f_1-f_3)g(X,Y)$$

$$+ a\_5\;\;[\{(n-1)f_1+3f_2-f_3\,\}g(Y,X)$$

$$-\{3f_2+(n-2)f_3\}\eta(X)\,\eta(Y)]. \tag{4.13}$$

Putting $Y=\xi$ in (4.13) we get

$$(\tau\,(\xi,X)\;.Z)(\xi,\xi)\;=\;2(a_1+\;a_2+\;a_3+a_4+a_5+\;a_6)\,(n-1)^2(f_1-f_3)^2\,\eta(X)$$

$$+ \varphi_1\,[2((a_1+\;a_2+\;a_3+a_4+a_5+\;a_6)\,(n-1)(f_1-f_3)\,\eta(X)\,],$$

or

$$(\tau\,(\xi,X)\;.Z)(\xi,\xi)\;\;=\;2(a_1+\;a_2+\;a_3+a_4+a_5+\;a_6)(n-1)(f_1-f_3)$$

$$\times\,\eta(X)\,\{(n-1)(f_1-f_3)\;+\;\varphi_1\}. \tag{4.14}$$

For Sasakian-space-form satisfying $\tau\;.Z\;=\;0$ we have

$$2(a_1 + a_2 + a_3 + a_4 + a_5 + a_6)\,(n-1)(f_1 - f_3)\;\eta(X)$$

$$\times\{(n-1)(f_1 - f_3) + \varphi_1\} = 0,$$

or

$$(a_1 + a_2 + a_3 + a_4 + a_5 + a_6)(f_1 - f_3)\,\{(n-1)(f_1 - f_3) + \varphi_1\} = 0.$$

Thus we have either

$$a_1 + a_2 + a_3 + a_4 + a_5 + a_6 = 0$$

or

$$f_1 = f_3$$

or

$$(n-1)(f_1 - f_3) + \varphi_1 = 0. \tag{4.15}$$

This proves the theorem.

Theorem 4.2. In a generalized Sasakian space form satisfying $\tau\,.S = 0$, either $a_1 + a_2 + a_3 + a_4 + a_5 + a_6 = 0$ or $f_1 - f_3 = 0$.

Proof. It is known that when $\varphi_1 = 0, Z = S$. Now putting $\varphi_1 = 0$ in (4.14) we get

$$(\tau\,(\xi,X)\,.S)(\xi,\xi) = 2(a_1 + a_2 + a_3 + a_4 + a_5 + a_6)$$

$$\times\,(n-1)^2(f_1 - f_3)^2\,\eta(X) \tag{4.16}$$

Therefore $\tau\,.S = 0$ implies

$$(a_1 + a_2 + a_3 + a_4 + a_5 + a_6)(f_1 - f_3)^2 = 0.$$

This proves theorem 4.2.

Using the conditions (1.3)-(1.22) in (4.14) we have the following

Corollary 4.1. In a generalized Sasakian-space-form,

$\{R(\xi,X)Z\}(\xi,\xi)$, $\{C(\xi,X)Z\}(\xi,\xi)$, $\{\tilde{C}(\xi,X)Z\}(\xi,\xi)$, $\{\hat{C}(\xi,X)Z\}(\xi,\xi)$, $\{\dot{C}(\xi,X)Z\}(\xi,\xi)$, $\{P(\xi,X)Z\}(\xi,\xi)$, $\{\tilde{P}(\xi,X)Z\}(\xi,\xi)$ and $\{M(\xi,X)Z\}(\xi,\xi)\{M(\xi,X)Z\}(\xi,\xi)$ all vanishes.

REFERENCES

Alegre P, Blair DE, Carriazo A (2004) Generalized Sasakian-space-forms. Israel journal of Mathematics 141(1): 157-183.

Alegre P, Carriazo A (2018) Semi-Riemannian Generalized Sasakian Space Forms. Bulletin of the Malaysian Mathematical Sciences Society 41: 1-14.

Bagewadi CS, Ingalahalli G (2014) A Study on Curvature tensors of a Generalized Sasakian space form. Acta Universitatis Apulensis 38: 81-93.

Chaubey SK (2018) Certain results on N(k)-quasi Einstein manifolds. Afrika Matematika. https://doi.org/10.1007/s13370-018-0631-z.

De UC, Majhi P (2013) Certain curvature properties of generalized Sasakian-space-forms. Proceedings of the National Academy of Sciences, India Section A: Physical Sciences 83(2): 137-141.

De UC, Pal P (2014) On almost pseudo-Z-symmetric manifolds. Acta Universitatis Palackianae Olomucensis. Facultas Rerum Naturalium. Mathematica 53(1): 25-43.

De UC, Sarkar A (2012) On the conharmonic curvature tensor of generalized Sasakian-space-forms. ISRN Geometry. https://doi:10.5402/2012/876276.

De UC, Sarkar A (2010) On the projective curvature tensor of generalized Sasakian-space-forms. Quaestiones Mathematicae 33(2): 245-252.

De UC, Majhi P (2019) On the Q curvature tensor of a generalized Sasakian-space-form. Kragujevac Journal of Mathematics 43(3): 333-349.

De UC, Majhi P (2015) φ-semisymmetric generalized Sasakian space-forms. Kragujevac Journal of Mathematics 21(1): 170-178.

Kishor S, Verma P, Gupta PK (2017) On W_9 -Curvature Tensor of Generalized Sasakian-Space-Forms. International Journal of Mathematics and its Applications 5: 103-112.

Kumari A, Chanyal SK (2015) On the T Curvature Tensor of Generalized Sasakian space form. IOSR Journal of Mathematics 11(3): 61-68.

Mallick S, De UC (2016) Z Tensor on N(k)-Quasi-Einstein Manifolds. Kyungpook Math. J. 56: 979-991.

Mantica CA, Suh YJ (2012a) Pseudo Z symmetric Riemannian manifolds with harmonic curvature tensors. Int J of Geometric Methods in Modern Physics 9(1): 1250004.

Mantica CA, Su, YJ (2012b) Recurrent Z forms on Riemannian and Kaehler manifolds. International Journal of Geometric Methods in Modern Physics 9(07): 1250059.

Mantica CA, Molinari LG (2012) Weakly Z-symmetric manifolds. Acta Mathematica Hungarica 135(1-2): 80-96.

Sarkar A, De UC (2012) Some curvature properties of generalized Sasakian-space-forms. Lobachevskii Journal of Mathematics 33(1): 22-27.

Singh JP (2016 a) Generalized Sasakian space forms with m-projective curvature tensor. Acta Math. Univ. Comenianae 85(1), 135-146.

Singh JP (2016 b) On a type of generalized Sasakian space forms. Journal of the Indian Math. Soc. 83(3-4): 363-372.

Tripathi MM, Gupta P (2011) T-curvature tensor on a semi-Riemannian manifold. J. Adv. Math. Stud 4(1): 117-129.

Science and Technology Journal Vol. 8 Issue 2 July 2020 ISSN: 2321-3388

Homotopy Analysis of Circular Plates Squeeze Film Bearings Lubricated with Couple Stress Fluids: Piezo-Viscous Model

J.P. Tripathi[1], U.P. Singh[2*] and B.K. Singh[3]
[1]Department of Mathematics, R.N. College, Hajipur (Vaishali), Bihar, India
[2]Department of Applied Sciences, Rajkiya Engineering College, Sonbhadra, Uttar Pradesh, India
[3]Department of Mathematics, Amity University, Raipur, Chhattishgarh, India
E-mail: *upsingh@recsonbhadra.ac.in

Abstract—The piezo-viscous effect is crucial in fluid flows under high-pressure applications such as fluid film lubrication, microfluidics, and geophysics. We have investigated the combined influences of piezo-viscous dependence and non-Newtonian couple stresses on the performance of circular plate squeeze film bearings using Stokes Micro-Continuum theory of couple stress fluids together with the exponential variation of viscosity with pressure. A closed-form solution for film pressure has been obtained using the homotopy analysis method. The numerical results for pressure and load capacity with different values of the viscosity-pressure parameter have been calculated and compared with iso-viscous couple stress and Newtonian lubricants. An enhanced pressure and load capacity are observed in the analysis. The response time for the bearing (plate approach time) has also been calculated and a significant increase is observed.

Keywords: Couple Stress Fluids; Hydrodynamic Bearings; Hydrodynamic Lubrication; Load-Carrying Capacity; Non-Newtonian Effects in Hydrodynamics; Squeeze-Film Lubrication; Viscosity-Pressure

INTRODUCTION

The squeeze film lubrication is observed to play a very important role in applications of engineering and technology such as ball bearings, matching gears, machine tools, rolling elements, and automotive engines. The squeeze film action is also seen during the approach of faces of disc clutches under lubricated conditions. The mechanical action (squeezing, shearing, etc.) changes the lubricants' temperature as well as viscosity and density (Dowson 1961; Wada and Hayashi 1971; Yadav and Kapur 1981; Singh et al. 2011b). The viscosity of lubricants depends much on pressure than the temperature (Rajagopal 2006). In such a high-pressure mechanism, the variation of viscosity is also more significant over the density variation (Rajagopal 2006; Renardy 2003). Denn (2008) emphasized that under a pressure of about 5 MPa, the dependence of viscosity on pressure become important even if the flow is incompressible. Therefore, it is reasonable to analyze the bearing performance with a pressure-dependent viscosity (Kalogirou et al. 2011) considering the isothermal, incompressible flow of lubricants of the form:

$$\mu = \mu_0 e^{\beta p} \tag{1}$$

where μ is the viscosity, p is the pressure, μ_0 is the viscosity at atmospheric pressure, and β is the pressure-viscosity coefficient. Kottke et al. (2003) reported the range of β between 10 to 70 $M\,Pa^{-1}$ for lubricants. Venner and Lubrecht (2000) reported that β may range between 10^{-8} to 2 × $10^{-8}\,Pa^{-1}$ for mineral oils. Bair et al. (2006) shown that the viscosity of b is (phenoxyphenoxy) benzene varies from 0.0251 Pa.s to 72 *Pa.s* under pressure variation $0.1-300MPa$, and the viscosity of dipentaerythritol hexaisostearate varies from 0.0251 *Pa.s* to 66.2 *Pa.s* with pressure variation 0.1942 *MPa* under isothermal condition.

The investigation of squeeze film characteristics between rectangular, porous rectangular, curved circular plates, etc. has been done time to time by various researchers using the classical Newtonian model (Burbidge and Servais 2004; Sunny 1994; Abell and Ames 1992; Gupta and Vora 1980; Gupta and Gupta 1977; Murti 1975; Wu 1972). (Singh and Gupta 2012; Singh et al. 2013b) investigated the squeezing characteristics of thin films between the sphere plate and cylinder-plate systems with cubic stress (Rabinowitsch) stress-strain model) and reported and presented cavitation analysis. After Stokes (1966) proposed micro-continuum theory (couple stresses in fluids) accounting the particle size effects of microstructures in lubricants, many researchers investigated the effect of couple stresses on the squeeze film characteristics of various systems. Manivasakan and Sumathi (2011) studied the effect of couple stress on squeezing films between curved circular plates. (Naduvinamani et al. 2005, 2015) studied the roughness and couple stress effect on squeezing plates and the sphere-plate system. Lin et al. (2008) analyzed the squeeze film characteristics between two different spheres. Some other authors also used couple stress fluids to study journal bearings under different hydrodynamic conditions (Nada and Osman 2007; Chiang et al. 2004; Ma et al. 2004). Singh (2014) presented and detailed mathematical analysis of simultaneous influences of couple stress and pressure dependent viscosity on squeezing flow between stepped circular plates. As discussed earlier, the viscosity-pressure dependence is important while studying the high-pressure phenomena in lubrication. In recent years, researchers also focused their attention on account the viscosity-pressure dependence to analyze the lubrication phenomenon. (Singh et al. 2011a,b, 2012, 2013a) analyzed different types of hydrostatic thrust bearings considering Rabinowitsch fluid model, which stabilize fluid under temperature variation. They obtained improved theoretical results for pressure and load capacity. Kalogirou et al. (2011) analyzed incompressible Poiseuille flows of Newtonian liquids with a pressure-dependent viscosity. But none of the researchers considered the piezo-viscous effect on the squeezing characteristics between parallel circular plates with non-Newtonian couple stress effect.

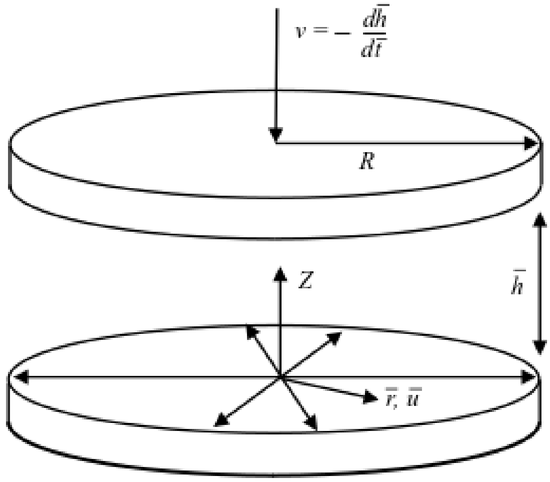

Fig. 1: Systematic Diagram of Circular Plate Squeeze Film Bearing

In the present theoretical investigation, the combined effects of piezo-viscous dependency and non-Newtonian couple stresses in squeezing characteristics between parallel circular plates have been studied. As the problem is non-linear, the Homotopy perturbation analysis (He 2004; Islam et al. 2009) is adopted to derive the closed-form solution for the pressure distribution.

ANALYSIS

The squeeze film lubrication between circular plates approaching each other with a normal velocity $d\bar{h}/d\bar{t}$ is shown in Fig. 1. The lubricant in the system is taken as non-Newtonian incompressible Stokes couple stress fluid (Stokes 1966). The body forces and body couples are assumed to be absent.

CONSTITUTIVE EQUATIONS

The field equations governing the motion of steady laminar couple stress fluid flow in the film region (in polar coordinates), as considered by Singh et al. (Singh et al. 2011b; Singh 2014; Singh et al. 2020), are as:

$$\frac{1}{\bar{r}}\frac{\partial}{\partial \bar{r}}(\bar{r}\,\bar{u}) + \frac{\partial \bar{w}}{\partial \bar{z}} = 0 \tag{2}$$

$$\mu\frac{\partial^2 \bar{u}}{\partial \bar{z}^2} - \eta\frac{\partial^4 \bar{u}}{\partial \bar{z}^4} = \frac{\partial \bar{p}}{\partial \bar{r}} \tag{3}$$

$$\frac{\partial \bar{p}}{\partial \bar{r}} = 0 \tag{4}$$

which are solved under the following boundary conditions

$$\bar{u} = \frac{\partial^2 \bar{u}}{\partial \bar{z}^2} = 0, \bar{w} = 0 \text{ at } \bar{z} = 0 \text{ and } \bar{u} = \frac{\partial^2 \bar{u}}{\partial \bar{z}^2} = 0, \bar{w} = -\frac{\partial \bar{h}}{\partial \bar{t}} \; at \; \bar{z} = \bar{h}$$

; where $\bar{u}$ and $\bar{w}$ are the velocity components in $\bar{x}$ and $\bar{z}$ directions, $\bar{h}$ is the film thickness between the bearings plates, μ is viscosity given by equation (1) and η is new material constant responsible for couple stresses in the fluids.

Taking the dimensionless quantities as

$$p = \frac{\bar{p}\bar{h}_o^3}{\mu_0 R^2 (d\bar{h}/d\bar{t})},\; r = \frac{\bar{r}}{R},\; z = \frac{\bar{z}}{h_o},\; u = \frac{\bar{u}h_o}{R(d\bar{h}/d\bar{t})},$$

$$w = \frac{\bar{w}}{(d\bar{h}/d\bar{t})},$$

$$\alpha = \frac{\beta\mu_o R^2 (d\bar{h}/d\bar{t})}{h_o^3},\; h = \frac{\bar{h}}{h_o},\; \mu = \frac{\bar{\mu}}{\mu_o} \; and \; \nu = \frac{1}{h_o}\sqrt{\frac{\eta}{\mu_o}}$$

the equations (1-4) take the dimensionless form

$$\mu = e^{\alpha p} \tag{5}$$

$$\frac{1}{r}\frac{\partial}{\partial z}(ru) + \frac{\partial w}{\partial z} = 0 \tag{6}$$

$$\mu\frac{\partial^2 u}{\partial z^2} - \nu^2\frac{\partial^4 u}{\partial z^4} = \frac{\partial p}{\partial r} \tag{7}$$

$$\frac{\partial p}{\partial z} = 0 \tag{8}$$

and the related boundary conditions become

$$u = \frac{\partial^2 u}{\partial z^2} = 0,\quad w = 0 \quad at\ z = 0;\quad u = \frac{\partial^2 u}{\partial z^2} = 0,\quad w = -1\ at\ z = h\,.$$

SOLUTION OF CONSTITUTIVE EQUATIONS

Solving equations (7) under the discussed boundary conditions, the radial velocity profile is obtained as:

$$u = \frac{1}{2\mu}\frac{\partial p}{\partial r}(z^2 - zh) + \frac{\nu^2}{\mu^2}\frac{\partial p}{\partial r}\left[1 - \frac{\cosh\left(\frac{\sqrt{\mu}}{\nu}\left(z - \frac{h}{2}\right)\right)}{\cosh\left(\frac{\sqrt{\mu}}{\nu}\frac{h}{2}\right)}\right] \tag{9}$$

Integrating equation (6) for w with the relevant boundary conditions using equations (5, 9), the modified Reynolds equation is obtained as

$$\frac{d}{dr}\left(r\,f\,(h,\alpha,\nu,p)\frac{dp}{dr}\right) = -12r \tag{10}$$

where

$$f\,(h,\alpha,\nu,p) = h^3 e^{-\alpha p} - 12h\nu^2 e^{-2\alpha p} + 24\nu^3 e^{-\frac{5}{2}\alpha p}\tanh\left(\frac{h}{2\nu}e^{\frac{1}{2}\alpha p}\right) \tag{11}$$

HOMOTOPY ANALYSIS METHOD (HAM)

The homotopy analysis method (HAM) is the combination of classical perturbation and homotopy technique. The basic idea of HAM to solve nonlinear equations is outlined as follows.

Let,

$$A(u) = f(\tau),\ \tau \in \Omega \tag{12}$$

be a non-linear differential equation with boundary conditions

$$B\left(u, \frac{\partial u}{\partial n}\right) = 0,\quad \tau \in \Gamma \tag{13}$$

where Ω is the domain of definition, Γ is the boundary of Ω and $\frac{\partial u}{\partial n}$ is the derivative of u in the outward drawn normal to the boundary Ω.

The operator L can be written as a combination of a linear operator N and a nonlinear operator Λ so that the equation (12) can be written as

$$L(u) + N(u) = f(\tau), \tau \in \Omega \tag{14}$$

the homotopy can be constructed as $w(\tau,\Lambda):\ \Omega \times [0,1] \to \Re$ which satisfies

$$H(w,\Lambda) = 0, \tau \in \Omega \tag{15}$$

$$H(w,\Lambda) = (1-\Lambda)\left[L(w) - L(u_o)\right] + \Lambda\left[A(w) - f(\tau)\right];\ \Lambda \in [0,1] \tag{16}$$

where, $\Lambda \in [0,1]$ is an embedding parameter and $L(u_o)$ is the solution of linear part of the equation.

It is now obvious from the equations (15,16) that

$$H(w,0) = L(w) - L(u_o) = 0 \tag{17}$$

$$H(w,1) = A(u) - f(\tau) = 0 \tag{18}$$

Thus, the variation of Λ from 0 to 1 is just to move from the initial solution to the solution of the original equation. In Topology, it is called the deformation of a continuous function $L(u) - f(\tau)$ to another continuous function $A(u) - f(\tau)$ without violating the boundary conditions (He 2004). It can be noted that the equations (15, 16) can be re-written as

$$L(w) - L(u_o) + \Lambda\left[N(w) + L(u_o) - f(\tau)\right] = 0 \tag{19}$$

Further, in this method, the imbedding parameter is assumed to be $\Lambda < 1$ and the function w is assumed of the series form

$$w = \sum_{j=0}^{\infty} \Lambda^j w_j \tag{20}$$

Now, substituting (20) in (19) gives

$$L\left(\sum_{j=0}^{\infty}\Lambda^j w_j\right) - L(u_o) + \Lambda\left[N\left(\sum_{j=0}^{\infty}\Lambda^j w_j\right) + L(u_o) - f(\tau)\right] = 0 \tag{21}$$

Finally, the desired solution for u is taken as

$$u = \lim_{\Lambda\to 1} w = \sum_{j=0}^{\infty} w_j \tag{22}$$

SOLUTION OF REYNOLDS EQUATION WITH HAM

Expanding $f(h,\alpha,\nu,p)$ in the series in powers of αp, the modified Reynolds equation (10) can be represented as

$$\frac{d}{dr}\left\{r(f_o+\alpha pf_1+\alpha^2p^2f_2+\alpha^3p^3f_3+.........)\frac{dp}{dr}\right\}=-12r \qquad (23)$$

$$\frac{d}{dr}\left(r\frac{dp}{dr}\right)+\frac{d}{dr}\left\{r(\alpha\frac{f_1}{f_o}p+\alpha^2\frac{f_2}{f_0}p^2+\alpha^3\frac{f_3}{f_o}p^3+.........)\frac{dp}{dr}\right\}=-\frac{12r}{f_o} \qquad (24)$$

where, $f_j(j=0,1,2,......)$ are coefficient of powers of αp given by

$$f_o=h^3-12hv^2+24v^3\tanh\left(\frac{h}{2v}\right) \qquad (25)$$

$$f_1=-h^3-30hv^2+60v^3\tanh\left(\frac{h}{2v}\right)-6hv^3\tanh^2\left(\frac{h}{2v}\right) \qquad (26)$$

$$f_2=\frac{1}{2}\left(\begin{array}{l} h^3-75hv^2-3h^2v\tanh\left(\frac{h}{2v}\right)+150v^3\tanh\left(\frac{h}{2v}\right) \\ +27hv^2\tanh^2\left(\frac{h}{2v}\right)+3h^2v\tanh^3\left(\frac{h}{2v}\right)\end{array}\right) \qquad (27)$$

The homotopy for the modified Reynolds equation (24) can be modeled as

$$L(w)-L(p_o)+\Lambda\left[N(w)+L(p_o)-f(\tau)\right]=0 \qquad (28)$$

where,

$$L(w)=\frac{d}{dr}\left(r\frac{dw}{dr}\right),\ f(r)=-\frac{12r}{f_o}$$ and

$$N(w)=\frac{d}{dr}\left\{r\left(\alpha\frac{f_1}{f_o}w+\alpha^2\frac{f_2}{f_0}w^2+\alpha^3\frac{f_3}{f_o}w^3+\cdots\right)\frac{dw}{dr}\right\} \qquad (29)$$

Substituting $w=\sum_{j=0}^{\infty}\Lambda^j w_j$, equation (24) takes the form

$$\sum_{j=0}^{\infty}\Lambda^j\frac{d}{dr}\left(r\frac{dw_j}{dr}\right)-\frac{d}{dr}\left(r\frac{dp_0}{dr}\right)-\Lambda\left[\frac{d}{dr}\left\{r\left(\alpha\frac{f_1}{f_o}\sum_{j=0}^{\infty}\Lambda^j w_j+\alpha^2\frac{f_2}{f_0}\left(\sum_{j=0}^{\infty}\Lambda^j w_j\right)^2\right.\right.\right.$$
$$\left.\left.\left.+\alpha^3\frac{f_3}{f_o}\left(\sum_{j=0}^{\infty}\Lambda^j w_j\right)^3+\cdots\right)\sum_{j=0}^{\infty}\Lambda^j\frac{dw_j}{dr}\right\}+\frac{d}{dr}\left(r\frac{dp_o}{dr}\right)+\frac{12r}{f_o}\right]=0 \qquad (30)$$

Comparing the terms occurring with the same powers of Λ, following system is obtained

$$\Lambda^0:\frac{d}{dr}\left(r\frac{dw_o}{dr}\right)=\frac{d}{dr}\left(r\frac{dp_o}{dr}\right) \qquad (31)$$

$$\Lambda^1:\frac{d}{dr}\left(r\frac{dw_1}{dr}\right)=-\alpha\frac{f_1}{f_o}\frac{d}{dr}\left(rw_o\frac{dw_o}{dr}\right)-\alpha^2\frac{f_2}{f_o}\frac{d}{dr}\left(rw_o^2\frac{dw_o}{dr}\right)-\frac{d}{dr}\left(rp_o\frac{dp_o}{dr}\right)-\frac{12r}{f_o} \qquad (32)$$

$$\Lambda^2:\frac{d}{dr}\left(r\frac{dw_2}{dr}\right)=-\alpha\frac{f_1}{f_o}\frac{d}{dr}\left(rw_o\frac{d}{dr}(w_ow_1)\right)-\alpha^2\frac{f_2}{f_o}\frac{d}{dr}\left(r\frac{d}{dr}(w_o^2w_1)\right) \qquad (33)$$

$$\Lambda^3:\frac{d}{dr}\left(r\frac{dw_3}{dr}\right)=-\alpha\frac{f_1}{f_o}\frac{d}{dr}\left(r\frac{d}{dr}(w_ow_2)+rw_1\frac{dw_1}{dr}\right)$$
$$-\alpha^2\frac{f_2}{f_o}\frac{d}{dr}\left(r\frac{d}{dr}(w_ow_1^2)+rw_o^2\frac{dw_2}{dr}+rw_ow_2\frac{dw_o}{dr}\right) \qquad (34)$$

where, the perturbation functions obey the boundary conditions for pressure

$$\left(\frac{dw_j}{dr}\right)_{r=0}=0,\ \left(w_j\right)_{r=1}=0 \qquad (35)$$

and the isoviscous pressure p_o is obtained by solving

$$\frac{d}{dr}\left(r\frac{dp_o}{dr}\right)=-\frac{12r}{f_o} \qquad (36)$$

under the pressure boundary conditions

$$\frac{dp_o}{dr}=0\ \ at\ \ r=0\ \ and\ \ p_o=0\ \ at\ \ r=1 \qquad (37)$$

Thus, equations (31-36) results in the following set of perturbed solutions

$$w_o=p_o=\frac{3}{f_o}\left(1-r^2\right) \qquad (38)$$

$$w_1=-\frac{9\alpha}{f_o^{\,3}}\left(1-r^2\right)^2-9\alpha^2\frac{f_2}{f_o^{\,4}}\left(1-r^2\right)^3 \qquad (39)$$

$$w_2=-\frac{27\alpha^2}{70}\frac{f_1^2}{f_o^{\,5}}(1-r)^4\left(16+29r+20r^2+5r^3\right)$$
$$-\frac{3\alpha^3}{14}\frac{f_1f_2}{f_o^{\,6}}(1-r)^5\left(128+325r+345r^2+175r^3+35r^4\right) \qquad (40)$$
$$-\frac{9\alpha^4}{77}\frac{f_2^{\,2}}{f_o^{\,7}}(1-r)^6\left(256+843r+1218r^2+938r^3+378r^4+63r^5\right)$$

The successive w_j's may be calculated in a similar manner to meet the desired accuracy.

The pressure distribution, as discussed in HAM, is as follows.

$$p=\lim_{\Lambda\to 1}w=w_o+w_1+w_2+\cdots \qquad (41)$$

The load carrying capacity of the bearing can be calculated as follows

$$\overline{W}=2\pi\int_0^R\overline{r}\,\overline{p}\,d\overline{r} \qquad (42)$$

which takes the dimensionless form

$$W=\frac{h_o^{\,3}}{2\pi\mu R^4\dfrac{dh}{dt}}\overline{W}=\int_0^1 r\,p\,dr \qquad (43)$$

The response time-height relation can be calculated by integrating the equation (46) under the condition that $\overline{h}=h_o\ \ at\ \ \overline{t}=0\ \ (i.e.\ \ h=1\ at\ t=0)$ as follows

$$t=\frac{\overline{w}h_o^{\,2}}{2\pi\mu R^4}\overline{t}=\int_h^1\left(\int_0^1 r\,p\,dr\right)dh \qquad (44)$$

Because the integrand in equation (44) is a nonlinear function of h, we have performed numerical integration to evaluate the response time t using *NIntegrate* facility of *Mathematica* software.

RESULTS AND DISCUSSIONS

In the present paper, the combined influence of couple stresses and the piezo-viscous dependency on the squeeze film characteristics of circular plates bearings have been predicted on the basis of Stokes couple stress fluid theory (Stokes 1966) and the exponential variation of viscosity with pressure avoiding the inertia and cavitation effects.

The piezo-viscous effect is analyzed using a dimensionless parameter α and the effect of couple stresses is analyzed using a dimensionless parameter $\nu = \frac{1}{R}\sqrt{\frac{\eta}{\mu_o}}$, where $\sqrt{\frac{\eta}{\mu_o}}$ has the dimension of length and it can be identified as the function of molecular length of polar additives in a non-polar lubricant. The results with piezo-viscous effect are compared with the iso-viscous results.

In figure 2(a), the variation of dimensionless pressure p with respect to the dimensionless radius r at film thickness $h = 0.5$ for piezo-viscous parameter $\alpha = 0,\ 0.02$ and different values of couple stress parameter $\nu = 0,\ 0.05,\ 0.1,\ 0.15$ have been plotted. Comparing with the iso-viscous Newtonian case $(\nu = 0)$, the pressure with iso-viscous couple stress lubricants is higher and it increases with an increase of couple stress parameter ν for each value of the radius. It establishes the validity of the present analysis for iso-viscous couple stress lubricants. It is further observed that for each value of the couple stress parameter, the pressure with the piezo-viscous effect is significantly higher than the pressure obtained in the iso-viscous analysis. The relative variation of pressure due to the piezo-viscous effect increases with the increase of the couple stress parameter. It proves the significance of viscosity-pressure variation in for couple stress lubricants.

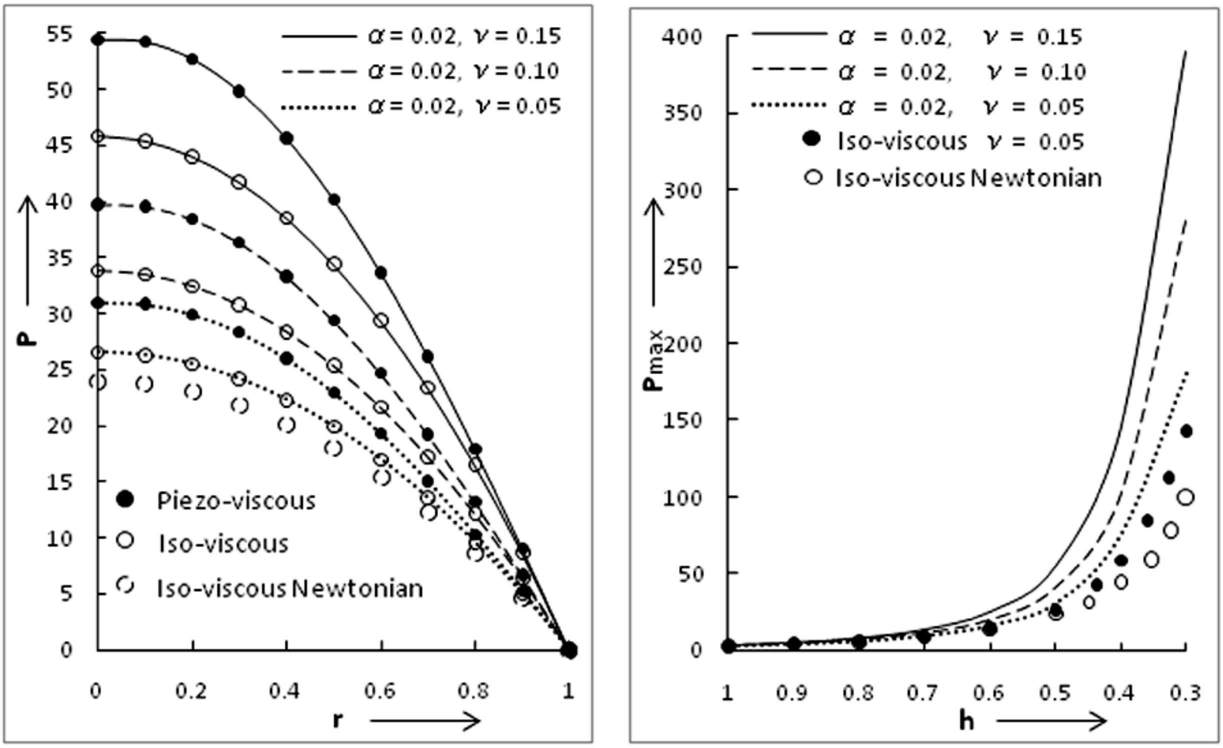

Fig. 2: (a) Variation of Dimensionless Pressure with Respect to Dimensionless Radius for Iso-Viscous and Piezo-Viscous Cases. (b) Variation of Maximum Pressure with Respect to Film Thickness for Iso-Viscous and Piezo-Viscous Cases

Figure 2(b) shows the variation of dimensionless maximum film pressure with respect to the dimensionless film thickness h, for piezo-viscous parameter α= 0, 0.02 and couple stress parameter ν= 0, 0.05, 0.1, 0.15. It is observed that the maximum pressure with iso-viscous couple stress lubricants (ν= 0.05, α= 0) is higher than that with iso-viscous Newtonian lubricants (ν= 0). A more increase in the maximum pressure is observed with the piezo-viscous effect (α=0.02) with the same value of couple stress parameter (ν= 0.05). Further, with the combined effect of piezo-viscous dependency and couple stresses (α= 0, ν= 0.1, 0.15), higher values of maximum pressure are obtained in the analysis.

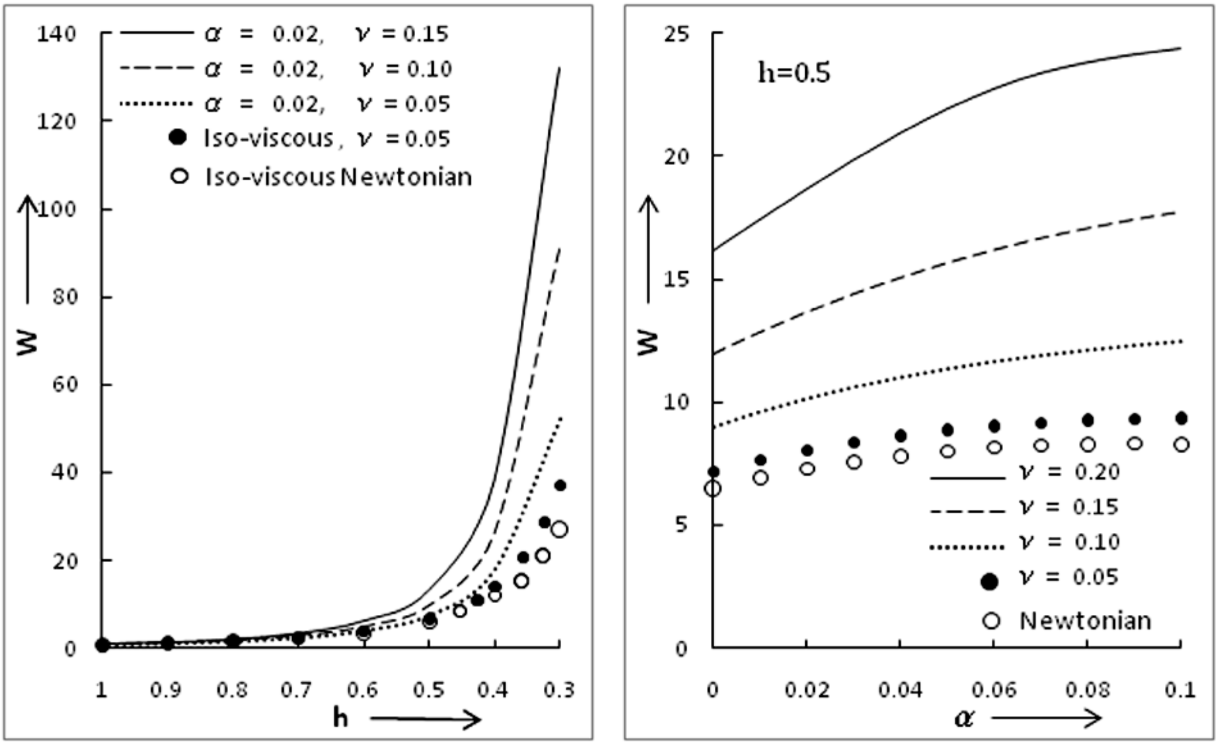

Fig. 3: (a) Variation of Dimensionless Load Capacity with the Dimensionless Film Thickness for Iso-Viscous and Piezo-Viscous Cases (b) Variation of Dimensionless Load Capacity with Piezo-Viscous Parameter (α) for Different Values of Couple Stress Parameter (*η*).

Figure 3(a) shows the variation of dimensionless load capacity with respect to the dimensionless film thickness h, for piezo-viscous parameter α= 0, 0.02 and couple stress parameter ν= 0, 0.05, 0.1, 0.15. The load capacity obtained with the iso-viscous couple stress lubricants (ν= 0.05, α= 0) is higher than that with iso-viscous Newtonian lubricants (ν= 0). For the same value of couple stress parameter (ν= 0.05), the piezo-viscous effect (α=0.02) significantly enhances the load capacity. Further, the higher load capacity is achieved with combined effects of piezo-viscous dependency and couple stresses (α= 0, ν= 0.1, 0.15) *i.e.* a sequential change from iso-viscous Newtonian to iso-viscous couple stress and iso-viscous to piezo-viscous couple stress increases the load capacity systematically.

Figure 3(b) shows the variation of dimensionless load capacity with respect to the piezo-viscous parameter (α) for dimensionless film thickness h=0.5 and different values of couple stress parameter (ν= 0, 0.05, 0.1, 0.15, 0.2). In both the cases of Newtonian and Couple stress lubricants, the load capacity increases with the increase of the piezo-viscous parameter α. However, the relative change in the load capacity is observed to increase with the increase of the couple stress parameter. The values of the load capacity in iso-viscous cases for each of the Newtonian and couple stress is lowest. Again, the load capacity in the couple stress case is observed to be higher than the Newtonian case and also higher for higher values of couple stress parameter.

Figure 4(a) shows the relation between the dimensionless film thickness (h) and the dimensionless response time (t) in iso-viscous and piezo-viscous cases for different values of couple stress parameter ν. It is clearly observed that for each value of film thickness, the response time for iso-viscous couple stress lubricant (ν= 0.05, α= 0) is longer than that in the iso-viscous Newtonian case and increased response time is observed for the same value of couple stress parameter with piezo-viscous effect (ν= 0.05, α= 0.02). A further increased response time is achieved with the combined effect effects of piezo-viscous dependency and couple stress lubricant (α=0.02, ν= 0.05, 0.1, 0.15). The variation of response time with piezo-viscous and couple stress effects is the result of enhanced film pressure. Because the piezo-viscous effect enhances the pressure in comparison with the iso-viscous case and couple stress lubricants generate higher pressure in comparison to the Newtonian lubricants, the bearing plates take longer squeezing time. Thus, both the piezo-viscous dependency and couple stresses increase the response time.

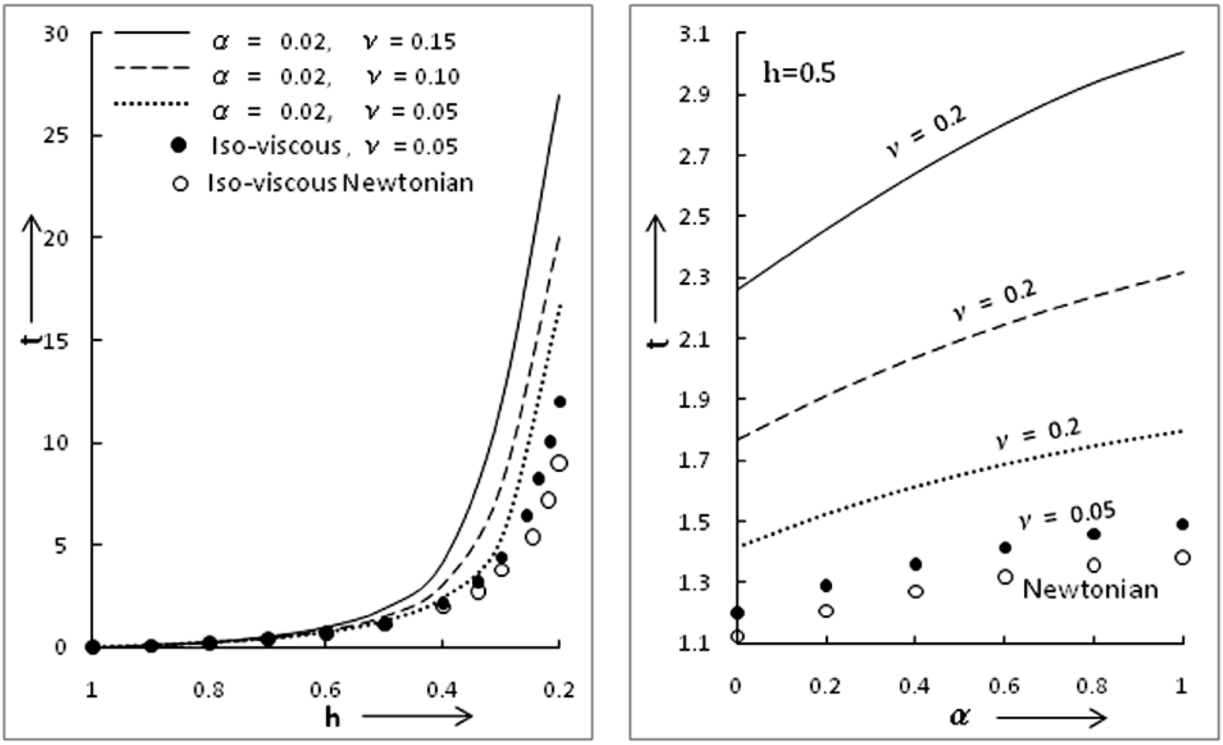

Fig. 4: (a) Variation of Dimensionless Response Time with the Dimensionless Film Thickness for Iso-Viscous and Piezo-Viscous Cases. (b) Variation of Dimensionless Response Time with Piezo-Viscous Parameter (α) for Different Values of Couple Stress Parameter (*η*).

Figure 4(b) shows the variation of dimensionless response time t to attain a particular dimensionless film thickness h=0.5 with respect to the piezo-viscous parameter (α) for different values of couple stress parameter (ν=0,0.05,0.1,0.15,0.2). The response time is observed to increase with the increase of the piezo-viscous effect for Newtonian as well as the Couple stress lubricants. However, the effect of a higher value of the piezo-viscous parameter is observed to produce a relatively longer change in the response time for larger values of the couple stress parameter. Again, the effect of couple stresses increase the response time significantly in comparison with the Newtonian lubricants.

CONCLUSIONS

Based on the Stokes micro-continuum theory of couple stress fluids and the viscosity-pressure dependence, the combined effects of piezo-viscous dependency and non-Newtonian couple stresses on the performance characteristics of squeezing film between two parallel circular plates are presented avoiding the inertia and cavitation effects. The analytical solution for pressure distribution is obtained using Homotopy Perturbation Method. Based on the present theoretical analysis, the following results have been drawn.

- The effects of piezo-viscous dependency and couple stresses increase the pressure and load-carrying capacity significantly.
- Both the couple stresses and piezo-viscous effects increase the response time of bearings.
- A small value of the piezo-viscous parameter $(\alpha = 0.02)$ increases the pressure and load capacity by nearly 15% and the response time by approximately 12% in comparison with the iso-viscous case.

We expect that the results in the present analysis are much nearer to the practical situation.

REFERENCES

Abell ML, Ames WF (1992) Symmetry reduction of Reynolds equation and applications to film lubrication. Journal of Applied Mechanics, Transactions ASME 59: 206–210.

Bair S, Liu Y, Wang Q. J (2006) The pressure-viscosity coefficient for Newtonian EHL film thickness with general piezoviscous response. Journal of Tribology 128: 624–631.

Burbidge AS, Servais C (2004) Squeeze flows of apparently lubricated thin films. Journal of Non-Newtonian Fluid Mechanics 124: 115–127.

Chiang HL, Lin JR, Hsu CH, Chang YP (2004) Linear stability analysis of a rough short journal bearing lubricated with non-Newtonian fluids. citealt Tribology Letters 17:(4) 867–877.

Denn MM (2008) Polymer melt processing: Foundations in fluid mechanics and heat transfer. Cambridge: Cambridge University Press.

Dowson D (1961) Inertia Efforts in Hydrostatic Thrust Bearings. Journal of Basic Engineering.

Gupta JL, Vora KH (1980) Analysis of squeeze films between curved annular plates. Journal of lubrication technology 102: 48–50.

Gupta PS, Gupta AS (1977) Squeezing flow between parallel plates. Wear 45(2): 177–182.

He JH (2004) Comparison of homotopy perturbation method and homotopy analysis method. Applied Mathematics and Computation.

Islam S, Shah A, Zhou CY, Ali I (2009) Homotopy perturbation analysis of slider bearing with Powell-Eyring fluid. Zeitschrift fur Angewandte Mathematik und Physik 60: 1178–1193.

Kalogirou A, Poyiadji S, Georgiou GC (2011) Incompressible Poiseuille flows of Newtonian liquids with a pressure-dependent viscosity. Journal of Non-Newtonian Fluid Mechanics 116: 413–419.

Kottke PA, Bair SS, Winer WO (2003) The measurement of viscosity of liquids under tension. Journal of Tribology 125(2): 260–266.

Lin JR, Chu LM, Liaw WL, Mou LJ (2008) Effects of non-Newtonian couple stresses on the squeeze film characteristics between two different spheres. Proceedings of the Institution of Mechanical Engineers, Part J: Journal of Engineering Tribology 222: 693–701.

Manivasakan V, Sumathi G (2011) Theoretical investigation of couple stress squeeze films in a curved circular geometry. Journal of Tribology 133:(1-8).

Ma YY, Wang WH, Cheng XH (2004) A study of dynamically loaded journal bearings lubricated with non-Newtonian couple stress fluids. Tribology Letters 17: 69–74.

Murti PRK (1975) Squeeze films in curved circular plates. Journal of Lubrication Technology 97:(650-652).

Nada GS, Osman TA (2007) Static performance of finite hydrodynamic journal bearings lubricated by magnetic fluids with couple stresses. Tribology Letters 27(3) 261–268.

Naduvinamani NB, Hiremath PS, Gurubasavaraj G (2005) Effect of surface roughness on the couple-stress squeeze film between a sphere and a flat plate. Tribology International 38: 451–458.

Naduvinamani NB, Siddangouda A, Hiremath Ayyappa G, Biradar SN (2015) Effects of pressure-dependent viscosity variation on the squeeze film lubrication between a sphere and a rough flat plate with couple stress fluids. Proceedings of the Institution of Mechanical Engineers, Part J: Journal of Engineering Tribology.

Rajagopal KR (2006) On implicit constitutive theories for fluids. Journal of Fluid Mechanics 550: 243–249.

Renardy M (2003) Parallel shear flows of fluids with a pressure-dependent viscosity. Journal of Non-Newtonian Fluid Mechanics 114: 229–236.

Singh UP (2014) Combined effects of piezo-viscosity and couple stress fluids on squeeze film between circular plates. International Journal of Fluid Mechanics Research 41(4): 1–11.

Singh UP,Gupta RS (2012) Non-newtonian effects on the squeeze film characteristics between a sphere and a flat plate:Rabinowitsch model. Advances in Tribology 2012 (Article ID 571036) : 1-7.

Singh UP, Gupta RS, Kapur VK (2011a) Effects of inertia in the steady state pressurized flow of a non-Newtonian fluid between two curvilinear surfaces of revolution: Rabinowitsch fluid model. Chemical and Process Engineering - Inzynieria Chemicznai Procesowa 32(4): 333–49.

Singh UP, Gupta RS, Kapur VK (2011b) On the steady performance of hydrostatic thrust bearing: Rabinowitsch fluid model. Tribology Transactions 54(5): 723–29.

Singh UP, Gupta RS, Kapur VK (2012) On the steady performance of annular hydrostatic thrust bearing: Rabinowitsch fluid model. Journal of Tribology 134(4): 1–5.

Singh UP, Gupta RS, Kapur VK (2013a) On the application of Rabinowitsch fluid model on an annular ring hydrostatic thrust bearing. Tribology International 58: 65–70.

Singh UP, Gupta RS, Kapur VK (2013b) On the squeeze film characteristics between a long cylinder and a flat plate: Rabinowitsch model. Proceedings of the Institution of Mechanical Engineers, Part J: Journal of Engineering Tribology 227(1): 34–42.

Singh UP, Sinha P, Kumar M (2020) Analysis of hydrostatic rough thrust bearing lubricated with Rabinowitsch fluid considering fluid inertia in supply region. Proceedings of the Institution of Mechanical Engineers, Part J : Journal of Engineering Tibology.

Stokes VK (1966) Couple stresses in fluids. Physics of Fluids 9: 1709–1715.

Sunny SA (1994) Squeezing flow between varying-permeability porous rectangular plates. Indian Journal of Pure and Applied Mathematics 25: 665–678.

Venner CH, Lubrecht AA (2000) Multilevel methods in lubrication. Elsevier Science, 1st ed.

Wada S, Hayashi H (1971) Hydrodynamic Lubrication of Journal Bearings by Pseudo-Plastic Lubricants : Part 2, Experimental Studies. Bulletin of JSME 14(69): 279–86.

Wu H (1972) An analysis of the squeeze film between porous rectangular plates. Journal of Tribology.

Yadav JS, Kapur VK (1981) On the viscosity variation with temperature and pressure in thrust bearing. International Journal of Engineering Science 19(2): 269–77.

Science and Technology Journal Vol. 8 Issue 2 July 2020 ISSN: 2321-3388

Finite Element based Crash and Impact Analyses of a Newly Developed Road Cum Rail Vehicle

Abhay Kumar Gupta[1], Sharad Kumar Pradhan[2*], Lokesh Bajpai[1] and Varun Jain[2]
[1]Department of Mechanical Engineering,
Samrat Ashok Technological Institute, Barkatullah University, Bhopal, M.P, India
[2]Department of Mechanical Engineering, National Institute of
Technical Teachers' Training and Research, Bhopal–462002, India
E-mail: spradhan@nitttrbpl.ac.in

Abstract—The two most significant engineering steps required in developing a good quality vehicle is crash and structural analysis in the field of automobile design. Simulating the crashworthiness of the vehicle is a significant step to design automobiles of the present age and automotive industry has probably the widest application of such simulations. Crash simulation is a virtual representation of a destructive crash test of a vehicle and its components using computer-aided analysis software to examine the level of safety of the vehicle and its occupants by analysing the level and nature of impact stresses occurring in the component and the magnitude and nature of the deformation happening in the cosmponent during a crash situation.

In the current study, a road cum rail vehicle is designed. The main purpose of the vehicle is to clean the rail track. Since the vehicle will be used on the live rail track so it is very important to know the dynamic behaviour of the vehicle during crash or impact. The dynamic behaviour of complete vehicle chassis with four rail wheel and for rubber wheel in contact with rails and moving at 60 km/hr is simulated under frontal crash. Further, 10g frontal impact and the 5g rear impact are also applied on the developed vehicle chassis at rest to investigate its dynamic behaviour.

Keywords: Dynamic, Rail track, Impact, Road cum Rail Vehicle, Crashworthiness, Crash.

INTRODUCTION

Indian Railways (IR) is one of the largest railway systems in the world. As pervision 2020 (Sharma and Kumar 2014) the major emphasis will be on track enhancement, environmental sustainability, and network development of railway, carbon footprint reduction and technological excellence. With the increase in rail technology, waste management is very important for IR. So a newly developed Road cum Rail vehicle is analysed in this paper as shown in figure 1. Figure 1 shows the developed rail scavenging vehicle with all its components. In present work only the chassis with load of individual components and eight wheels is considered for simulation. In current work three dynamic simulation case studies are considered viz. 10g frontal impact case, 5g rear impact case and the last case of crash analysis of the chassis hitting a static wall with 60 km/h speed. Kirkpatrick et al (1999) developed and validated a high fidelity finite element model of a full-size car for crashworthiness analysis. Studied the part of an overall program to develop a set of detailed finite element models for various vehicles that represent the range of vehicle types currently on the road. Vehicle frontal and side-impact tests had been performed on the Crown Victoria. Data from these full vehicle crash tests provided a primary set of measurements for validating the crash model. However, complete validation of the model-based only on the existing vehicle crash tests is difficult because of the complexity of the crash responses and the limited number of measurements in the tests. In the JNCAP, both full and offset frontal impact tests are performed (Mizuno et al. 2003). The crashworthiness and injury parameters in both tests were examined. Scores in both crash tests are strongly affected by chest and tibia injury criteria. Some cars score well on both tests, while others have poor scores in the offset impact tests because of the large intrusion into the passenger compartment. Wach and Unarski (2007) proved the necessity of including the problem of uncertainty in calculations related to vehicle collision mechanics and to justify the application of different error analysis methods recommendable in vehicle collision reconstruction. Hu et al.

(2012) presented the simulations of various impact crashes for an off-road utility vehicle (OUV) to assess the structural crashworthiness and the potential occupant injuries. The full vehicle finite-element model (FEM) is established while structural deformations and internal energies are extracted from simulation results for evaluating crashworthiness of the full vehicle structure. Head Injury Criterion (HIC) and Thoracic Trauma Index (TTI) obtained from the dummy are used to assess the potential injuries of the occupant during the impact crashes. The simulations results help identify weaker parts of body structure for future vehicle design improvement. Ambati et al. (2012) simulated a frontal impact crash of a Chevrolet C1500 pick-up truck and validated the results. The aim is also to alter some of the materials of the components to reduce the forces experienced during the crash. Computer models are used to test the crash characteristics of the vehicle in the crash using LS-DYNA software. The results obtained by the simulation are then validated by comparing it with test performed by the NCAC (National Crash Analysis Centre).

Fig. 1: Designed and Developed Rail Track Scavenging Vehicle

Gu *et al*. (2013) investigated Occupant Restraint System (ORS) and its effectiveness to protect passengers from severe injury in a vehicle collision. To address the issue, this paper combines a Kriging (KRG) model with Non-dominated Sorting Genetic Algorithm II (NSGA-II) for vehicle ORS design. The ORS design of a 40% Offset Deformable Barrier (ODB) frontal impact test with the collision speed of 64 km/h is exemplified for the presented method. The results show that the KRG model can well predict the ORS responses for the design. Finally, the optimum result is verified using sled physical tests. It is found that ORS performance can be substantially improved for meeting product development requirements through the proposed approach. Bambach (2013) investigated the composite energy absorbers. These are externally fibre-reinforced metal tubes, where fibres are bonded to the metal tube surface. Such composites take advantage of the favourable characteristics of each material, being the stable, ductile plastic collapse mechanism of the metal and the high strength to weight ratio of the fibre–resin composite. Nguyen et al. (2015) presented an analysis of the vehicle structural performance based on a computer-based crash simulation model in the event of a small-overlap frontal impact (SOFI). According to Lokhande et al. (2016), vehicle crash is highly non-linear transient dynamics phenomenon. The chassis is designed using Creo-2.0 and then the analysis is done with the help of analysis software ANSYS to select the optimum design. The crash analysis simulation and results are used to assess both the crashworthiness of designed chassis and to investigate ways to improve the design.

Dima et al. (2017) discussed that reconstruction of car accidents is a complex task, with many unknown variables. Among the parameters used to assess the accident severity, in case of a frontal collision between two vehicles, are the change in velocity (delta-v) and the Energy Equivalent Speed (EES). This study presented a full-scale crash test that involves two vehicles in a frontal collision. Longa et al. (2019) presented a study on the response of a side impact beam located in a car door to impact loading. In their study a numerical model of a light-weight passenger car, developed by the National Crash Analysis Centre (NCAC) of The George Ishington University under a contract with the Federal Highway Administration (FHWA) and National Highway Traffic Safety Administration (NHTSA) of the United States Department of Transportation (US DOT), is used to simulate a side impact on the front side door using the LS-DYNA R7.1.1 explicit solver.

Many studies have focused on the topic of vehicle safety, including the study on crashworthiness (Abdullah et al. 2019). Li et al. (2020) proposed a new type of multi-cell circumferentially corrugated square tubes (CCSTs) by implementing multi-corrugation on the cross-sections of the traditional multi-cell square tubes (STs). Experimental, numerical and theoretical methods are adopted to investigate the crashing mechanics of the multi-cell CCSTs. The results showed that the crashworthiness performance of the multi-cell CCSTs is significantly superior to that of the multi-cell STs.

SIMULATION STUDY

In current work three dynamic simulation case studies are considered viz. 10g frontal impact case, 5g rear impact case and the last case of crash analysis of the chassis hitting a static wall with 60 km/h speed to establish the crash worthiness of the developed vehicle.

CASE 1: STATIC STRUCTURAL ANALYSIS OF COMPLETE VEHICLE CHASSIS WITH 5G REAR IMPACT LOAD

To start with the static structural analysis, the required material properties of the different components are shown in table 1. Since the road, cum rail vehicle is friction driven so the rubber Tire material properties are also an important factor. The material properties of the rubber Tire are shown in table 2. The design loads for the analysis are taken as total load on the vehicle of 16182 N (sum of individual component load); Rear Impact load of 185899.5 N (equivalent to 5G), tire pressure of 0.2 M.Pa. and the friction coefficient between Rail wheel & Rail and Rubber Tire& Rail is 0.35. Figure 2(a) shows the CAD model of the vehicle chassis considered.

Table 1: Material Properties of the Rail, Rail Wheel, Vehicle Chassis

Part	Density Kg/m3	Young's Modulus M.Pa.	Poisson's Ratio
Rail	7850	2.1E5	0.3
Rail Wheel	7850	2.1E5	0.3
Vehicle Chassis	7850	2.1E5	0.3

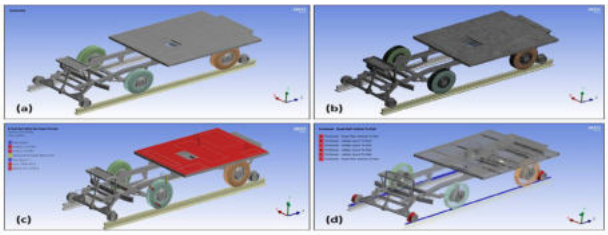

Fig. 2: (a)3D Model of Complete Vehicle Chassis (Isometric View), (b) Finite Element Model (Mesh Model of Complete Vehicle Chassis), (c) Boundary Condition & Loading on Complete Vehicle Chassis and (d) Frictional Contact between Rail Wheel and Rail and Rubber Tire and Rail

Table 2: Material Properties of the Rubber Tire

Rubber Tire Part	Density Kg/m3	Young's Modulus M.Pa.	Poisson's Ratio
Tread	1173	14	0.45
Carcass	1351	107	0.451
Inner liner	2497	3181	.454
Side wall	1132	5.05	.45

A program-controlled meshing is done with 3D Solid Element of Hexahedral shape for Rail, Tetrahedral shape for vehicle chassis as shown in figure 2(b).

1 Type of element = Solid 186, Solid 187

2 Total numbers of nodes = 346669

3 Total numbers of elements = 173732

The applied boundary conditions with loading on the CAD model are shown in figure 2 (c) and (d). The bottom surface of the Rail (location A) and the front end of the Vehicle Chassis (Location D) are fixed. Frictional coefficient between Rail Wheel-Rail and Rubber Tire-Rail is taken as 0.35. Total Load of 16182 N (Sum of individual component load) is applied downward (- Y direction) at the Vehicle Chassis (Location F). Rear Impact load of 185899.5 N (equivalent to 5G) is applied at location E while the Tire pressure of 0.2 M.Pa. is applied to the inner surface of Rim and Tire (location B & C). Standard Earth Gravity of 9806.6 mm/s^2 is applied downward (- Y direction) to the Complete Vehicle Chassis (location G). After preparing the CAD model, assigning the material, creating the Finite elements and applying the boundary conditions with desired loads, the complete solution is carried out. After performing Finite Element Analysis it is found that the max. Deformation is coming as 4.9688 mm and the maximum Von-Mises Stress on the complete Vehicle Chassis is 164.5 MPaas depicted through Table 3-Figure 3(a) and Table 4-Figure 3(b) respectively.

Table 3: Deformation of Complete Vehicle Chassis

Part	Location	Deformation mm	Result
Complete Vehicle Chassis	Rubber Tire	4.9688	Acceptable

Table 4: Von-Mises Stress

Part	Location	Ultimate Strength MPa	Yield Strength MPa	Von-Mises Stress MPa	Factor of Safety	Result
Complete Vehicle Chassis	At the Vehicle Chassis	680	340	164.5	2.066	Accep-table

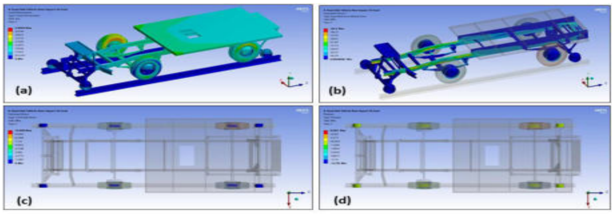

Fig. 3: (a) Deformation Plot of Complete Vehicle Chassis (Isometric View), (b) Von-Mises Stress Plot of Complete Vehicle Chassis (Inside View), (c) Frictional Stress Plot of Complete Vehicle Chassis (Rail Wheel & Rail and Rubber Tire & Rail) and (d) Contact Pressure Plot of Complete Vehicle Chassis (Rail Wheel & Rail and Rubber Tire & Rail)

Figure 3(a) represents the distribution of deformation values with maximum deformation at the bottom and top of the rubber tires, which is quite obvious. The max von misses stresses are coming in the longitudinal C-section members of the chassis as depicted by figure 3(b). The maximum Frictional stress obtained is 10.698 M.Pa. as shown in figure 3(c) while the Maximum contact pressure value is coming as 8.2831 M.Pa. and the location is presented in figure 3(d).

CASE 2: STATIC STRUCTURAL ANALYSIS OF COMPLETE VEHICLE CHASSIS WITH 10G FRONT IMPACT

To perform this analysis, the digital model, material properties and meshing, are exactly same as that of the previous case except direction and magnitude of applied impact load. The design loads for the analysis are taken as total load on Vehicle of 16182 N (sum of individual component load. The new boundary condition for static structural analysis of complete vehicle chassis with 10G front impact load shown in figure 4(a). The bottom surface of the Rail (location A)and the rear end of the Vehicle Chassis (Location D) are fixed. Front Impact load of 371799N (equivalent to 10G), is applied at location E. The Tire pressure of 0.2 M.Pa. is applied to the inner surface of Rim and Tire (location B & C) and frictional coefficient between Rail Wheel & Rail and Rubber Tire& Rail is 0.35. The standard Earth Gravity of 9806.6 mm/s^2 is applied downward (- Y direction) to the Complete Vehicle Chassis (location G).

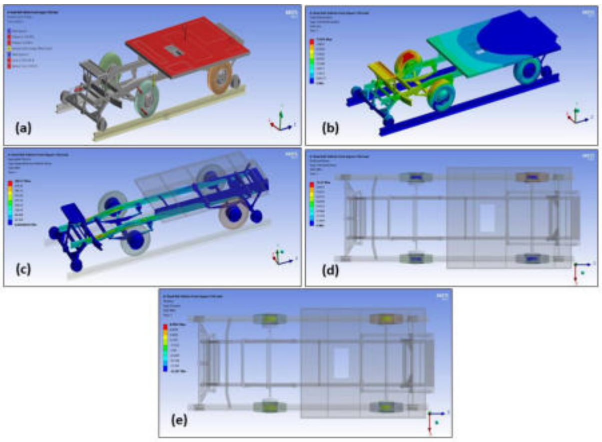

Fig. 4: (a) Boundary Condition & Loading on Complete Vehicle Chassis, (b) Deformation Plot of Complete Vehicle Chassis under 10 G Frontal Impacts (Isometric View), (c) Von-Mises Stress Plot of Complete Vehicle Chassis under 10 G frontal Impacts (Inside View), (d) Frictional Stress Plot of Complete Vehicle Chassis under 10 G Frontal Impacts (Rail Wheel & Rail and Rubber Tire & Rail) and (e) Contact Pressure Plot of Complete Vehicle Chassis under 10 G frontal Impacts (Rail Wheel & Rail and Rubber Tire & Rail)

After preparing the CAD model, assigning the material, creating the Finite elements and applying the boundary conditions with desired loads, the complete solution is carried out. After performing Finite Element Analysis it is found that the max. Deformation is coming as 7.9534 mm and the maximum Von-Mises Stress on the complete Vehicle Chassis is 380.73 M.Pa. as depicted through Figure 4 (b) and (c) respectively. Figure 4(b) represents the distribution of deformation values with maximum deformation at the bottom and top of the rubber tires, which is quite obvious. The max von misses stresses are coming in the longitudinal C-section members of the chassis as depicted by figure 4(c). The maximum Frictional stress obtained is 12.32 M.Pa.as shown in figure 4(d) while the Maximum contact pressure value is coming as 8.9942 M.Pa. and the location is presented in figure 4(e).

CASE 3: CRASH ANALYSIS OF COMPLETE VEHICLE CHASSIS MOVING WITH 60 KM/HR.

New CAD Model, Meshing and the boundary condition are generated to perform the crash analysis of complete vehicle moving with 60 km/h (16660 m/s) and hitting a rigid static wall. The Tire pressure of 0.2 M.Pa. and the friction coefficient between Rail wheel & Rail and Rubber Tire& Rail is 0.35 are again same. The time of the Crash Analysis is taken as 0.02 second. The CAD model (wall and vehicle) for the crash analysis is shown in figure 5(a) (Isometric view).

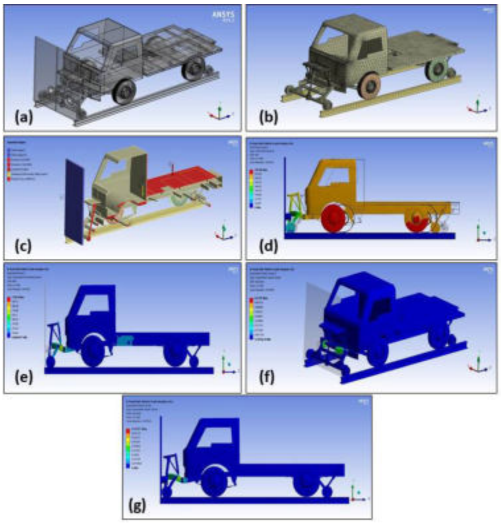

Fig. 5: (a) 3D Model of Complete Vehicle Chassis with Rigid Wall (Isometric View), (b) Finite Element Model (Mesh Model of Complete Vehicle Chassis), (c) Boundary Condition & Loading on Complete Vehicle Chassis, (d) Deformation Plot of Complete Vehicle Chassis (Side View), (e) Von-Mises Stress plot of Complete Vehicle Chassis (Side View), (f) Equivalent Elastic Strain of Complete Vehicle Chassis and (g) Equivalent Plastic Strain of Complete Vehicle Chassis

A program-controlled meshing is done with 3d Solid Element of Hexahedral shape for Rail, Tetrahedral shape For Vehicle Chassis as shown in figure 5(b).Type of element = Solid 186, Solid 187, Total numbers of nodes = 29390, Total numbers of elements = 91663. The applied boundary conditions for the crash analysis are shown in figure 5(c). The bottom surface of the Rail (location B) and Rigid Wall (location A) are fixed. The symmetry boundary condition are used at the mid surface of Vehicle Chassis and Rigid wall (location G). Total Load of 8090.8 N (Sum of individual component load) is applied downward (- Y direction) at the Vehicle Chassis (Location F).The Tire pressure of 0.2 M.Pa. is applied to the inner surface of all the Rims and Tires (location C & D). The standard Earth Gravity of 9806.6 mm/s^2 is applied downward (- Y direction) on the Complete Vehicle (location E).After preparing the CAD model, assigning the material, creating the Finite elements and applying the boundary conditions with desired loads, the complete solution is carried out. After performing Finite Element Analysis it is found that the max. Deformation is coming as 332.88 mm and the maximum Von-Mises Stress on the complete Vehicle Chassis is 1139.8M.Pa.as depicted through Figure 5(c) and (d) respectively. Maximum equivalent elastic strain obtained is 0.5195 while the maximum Equivalent Plastic Strain value is 0.71071 as shown in figures 5(e) and (f) respectively.

CONCLUSIONS

In Case 1 with 5g rear impact the Stress distributions and Deformation of Complete Vehicle Chassis for the given boundary and loading condition did not exceed the allowable stresses and it can withstand the design load safely while for Case 2 with 10g front impact the Von-Mises stress values are just above the yield strength of the material. In third case when vehicle is moving with 60Km/h speed and hitting a rigid wall the Von-Mises stresses and deformation are of very high magnitude viz. 332.88 mm and 1139.8M. Pa.respectively, which indicates failure of the vehicle. To avoid this, frontal components of the vehicle should be changed/redesigned with honey-comb structure/energy absorbing material so that the impact energy produced can be stored in the form of strain energy of these frontal components.

ACKNOWLEDGEMENTS

This work is an output of a DST funded project ‘Multifunctional Railway Track Scavenging Vehicle’, DST/TSG/AMT/369. We are thankful to the Department of Science and Technology, Government of India for providing financial support.

REFERENCES

Abdullah NAZ, Sani MSM, Salwani MS and Husain NA (2019) A review on crashworthiness studies of crash box structure. Thin-Walled Struct. 153:106795.

Ambati T, Srikanth KVNS and Veeraraju P (2012) Simulation of Vehicular Frontal Crash-Test. Int. J. Appl. Res. Mech. Eng. 2:2231–5950.

Bambach MR (2013) Fibre composite strengthening of thin-walled steel vehicle crush tubes for frontal collision energy absorption. Thin-Walled Struct. 66:15–22.

Dima DS and Covaciu D (2017) Solutions for acceleration measurement in vehicle crash tests. IOP Conf. Series: Mater. Sci. Eng. 252:012007.

Gu X, Sun G, Li G, Huang X, Li Y and Li Q (2013) Multi objective optimization design for vehicle occupant restraint system under frontal impact. Struct. Multidiscip. Optim. 47:465–477.

Hu H, Lu WJ and Lu Z (2012) Impact crash analyses of an off-road utility vehicle - Part II: Simulation of frontal pole, pole side, rear barrier and rollover impact crashes. Int. J. Crashworthiness 17:163–172.

Kirkpatrick SW, Simons JW and Antoun TH (1999) Development and validation of high fidelity vehicle crash simulation models. Int. J. Crashworthiness 4:395–406.

Li Z, Ma W, Hou L, Xu P and Yao S (2020) Crashworthiness analysis of corrugations reinforced multi-cell square tubes. Thin-Walled Struct.150:106708.

Lokhande AP, Darekar AG, Nimbalkar SCN, Patil AP (2016) Crash Analysis of Vehicle. Int. Res. J. Eng. Techno 1.3:1070–1075.

Longa CR, Chung S, Yuena K and Nuricka GM (2019) Analysis of a car door subjected to side pole impact. Lat. Am. J. Solids Struct.16:1–17.

Mizuno K, Wani K, and Yonezawa H (2003) Vehicle crashworthiness in full and offset frontal impact tests, JSAE Rev. 24:173–181.

Nguyen PTL, Lee JY, Yim HJ et al (2015) Analysis of vehicle structural performance during small-overlap frontal impact. Int. J. Automot. Technol 16:799-805.

Sharma SK and Kumar A (2014) A Comparative Study of Indian and World Wide Railways. Int. J. Mech. Eng. Robotics Res.1:114-120.

Wach W and Unarski J (2007) Uncertainty of calculation results in vehicle collision analysis. Forensic Sci. Int. 167:181–188.

Science and Technology Journal Vol. 8 Issue 2 July 2020 ISSN: 2321-3388

Scalar Tensor Theories of Gravitation in Ruban's Space Time

Anil S. Nimkar[1], Vaishnvi M. Wankhade[2] and Ashok M. Pund[3]
[1,2]Department of Mathematics,
Shri. Dr. R.G. Rathod Arts & Science College, Murtizapur, Dist. Akola (M.S.) India
[3]Department of Mathematics, Shri Shivaji Education Society Amravati's Science College,
Congress Nagar, Nagpur (M.S.) India
E-mail: anilnimkar@gmail.com, *ashokpund64@rediffmail.com

Abstract—In this paper, we have studied the field equation in the context of cosmic string source in the scalar-tensor theories of gravitation given by Brans and Dicke and Saez-Ballester with the aid of Ruban's Space time. Exact cosmological models in both the theories are presented with the help of special law of variation suggested by Berman (1983) and relation between metric coefficient $Q = x^n R^n$. Finally, some physical and kinematical properties of the model are carried out.

Keywords: Cosmic string, Brans-Dicke and Saez-Ballester theory, Scalar field.

INTRODUCTION

The most natural generalizations of general relativity are considered Scalar-tensor theories of gravity. In these theories gravity is mediated by the metric of space-time and by the scalar field. To describe gravitational interactions near the Plank scale the Scalar-tensor theories seem to be essential: string theory, extended inflation, higher order theories in the Ricci scalar, and many others theories imply scalar field. The arbitrary functions of the scalar field that determine the gravitational constant as a dynamical variable is contained in the Scalar-tensor theories and it should be noted that specific from a theoretical point of view, scalar-tensor theories arise naturally as a low-energy limit of string theory. Scalar-tensor theories have additionally magnetized much interest in cosmology. The progress in the understanding of scalar-tensor theories of gravity is closely connected with finding and investigation of exact solutions. A theoretical discussion of many aspects of the early universe, gravitational waves, gravitational collapse and the structure of the compact objects within the framework of scalar-tensor theories necessitates the use of exact solutions. Solving of scalar-tensor theories equations in the presence of a source is a difficult task due to their complexity in the general case. In fact, scalar-tensor gravity equations are much more complicated than Einstein equations. In the so called Einstein frame the source less scalar-tensor equations are reduced to Einstein equations with a minimally coupled scalar field. In this case much progress has been achieved in finding exact homogeneous and inhomogeneous cosmological solutions. Particular classes of solutions were presented for specific choice of $\omega(\phi)$ including Brans-Dicke, Saez-Ballester, Barker and Bekenstein theories.

Brans-Dicke (1961) field equations for combined scalar and tensor fields are

$$G_{ij} = -8\pi\varphi^{-1}T_{ij} - \omega\varphi^{-2}\left(\varphi_{,i}\varphi_{,j} - \frac{1}{2}g_{ij}\varphi_{,k}\varphi^{'k}\right) - \varphi^{-1}\left(\varphi_{i\,;j} - g_{ij}\,\varphi\right) \tag{1}$$

$$\varphi = \varphi^{'k}_{;k} = 8\pi\varphi^{-1}(3+2\omega)^{-1}T, \tag{2}$$

and Saez and Ballester (1985) field equations are

$$G_{ij} - \omega\varphi^{n}\left(\varphi_{,i}\varphi_{,j} - \frac{1}{2}g_{ij}\varphi_{,k}\varphi^{,k}\right) = -8\pi T_{ij} \tag{3}$$

$$2\phi^{n}\phi^{i}_{;i} + n\phi^{n-1}\phi_{,k}\phi^{,k} = 0, \tag{4}$$

where $G_{ij} = R_{ij} - \frac{1}{2}Rg_{ij}$ is the Einstein tensor, R_{ij} is the Ricci tensor, R is the scalar curvature, n an arbitrary constant, ω is a dimensionless coupling constant and T_{ij} is the matter energy-momentum tensor. Here comma and semicolon denote partial and covariant differentiation respectively.

The energy conservation equation

$$T^{j}_{;j} = 0, \tag{5}$$

is a consequence of field equations in both the theories.

The study of cosmological models in the frame work of scalar-tensor theories has been the active area of research for the last few decades. Singh and Rai (1983) gives a detailed discussion of Brans-Dicke Cosmological models. Saez-Ballester (1985), Shri Ram and Tiwari (1998) have investigated several aspects of cosmological model in Saez-Ballester scalar tensor theory of gravitation. Berman (1983) presented law of variation of Hubble's parameter that yields constant declaration parameter models of the universe. Reddy and Venkateswara Rao (2001) have obtained some cosmological models within the frame work of Saez-Ballester (1985) scalar tensor theory of gravitation with the help of special law of variations for Hubble's parameter. Also, detailed discussion of Brans- Dicke and Saez -Ballester cosmological model is contained in the work of Adhav *et al.* (2007), katore *et al.* (2012), Reddy. *et al.* (2012), Kandalkar S.P. *et al.* (2012). Ugale (2014) *et al.* and Pawar D.D.*et al.* (2015). The purpose of this paper is to obtain string equations and solutions in scalar-tensor theories of gravitation proposed by Brans-Dicke (1961) and Saez-Ballester (1985) with the aid of Ruban's space time.

METRIC AND FIELD EQUATION IN BRANS-DICKE

We consider Ruban's space time [7] in the form

$$ds^2 = dt^2 - Q^2(x,t)dx^2 - R^2(t)(dy^2 + h^2dz^2) \tag{6}$$

where $h(y) = \dfrac{\sin\sqrt{k}y}{\sqrt{k}} = \begin{matrix} \sin y & if & k=1 \\ y & if & k=0 \\ \sinh y & if & k=-1 \end{matrix}$

The energy momentum tensor for cosmic strings is given by [Letelier, 1983]

$T_i^j = \rho\, u_i u^j - \lambda\, x_i x^j$ (7) where ρ is the rest energy density of cloud of strings' with particles attached to them, $\rho = \rho_p + \lambda$, ρ_p being the rest energy density of particles attached to the strings and λ the tension density of the system of strings. As pointed out by Letelier (1983), λ may be positive or negative, u^i describes the system four-velocity and x^i represents a direction of anisotropy, i.e. the direction of the strings.

We have

$u^i u_i = -x^i x_i = 1$, and $u^i x_i = 0$ (8)

We consider

$$\rho = \rho_p + \lambda \tag{9}$$

Where ρ_p is the rest energy density of the particles attached to the string.

Here ρ and λ are the functions of *t* only.

Using the co moving coordinate system, the non-vanishing components T_j^i can be obtained as

$$T_1^1 = \lambda \quad ,T_2^2 = T_3^3 = 0, T_4^4 = \rho \tag{10}$$

The field equations (1), (2) and (5) for the metric (6) with the help of (8) to (10) can be written as

$$2\frac{\ddot{R}}{R} + \left(\frac{\dot{R}}{R}\right)^2 + \frac{k}{R^2} + \frac{\omega}{2}\left(\frac{\dot{\phi}}{\phi}\right)^2 + 2\frac{\dot{R}}{R}\frac{\dot{\phi}}{\phi} + \frac{\dot{\phi}}{\phi} = 8\phi^{-1}\lambda \tag{11}$$

$$\frac{\dot{R}}{R}\frac{\dot{Q}}{Q} + \frac{\dot{R}}{R} + \frac{\dot{Q}}{Q} + \frac{\omega}{2}\left(\frac{\dot{\phi}}{\phi}\right)^2 + \frac{\dot{\phi}}{\phi}\left(\frac{\dot{Q}}{Q} + \frac{\dot{R}}{R}\right) + \frac{\dot{\phi}}{\phi} = 0 \tag{12}$$

$$2\frac{\dot{R}}{R}\ \frac{\dot{Q}}{Q} + \left(\frac{\dot{R}}{R}\right)^2 + \frac{k}{R^2} - \frac{\omega}{2}\left(\frac{\phi_4}{\phi}\right)^2 + \frac{\phi_4}{\phi}\left(\frac{\dot{Q}}{Q} + 2\frac{\dot{R}}{R}\right) = 8\phi^{-1}\rho \tag{13}$$

$$\ddot{\phi} + \left[2\frac{\dot{R}}{R} + \frac{Q}{Q}\right]\dot{\phi} = \frac{8\pi(\rho + \lambda)}{\phi(3 + 2\omega)} \tag{14}$$

$$\dot{\rho} + (\rho - \lambda)\frac{\dot{Q}}{Q} + 2\rho\frac{\dot{R}}{R} = 0 \tag{15}$$

Here an overhead dot denotes differentiation with respect to *t.* For a cosmological model corresponding to string in Brans-Dicke theory with the help of special law of variation by using Hubble's parameter presented by Berman (1983) that yields constant deceleration parameter models of the universe. We consider only constant deceleration parameter model defined by

$$q = -\left[\frac{R\ddot{R}}{\left(\dot{R}\right)^2}\right] = cons\tan t \tag{16}$$

Where *R* is the overall scale factor. Here the constant is taken as negative. The solution of (16) is

$$R = (at + b)^{\frac{1}{1+q}}\ , \tag{17}$$

Where $a \neq 0$ and b are constants of integration. This equation implies that the condition of the expansion is $1 + q > 0$ (because the scale factor R cannot be negative as well as we know that if $q > 0$ then $\frac{dR}{dt}$ is slowing down and if $q < 0$ then $\frac{dR}{dt}$ is speeding up.

Also the equations being highly non-linear, we assume a relation between metric coefficients given by $Q = x^n R^n$.

Now with the help of (16), the field equations of Brans-

Dickey theory admit an exact solution given by

$$R = M\left(at+b\right)^{N}, \text{ where } M = \left(\frac{1}{x^{n}h}\right)^{\frac{1}{n+2}} \tag{18}$$

$$Q = M_{1}\left(at+b\right)^{N_{1}}, \text{ where } N_{1} = nN \tag{19}$$

$$\phi = \frac{c_{4}}{T^{N_{2}-1}} \tag{20}$$

$$\rho = \frac{C_{6}}{T^{N_{3}}}, \text{ where } C_{6} = \frac{C_{5}}{x^{2n}\left(M\right)^{2n+2}}, \quad N_{3} = N(2n+2) \tag{21}$$

Using (18) and (19), the line element (6) become

$$ds^{2} = dt^{2} - M_{1}^{2}\left(at+b\right)^{2N_{1}} dx^{2} - M^{2}\left(at+b\right)^{2N}\left(dy^{2} + h^{2}dz^{2}\right) \tag{22}$$

COSMIC STRING IN SAEZ-BALLESTER THEORY

In this section, we obtain a cosmological model corresponding to cosmic string in Saez- Ballester (1985) theory.

The field equations (3) to (5) for the metric (6) with the help of (7) to (10) can be written as

$$2\frac{\ddot{R}}{R} + \left(\frac{\dot{R}}{R}\right)^{2} + \frac{k}{R^{2}} - \frac{\omega}{2}\varphi^{n}\left(\dot{\varphi}\right)^{2} = 8\pi\lambda \tag{23}$$

$$\frac{\dot{R}}{R}\frac{\dot{Q}}{Q} + \frac{\dot{R}}{R} + \frac{\dot{Q}}{Q} - \frac{\omega}{2}\phi^{n}\left(\dot{\phi}\right)^{2} = 0 \tag{24}$$

$$2\frac{\dot{R}}{R}\frac{\dot{Q}}{Q} + \left(\frac{\dot{R}}{R}\right)^{2} + \frac{k}{R^{2}} + \frac{\omega}{2}\varphi^{n}\left(\dot{\varphi}\right)^{2} = 8\pi\rho \tag{25}$$

$$\ddot{\phi} + \left(\frac{\dot{Q}}{Q} + 2\frac{\dot{R}}{R}\right)\dot{\phi} + \frac{n}{2}\frac{\left(\dot{\phi}\right)^{2}}{\phi} = 0 \tag{26}$$

$$\dot{\rho} + \left(\rho - \lambda\right)\frac{\dot{Q}}{Q} + 2\rho\frac{\dot{R}}{R} = 0 \tag{27}$$

The set of above equations (23) to (27) containing five unknown $R, Q, \phi, \lambda, \rho$ To get a determinate solution we again use the special law of variation of Hubble's parameter given by Berman (1983). Proceeding just as in above section, we again obtain the same cosmic string model given by (22) with ϕ, ρ, λ given by

$$\phi = C_{9}\frac{1}{\left(T\right)^{\frac{2(N+2N-1)}{n+2}}} \tag{28}$$

where

$$C_{9} = \left[\left(\frac{n+2}{2}\right)\frac{C_{8}}{1-N\left(n+2\right)}\frac{1}{a}\right]^{\frac{2}{n+2}}$$

$$\rho = -\lambda = \frac{C_{6}}{\left(T\right)^{N_{3}}} \text{ where } N_{3} = N\left(2n+2\right) \tag{29}$$

SOME PHYSICAL AND KINEMATICAL PROPERTIES FOR THE MODEL (22)

In this section we discuss some physical and kinematical properties of cosmic string models in Brans-Dicke and Saez–Ballester theory. The cosmic string models in these theories are given by (22). The physical quantities that are important in cosmology are special volume *V*. The expansion scalar θ ,shear scalar σ^{2} and the Hubble's parameter H and have the following expression for the model given by (22):

Spatial volume $V = \left(T\right)^{\frac{1}{1+q}}$ (30)

Expansion Scalar $\theta = \frac{1}{3}U^{i}_{;i} = \frac{N_{2}}{T}$ (31)

where $N_{2} = a\left(N_{1} + 2N\right)$

Shear Scalar $\sigma^{2} = \frac{1}{2}\sigma_{ij}\sigma^{ij} = \frac{N_{3}}{T^{2}}, N_{3} = \frac{N_{2}^{2}}{6}$ (32)

$$H = \frac{aN}{T} \tag{33}$$

The model (22) has no singularity, while the rest energy density and tension density of the string in Brans-Dicke theory are given by (21) whereas in Saez-Ballester theory are given by (29) respectively. It may be observed that at initial moment, when *T=0* the spatial volume will be zero while the energy density diverges. when $T \to 0$,then expansion scalar θ,shear scalar σ^{2} and the Hubble's parameter H tends to ∞.

Also, Since $\lim_{T\to\infty}\left(\frac{\sigma}{\theta}\right) \neq 0$ and hence the model does not approach isotropy for large values of *T*. The scalar field ϕ increases indefinitely as time $T \to \infty$ and is free from initial singularity.

CONCLUSION

In this paper we have Investigated Ruban's cosmological models in scalar-tensor theories of gravitation formulated by Brans-Dicke and Saez-Ballester in presence of cosmic string source with the help of special law of variation also for solving the field equations relation between metric coefficient and Reddy string are used. After finding the value of Spatial Volume, energy density, shear scalar and Hubble parameter, in Both Theories Brans-Dicke and Saez-Ballester following similar results obtain-

- It may be observed that at initial moment, when $T = 0$ the spatial volume will be zero
- The energy density diverges. when $T \to 0$, then expansion scalar θ, shear scalar σ^2 and the Hubble's parameter H tends to ∞.
- $\lim_{T\to\infty}\left(\frac{\sigma}{\theta}\right) \neq 0$ and hence the model does not approach isotropy for large values of *T*.
- The scalar field ϕ increases indefinitely as time $T \to \infty$ and is free from initial singularity

The models in both the theories are similar and behave alike.

ACKNOWLEDGEMENT

We sincerely appreciate all valuable **c***omments* and suggestions, which helped us to improve the quality of the research paper.

REFERENCES

Adhav KS, Nimkar AS, Dawande MV (2007) *N*-dimensional string cosmological model in Brans–Dicke theory of gravitation. Astrophysics Space Sci.310:231- 235.

Berman MS (1983) A Special law of variation for Hubble parameter. II Nuovo Cimento 74B. Number 2: 182-186.

Brans CH. and Dicke RH (1961) Physical Review 124: 925-935.

Kandalkar SP. and Samdurkar SW (2012) Bianchi Type-I Cosmological Model in Scalar Tensor Theories of Gravitation with Viscous Fluid Distribution. IOSR Journal of Mathematics 2(3): 39-43.

Katore SD, Shaikh AY (2012) Plane symmetric dark energy model in Brans-Dicke theory of gravitation. Bulgarian Journal of Physics 39(3):241-247.

Letelier PS (1983) String cosmologies. Phys. Rev. D.28: 2414-2419.

Lima JAS, Nobre MAS (1990) Class. Quantum Grav.7 :399-409.

Pawar DD. and Dagwal VJ. (2015) Tilted Kasner-Type Cosmological Models in Brans-Dicke Theory of Gravity. Prespacetime Journal 6(11):1165- 1170.

Reddy DRK., Santikumar R, Naidu RL (2012) Bianchi type-III cosmological model in *f(R,T)* theory of gravity. Astrophysics and space Science 342(1).249-252.

Reddy DRK. and Venkateswara Rao N (2001) Some cosmological models in scalar- tensor theory of gravitation. Astrophysics Space Sci.277(3):461-472.

Saez D and Ballester VJ.(1985) A Simple Coupling with Cosmological Implications Physical Letters A113(9):467-470.

Shri Ram and Tiwari SK (1998) Inhomogeneous Plane Symmetric Models in a Scalar- Tensor Theory. Astrophys. Space Sci,259: 91-97.

Singh T and Rai LN (1983).General Relativity and Gravitation B 15:875-902.

Ugale MR (2014) Cosmological model in Saez-Ballester theory of gravitation. International Journal of Mathematical Archive 5(3):280-282.

Science and Technology Journal Vol. 8 Issue 2 July 2020 ISSN: 2321-3388

The 2,2’ Dipyridyl-Induced Iron Starvation and its Effects on Growth and Photosynthesis in Cyanobacterium *Nostoc punctiforme* ATCC 29133

Rebecca Vanlalsangi[1], Loknath Samantha[2] and Jyotirmoy Bhattacharya[3]*
[1,2,3]Department of Biotechnology, Mizoram University,
PB No 190, Aizawl-796004, Mizoram, India
E-mail: [1]vanlalsangikawlni@gmail.com,
[2]loknathsamantha@gmail.com, [3]jyotirmoyb@rediffmail.com

Abstract—Iron is essential for growth of most organisms, including cyanobacteria, a ubiquitous and ecologically important group of microorganisms in nature. The present study was initiated to investigate the effects of iron starvation on the growth, frequency of heterocysts (the sites for nitrogen-fixation), photosynthetic pigments and photosynthesis in the filamentous, nitrogen-fixing cyanobacterium *Nostoc punctiforme* ATCC 29133. Iron starvation was achieved in cyanobacterial cultures by growing them in medium free of combined nitrogen containing 2,2’dipyridyl (a high affinity iron-chelator) without any addition of iron source. Compared to iron-sufficient control cultures, the iron-starved cultures showed decrease in growth determined for 15 days. The reduction in growth was coupled with a decreased heterocyst (N_2-fixation sites) frequency and the number of cells per filament measured after 2 and 4 days of iron-starvation. Similarly, a considerable drop in the concentration of photosynthetic pigments such as, phycocyanin and chlorophyll *a* were also noticed in iron-starved cultures. Carotenoid level, however, was higher in iron-starved cultures compared to control. The maximum quantum yield of photosystem II photochemistry indicating the photosynthetic efficiency was severely affected in iron-starved *Nostoc punctiforme* ATCC 29133. Overall, the results presented in this study suggest that deficiency of iron negatively impacts growth, photosynthesis and perhaps nitrogen-fixation in the cyanobacterium *N. punctiforme* ATCC 29133. Given the role of cyanobacteria in biofertilizer technology, it is suggested that iron bio-availability in agricultural fields may strongly impact the biofertilizer potential of diazotrophic cyanobacteria. Therefore, efforts to improve biofertilizer potential of cyanobacteria may be directed towards identifying strains which can better adapt to iron deficiency.

Keywords: Cyanobacteria, *Nostoc punctiforme*, Iron starvation, Heterocyst, Photosynthetic pigments.

INTRODUCTION

Iron is one of the most abundant elements on earth’s crust (5%). It exists in two redox forms, ferrous (Fe^{2+}) and ferric (Fe^{3+}). The Fe^{2+} (soluble) is rapidly oxidized to Fe^{3+} in aerobic and alkaline environments, leading to predominance of Fe^{3+} (insoluble) in many ecosystems ranging from earth’s oceans to soils. Thus, poor availability of iron, an essential nutritional element, becomes a key issue for most organisms, including oxygen-evolving photosynthetic cyanobacteria (Straus, 1994; Michel and Pistorius, 2004). Cyanobacteria exhibit many alterations in morphology, physiology, and gene expression as a response to iron deficiency. Prominent among them are changes in cell size, filament length reduction, loss of phycobilins, components of light harvesting pigment-protein complexes. The photosynthetic apparatus composed of photosystem II (PSII), PSI, the intersystem electron transport complex cytochrome b_6f, and the terminal electron acceptor ferredoxin are also synthesized at reduced levels in cyanobacteria undergoing iron starvation due to high requirement of iron (approximately 23-24 atoms) (Shi *et al.*, 2007). As a consequence the photosynthetic activity is severely reduced in iron-starved cyanobacteria. Similarly, in diazotrophic cyanobacteria, the frequency of heterocysts, (sites of N_2-fixation) transcript levels of nitrogenase-encoding genes (*nifHDK*), and nitrogenase activity have all been found to decrease considerably in diazotrophs facing iron limitation (Narayan *et al.*, 2011; Shi *et al.*, 2007; Wen-

Liang *et al.*, 2003). The assimilation of nitrate and nitrite (alternate nitrogen sources) also seems to be affected as nitrate- and nitrite-reductases lose their activities due to shortage of electron-donor, ferredoxin (Hardie *et al.*, 1983; Verstreate *et al.*, 1980). Thus, deficiency of iron creates secondary nitrogen limitation in cyanobacteria (Straus, 1994). Indeed, low iron availability has been reported to limit growth of phytoplanktons in many parts of the world’s oceans (Behrenfeld *et al.*, 1996).

In many cyanobacteria, adaptation to iron deficiency includes synthesis and secretion of siderophores and induction of highly efficient iron acquisition systems to scavenge iron from the environment (Hopkinson and Morel, 2009; Michel and Pistorius, 2004; Straus, 1994). Iron thus acquired from the environment is then stored in ferritin-like proteins to be used during protracted periods of iron starvation (Ekman *et al.*, 2014). The accumulation of an alternate Chlorophyll (Chl) *a*-binding complex CP43’, encoded by *isiA* (iron stress induced protein A), has also been shown to be important for acclimation to iron deficiency in many cyanobacteria (Michel and Pistorius, 2004; Singh and Sherman, 2007). IsiA binds to PSI trimers forming an IsiA-PSI supercomplex that increases effective cross-section of PSI so that more light can be harvested to sustain photosynthesis in absence of iron. Such large aggregates of IsiA can also dissipate excess light energy and thus protect cells from oxidative stress whether associated or not with PSI (Bibby *et al.*, 2001; Boekema *et al.*, 2001; Wang *et al.*, 2010). It has also been proposed that IsiA (Chl-reserve) may assist cells recover faster from iron deficiency stress by providing Chl to PSI, if and when iron becomes available (Fraser *et al.*, 2013; Singh and Sherman, 2007). Additionally, many cyanobacteria synthesize flavodoxin to functionally compensate the loss of iron-rich ferredoxin during iron-deficient growth (Michel and Pistorius, 2004; Straus, 1994).

A bioinformatics-based analysis has revealed that the filamentous, N_2-fixing cyanobacterium *Nostoc punctiforme* do not possess the gene encoding for *isiA* in its genome (Singh *et al.*, 2004). Similarly, it lacks the genes encoding for citrate-based siderophores (Hopkinson and Morel, 2009). Despite these unusual features, its response to iron starvation has not been studied earlier. Therefore, the present study was undertaken to determine the impact of iron starvation on growth, cellular morphology, pigmentation, and PSII photochemistry of this cyanobacterium.

MATERIALS AND METHODS

Strain and Culture Conditions: The cyanobacterium *Nostoc punctiforme* (hereafter referred to as *N. punctiforme*) was grown photoautotrophically at 25 °C in $BG11_0$-medium (pH 7.5) containing 30 μM ferric ammonium citrate (+Fe medium), and $BG11_0$-medium lacking ferric ammonium citrate, but added with 50 μM 2,2’-dipyridyl (-Fe medium) under continuous illumination (20 μmol m^{-2} s^{-1}) (Rippka *et al.*, 1979).

Microscopy: The number of cells was counted in approximately 7-10 filaments (vegetative cells and heterocysts) of *N. punctiforme* culture using a light microscope (Olympus). The frequency of heterocysts was calculated as: Heterocyst frequency (%) = Number of heterocysts/Number of vegetative cells + Number of heterocysts ×100.

Measurement of Growth: The growth of *N. punctiforme* cultures was measured by following optical density of cell suspensions at 750 nm, in a Cary 60 spectrophotometer (Agilent Technologies, USA).

Measurements of Photosynthetic Pigments: The levels of photosynthetic pigments phycocyanin (PC), chlorophyll *a* (Chl *a*), and carotenoids (Car) of intact *N. punctiforme* cultures were determined from the absorption spectra (visible range; 400-800nm) obtained using a Cary 60 spectrophotometer. The concentrations of PC were calculated from absorption at 620nm, Chl *a* at 680nm, and Car at 490 nm. The values of PC/cell, Chl *a*/cell, and Car/cell were derived using the formula $(A_{620}\text{-}A_{750})/A_{750}$, $(A_{680}\text{-}A_{750})/A_{750}$, and $(A_{495}\text{-}A_{750})/A_{750}$, respectively (Fraser *et al.*, 2013).

Photosynthetic Measurement by Chlorophyll Fluorescence: The chlorophyll fluorescence is a widely used in vivo method to measure photosynthetic performance of plants, algae and cyanobacteria (Baker, 2008). A pulse amplitude modulated fluorometer, Dual-PAM-100, (Waltz, Effeltrich, Germany) was used for photosynthetic measurements in cultures of *Nostoc punctiforme*, stirred in 1 cm^{-1} cm cuvettes at 25 °C. The maximum quantum yield of photosystem II (PSII) photochemistry (F_v/F_m; reflects maximum efficiency at which light absorbed by PSII is used for reduction of primary quinine electron acceptor of PSII, Q_A) was determined after incubation of the cyanobacterial cultures in dark for 15 min followed by illumination of the sample with a low-irradiance measuring light (0.24 μmol m^{-2} s^{-1}) to determine F_o (minimal fluorescence yield of dark-adapted samples with all PSII centers open/oxidized). A saturating pulse of white light (600 ms, 1000 μmol m^{-2} s^{-1}) was then applied to the sample to determine F_m (maximal fluorescence of dark-adapted samples with all PSII centers closed/reduced). The F_v value (variable fluorescence of dark-adapted samples) was then derived from (F_m-F_0) (Genty *et al.*, 1989).

RESULTS

The effect of iron-limitation on growth was assessed by using log-phase cultures of *N. punctiforme* grown in iron-sufficient BG11o-medium as source of inoculum. Such cultures were washed twice with $BG11_0$-medium devoid of any iron source (30 µM of ferric ammonium citrate) before re-suspending in the same medium containing 50 µM of 2,2'-dipyridyl, an high affinity iron chelator (-Fe-medium). The changes in optical density (OD) of cultures were periodically monitored at 750 nm. As shown in Fig. 1, *N. punctiforme* grew well in medium containing normal concentration of iron. However, its growth was completely ceased in medium devoid of free iron. The number of cells per filament and frequency of heterocysts were evaluated by light microscopy in cultures of *N. punctiforme* after 2 and 4 days of incubation in medium with and without iron. Such examination did not reveal lysis of cells. Compared to iron-sufficient cultures, the number of cells per filament in *N. punctiforme* (Fig. 2 A) dropped from 67 to 38 and from 76 to 26 after 2 and 4 days of incubation, respectively. Whereas, an approximately 50 % drop was noted in the frequency of heterocysts in iron-starved cultures after day 2. No further significant drop in heterocyst frequency was detected after day 4 (Fig. 2B). These results suggest that iron starvation leads not only to reduction in growth, but also reduces number of cells per filament and frequency of heterocysts in *N. punctiforme*.

Such effects on growth and morphology of iron-starved *N. punctiforme* was paralleled by a clear change in cellular pigment concentration; the appearance of *N. punctiforme* cultures changed progressively from blue green to yellow as incubation was prolonged in medium devoid of iron (data not shown). To quantify the changes in the concentration of photosynthetic pigments, chlorophyll *a* (Chl *a*), phycocyanin (PC), and carotenoid (Car) levels were determined from the whole-cell absorption spectra of iron-sufficient and iron-starved cultures of *N. punctiforme* (Fig. 3 A, B and C). The levels of both Chl *a* and PC decreased in iron-starved cultures compared with their respective iron-sufficient cultures on per cell basis. The reduction in Chl *a* concentration was faster than reduction in PC level. However, the Car levels per cell did not decrease in the iron-starved cultures, and instead, was maintained at somewhat higher levels than in iron-sufficient cultures. These results suggest that, except Car, iron starvation impacts the accumulation of Chl *a* and PC in *N. punctiforme*. The photosynthetic performance was also measured in the cultures of *N. punctiforme* iron-starved for 2 days. The maximal PSII quantum yield (F_v/F_m) in iron-starved *N. punctiforme* (Fig. 4) decreased by 58 %, compared with control cultures. These results suggested that iron starvation affects photosynthetic pigments and photosynthetic activity in *N. punctiforme*.

Fig. 1. Effect of iron starvation on growth of *N. punctiforme.* The log-phase cultures of *N. punctiforme* were harvested and washed. Such cultures were transferred to $BG11_0$-medium (iron-sufficient, +Fe; iron-deficient, containing 50 µM 2,2'-dipyridyl and lacking ferric ammonium citrate, -Fe) at equal culture density and growth was measured at regular intervals by following optical density (OD) at 750 nm. Error bars, sometimes smaller than the symbols, represent mean±standard deviation of three experiments.

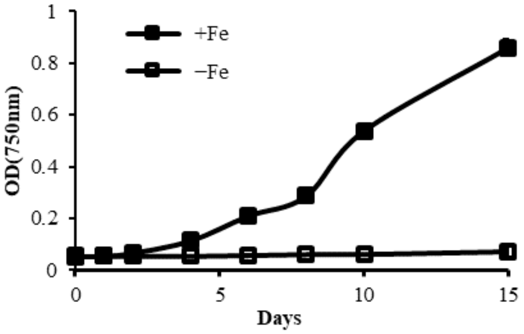

Fig. 1

Fig. 2. Effect of iron starvation on number of cells per filament and heterocyst frequency in *N. punctiforme*. The number of cells per filament and heterocyst frequency (A and B, respectively) was counted in 2 and 4 days-old +Fe and -Fe grown cultures. Approximately 1000 cells of each were counted under a light microscope and the error bars shown represent mean±standard deviation of three experiments. Asterisks (**, *P*<0.01; ***, *P*<0.001) above the bar denote significant difference from control values.

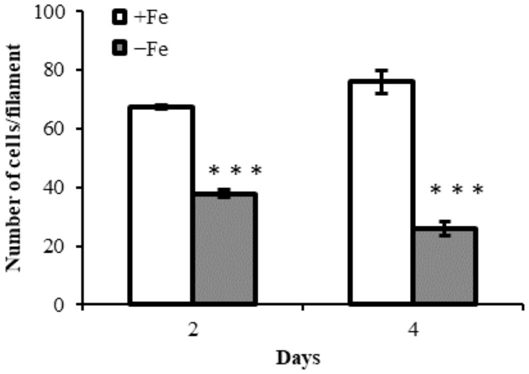

Fig. 2A

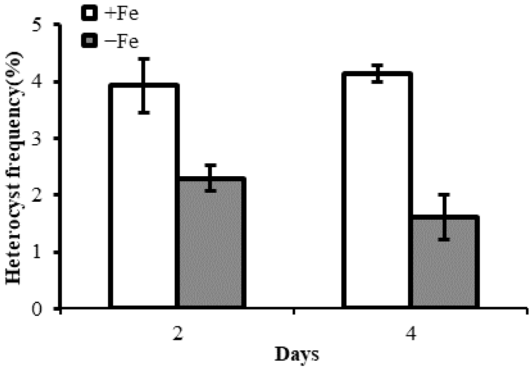

Fig. 2B

Fig. 3. Effect of iron starvation on photosynthetic pigments in *N. punctiforme*. The pigment levels, chlorophyll *a* (Chl *a*/cell) phycocyanin (PC/cell) and carotenoid (Car/cell) (A, B and C, respectively) were determined from whole-cell absorption spectra of 2, 4, and 8-days old +Fe and –Fe grown cultures. Error bars shown represent mean±standard deviation of three experiments.

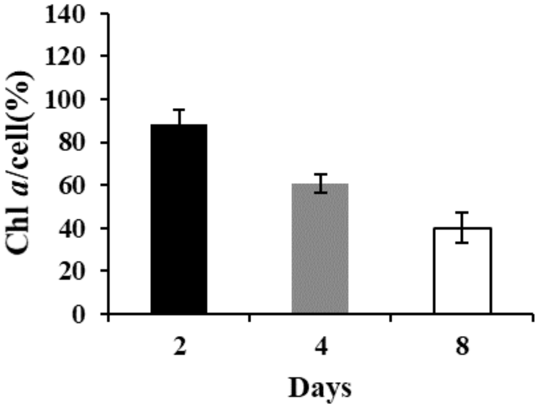

Fig. 3A

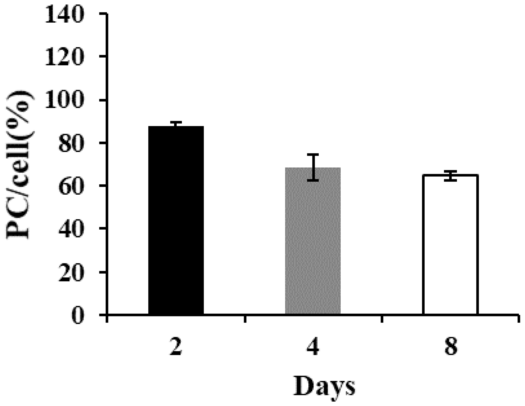

Fig. 3B

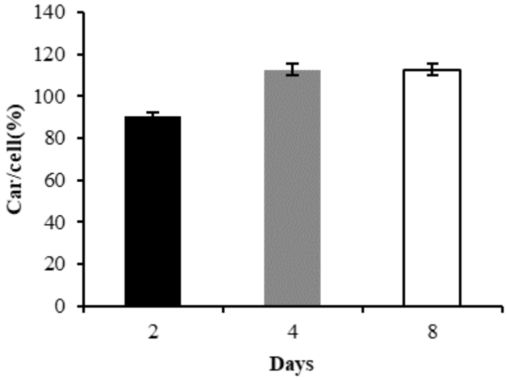

Fig. 3C

Fig. 4. Effect of iron starvation on maximal quantum yield (F_v/F_m) of PSII photochemistry in *N. punctiforme*. The 2-days old cultures grown in BG11$_0$-medium (iron-sufficient, +Fe; iron-deficient, containing 50 µM 2,2’-dipyridyl and lacking ferric ammonium citrate, -Fe) were harvested, washed and used for maximal quantum yield measurement at a Chl *a* concentration of 3 µg Chl *a*.ml^{-1} by pulse amplitude modulated fluorometry. Error bars represent mean±standard deviation of three experiments.

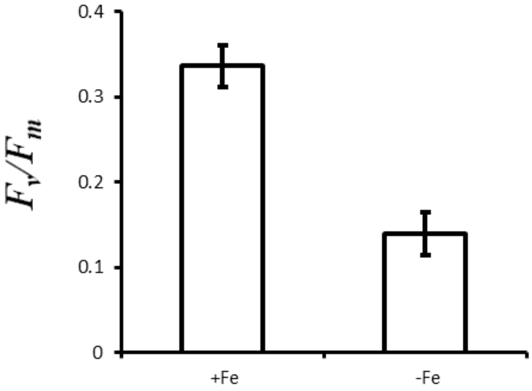

Fig. 4

DISCUSSION

The method commonly used to hasten the process of iron-starvation in cyanobacteria is to add iron-chelators (deferoxamine B/diethylenetriaminopentaacetic acid/EDTA) to iron-free growth medium (Shcolnick *et al*., 2009). During the present study, quick and complete growth arrest was achieved in *N. punctiforme* by the addition of 2,2’-dipyridyl (50 µM) in BG11$_0$-medium lacking iron-source. Similar effect of 2,2’-dipyridyl, an high affinity iron chelator, has been observed earlier on growth of *Anabaena* PCC 7120 and *Synechocystis* PCC 6803 (Cheng and He, 2014; Latifi *et al*., 2005; Xu *et al*., 2003). Morphological analysis revealed that the number of cells per filament of *N. punctiforme* reduced as the incubation continued in iron-free medium. A similar fragmentation and short filaments were also noticed in *Trichodesmium* IMS101 during iron-limited growth (Küpper *et al*., 2008). In *Synechococcus elongatus*, the cell length was found to be reduced, whereas enlarged and vacuolated cells were observed in filaments of *Fremyella diplosiphon* in response to iron-limitation (Benešová *et al*., 2000; Pattanaik *et al*., 2014). These results suggest that iron starvation differentially affects cellular morphology in cyanobacteria. Concomitant with changes in number of cells per filament, the frequency of heterocysts also declined in iron-starved cultures. Since nitrogenase (catalyzes conversion of molecular nitrogen into ammonia) is localized in heterocysts, it is quite possible that a loss in heterocyst frequency would also be paralleled by simultaneous decrease in nitrogenase abundance and activity. Indeed, iron-starvation has been shown to affect heterocyst frequency, transcript levels of nitrogenase and activity in diazotrophic cyanobacteria (Narayan *et al*., 2011; Shi *et al*., 2007; Wen-Liang *et al*., 2003).

One of the visual indicators of iron-deficient growth in cyanobacteria is chlorosis, also observed in iron-starved *N. punctiforme*. It is known that the biosynthesis of chromophores requires haem and ferredoxin-dependent reductases (Beale, 1994). Hence, it is quite likely that lack of iron would lead to decreased synthesis of photosynthetic pigments (Cheng and He, 2014; Fraser *et al*., 2013; Michel and Pistorius, 2004; Straus, 1994). Consistent with this reasoning, pigment analysis revealed that the accumulation of PC and Chl *a* reduced in iron-starved cultures this cyanobacterium compared with its iron-sufficient cultures. It has been demonstrated earlier that there are variations among cyanobacteria in the way they modulate their photosynthetic pigment levels during iron-limited growth; the PC/Chl *a* ratio decreases in *Synechococcus elongatus* and *Thermosynechococcus elongatus*, whereas this ratio either increases or remains constant in *Synechocystis* PCC 6803 and *Arthrospira maxima* (Boulay *et al*., 2008). Possibly, *N. punctiforme* represents the latter group, as its PC/Chl *a* ratio was slightly higher during iron-starved growth than when it was grown with sufficient iron. The pigment analysis also suggested that the Car/cell levels increased in iron-starved cultures of *N. punctiforme* compared to control cultures. Possibly, enhanced carotenoid levels dissipate excess light energy, and thereby curtail iron starvation induced formation of reactive oxygen species (ROS) in *N. punctiforme* (Boulay *et al*., 2008). An increase in carotenoid level has been detected earlier in an IsiA-lacking mutant of *Synechococcus* PCC 7942 (Burnap *et al*., 1993). Furthermore, the iron-starved *N. punctiforme* cultures displayed marked alteration in PSII photochemistry. The maximum quantum efficiency of open PSII centers measured as F_v/F_m ratio decreased considerably in iron-starved cultures, suggesting that the photosynthetic performance of this cyanobacterium is severely compromised due to lack of iron. Such an effect of iron-starvation on photosynthetic performance has also been demonstrated for many other iron-starved cyanobacteria (Cheng and He, 2014; Fraser *et al*., 2013; Ivanov *et al*., 2000; Straus, 1994).

CONCLUSION

The results presented in this study suggests that 2,2'-dipyridyl induced iron starvation leads to multiple defects in the diazotrophic cyanobacterium *N. punctiforme*. Such defects include (1) impairment of diazotrophic growth, (2) reduction in number of cells per filament, (3) decrease in heterocyst frequency, (4) reduction in the levels of phycocyanin and chlorophyll *a*, but not carotenoids, and (5) decreased PSII photochemistry measured as maximal quantum yield of photosynthesis. Based on these observations in *N. punctiforme*, it is suggested that poor bio-availability of iron, commonly occurring in many agricultural fields, may be a crucial factor limiting biofertilizer potential of diazotrophic cyanobacteria.

ACKNOWLEDGEMENTS

RV, LS and JB acknowledge the financial support from University Grant Commission (UGC) and Department of Biotechnology (DBT), Government of India.

REFERENCES

Baker NR (2008): Chlorophyll fluorescence: A probe of photosynthesis in vivo. Annu Rev Plant Biol 59: 89-113.

Beale SI (1994) Biosynthesis of cyanobacterial tetrapyrole pigments: hemes, cholorophylls, and phycobilins. In: Bryant DA (ed) The Molecular Biology of Cyanobacteria. Kluwer Academic Publ, Dordrecht, The Netherland, pp. 519-558.

Behrenfeld MJ, Bale AJ, Kolber ZS, Aiken J, Falkowski PG (1996) Confirmation of iron limitation of phytoplankton photosynthesis in the equatorial Pacific ocean. Nature 383: 508-511.

Benesova J, Nickova K, Ferimazova N, Stys D (2000) Morphological and physiological differences in *Synechococcus elongatus* during continuous cultivation at high iron, low iron, and iron deficient medium. Photosynthetica 38: 233-241.

Bibby TS, Nield J, Barber J (2001) Iron deficiency induces the formation of an antenna ring around trimeic photosystem I in cyanobacteria. Nature 412: 743-745.

Boekema EJ, Hifney A, Yakushevska AE, Piotrowski M, Keegstra W, Berry S, Michel KP, Pistorius EK, Kruip J (2001) A giant chlorophyll-protein complex induced by iron deficiency in cyanobacteria. Nature 412: 745-748.

Boulay C, Abasova L, Six C, Vass I, Kirilovsky D (2008) Occurrence and function of the orange carotenoid protein in photoprotective mechanisms in various cyanobacteria. Biochim Biophys Acta 1777: 1344-1354.

Burnap RL, Troyan T, Sherman LA (1993) The highly abundant chlorophyll-protein of iron-deficient *Synechococcus* sp. PCC 7942 (CP43') is encoded by the *isiA* gene. Plant Physiol 103: 893-902.

Cheng D, He Q (2014) PfsR is a key regulator of iron homeostasis in *Synechocystis* PCC 6803. PLoS One 9: e101743.

Ekman M, Sandh G, Nenninger A, Oliveira P, Stensjö K (2014) Cellular and functional specificity among ferritin-like proteins in the multicellular cyanobacterium *Nostoc punctiforme*. Environ Microbiol 16: 829-844.

Fraser JM, Tulk SE, Jeans JA, Campbell DA, Bibby TS, Cockshutt AM (2013) Photophysiological and photosynthetic complex changes during iron starvation in *Synechocystis* sp. PCC 6803 and *Synechococcus elongatus* PCC 7942. PLoS One 8: e59861.

Genty B, Briantais JM, Baker NR (1989) The relationship between the quantum yield of photosynthetic electron transport and quenching of chlorophyll fluorescence. Biochim Biophys Acta 990: 87-92.

Hardie LP, Balkwill DL, Stevens SE Jr (1983) Effects of iron starvation on the physiology of the cyanobacterium *Agmenellum quadruplicatum*. Appl Environ Microbiol 45: 999-1006.

Hopkinson BM, Morel FM (2009) The role of siderophores in iron acquisition by photosynthetic marine microorganisms. Biometals 22: 659-669.

Ivanov AG, Park YI, Miskiewicz E, Raven JA, Huner NP, Öquist G (2000) Iron stress restricts photosynthetic intersystem electron transport in *Synechococcus* sp. PCC 7942. FEBS Lett 485: 173-177.

Küpper H, Setlík I, Seibert S, Prásil O, Setlikova E, Strittmatter M, Levitan O, Lohscheider J, Adamska I, Berman-Frank I (2008) Iron limitation in the marine cyanobacterium *Trichodesmium* reveals new insights into regulation of photosynthesis and nitrogen fixation. New Phytol 179: 784-798.

Latifi A, Jeanjean R, Lemeille S, Havaux M, Zhang CC (2005) Iron starvation leads to oxidative stress in *Anabaena* sp. strain PCC 7120. J Bacteriol 187: 6596-6598.

Michel KP, Pistorius EK (2004) Adaptation of the photosynthetic electron transport chain in cyanobacteria to iron deficiency: the function of IdiA and IsiA. Physiol Plant 120: 36-50.

Narayan OP, Kumari N, Rai LC (2011) Iron starvation-induced proteomic changes in *Anabaena* (*Nostoc*) sp. PCC 7120: exploring survival strategy. J Microbiol Biotechnol 21: 136-146.

Pattanaik B, Busch AW, Hu P, Chen J, Montgomery BL (2014) Responses to iron limitation are impacted by light quality and regulated by RcaE in the chromatically acclimating cyanobacterium *Fremyella diplosiphon*. Microbiology 160: 992-1005.

Rippka R, Deruelles J, Waterbury JB, Herdman M, Stanier RY (1979) Generic assignments, strain histories and properties of pure cultures of cyanobacteria. J Gen Microbiol 111: 1-61.

Shcolnick S, Summerfield TC, Reytman L, Sherman LA, Keren N (2009) The mechanism of iron homeostasis in the unicellular cyanobacterium *Synechocystis* sp. PCC 6803 and its relationship to oxidative stress. Plant Physiol 150: 2045-2056.

Shi T, Sun Y, Falkowski PG (2007) Effects of iron limitation on the expression of metabolic genes in the marine cyanobacterium *Trichodesmium erythraeum* IMS 101. Environ Microbiol 9: 2945-2956.

Singh AK, Sherman LA (2007) Reflections on the function of IsiA, a cyanobacterial stress-inducible, Chl-binding protein. Photosynth Res 93: 17-25.

Singh AK, Li H, Sherman LA (2004) Microarray analysis and redox control of gene expression in the cyanobacterium *Synechocystis* sp. PCC 6803. Physiol Plant. 120: 27-35.

Straus NA (1994) Iron deprivation: physiology and gene regulation. In: Bryant DA (ed) The Molecular Biology of Cyanobacteria. Kluwer Academic Publ, Dordrecht, The Netherland, pp. 731-750.

Verstreate DR, Storch TA, Dunham VL (1980) A comparison of the influence of iron on the growth and nitrate metabolism of *Anabaena* and *Scenedesmus*. Physiol Plant 50: 47-51.

Wang Q, Hall CL, Al-Adami MZ, He Q (2010) IsiA is required for the formation of photosystem I supercomplexes and for efficient state transition in *Synechocystis* PCC 6803. PLoS One 5: e10432.

Wen-Liang X, Yong-Ding L, Cheng-Cai Z (2003) Effect of iron deficiency on heterocyst differentiation and physiology of the filamentous cyanobacterium *Anabaena* sp. PCC7120. Wuhan Univ J Nat Sci 8: 880–884.

Xu WL, Jeanjean R, Liu YD, Cheng-Cai Z (2003) *pkn22* (*alr2502*) encoding a putative Ser/Thr kinase in the cyanobacterium *Anabaena* sp. PCC 7120 is induced by both iron starvation and oxidative stress and regulates the expression of *isiA*. FEBS Lett 553: 179-182.

Author Index